University of Alberta

High Temperature Behaviour of WC and B_4C in Ni-Based Metal Matrix Composites.

by

Kimberley Anne Sandy ©

A thesis submitted to the Faculty of Graduate Studies and Research

in partial fulfillment of the requirements for the degree of

Master of Science

In

Materials Engineering

Department of Chemical and Materials Engineering

Edmonton, Alberta

Fall 2006

Abstract

Metal matrix composites (MMC) can be applied to steel substrates as wear coatings. MMC's consist of a reinforcing phase combined with a tough metal matrix. The behaviour of two nickel MMC's is investigated: Ni-WC and Ni-B_4C. Experiments were designed and carried out where WC or B_4C were added to molten Ni. The melt was sampled following the addition of the ceramic. Analysis techniques included chemical analysis, optical microscopy, electron microprobe microanalysis and x-ray diffraction. In the Ni-WC system a portion of WC reacted, dissolving W in the nickel. Reactions in the Ni-B_4C system produced nickel-borides. A thermodynamic analysis of the systems was also completed. The Ni-WC thermodynamics supported the experimental results. The Ni-B_4C thermodynamics was also in agreement with the experimental results in all but one case. The thermodynamic analysis also explored the use of Cr, Mn and Cu as matrix materials. This analysis suggested that Cu might be suitable in a Cu-Ni alloy.

Acknowledgements.

I would like to take the time to thank several people who made this thesis possible.

To my supervisor, Dr. Hani Henein, your enthusiasm, encouragement and faith was unfailing. I could not have done it without you.

Thank you to Dr. Kevin Jaansalu of Montana Tech. of the University of Montana for much-appreciated advice in thermodynamic analyses. This advice proved invaluable in the writing of this thesis. I would like to thank Stefano Chiovelli of Syncrude Canada Ltd. for the idea as well as technical support. I would also like to thank Syncrude Canada Ltd. and NSERC for their financial support. Dr Qi Liu at the University of Alberta for advice in sample preparation. Diane Caird for numerous hours spent analysing X-Ray samples.

I would like to thank my research group at the Advanced Materials and Processing Lab at the University of Alberta.

Finally I would like to thank my family: my parents for their optimism and support; my husband for his love and belief; my brother and sister-in-law for their confidence in me. Last, thank you to my niece and my nephew for bringing sunshine and hope into my life.

To my family for their infallible support and encouragement.

Table of Contents.

List of Tables.

List of Figures.

Nomenclature.

A	amperes (A)
L	polynomial for excess Gibb's free energy
N	number of data points (number)
P	pressure (Pa)
R	universal gas constant (8.314 J/mol*K)
R$_1$	vertical dimension of electron beam within the sample interaction volume (μm)
S	horizontal dimension of electron beam/ sample interaction volume (μm)
T	temperature (K)
V	volts (V)
E$_o$	accelerating voltage (V)
G$_{ex}$	excess Gibb's free energy (J/mol)
I_a^+	ion current of species a (A)
I_b^+	ion current of species b (A)
M$^o_{(Ni/B4C)}$	nominal molar ratio (moles of Ni/ moles of B_4C)
M$^o_{(Ni/WC)}$	nominal molar ratio (moles of Ni/ moles of WC)
MPa	megapascales (MPa)
d	interplanar spacing in a material (m)
g	grams (g)
(g)	gas

g_i	free energy of component I (J/mol)
h	hours
l	litres (l)
(l)	liquid
m	metres (m)
n	integer (number)
s	seconds (s)
(s)	solid
$\bar{x}$	average of data values, x
at%	atomic percent (%)
cm	centimetres (cm)
min	minutes (min)
mm	millimetres (mm)
vol%	volume percent (%)
wt%	weight percent (%)
x_a	mole fraction of species a
x_b	mole fraction of species b
x_c^*	mole fraction of C
x_i	data value at data point I
x_B	mole fraction of B
ΔCp	heat capacity change (J/mol*K)
ΔG°	standard Gibb's free energy change (J/mol)

λ	wavelength (nm)
γ_α	activity coefficient of species A
θ	angle of diffraction (^{o})
ρ	density (kg/m^3)
σ	standard deviation

1.0 Introduction.

Wear of components cost the oil and mining industry billions of dollars annually as a result of digging, transporting and processing of ore[1,2]. One of the methods to minimise wear of component parts is to coat them with a wear resistant material. There are many different types of coatings that are used in different situations[1, 2, 3, 4, 5, 6, 7]. Coatings made of metal matrix composite (MMC) materials are being developed and used industrially[3]. These MMC coatings consist of hard, particulates dispersed throughout a ductile metal matrix[3]. The combination of particulate hardness and matrix ductility result in a material that is both strong and tough[3]. To take advantage of the strength and toughness it is necessary to create a bond between the matrix material and the particulates. This bond behaves as the pathway for the transmission of an applied load when the material is under stress[3]. The coatings are processed at high temperature to facilitate this bond[3].

In MMC coatings, the reinforcing particulates are frequently ceramic materials[3, 4, 5, 7]. Tungsten carbide (WC) has been frequently used as the reinforcing material[3, 4, 5, 7]. Creating wear-resistant overlays with WC using high-temperature processes, such as plasma transferred arc welding (PTA), has been successful. Recently, interest in using boron carbide (B_4C) as the ceramic in MMC's has increased. This is because boron carbide is both harder and less dense than tungsten carbide. Optimizing a procedure for creating a boron carbide MMC coating using a high-temperature processing route, such

1

as PTA, has been fraught with difficulty.

The experimental set-up for the PTA process is shown in Figure 1.1[3, 4]. The PTA process
uses a non-consumable tungsten (W) electrode with a two-nozzle system used to
minimize the arc maintained between the electrode and the nozzle. The work-piece is
placed below the electrode, while the orifice and shield gases are blown over the piece.
The ceramic powder is physically mixed with the metal matrix powder and the orifice
gas[3]. The powder and gas are fed together[3]. One of the drawbacks of this technique is that
the extremely high temperatures reached in the plasma arc can degrade the properties of
the ceramic material[4].
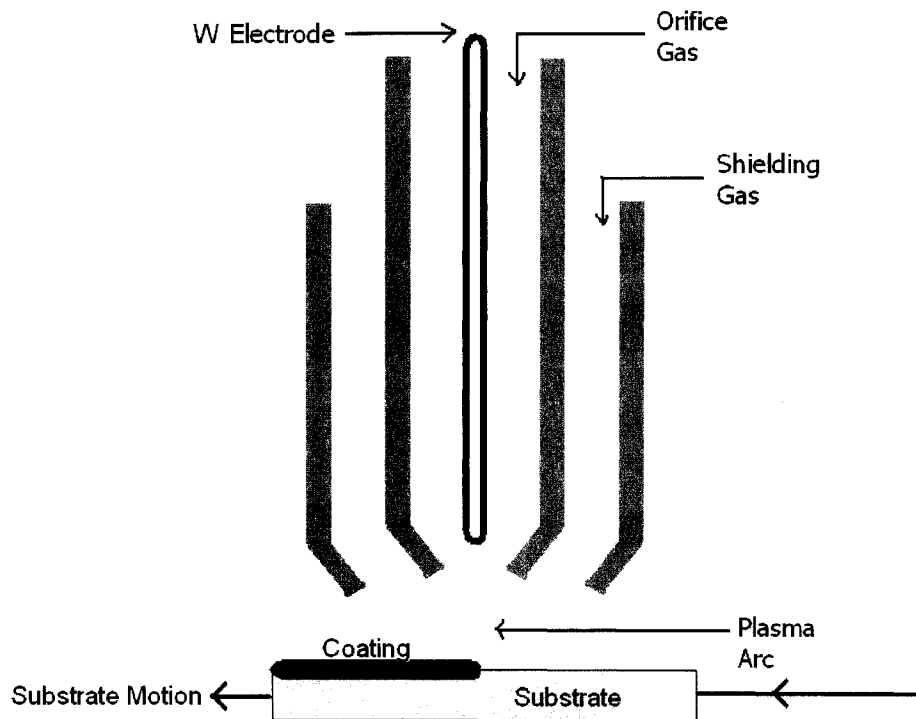
Figure 1.1: Experimental set-up for PTA[3, 4].

2

1.1 PTA using Tungsten Carbide.

There are several operating parameters that must be considered for the PTA process.

These parameters include current, voltage and powder feed rate. Typical PTA parameters

for PTA are found in Table 1.1[4]. These parameters enabled a good dispersion of tungsten

carbide throughout the metal matrix[4]. Neville et al. utilized a NiCrB alloy as the matrix

material.

Table 1.1: Typical PTA parameters for WC- NiCrB matrix[4].

Current (A)	Voltage (V)	Powder Feed Rate (kg/s)	Carrier Gas Flow (l/s)	Shielding Gas Flow (l/s)	Plasma Gas Flow (l/s)
100-130	24-25	6.7×10^{-4}	0.1	0.467	0.167

The powdered feed material consisted of 65wt% WC (balance NiCrB alloy). An as-

welded sample of this material, showing the dispersion of tungsten carbide particles, is

seen in Figure 1.2[5]. A homogeneous dispersion of tungsten carbide particles is seen in

this figure. As previously mentioned, this is the desired situation. As the material is

loaded, both the ductile, nickel-based matrix and the hard WC particles can carry a

portion of the load. It is necessary to metallurgically bond the WC to the NiCrB matrix,

but, if the reaction between the two proceeds too far, the MMC properties will be

degraded[3, 4]. For example, if a significant portion of the WC particles breakdown,

3

graphite would be present in the sample. Graphite is a solid lubricant, and, therefore, would be a weak spot in the MMC under loading. In Figure 1.2, the edges of the WC particles appear to be angular, similar to the WC feed material[3]. The appearance of the WC particles in Figure 1.2 suggests that the WC was not highly degraded during PTA. This indicates that the plasma transfer arc welding of tungsten carbide with a nickel matrix is successful.
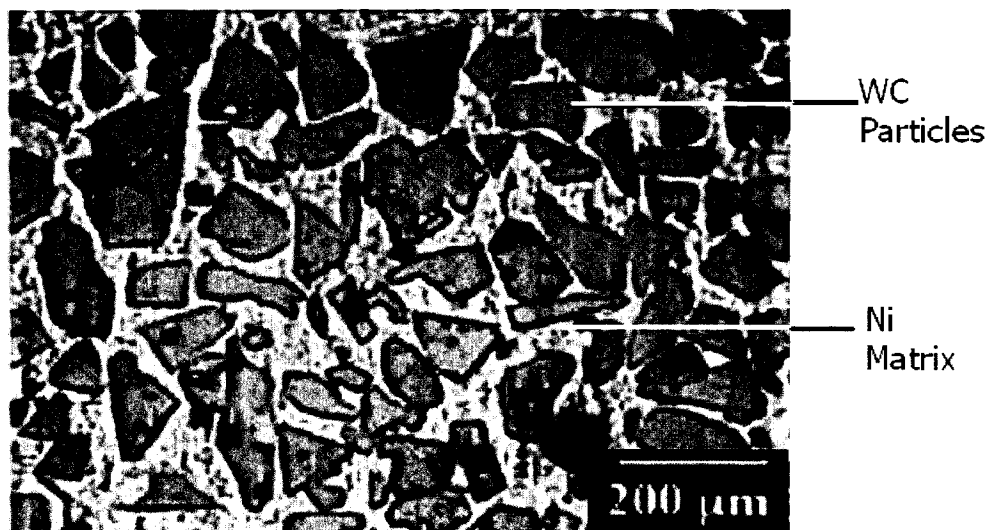
Figure 1.2: Micrograph of PTA welded Ni-WC sample[5] using WC particles of 80-325mesh (45-180 μm).

1.2 PTA using Boron Carbide.

The PTA process has been used in an attempt to create wear-resistant B_4C-containing, MMC. When this was attempted using a NiCrB matrix, degradation and poor distribution of the B_4C was seen[4].

4

It was anticipated that the behaviour of B_4C, when PTA welded with a NiCrB matrix, would be similar to that of WC[4]. Therefore, similar PTA parameters were employed for PTA welding of boron carbide (Table 1.1). These parameters were varied in an attempt to find a combination that would lead to the successful creation of a B_4C-NiCrB MMC. Following PTA, experimental samples of B_4C/ Ni were microscopically evaluated. It was noted that the majority of the boron carbide powder was not present in the final weld overlay[4]. There are three possible explanations for this. The first is that the B_4C powder did not actually enter the weld due to the high rate of powder feed. The flow rate of the carrier gas caused the boron carbide powder to be bounced off of the weld area. The second possibility is that the B_4C particles were degraded due to the high temperature of the torch. For thermal degradation to occur, the B_4C particles may have reached a temperature exceeding approximately $2723K$[8], above which liquid is formed.

Temperatures exceeding $2723K$ are attainable by PTA[4]. The third possibility is that the B_4C reacted with the matrix. Both energy dispersive x-ray analysis (EDX) and Micro-Raman spectroscopy were utilized. These analyses revealed that particles that were previously, microscopically, identified as "carbides" contained carbon but no boron[4]. These degraded B_4C particles can be seen in Figure 1.3. This absence of boron was taken as evidence of B_4C degradation.

In an attempt to reduce the degradation of the B_4C powder, a nickel coating was applied

5

to it. This coating was intended to protect the powder from thermal degradation and

increase the weight of the powder so the boron carbide particles were not bounced from

the weld by the force of the carrier gas. The coated powder[4] had an average density of

approximately 4500 kg/m^3. Examination by microscopy revealed that much of the boron

carbide powder was still thermally degraded[4]. However, there were powder particles that

retained small amounts of boron carbide. Though this was a positive development,

porosity was evident surrounding the powder particles due to the degradation[4]. Further

testing, varying the thickness of the nickel coating, was done. The results of these tests

showed that increasing the nickel thickness did increase the amount of B_4C remaining but

degradation still occurred[4], making the results undesirable.
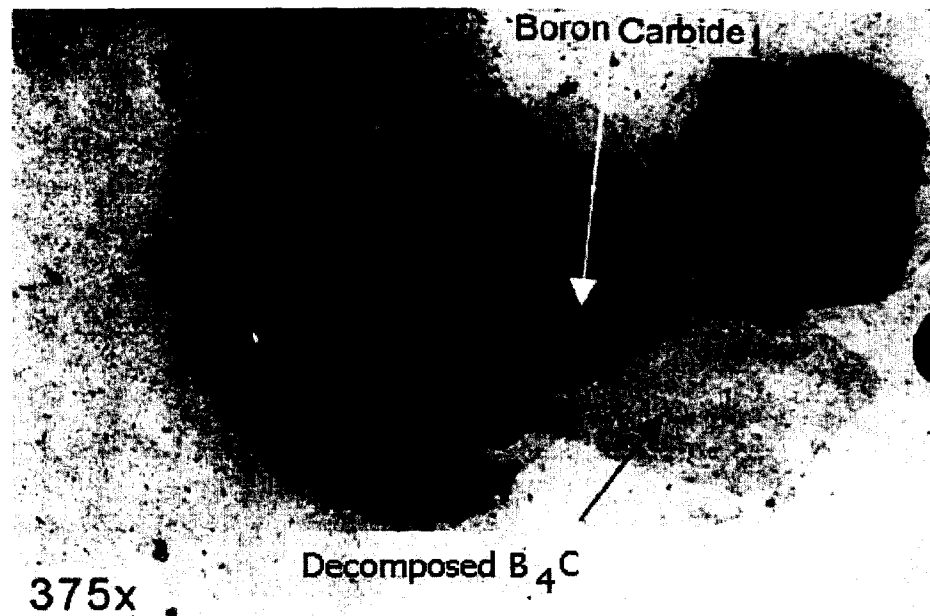
Figure 1.3: Mixed B_4C and degraded B_4C sample[4].

6

1.3 Summary.

It has been shown that there are difficulties associated with replacing WC with B_4C in PTA welded samples[4]. When PTA was carried out with uncoated B_4C particles, there was no B_4C left in the weld overlay. This was attributed to either the high flow rate of the carrier gas or to thermal decomposition of the B_4C particles. An attempt was made to see if coating B_4C powder with nickel would improve the durability of the boron carbide particles. This resulted in limited success. The boron carbide particles still degraded but not to the extent that the uncoated particles degraded[4]. Therefore, a more in-depth investigation into the high temperature behaviour of B_4C and nickel was warranted.

The present study is an attempt to better understand why the high temperature behaviour of WC is drastically different from that of B_4C. This difference in behaviour causes the processing of WC-Ni MMC's to be successful and the PTA of B_4C-Ni MMC's to be unsuccessful. A review of the literature describing the high temperature behaviour of WC, B_4C and Ni was prepared (Chapter 2.0).

Once the behaviour of these two systems was better understood, experiments to further investigate the high-temperature behaviour of the two systems, Ni-WC and Ni-B_4C, were designed and carried out (described in Chapter 3.0). In Chapter 3.0, experimental samples were analysed using several techniques including, chemical analysis, optical microscopy (OM), electron microprobe (EPMA) and X-Ray Diffraction (XRD). When considered in

7

combination, these techniques allowed several conclusions to be drawn regarding the behaviour of the Ni-WC and the Ni-B$_4$C systems. Chapter 5.0 discusses thermodynamic calculations that were done on the Ni-WC, Ni-B$_4$C systems as well as the analysis prepared for systems utilizing metals other than Ni as the matrix material. Finally, in Chapter 6.0, the summary and future work are presented.

8

2.0 Literature Survey.

A literature search of the two systems of interest, Ni-WC and Ni-B$_4$C was carried out. The properties and behaviours of the two ceramics, WC and B$_4$C were considered. Of particular interest was the binary phase diagrams of the W-C, B-C and Ni-B systems, which were used to determine the temperature transitions and the stoichiometry of any compounds formed. The high-temperature behaviour of WC and B$_4$C separately as well as in contact with other materials was also reviewed.

2.1 Tungsten Carbide.

The use of tungsten carbide has been driven by its high hardness and strength[9]. It is the properties of WC, which make it an appropriate ceramic additive for wear resistant coatings in many industrial applications such as slurry transport lines[4]. A popular matrix material is nickel or a nickel alloy[1, 2, 5]. There are several methods used to form MMC coatings with Ni or a Ni alloy and WC. These are PTA welding[3, 4, 5], liquid phase sintering[3] as well as laser cladding[7, 12]. PTA has been discussed in Chapter 1.0.

2.1.1 Properties and phase diagram for WC.

Tungsten carbide was first discovered in the 1890's[8]. It is among the hardest materials that are readily available for industrial use[9]. Some of the properties of this ceramic, such

9

as the high hardness and elevated melting point temperature, make it suitable for use in situations where wear occurs. Table 2.1 shows a list of pertinent physical properties of WC.

Table 2.1: Physical properties of WC[9].

Property	Value
Hardness (Knoop, 100g)	2.1×10^7 kg/ m^2
Melting Point	2873 K
Density	1.57×10^4 kg/m^3
Crystal Structure	Hexagonal

The binary W-C phase diagram[10], at 1 atm, is shown in Figure 2.1. It can be seen that there are three tungsten carbides that are possible: WC, W$_2$C and WC$_{1-x}$ (cubic structure). There is a eutectic reaction at 2980K, which results in the formation of a mixture of W and W$_2$C up to approximately 3wt% C[10]. W$_2$C is formed below approximately 3004K around 3wt% C[10]. As the temperature is decreased from 3004K, there is an area of stability for W$_2$C, which extends to a minimum of approximately 2.4wt% C at 2975K and a maximum of approximately 3.1wt% C at 2800K. This area converges at 1523K and approximately 3wt% C. Below this temperature, over the composition range from 0 wt % C to 3wt % C, there is a eutectoid reaction which results in the formation of a mixture of WC and W. WC is seen at its stoichiometric ratio at a weight percent carbon of 6.1.

10

Above 6.1wt% C, a mixture of WC and graphite is seen[3]. It can also be seen from the

phase diagram that the only binary W-C compound, which is stable at room temperature,

298K, is WC. However, the decomposition of W_2C is very slow, taking hundreds of

hours[10]. This could result in metastable W_2C being present at room temperature.
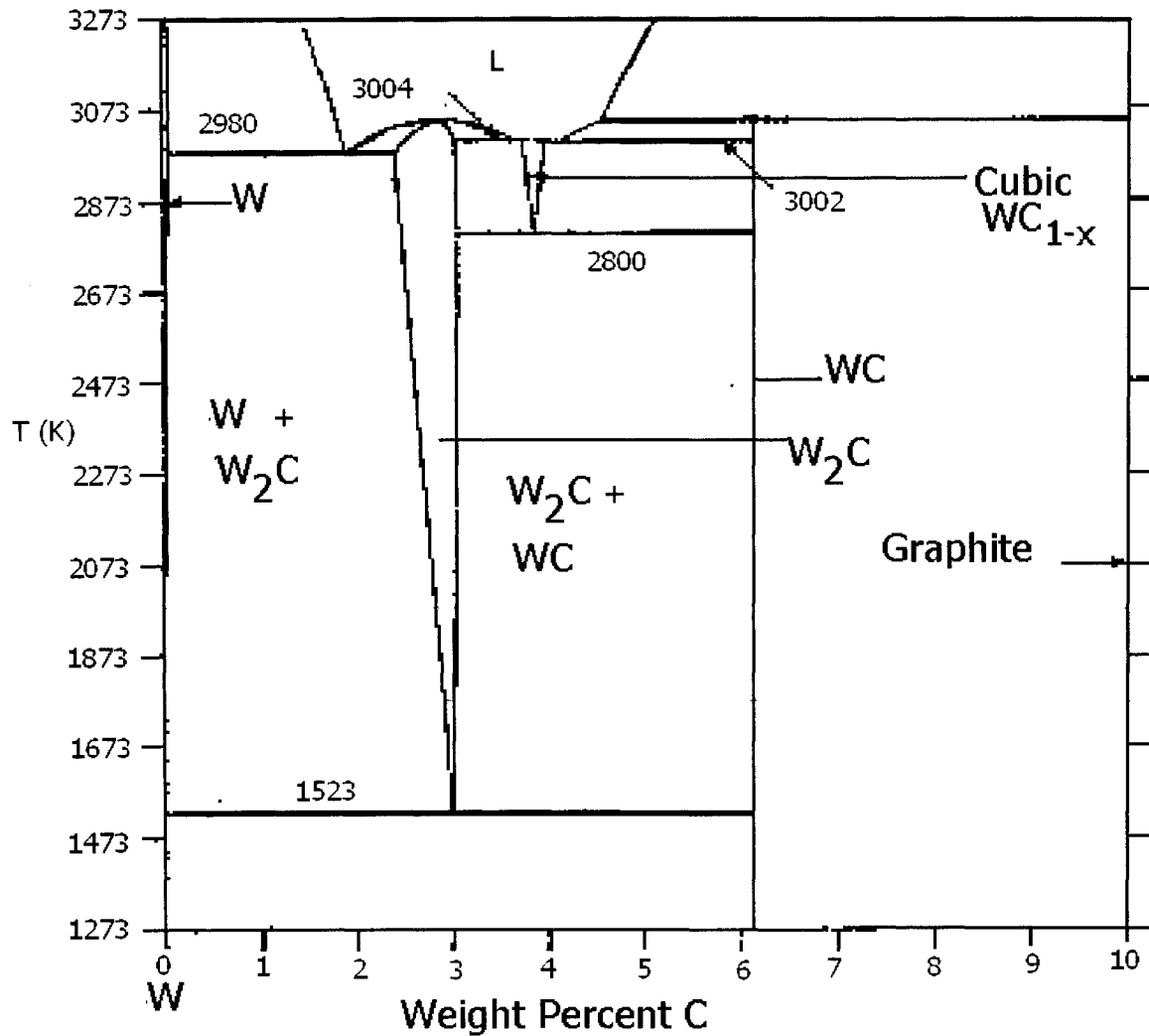
Figure 2.1: W-C phase diagram[10].

11

2.1.2 WC in a Ni-Based MMC.

The addition of WC particles to Ni alloys, for the purpose of wear resistance is a common industrial practise[6]. Frequently, Ni-alloys include B, Si and Cr in amounts less than 20wt%[4]. In the instance where a nickel alloy is used as a coating on steel, the B and Si provide oxidation resistance[6]. The function of Cr in a nickel alloy is to aid in wear resistance[6] by the formation of chromium carbides. The high hardness of WC provides wear resistance and the nickel alloy effectively wets WC[6, 11]. Meng et al. indicates that this wetting is non-reactive, suggesting that a chemical reaction between the Ni and WC does not occur[11]. Therefore, the driving force for wetting in this system comes from sources such as Van der Waals forces and dispersion forces[11]. Two methods of processing Ni-WC MMC's, liquid phase sintering[6] and laser cladding[7, 12] will next be discussed.

2.1.2.1 Liquid Phase Sintering of Ni Alloy- WC.

Liquid phase sintering of WC particles with a NiBSi alloy containing 10.5 wt% Cr was reported[6]. The WC that was used was 99.5% pure with an average particle size of 45μm. Table 2.2 shows the composition of the nickel alloy that was used. The nickel alloy also had a nominal particle size of 45μm[6].

12

Table 2.2: Nickel alloy composition used in liquid phase sintering tests[6].

Alloy	Si	B	Fe	Mn	Cr	C	Ni
$Ni_{10}CrBSi$	2.75	2.0	3.0	~	10.5	0.4	Balance

The nickel alloy powder and the WC powder were mechanically mixed. A sample containing 15vol% WC (23wt% WC) was uniaxially pressed and heated to 1373K under argon[6]. The sample was held at 1373K for 60 minutes[6]. A micrograph of the nickel alloy sample with WC reinforcement showed four distinct areas. Further investigation using wavelength dispersive spectroscopy (WDS) and energy dispersive spectroscopy (EDS) analysis revealed that these areas were as follows: WC particles, Cr carbides, a boron-rich area and the nickel alloy itself[6]. WDS/EDS analysis also revealed that there were small amounts of W dissolved into the Ni-alloy matrix, indicating a reaction between the nickel alloy matrix and the WC reinforcement likely took place[6].
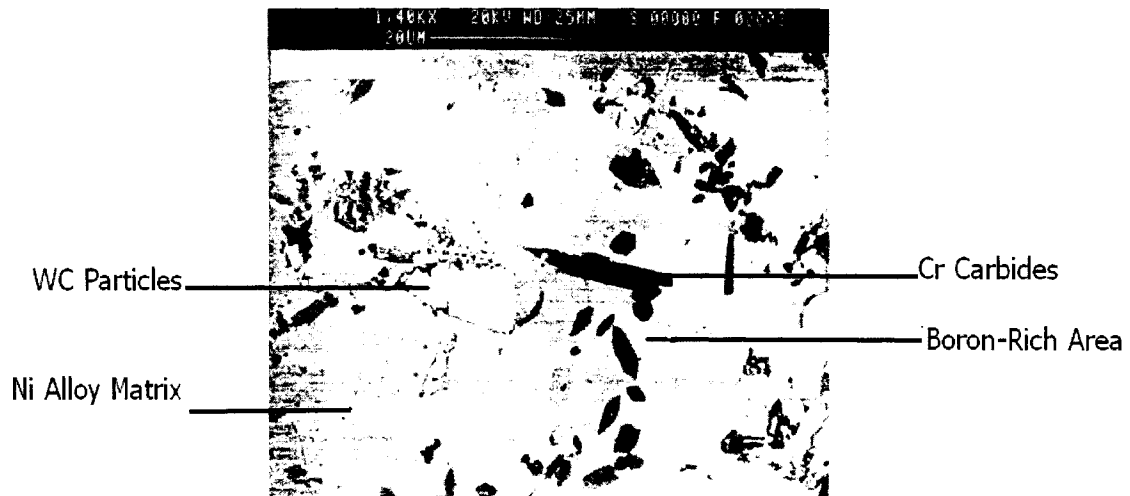
Figure 2.2: SEM micrograph of the $Ni_{10}CrBSi$ alloy with WC reinforcement[6].

13

Grigorescu et al. showed that liquid phase sintering of WC particles with Ni alloys of different compositions successfully produce MMC's[6]. Evidence of a reaction between the alloy matrix and the carbide additive was seen. This evidence included the presence of W within the nickel alloy matrix[6]. It is not clear that this method would be successful should this material be used as a wear resistant coating because of the four distinct regions created by the process[6]. Further testing is required to determine if this material, processed by liquid phase sintering, would be applicable as a wear resistant coating.

2.1.2.2 Laser Clad Ni-WC Coatings.

Laser clad coatings of Ni and WC can be used as wear resistant coatings[7, 12]. This process is similar to PTA except that a laser is used rather than a plasma gas stream[3, 7, 12]. Laser cladding involves depositing any weldable material onto the surface of a substrate. In the laser cladding procedure, a laser beam is used to attain a high enough temperature to encourage a metallurgical bond between the substrate material and the coating material. In the case of tungsten carbide, caution must be used to prevent the WC particles from being degraded by the heat of the process[7, 12]. Wu et al. accomplished this by altering the laser power during the process[7].

A mixture of nickel alloy powder and Ni-clad WC powder (at 15wt% Ni) was used as the coating material[7]. The particle size of these powders was between 60μm and 100μm. The

14

alloy contained approximately 71wt% Ni. The other components of the nickel alloy included Cr, B, Si, C, and Fe[7]. The specific composition of the Ni alloy is found in Table 2.3.

Table 2.3: Wu et al. Ni alloy composition[7].

Cr (wt%)	B (wt%)	Si (wt%)	C (wt%)	Fe (wt%)	Ni (wt%)
10	2.1	2.8	0.1	14	balance

A 2kW continuous wave CO_2 laser was used[7]. The laser cladding parameters are given in Table 2.4. Low carbon steel was used as the substrate material with two coatings being pre-sprayed onto their surfaces using a powder flame gun. This process resulted in 0.5mm coatings on the steel.

Table 2.4: Wu et al. laser cladding parameters[7].

Beam Diameter	Transverse Velocity	Laser Power
4×10^{-03} m	3×10^{-03} m/s	0.6 – 1.2 kW

Low-C steel substrates were then subjected to the laser cladding treatment. The power of the laser was varied from 0.6 to 1.2 kW[7]. Argon gas was used to provide an oxygen-purged environment. Scanning electron microscopy (SEM) was used to examine the microstructure of the resulting coated samples.

15

Testing was conducted at various powers of the laser. At 600W, the coating is inefficient, containing several areas of porosity (Figure 2.3a). Also, this coating is not sufficiently metallurgically bonded to the substrate as seen by the jagged and porous appearance of the interface (Figure 2.3a). At 800W, it can be seen that the coating is improved. The coating itself does not contain obvious pores, making it a much more efficient barrier to erosion and corrosion (Figure 2.3b). In addition, the interface between the coating and the substrate does not appear jagged or porous (Figure 2.3b).
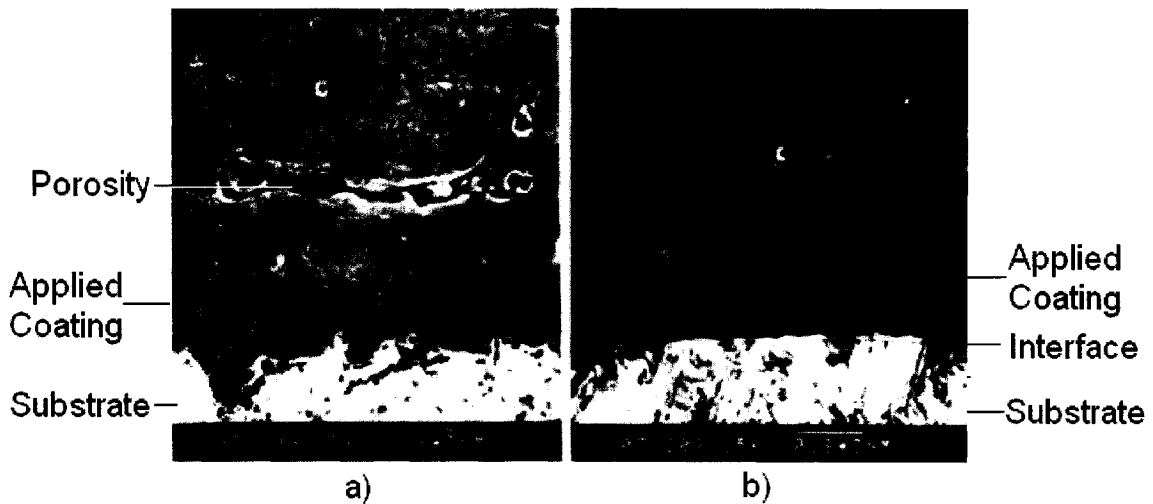
Figure 2.3: SEM micrographs of laser clad coatings at a) 600W and b) 800W[7].

However, at 800W, when the magnification is increased, Figure 2.4, it can be seen that there is no discernible metallurgical bond created between the WC particles and the nickel matrix. Therefore, further testing was carried out up to 1200W to determine if a power that would facilitate a metallurgical bond could be identified.

16
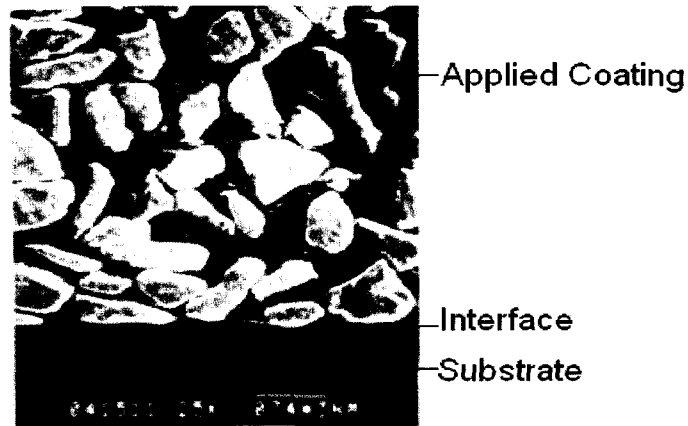
Figure 2.4: SEM micrograph showing the coating microstructure, 800W[7].

At a power of 1000W, there is clear evidence of a reaction between the Ni and the WC particles (Figure 2.5a). At 1000W, the distribution of the WC particulates throughout the matrix appears to be almost uniform (Figure 2.5a)[7]. In Figure 2.5a, the needle-like shapes are thought to be dendrites which grew from the WC particles. XRD analysis suggested that these dendrites are the compound Ni_2W_4C. At 1200W, the WC particle distribution is no longer uniform (Figure 2.5b). In any application, this distribution would cause uneven wear of the coating material.
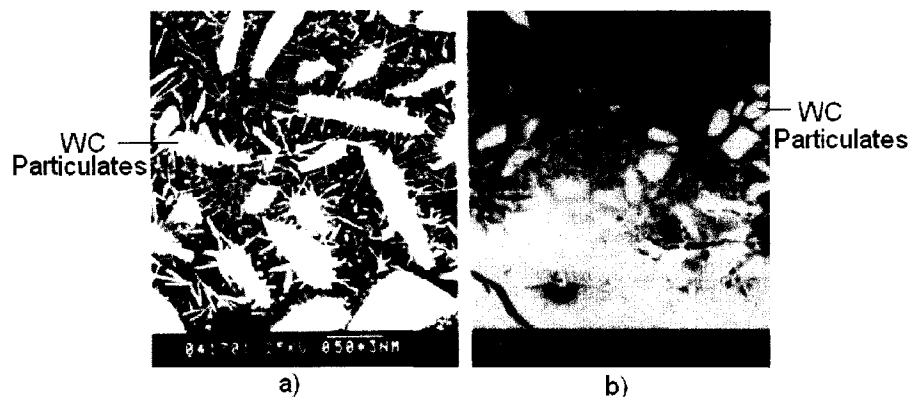
Figure 2.5: SEM coating microstructure, a) 1000W and b) 1200W respectively[7].

17

The experimental conditions utilized by Li t al differed from Wu et al. The Ni alloy

powder was of different composition, containing around 76wt% Ni. The compositions of

the other components of the Ni alloy are found in Table 2.5. Secondly, as can be seen by

comparing Table 2.6 to Table 2.4, it can be seen that Li et al. used a smaller beam

diameter, a higher transverse velocity as well as an increased laser power. Third, the

SEM micrographs that were taken by Li et al. are at much higher magnification than Wu

et al., allowing a better view of the matrix-WC particulate interface.

Table 2.5: Li et al. Ni alloy composition[12].

Cr (wt%)	B (wt%)	Si (wt%)	C (wt%)	Fe (wt%)	Ni (wt%)
16	3.5	4.5	0.8	1.2	Balance

Table 2.6: Li et al. laser cladding parameters[12].

Beam Diameter	Transverse Velocity	Laser Power
3x10-03 m	0.2 m/s	1.65 kW

SEM analysis was used to investigate the matrix-WC particulate interface. Figure 2.6

shows high magnification detail of the WC-matrix interface. In Figure 2.6 the rough

appearance of the WC particulate edge can be seen. At higher magnification, in Figure

2.6 the block-like structure of the WC particulates can be seen.

18
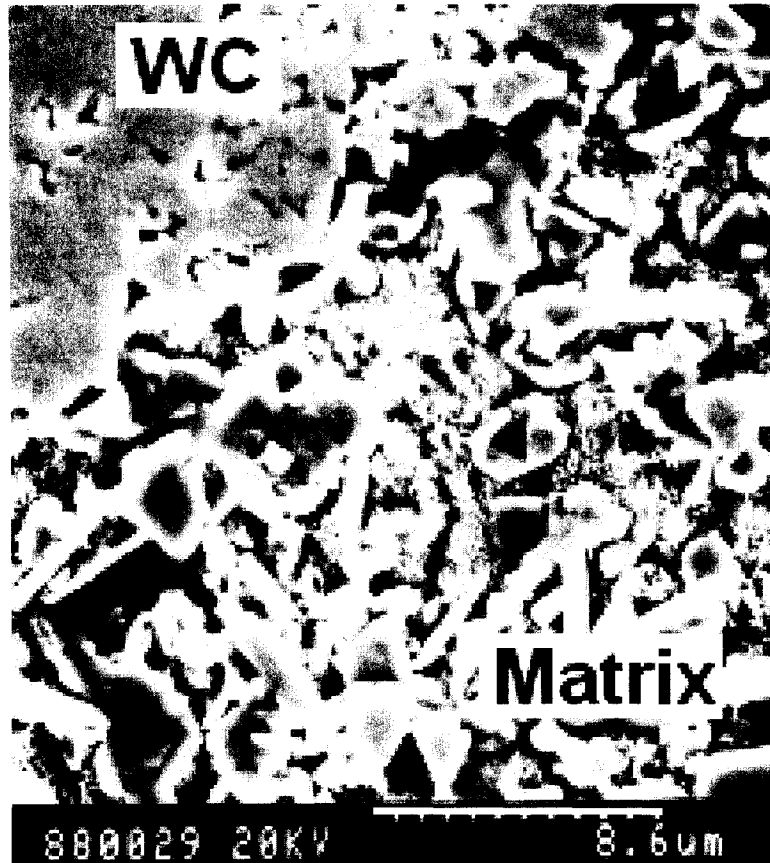
Figure 2.6: SEM micrograph of WC/ matrix interface within the laser clad layer[12].

A high-magnification micrograph was also taken of the matrix material a distance away

from the interface. This micrograph is shown in Figure 2.7. A comparison of the matrix

identified in Figure 2.6 and Figure 2.7 shows that the appearance of the matrix material

close to the interface as well as a distance from the interface is similar. This indicates that

any reaction between the matrix and the WC particles was relatively small.

19

Figure 2.7: SEM micrograph of the Ni-matrix material from Li et al.[12]

2.2 Boron Carbide.

Boron carbide was first discovered in 1858[13]. The discovery was followed by the

identification of the compounds B_3C and B_6C in 1894 with B_4C being recognized as the

stoichiometric formula in 1934[13]. Since the middle of the 20th century, there has been a

lot of research done regarding the behaviour of boron carbide[4, 13, 14, 15, 16, 17, 18]. In this

section, the phase diagram for the binary boron-carbon system will first be discussed,

followed by a discussion of the hardness of B_4C. The subject of the current study

involves the behaviour of B_4C and Ni at high temperature; therefore, the phase relations

of the Ni-B-C system were addressed. The high temperature behaviour of B_4C is also

20

examined. The behaviour of B_4C when contacted by some metal elements, at elevated temperatures, was investigated. Al[17] and type 304 stainless steel[18] are two relevant examples of the metals contacted with B_4C. Also investigated was the behaviour of Mg-B_4C composites produced using cold pressing and subsequent hot isostatic pressing (HIP)[19]. Also the microstructures of Fe-alloy- B_4C composites formed by PTA are discussed[20].

2.2.1 Bonding and Phase Diagram of Boron Carbide.

The bonding that exists between the carbon and boron atoms in the boron carbide molecule is responsible for the unique behaviour of boron carbide[15]. Electronegativity and atomic size affect the bonding in the molecule[15]. The electronegativity of carbon is 2.5 while the value for boron is 2.0[9]. The difference in these two electronegativities indicates that the bonding in a boron-carbon molecule will be polar covalent[9]. The atomic radius of boron is 0.088nm[15] and the atomic radius of carbon is 0.078nm[15]. The small difference in the radii of the two atoms also suggests the formation of a covalent bond between the two elements. Since the electronegativity and atomic radii of the carbon atom and the boron atom are close in value, it is possible for the two atoms to replace each other within the boron carbide molecule. This ability can cause the stoichiometry of the molecule to change as the atoms move about[15].

It is generally the stoichiometric form of boron carbide, B_4C that is referred to in the literature[15]. The binary phase diagram for the boron-carbon system is shown in Figure 2.8[8]. The boron and carbon atoms within the boron carbide molecule are able to substitutionally replace each other in the boron carbide molecule leading to the formation of molecules such as $B_{13}C_2$[15], which are not shown on the B-C phase diagram (Figure 2.8). On the binary B-C phase diagram, there is a eutectic line, located at approximately 2348K, between 0wt% C and 8wt% C[8]. As the temperature is lowered below this line, a mixture of boron and boron carbide is formed. A eutectic reaction occurs at approximately 1wt% C, forming a mixture of B and B_4C below 2348K. There is a second eutectic located at approximately 31wt%C, forming a mixture of B_4C and C below 2648K. At heightened levels of carbon, above approximately 20.5wt% C, a mixture of boron carbide and graphite is formed[13] below the solidus at 2648K, identified in Figure 2.8.
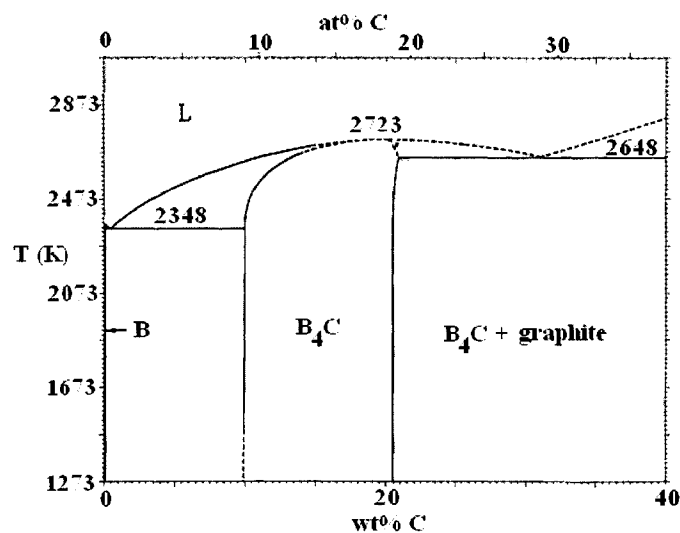
Figure 2.8: Phase diagram for the binary B-C system[15].

22

2.2.2 Hardness of B₄C.

The extreme hardness of boron carbide[4, 9, 15] is one of its most attractive properties. When considering boron carbide, the influence of carbon content on the hardness is central[13]. Knoop microhardness testing, at 200g, was utilized in an attempt to reveal a trend in the hardness values for boron carbide[13]. Solidified samples of boron carbide were mechanically polished to create a smooth testing surface, keeping in mind that the mechanical polishing caused a surface strain[13]. It was found that the Knoop microhardness increased linearly with carbon content in the phase homogeneity range for boron carbide (approximately between 8wt % C and 20 wt% C)[13]. The hardness values were approximately 2910 kg/mm^2 for 11.5wt % C and approximately 3770 kg/mm^2 at 22wt % C[13]. For the range of wt% C tested, it was found that the hardness decreased in the presence of free graphite in the sample. The other noted trend was that the hardness decreased linearly with increasing temperature[13].

2.2.3 Ni-B and Ni-C Systems.

It was important to understand the binary systems Ni-B and Ni-C to be able to interpret the ternary system Ni-B-C as it would be relevant in reactions involving Ni and B₄C. The reaction behaviour of nickel and boron is well known [14, 21] In the Ni-C system, it has been reported that there are no stable compounds formed[21].

23

There are several liquidus lines on the Ni- B phase diagram, shown in Figure 2.9[21]. At all points above these lines, B is soluble in liquid nickel (Figure 2.9). Below the several solidus lines, nickel borides are formed. There are several thermodynamically stable nickel-borides formed[21] (Figure 2.9). At low concentrations of boron, up to 6 wt%, a mixture of Ni and Ni_3B is formed. At exactly 6 wt%, only Ni_3B is formed. From 6 wt% up to 8.4 wt%, a mixture of Ni_3B and Ni_2B is formed, with pure Ni_2B being formed at exactly 8.4 wt%. As the boron content is increased, Ni_4B_3, in orthorhombic and monoclinic forms, begins to appear. A mixture of Ni_2B and orthorhombic Ni_4B_3 is formed from 8.4 wt% up to 11.5 wt%, where only orthorhombic Ni_4B_3 is formed. Beyond 11.5 wt%, a mixture of orthorhombic and monoclinic Ni_4B_3 is found. At 12.5 wt% B, only monoclinic Ni_4B_3 is seen. NiB is found in a mixture with monoclinic Ni_4B_3 from 12.5wt% to 16wt%. At 16wt% B, only NiB is formed[21].

24
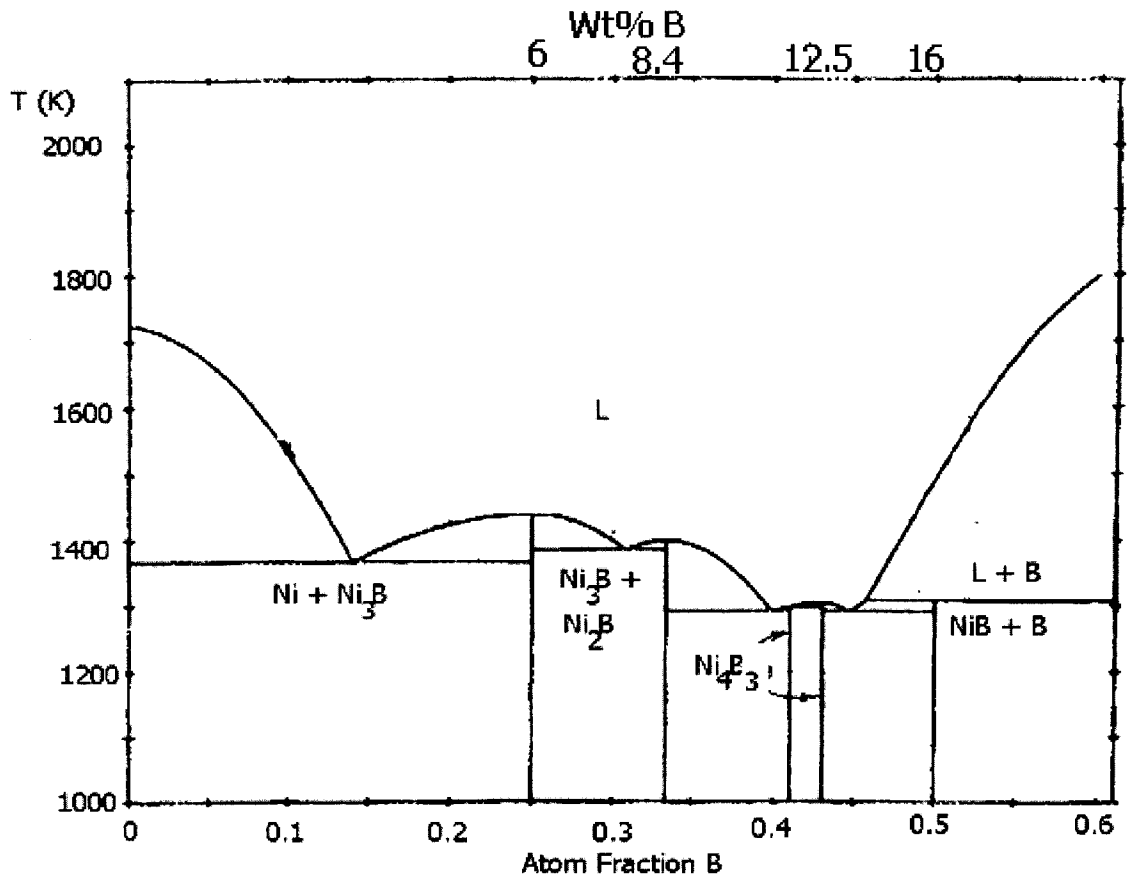
Figure 2.9: Partial phase diagram for the Ni-B system[14].

The nickel-carbon binary system, as seen in Figure 2.10 does not show the formation of any stable compounds[21]. In Figure 2.10, the area labelled Ni is the only region where C and Ni form a solid solution. Below the eutectic line at 1599K, a Ni-C solid solution is in equilibrium with graphite[21].

25
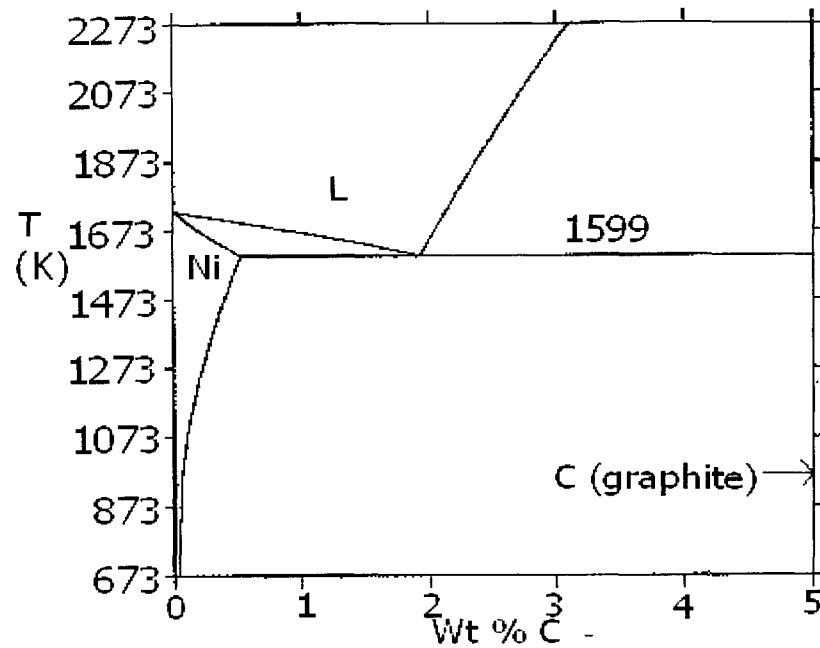
Figure 2.10: Ni-C phase diagram[21].

The C that is present in the nickel will segregate to the grain boundaries during cooling, to reduce strain[22]. This grain-boundary graphite would cause significant weakening of the grain boundaries as graphite is a solid lubricant. It is also assumed that the C atoms will bond strongly to each other while bonding very weakly, if at all to the nickel matrix, further weakening the grain boundaries[22].

2.2.4 Ni-B-C System.

The ternary Ni-B-C system was also considered. A ternary phase diagram of the Ni-B-C

26

system has been developed at 1173K (Figure 2.11)[14]. It appears that, at 1173K, there is

no interaction between all three elements, Ni, B and C. There, as expected, is interaction

between the Ni and the B.
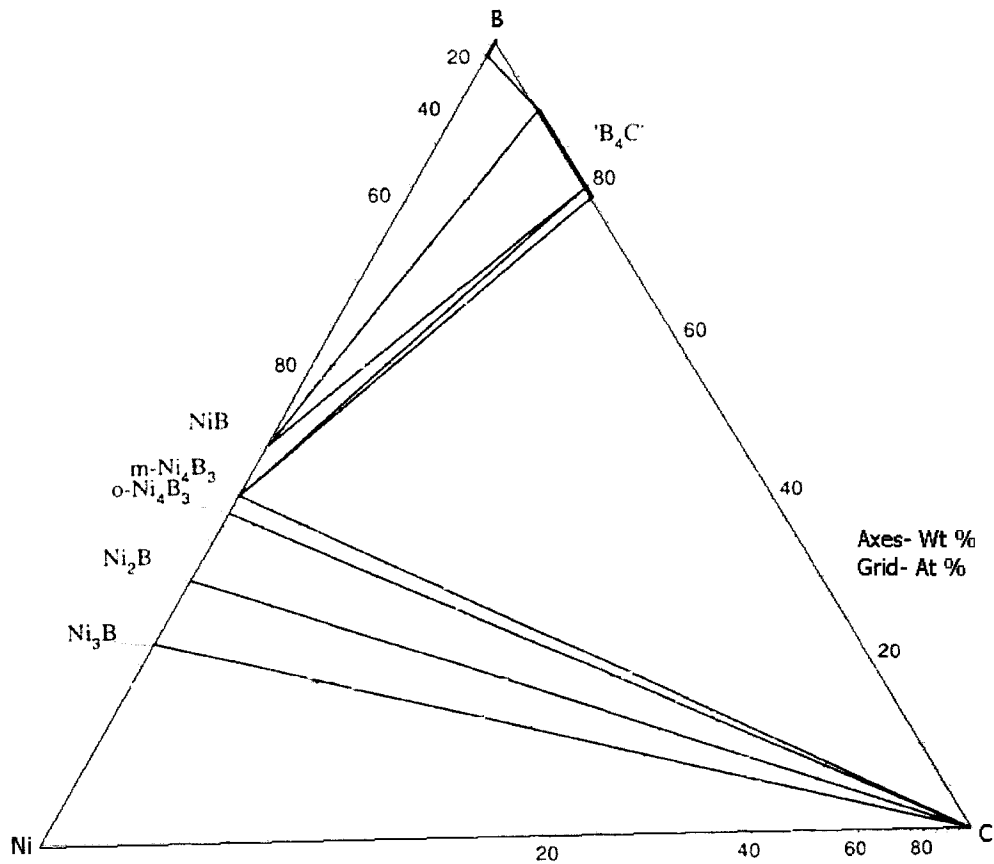
Figure 2.11: Ternary phase diagram for the Ni-B-C system at 1173K[14].

At a higher temperature, 1600K, there has been experimentation on Ni-B-C which

revealed that boron activity in C-saturated nickel was higher than the boron activity in C-

unsaturated nickel[23]. This suggests an interaction at elevated temperatures between B and

C. Experiments investigating the thermodynamic behaviour of Ni-B-C systems, at 1600K

27

were carried out[23]. A molten mixture of nickel and boron was prepared using arc-melting with the carbon level in each sample being altered. The boron samples contained between 0.54 wt%C (though not explicitly specified, Storms et al. imply that this composition is by weight) and less than 10ppm carbon[23], and samples placed within a graphite cup. Following arc-melting, the samples were pulverized.

The Knudsen effusion technique was used to determine the vapour pressure of the solid samples[23]. This technique employed a 1mm diameter orifice Knudsen cell connected to a magnetic mass spectrometer. The output of the mass spectrometer, in the form of ion current, was converted to activity values. This conversion, utilizing a form of the Gibbs-Duhem equation, shown in Equation, (2-1), is described by Copland and Jacobson[24].

$$\ln \gamma_a = - \int_1^{xa} x_a d[(\frac{\ln I_a^+}{\ln I_b^+}) - \ln(\frac{xa}{xb})]$$

(2-1)

The experiments having the molten mixture in contact with the graphite cup showed that carbon content did in fact, have a significant effect on the system. The ultra-pure samples, with less than 10ppm of C and the pure sample, with 0.54wt% C, were not significantly different from each other[23]. However, when the sample was contacted with graphite, the activity of the liquid changed dramatically[23]. When the wt% boron in the melt is between 0 and approximately 16.5 (Figure 2.12), the activity of nickel does not follow a smooth curve for the carbon-saturated sample, as it did for the pure and ultra-

28

pure samples (Figure 2.12). This deviation for a wt%B between 0 and 11.5, shows that the log of the nickel activity is smaller than the pure and ultra-pure samples (Figure 2.12). Once the wt%B reaches 16.5, the log of the activity (Storms et al. do not indicate what type of activity is being plotted) of the nickel in the carbon saturated sample is larger than that of the pure and ultra-pure samples (Figure 2.12)[23].

Thus, in liquid nickel, it is expected that both boron and carbon are soluble in a similar manner to the binary systems. To further investigate this behaviour, a ternary Ni-B-C phase diagram, at 1773K is developed in Chapter 5.0.
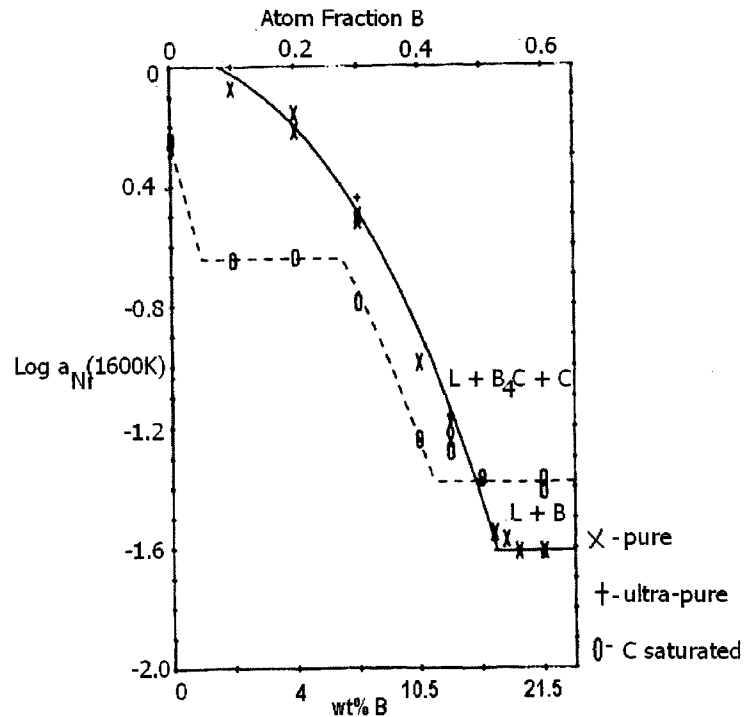
Figure 2.12: Activity of Ni-B liquid (1600K)[23].

2.2.5 Chemical Behaviour of B$_4$C.

2.2.5.1 High Temperature Behaviour of Boron Carbide.

Boron carbide oxidizes in air at high temperature[13, 15]. Consequently, high-temperature work with boron carbide habitually takes place either in a vacuum or in an inert atmosphere of argon (Ar). In an oxygenated atmosphere, the oxidation of boron carbide starts at around 873K[13, 15]. When weight loss/ gain analysis is performed for boron carbide in an oxygenated atmosphere, up to around 1273K, no significant changes in weight are noted. However, above 1273K, this is not the case as the boron carbide readily converts to B$_2$O$_3$ at these temperatures[15].

2.2.5.1.1 Photoabsorption and Photoemission Study of Boron Carbide.

The behaviour of boron carbide at elevated temperature, up to 2100K, in a vacuum, has been investigated[16]. This investigation involved heating boron carbide samples, in a vacuum, to high temperatures and in-situ analysis by photoabsorption and photoemission spectra[16]. Both of these techniques are sensitive to any changes in bonding character in the molecule being investigated[16]. Photoemission spectroscopy is used to observe surface changes of the heated boron carbide while photoabsorption reveals changes below the surface of the samples.

Photoabsorption testing was carried out on one untreated boron carbide sample and four

30

boron carbide samples that had been heated to various temperatures in a vacuum[16].

Photoabsorption monitors emitted photons, in the case of Jiminez et al., of energies

between 100 and 150eV[16]. The photoelectrons measured are from the 1s orbital of B and

C (B(1s) and C(1s) respectively)[16]. Figure 2.13 is divided into the boron B(1s) and the

carbon C(1s) spectra. On the boron spectra, the boron powder reference pattern is labeled

as f1, while the sp^2 and sp^3 bond reference spectra are labeled as f2 and f3 respectively.

Reference spectra for carbon are shown on the C(1s) spectra. The reference spectra for

graphite is labeled as f4 and the diamond reference is labeled f5. These carbon reference

spectra are guides to the sp^2 and sp^3 bonds for carbon.
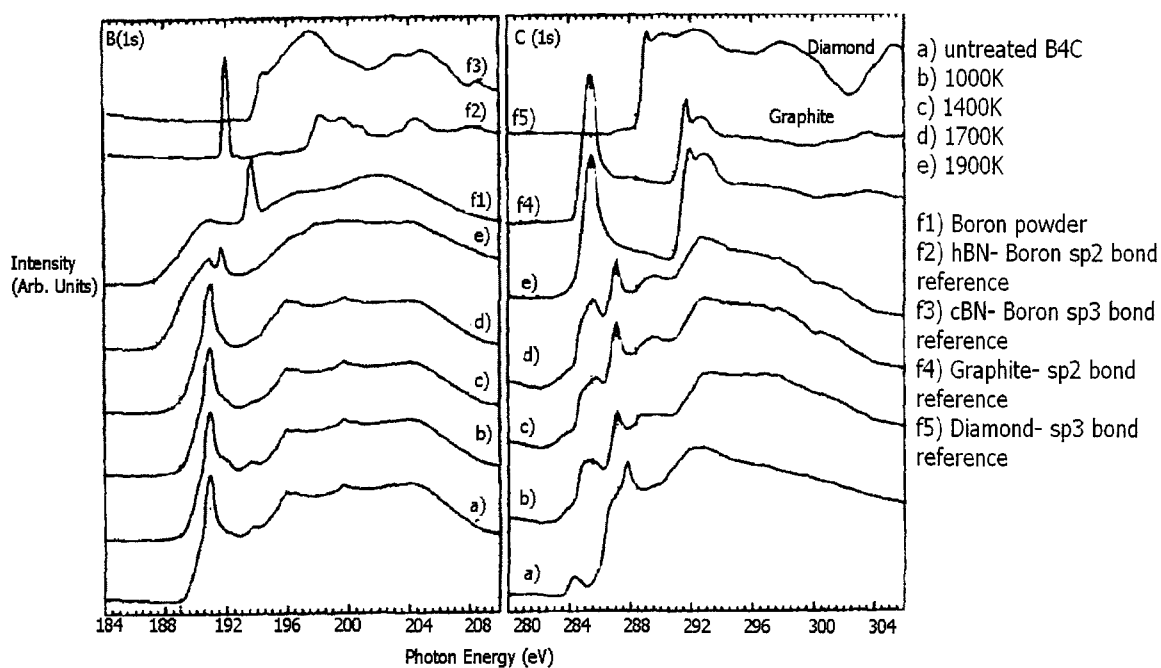
Figure 2.13: Photoabsorption spectra for heat treated boron carbide samples[16].

31

At temperatures ranging from room temperature (the untreated boron carbide sample) up to 1700K, Figure 2.13 a-d, there are not significant differences in the bonding as a result of the heat treatment. Above 1800K, there are changes in the spectra that are noticeable. Since photoabsorption reveals surface changes, this can be attributed to a change in the character of the boron carbide around this temperature, possibly indicating a change in stoichiometry. If the f1 curve is compared to the 1900K curve on the B(1s) curve, it can be concluded that there has been a shift to a boron-rich boron carbide at 1900K. The 1900K spectra on the C(1s) curve, is showing peaks almost identical to the peaks seen in the f4 graphite reference spectra. The appearance of these peaks at the same temperature as the changes in the B(1s) spectra support the formation of a boron-rich boron carbide because the carbon concentration would need to decrease. Therefore, the photoabsorption results suggest the formation of a graphite layer on the surface of the boron carbide sample[16].

Jiminez et al. also performed photoemission spectroscopy on heated boron carbide samples[16]. A reference spectra for graphite is provided for comparison with the results from the heated samples. The relevant results were seen in the C(1s) spectra (Figure 2.14, Curve c) where two peaks are seen. These peaks are indicative of the presence of graphite and the presence of carbon bonded in a way that is dissimilar to the graphite bonds. Since photoemission gives analysis below the top-most atomic layers and the heated samples are known to be boron carbide, this second feature is identified as being due to the

32

bonding of carbon in the boron carbide molecule. This indicates that the thickness of the

graphite layer has not yet reached a thickness, which impedes the photoemission process.

This boron carbide feature is seen in the spectra for the samples heated to 1000K and

1400K, as well as the untreated sample at 300K[16].
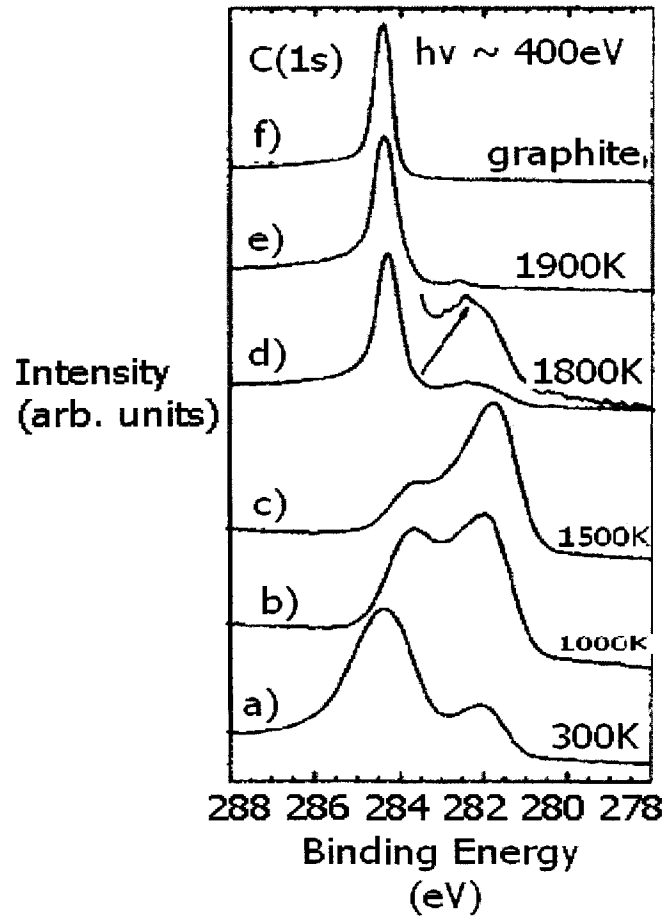
Figure 2.14: Photoemission spectra for C(1s) in B₄C annealed samples[16].

As a result of these tests, it can be said that, even in a vacuum, boron carbide is subject to

surface bonding changes at elevated temperature. It is likely that the formation of a

33

graphite layer on the surface of the boron carbide would cause some changes in the reactive behaviour of a sample. For example, prior to the boron carbide being reacted, the graphite layer would have to be removed or reacted. A second complication that arises from the presence of this graphite layer is that graphite is a solid lubricant[9]. If left on the sample, it could cause sliding between particles. Furthermore, this surface carbon would affect the contact between the B_4C and the metal matrix in an MMC.

2.2.5.2   Chemical Behaviour with Aluminium.

The behaviour of powdered mixtures of B_4C when contacted with Al has been studied[17] from 900K to 1273K. This temperature range covers the behaviour of solid as well as liquid aluminium with boron carbide. The testing described was carried out in an argon-purged environment to minimise interaction with oxygen. Viala et al. reported the experimental samples to be 99.8% pure powdered aluminium, 99.4% pure boron powder, spectrographic grade carbon, stoichiometric grade boron carbide (trace C) and stoichiometric aluminium carbide[17]. The experimental parameters employed in these tests indicates that it may be useful to test boron carbide, in high temperature situations, under an argon purified environment, preventing oxidation of the boron carbide.

2.2.5.2.1   Experimental Procedure.

The aforementioned sample powders were blended by mechanical alloying using a

34

tungsten carbide ball mill and cold pressed into rods (pressed at 270 MPa). The pressed

samples were then placed in a tube furnace. Careful measurements of the weights of these

specimens were made before and after the isothermal heat treatments in the furnace[17].

Specimens were analyzed using XRD, OM, SEM and EPMA.

The reactivity of boron carbide with aluminium was determined using three variables:

treatment time (1h- 450h), temperature (900K- 1273K) and composition. The

compositions that were tested in these experiments, in wt% Al:B:C were 61:30:8,

11:69:19, 30:55:15 and 98:2:trace. While two of these variables were fixed, the third was

altered, allowing for observations of the effect of each to be seen[17]. OM and SEM were

used on sectioned pieces of the experimental rods. OM was used to obtain a general idea

of the structure and overall composition percents of the sectioned rods. It was difficult to

obtain good OM pictures due to the varying phase hardness's in the samples so the SEM

was employed for better resolution. EPMA was used to characterize the phases present in

the specimens. There were eight product phases presented in the literature for this

reaction system (Table 2.7).

2.2.5.2.2 Effect of Temperature.

A pressed sample were heated to varying temperatures and held for 160 hours and rapidly

cooled[17]. The ratio tested by Viala et al., in wt%, Al:B:C = 61:30:8 (at%, Al:B:C =

35

40:48:12). For the temperatures 900K and 920K, it was found, using the identification methods previously mentioned, that B_4C and Al were the main two phases identified. Very small amounts of Al_4BC were thought to be present but not enough evidence of this phase was present to make a determination.

Table 2.7: Phases characterized for system containing Al, B and C[17].

Chemical Formula	Decomposition T(K) Composition Range (at%)
Al4C3	2429 very small
B4C	2723 8.8 < C < 20
AlB2	1165[a] very small
AlB12	High T type 2323
	Low T Gamma
Al3B48C2 (beta-AlB12)	2300 Low T form A
	Low T form B
AlB24C4 (AlB10)	2000
Al8B4C7 (Al8BxC6)	2110 2<x<4
Al3BC (X, Al4BC)	1273[a]

a = present work's findings

The results of this test were discussed with respect to XRD though no spectra were presented[17]. XRD revealed the presence of B_4C, Al_2O_3, Al and AlB_2 in the sample[17].

36

EPMA analysis identified which particulates in the SEM image were B_4C, Al_2O_3 and AlB_2[17] as seen in Figure 2.15. In this figure, there are B_4C particulates embedded within the Al matrix. Located on these particulates is a product layer of Al_2O_3.
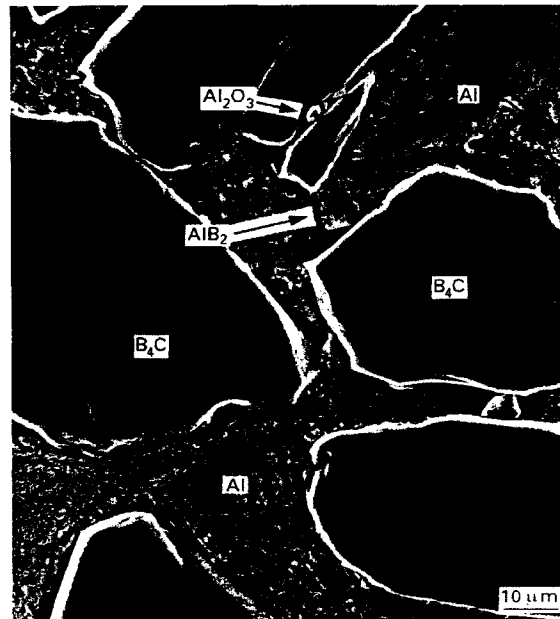
Figure 2.15: SEM image after testing for 160h at 900 K[17].

At 950K, just above aluminium's melting point, B_4C and Al were shown to have reacted, producing Al_3BC and AlB_2 (Figure 2.16). Also, these two phases form in different areas. It appears that the Al_3BC particles are nucleated around the rough edges of the remaining B_4C particles, leaving these B_4C particles un-reacted once a reaction layer has formed. The AlB_2 particles form within the aluminium matrix (Figure 2.16). The same experimental results were seen for tests done at temperatures up to 1100K. As the temperature increased, there was a corresponding increase in the amount of each of the

37

phases, Al_3BC and AlB_2. The amount of the phases was estimated using OM and SEM[17].
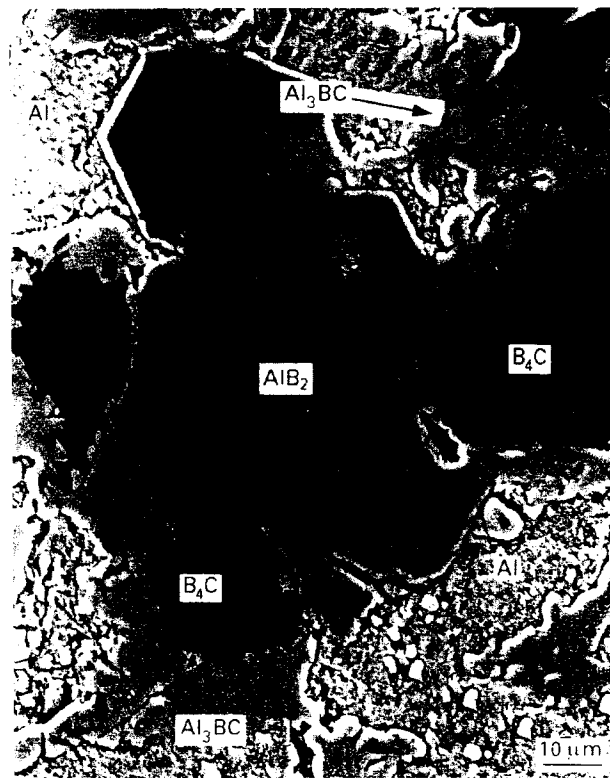
Figure 2.16: SEM image after testing for 160h at 950 K[17].

Once testing reached a temperature of 1150K, AlB_2 stopped being produced while Al_3BC

and $Al_3B_{48}C_2$ were identified. This was confirmed using x-ray diffraction. At an even

higher temperature, 1273K, it was found that the B_4C was almost completely consumed

by reaction with the Al (Figure 2.17)[17].

38
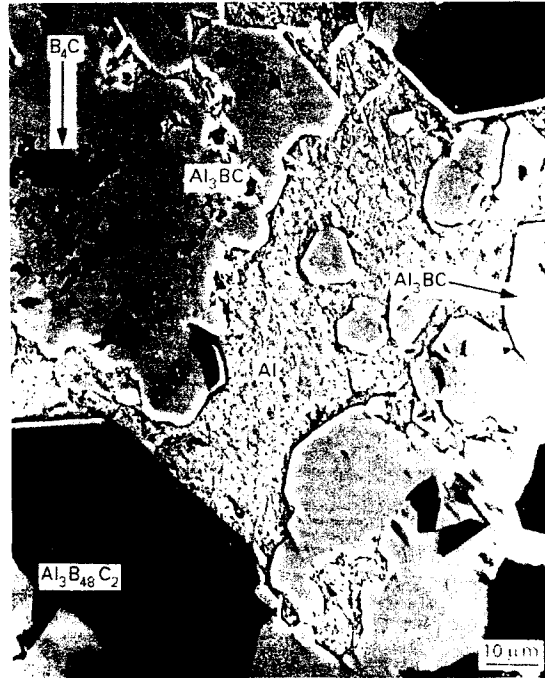
Figure 2.17: SEM image after testing for 160h at 1273 K[17].

It is possible to separate the results from the temperature dependence tests into three

distinct regions[17]. The first is a low temperature region in which any reaction between

B_4C and the Al matrix does not observably occur. The second is a temperature range

extending from the melting point of Al, 933K, to 1100K where Al_3BC and AlB_2 are

produced. Finally, a high temperature region, where ternary carbides are produced, that

extends from 1100K to 1273K[17].

2.2.5.2.3   Effect of Composition.

The composition of the experimental samples was altered to discern the effect this may

39

have on the resulting products. Al-rich and boron-carbide rich samples were tested[17].

When the amount of each of the reactants was altered, the same phases appeared in the

final product though the amounts changed proportionally with the amount of each

reactant charged. It is noted that the phases present at 900K remain the same as they did

when the temperature tests were undertaken.

Viala et al. tested three Al:B:C ratios: 12:69:19, 30:55:15 and 98:2:trace (all in wt%)[17].

Two different temperatures, 1000K and 1273K were chosen for testing, based on

previous results. It was found that the results from these tests were consistent with results

discussed in the previous section.

2.2.5.2.4   Effect of Reaction Time

In any system, reactions can occur at very slow rates. It is therefore important to consider

what happens in a reaction system when additional time is allotted. There may be

reactions occurring very slowly in a system where it was thought that none were

occurring.

First, it was of interest to discern whether or not there was a reaction possible between

solid Al and B_4C if more time for reaction was given. For a sample heated to a

temperature of 920K for 450 hours, the reaction products Al_3BC and AlB_2 were present.

40

This indicates that a reaction does indeed take place at 920K between solid aluminium

and boron carbide[17]. Tests were then performed at 1000K for reaction times varying from

3h to 400h. Again, the products were identified as AlB_2 and Al_3BC. As would be

expected in this system, based on the results seen at 920K, the aluminium and boron

carbide should react. In fact, these tests show behaviour that produces AlB_2 and Al_3BC in

a non-linear fashion until the reaction time is around 50h (Figure 2.18a)[17]. Around 50h,

the consumption of the reactants and the production of the products levels off.

a)   b)

Al- △   B4C- ■   Al3BC- ●   AlB2- ○
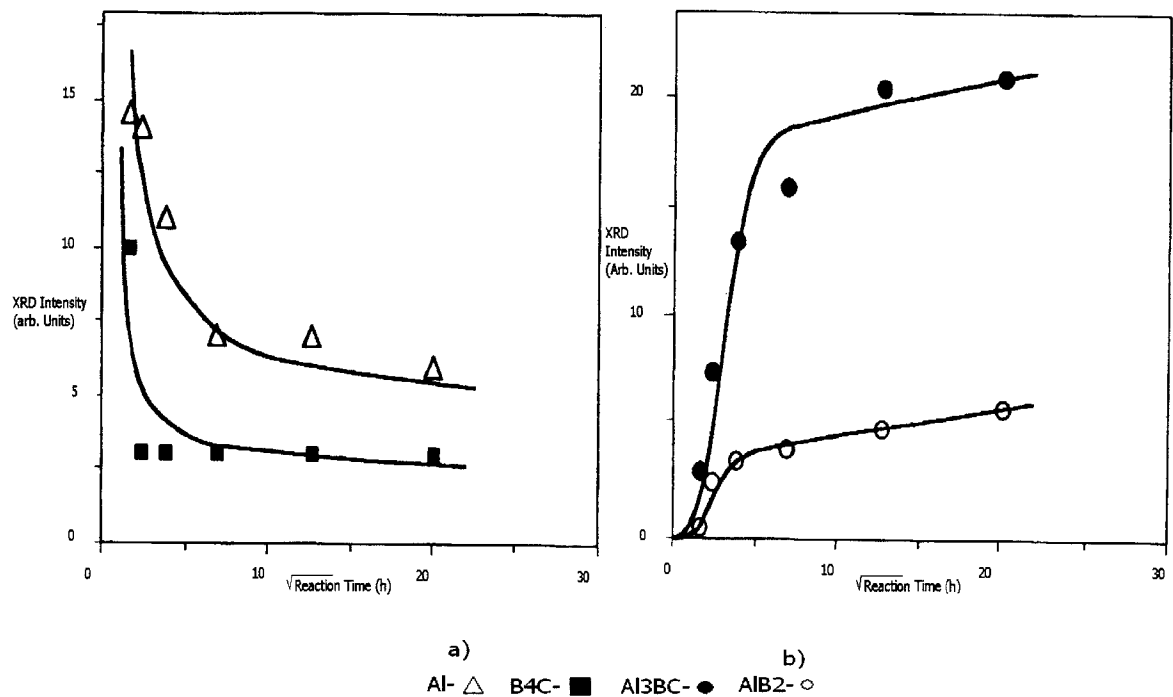
Figure 2.18: Time dependence of the relative quantities (from XRD) of a) reactants,

Al and B_4C and b) products, Al_3BC and AlB_2 at 1000K[17].

There appears to be an incubation period during which no discernable reaction occurs;

this is likely while the oxide film on the Al is being deteriorated[17]. Following this

41

incubation, it appears that the Al becomes saturated with boron and carbon. In the instances where the temperature is below the melting point of Al, this occurs via solid-state diffusion. The carbon and boron atoms move away from the surface of the boron and carbide and towards the mixed-species crystals that grow in size due to metal precipitation[17]. Above the melting point of Al, this saturation occurs by the dissolution of the boron carbide. The saturation point for each of these atoms in Al is quite small[17], therefore, this process is completed rapidly. Nucleation of the mixed Al-B-C phases[17] proceeds via a classic dissolution-precipitation mechanism. In both the high and low temperature reaction systems, the formation of Al_3BC on the surfaces of the boron carbide particles not yet dissolved results in a layer of Al_3BC being present. As the reactions progress, this layer covers more and more of the un-reacted B_4C particles.

In the low temperature system, reactions progressed via solid-state diffusion from the beginning. In the high-temperature system, this layer begins to cover the B_4C particles, making it necessary for solid-state diffusion through this layer to occur to facilitate further reaction[17].

2.2.5.2.5   Summary.

Boron carbide has been shown to react with Al between 900K and 1273K. At temperatures below the melting point of Al, reaction proceeded via solid-state diffusion,

42

first through the aluminium matrix and then through the product layer formed on the boron carbide particles. Above the melting point of aluminium, 933K, reactions proceeded via a dissolution-precipitation reaction mechanism. As a product layer was formed on the un-reacted boron carbide particles, solid-state diffusion through this layer began to control the reaction system.

2.2.5.3 Chemical Behaviour of Boron Carbide with Type 304 Stainless Steel.

A study was conducted by Nagase et al.[18] that focused on elucidating the behaviour of boron carbide when contacted by type 304 stainless steel. The testing undertaken attempted to gain a fundamental understanding of the contact behaviour for the temperature range 1073K to 1623K[18].

2.2.5.3.1 Experimental Procedure:

Isothermal annealing was carried out using a stainless steel vessel coupled with samples of pelletised or powdered B_4C. Boron carbide was presented in these two forms to determine if the surface area of the boron carbide had any effect on the contact behaviour. The pelletised B_4C or the powdered B_4C was placed within the stainless steel vessel and then heated to the appropriate temperature (Figure 2.19) under an atmosphere of Ar[18]. Equal weights of B_4C pellets and B_4C powder were tested.

43
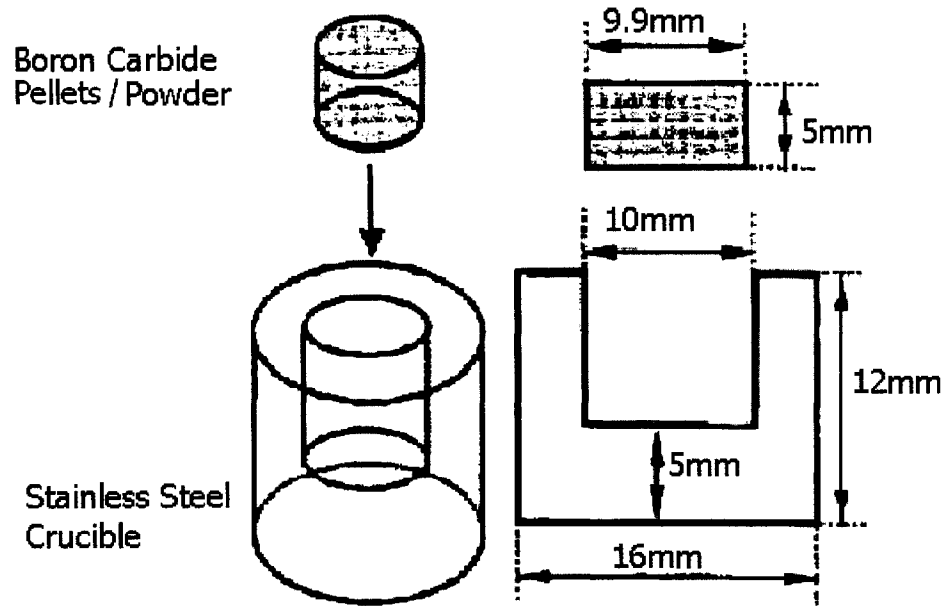
Figure 2.19: Reaction couple set-up[18].

After testing was complete, the samples were sectioned, polished and examined using electron probe microanalysis (EPMA), the scanning electron microscope (SEM) and energy dispersive x-ray analysis (EDX) or wavelength dispersive spectroscopy (WDS).

2.2.5.3.2 Reactions Between B₄C Pellets and 304 Stainless.

Tests were conducted at 1373K to assess the behaviour of the system at this temperature. This temperature is below a eutectic temperature at 1473K where liquid is formed at the reaction interface[18]. There were two reaction layers that were obvious when looking at the experimental samples[18]. The first reaction layer was located at the interface between the boron carbide and stainless steel. In this layer, the precipitates identified were FeB,

44

CrB, NiB and Fe_2B, Cr_2B and Ni_2B. The second layer was located within the stainless steel. These precipitates appeared to be grain-boundary and grain precipitates[18] of Fe_2B, Cr_2B and Ni_2B.

Testing was also carried out for temperatures above the eutectic temperature of the stainless steel, 1473K. At 1473K, it was found that the average thickness of the reaction layer was slightly larger than a millimetre when heated for 25h. As the treatment temperature was increased, it was noted that the reaction rate increased substantially, even with small increases in temperature. This was evidenced by the fact that for a reduced heating time of 30minutes at 1498K, the reaction layer that formed surpassed the thickness of the 1473K reaction layer.

As the liquefied region within the reaction samples increased, precipitate growth seemed to occur in a different manner than at low temperatures. It is probable that dendritic growth of the precipitates began to occur.

2.2.5.3.3 Reactions Between Boron Carbide Powder and 304 Stainless.

The second set of tests, using powdered boron carbide, was conducted under similar experimental conditions. The behavior of the system was found to be significantly different than the behavior when the boron carbide was in pellet form[18]. Microscope

45

evaluations showed that there was penetration of boron into the stainless steel. At temperatures above the eutectic, 1473K, it was found that the molten metal invaded the boron carbide powder through the spaces between the powdered particles. Also, the stainless steel crucible was markedly dissolved during the process. Both of these observations indicate that the surface area of the boron carbide plays a role in the behavior of the system.

2.2.5.3.4   Reaction Kinetics.

For the purposes of kinetic studies, the thickness of the reaction layers was measured. EPMA was used to measure the penetration of boron into the stainless steel. The thickness decrease in the stainless steel vessel was measured for tests conducted above the eutectic, 1473K. The thickness of the reaction layer versus the square root of the annealing time is plotted (Figure 2.20). It is seen that a close to linear relationship exists.

Obtaining a linear plot in this case indicates that the reaction is following a parabolic rate law. The slope of the curves of the reaction layer thickness plot, are taken to be the rate constant for the system though this value will also include constants and calculations for the forming of the liquid phase (Figure 2.20).

Below the eutectic temperature, it was shown that the change in the reaction layer

46

thickness was almost equal to the decrease in thickness of the stainless steel vessel. It was also noted that the reaction rates for the pelletised B$_4$C and the powdered B$_4$C were, for the most part, close in value.

For temperatures above 1473K, the boron carbide pellet often moved about in the now molten metal. The decrease in thickness of the stainless steel vessel was measured at the bottom of the vessel using SEM images of the samples. The measurements taken over the vessel were averaged to give an overall thickness decrease (Figure 2.21).
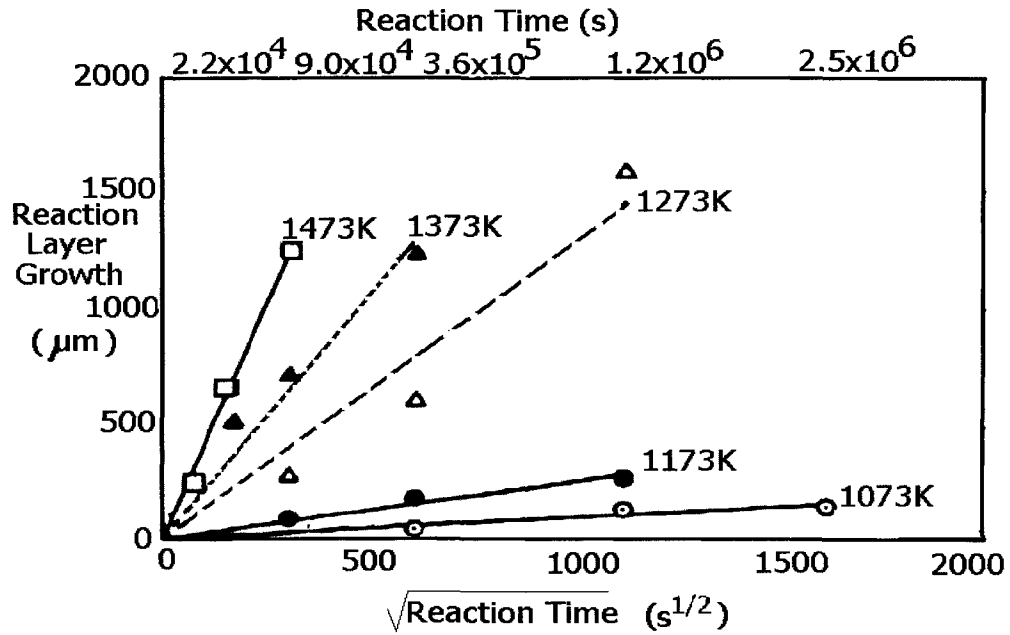
Figure 2.20: Reaction layer growth on reaction couple as a function of testing time for T < T$_{eutectic}$[18].

47
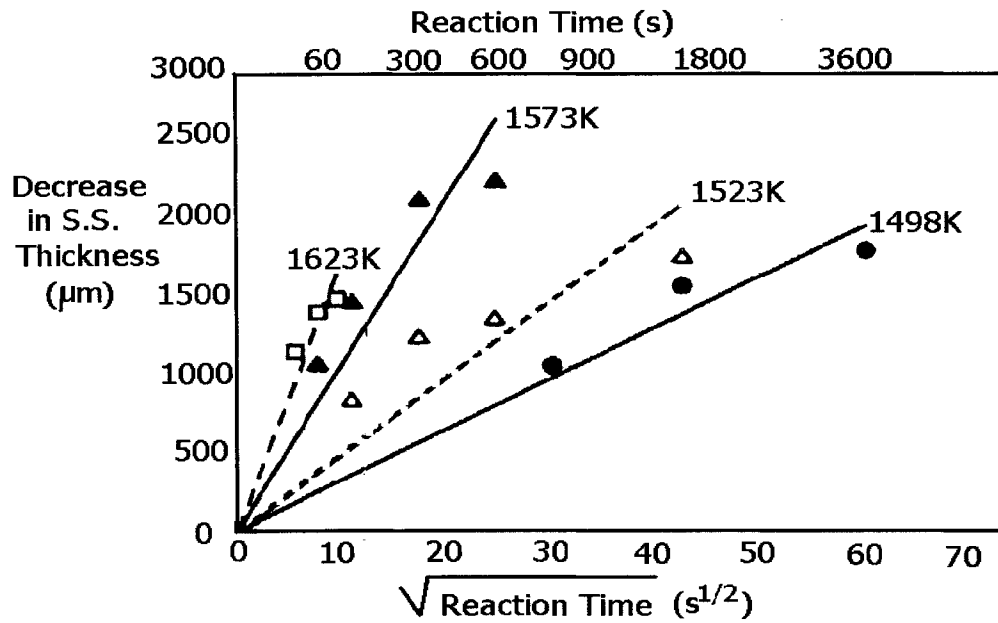
Figure 2.21: Reaction layer growth on reaction couple as a function of testing time at T > T$_{eutectic}$[18].

It was found that the resulting rate constants (derived from the results in Figure 2.20, Figure 2.21) were slightly different in value depending on the initial physical condition of the test sample in each case[18]. The pelletised boron carbide has a different surface area of contact with the stainless steel than the powdered boron carbide. This difference in contact accounts for the difference in the rate constants. This suggests that the initial physical condition of the boron carbide is not having a substantial effect on the kinetics of the system below 1473K[18].

It is obvious that the rate constants for this reaction system increase with increasing temperature (Figure 2.20, Figure 2.21)[18]. An Arrhenius plot, seen in Figure 2.22, shows

48

that there is not a uniform controlling mechanism for the system. The discontinuity at the

eutectic temperature, 1473K, is clearly seen in the Arrhenius plot[18].

The activation energy was calculated for each of the two physical conditions of the boron

carbide. Below 1473K, the activation energy required for both the pelletised and the

powdered boron carbide were similar in value. Once the temperature was raised above

the eutectic temperature, the activation energy differed by just under 100J/mole. In terms

of kinetics, the pelletised boron carbide requires more energy to activate a reaction and

would therefore be a slower reaction when compared to the powdered boron carbide[18].
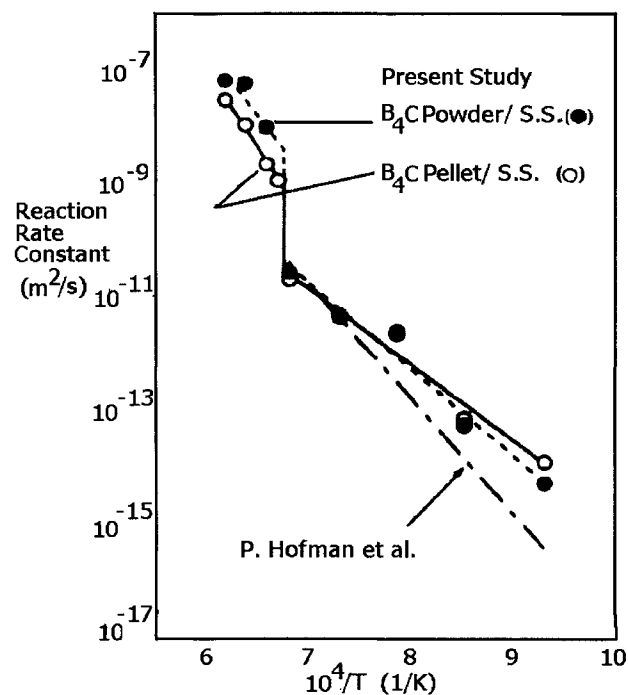
Figure 2.22: Arrhenius plot of rate constants for T>T_eutectic[18].

49

2.2.5.4　Sintering of B₄C- Magnesium (Mg) Composites.

In an MMC, it is advantageous to use a metal with a low density, reducing the weight of an applied coating[19]. Magnesium (Mg) is the lightest of the structural materials that are currently used industrially[25]. The density of magnesium[9] is approximately 1740 kg/m³. There have been several studies of the behaviour of Mg alloys with various ceramic reinforcements such as Al_2O_3[25] and SiC[26]. The densities[27] of Al_2O_3 and SiC are 3900kg/m³ and 3100kg/m³ respectively. To form a lighter MMC, the combination of Mg and B₄C, with a density[27] of approximately 2510kg/m³, has been considered[19].

2.2.5.4.1　Experimental Procedure.

Powdered mixtures containing 14wt% and 27wt% (10vol% and 20vol% respectively) B₄C were prepared[19]. An image of the reactant B₄C powder is shown in Figure 2.23. The B₄C powder, when analysed, contained some monolithic B[19].
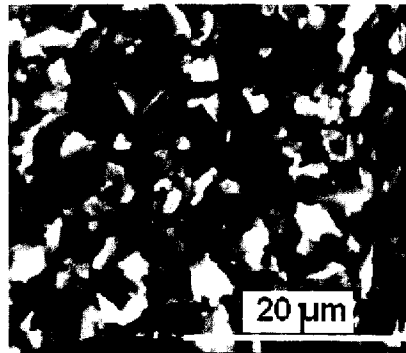
Figure 2.23: SEM microstructure of B₄C Reactant[19].

Mechanical mixtures, formed by ball milling (6h), of 95% pure B₄C and 98% pure Mg,

50

powders was done[19]. The particles size of the B$_4$C powder was less than 6μm while the

Mg powder had a nominal particles size of 106μm[19]. The milled samples were then cold-

pressed into cylinders[19, 20] using 20-25Mpa in air. As a result of this pressing occurring in

air, some oxygen is trapped within the cylinders. These cylinders were then subjected to

sintering treatment (823K-893K, 5MPa (10min)) using an Ar atmosphere[19]. The samples

were then analysed using SEM and XRD[19].

2.2.5.4.2 Discussion of Results.

Figure 2.24 shows typical microstructures for composites sintered at 14wt% and

27wt%[19]. It can be seen in these images that the B$_4$C particles are not well dispersed

throughout the Mg matrix[19]. Clusters of material can be seen in Figure 2.24. These

clusters were not identified in the analysis[19]. However, the appearance of these clusters is

similar to the B$_4$C reactant powder shown in Figure 2.23.
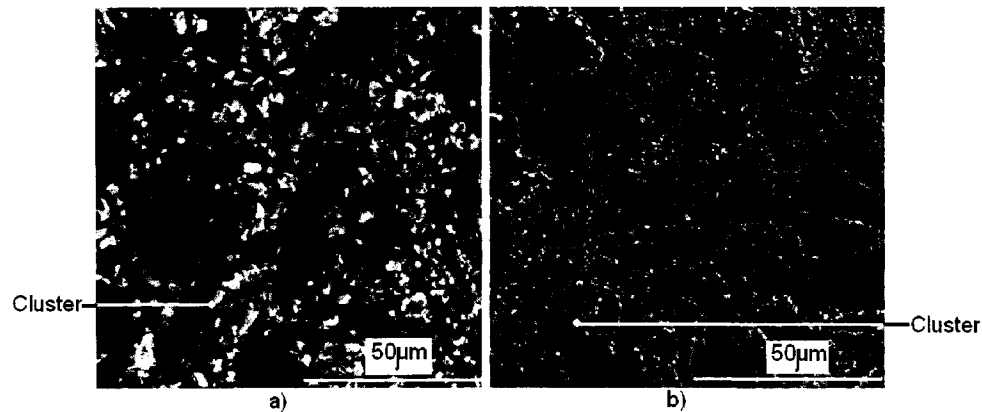
Figure 2.24: SEM images of sintered composites[19]. a) 14wt%B$_4$C b) 27wt% B$_4$C.

51

XRD for samples containing 14wt%, 27wt% and 38wt% B₄C are shown in Figure 2.25.

The diffraction peaks for Mg, MgO, B₄C and MgB₂ are identified.
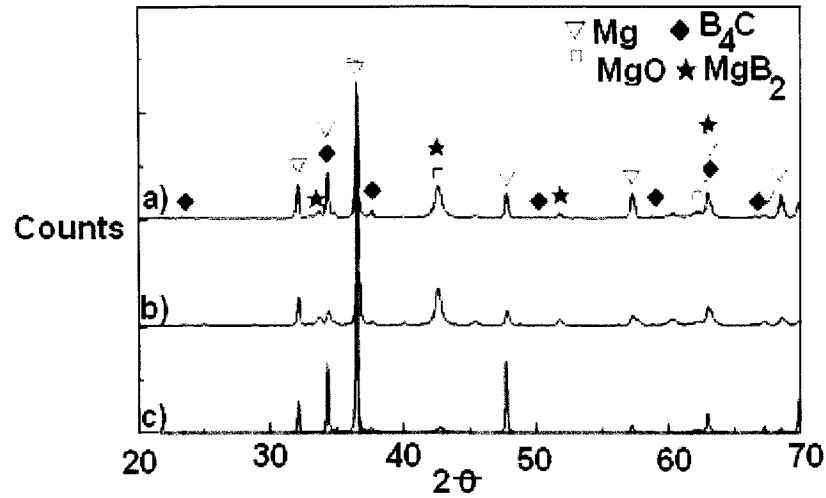
Figure 2.25: Jiang et al. XRD patterns for a) 14wt% b) 27wt% and 38wt% B₄C.

As a result of the oxygen trapped in the cylindrical samples, some of the B₄C probably

oxidized during the sintering treatment (823K-893K), to form a layer of B_2O_3 on the B₄C

particulate surfaces[19] according to Equation (2-2) and Equation (2-3).

$$B_4C(s) + 4O_2(g) \leftrightarrow 2B_2O_3(l) + CO_2(g)$$

(2-2)
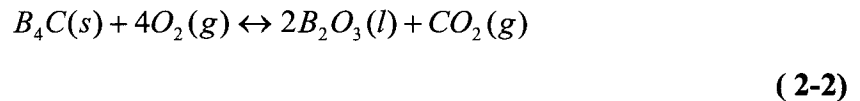
$$\Delta G^o = -2,811,450 + 413.98T \quad (J/mol)$$

(2-3)

There are two explanations for the presence of MgO. The first is, that, during cold

pressing, in air, there was some O_2 trapped within the cylindrical samples. During

subsequent sintering, this oxygen reacted with Mg to form MgO[19] according to

52

Equation (2-4).

$$2Mg(s) + O_2(g) \leftrightarrow 2MgO(s)$$

<div align="right">(2-4)</div>
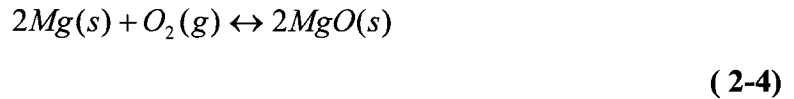
The standard free energy of the process described by Equation (2-4) is shown in

Equation (2-5).

$$\Delta G^o = -1,202,460 + 215.18T \quad (J/mol)$$

<div align="right">(2-5)</div>

The second explanation is that MgO is formed from a reaction of B_2O_3 and Mg,

according to Equation (2-6). As the proportion of B_4C is increased towards 38wt%, the

diffraction peak, there is a corresponding increase in the amount of B_2O_3 in the system.

$$B_2O_3(l) + 4Mg(s) \leftrightarrow 3MgO(s) + MgB_2(s)$$

<div align="right">(2-6)</div>
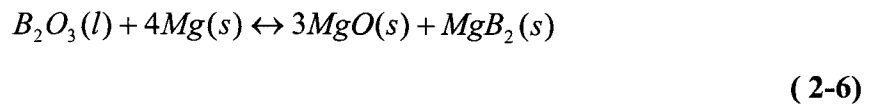
The standard free energy change for this reaction is shown in Equation (2-7).

$$\Delta G^o = -666,940 + 123.19T \quad (J/mol)$$

<div align="right">(2-7)</div>

With respect to MgB_2, there are two methods this boride may form. The first is described

by Equation (2-6). The second is the monolithic B that was identified in the B_4C reactant

will react with Mg to form MgB_2. described by Equation (2-8). The standard free energy

of this process is described by Equation (2-9).

$$Mg(s) + 2B(s) \leftrightarrow MgB_2(s)$$

<div align="right">(2-8)</div>

53
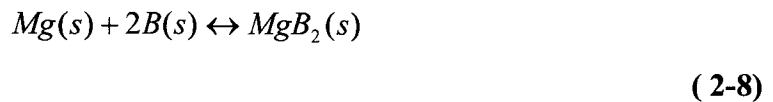
$$\Delta G^o = -92{,}050 + 10.46T \text{ (J/mol)}$$

<div align="right">(2-9)</div>

To determine the thermodynamic process, which likely occurs, Equation (2-3), Equation

(2-5), Equation (2-7) and Equation (2-9) were plotted as a function of temperature. This

plot is shown in Figure 2.26. This plot shows that the process which is most

thermodynamically likely is described by Equation (2-2). The next most

thermodynamically process is described by Equation (2-6).
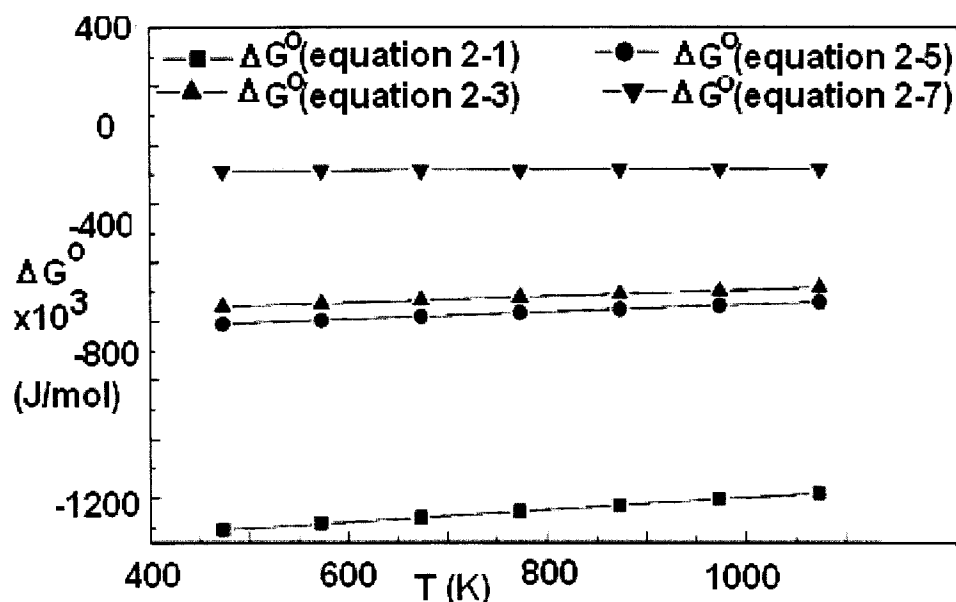
Figure 2.26: Jiang et al. Gibbs Free Energy Plots.

Since the melting temperature of B_2O_3 is 723K, at temperatures above this, liquid B_2O_3

will be interacting with solid Mg to form MgO and MgB_2. However, the thermodynamic

probability of Equation (2-2) and Equation (2-6) occurring does not preclude the

<div align="center">54</div>

occurrence of Equation (2-4) and Equation (2-8). Jiang et al. did not discuss the reaction

mechanism to form MgO and MgB_2 nor did Jiang et al. describe an overall equilibrium of

the system.

2.2.5.5   Laser-Clad Coatings of B_4C/ NiCrBSi powders.

An experimental study investigating the laser cladding of a powdered mixture of NiCrBSi

and B_4C onto Ti-based substrates has been reported by Meng et al.[28]. This study will be

discussed in this section.

2.2.5.5.1   Experimental Procedure.

In laser cladding, the powdered mixture of NiCrBSi and B_4C is applied onto the surface

of the substrate material[28] prior to being subjected to laser treatment[28]. The composition

of the cold-rolled substrate alloy is given in Table 2.8.

Table 2.8: Meng et al. alloy composition[28].

Al (wt%)	V (wt%)	Ti (wt%)
6	4	Balance

A powdered mixture of B_4C and NiCrBSi alloy was placed onto the surface of the

substrate[28]. The composition of this alloy is shown in Table 2.9. This alloy had a nominal

particle size between 50μm and 80μm. The particle size of the B$_4$C powder was between 3μm and 5 μm. No compositional testing of the B$_4$C powder was carried out by the authors.

Table 2.9: Meng et al. NiCrBSi alloy composition[28].

Cr (wt%)	B (wt%)	Si (wt%)	C (wt%)	Fe (wt%)	Ni (wt%)
15-20	3-5	3-6	1	<5	balance

The coating powder consisted of 5wt% B$_4$C and 95wt% NiCrBSi alloy[28]. This weighed powder mixture was mechanically mixed in a rolling mixer to ensure homogeneity[28]. After mixing, the powdered mixture, now placed on the substrate, was subjected to laser treatment. A transverse flow, 1.5kW, CO$_2$ laser[28] was used. The parameters for this laser are shown in Table 2.10. Meng et al. did not employ Ar gas to maintain an inert atmosphere during laser cladding[28].

Table 2.10: Meng et al. laser cladding parameters[28].

Beam Diameter	Transverse Velocity	Laser Power
3x10^{-03} m	5x10^{-03} m/s	0.75 kW

56

2.2.5.5.2 Discussion of Results.

The resulting experimental specimens were examined using SEM and XRD[28]. A micrograph of a laser-clad sample from Meng et al. is shown in Figure 2.27. In this micrograph, the coating and the substrate are clearly seen. Also, the interface between the coating and the substrate is seen[28].
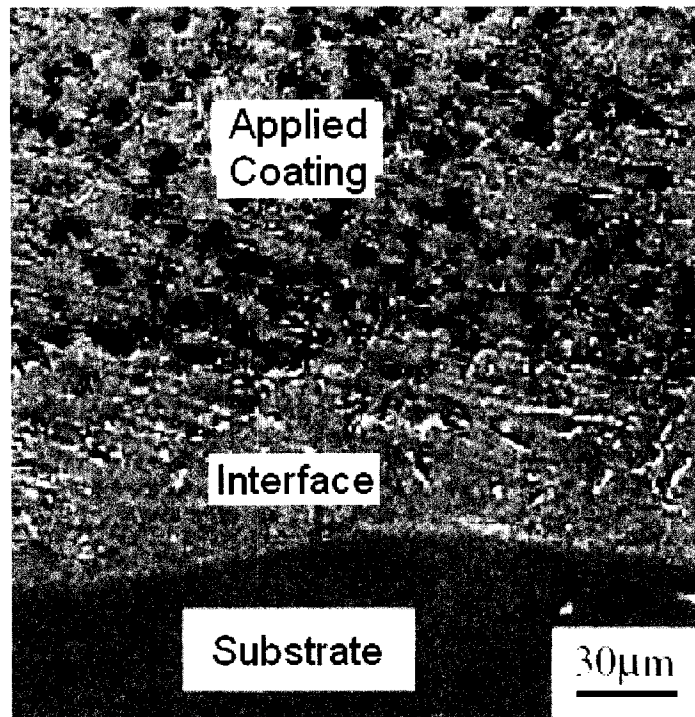
Figure 2.27: SEM micrograph of Meng et al. laser-clad sample[28].

Figure 2.28 shows an XRD diffraction pattern of the NiCrBSi alloy that was blended with B_4C powder for the coating. In this diffraction pattern, Ni, Ni_3B, CrB and Cr_7C_3 were

57

identified.
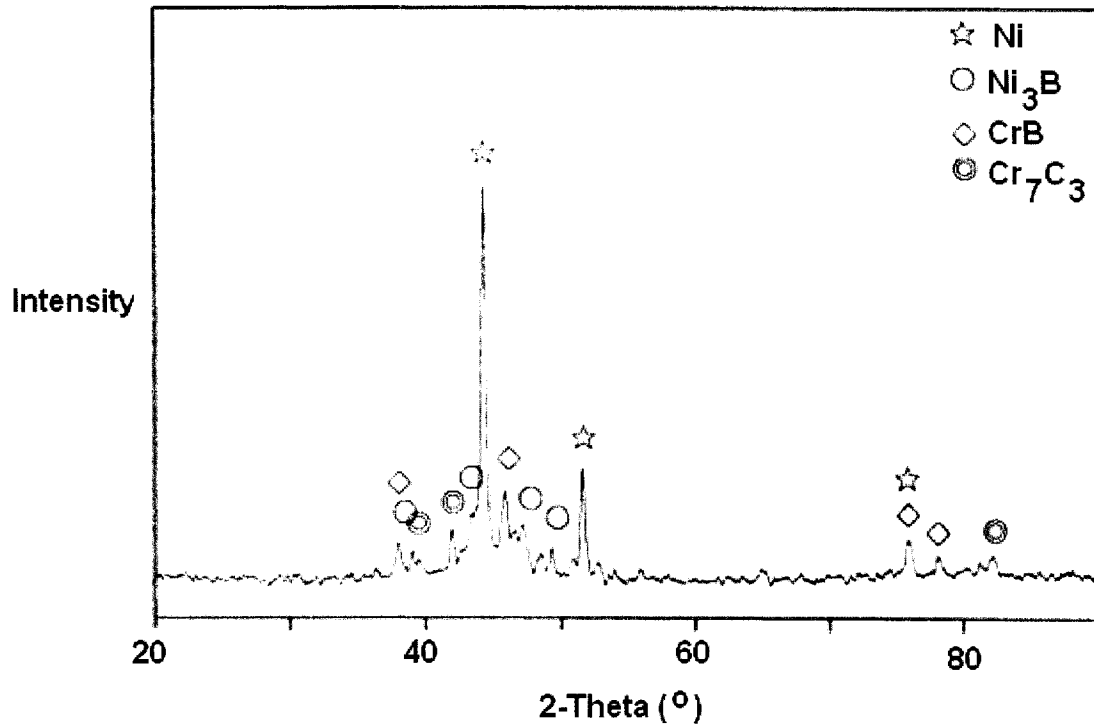
Figure 2.28: Meng et al., diffraction pattern of NiCrBSi alloy.

After the laser cladding treatment, XRD analysis of the coated material revealed the presence of Ni, Ti, TiB_2, TiC and CrB^{28}. It was also suggested that small amounts of Ni_3B and Cr_7C_3 might be present below the detection limit of the XRD test[28]. There was no B_4C found by XRD^{28}. This suggests that the 5wt% B_4C, in the original mixture, was reacted during laser cladding[28], or is present below the detection limit of the XRD equipment.

58
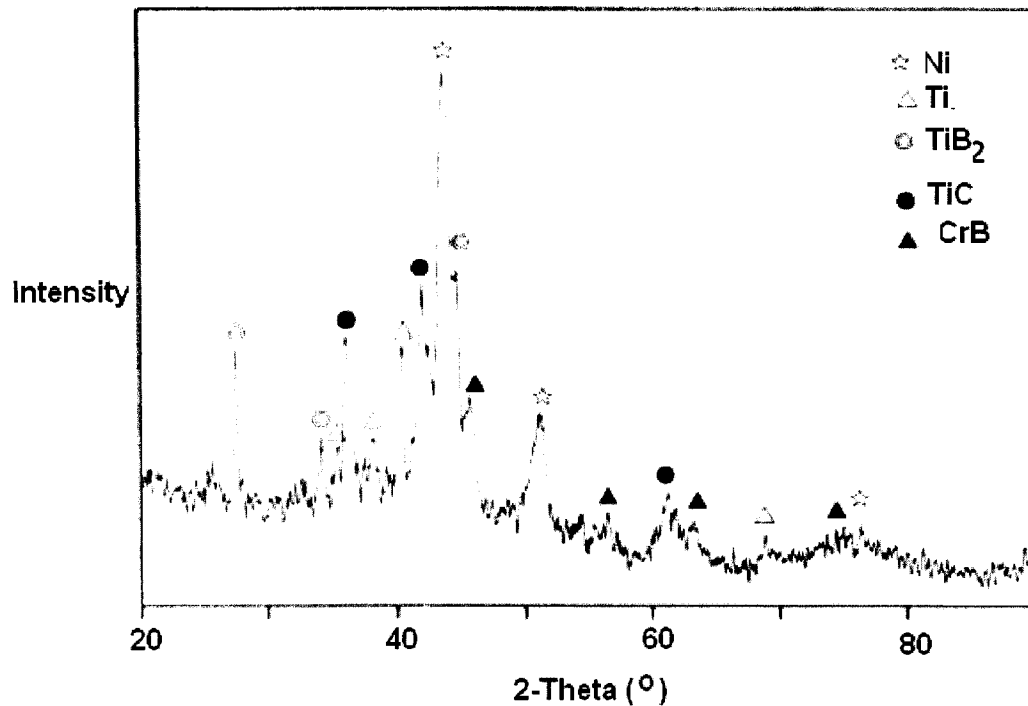
Figure 2.29: Meng et al., diffraction pattern of applied coating.

2.2.5.6   PTA using B_4C in Fe-Based Alloy.

The behaviour of B_4C under PTA surfacing conditions, using an Fe-alloy matrix, has

been studied[20]. The combination of a Fe-alloy, with a density[27] of 6150kg/m³ and B_4C,

with a density[27] around 2510kg/m³, would result in a heavier MMC than the Mg-B_4C,

MMC previously discussed[19]. However, the use of an Fe-alloy as matrix is cheaper than

Mg powder. In addition, a discussion of the metallurgical behaviour of B_4C under

varying PTA conditions is of interest when determining if B_4C is appropriate for PTA

surfacing[20].

59

2.2.5.6.1   Experimental Procedure.

The composition of the steel substrate is shown in Table 2.11. The PTA parameters that were used by Wang are shown in Table 2.12. In Wang's tests, the current of the plasma arc was varied between 80 and 250A[20]. The gas used for both the plasma and the powder transport was Ar.

Table 2.11: Wang PTA substrate composition[20].

C (wt%)	Mn (wt%)	Si (wt%)	Fe (wt%)
0.18	1.32	0.53	balance

Table 2.12: Wang PTA parameters[20].

Current (A)	Voltage (V)	Powder Feed Rate (kg/s)	Powder Gas Flow (l/s)	Plasma Gas Flow (l/s)
80-250	30-32	3×10^{-4}	8.3×10^{-3}	6.7×10^{-3}

Table 2.13 shows that composition of the powdered Fe-alloy for the coating. The nominal particle size for this powdered alloy was less than $150 \mu m$[20]. This Fe-alloy powder was combined, presumably by mechanical mixing, with B_4C powder. A detailed analysis of the B_4C powder was not provided. This B_4C powder had a nominal particle size less than $50 \mu m$[20].

60

Table 2.13: Wang Fe-alloy powder composition[20].

C (wt%)	Mn (wt%)	Si (wt%)	O (wt%)	Fe (wt%)
0.07	0.45	0.25	≤ 3.2	balance

The two powders, Fe-alloy and B_4C, were combined in different proportions for several tests[20]. The mechanically mixed powder, B_4C and Fe-alloy, was prepared with 5wt%, 10wt%, 20wt% and 30wt%B_4C[20]. The densities of the Fe alloy and the B_4C, are

$6150kg/m^3$ and 2520^9, [20]kg/m^3 respectively. The density of the Fe-alloy[20] used by Wang is given as $6150 \ kg/m^3$. Since the densities of the two powders are so different, to attain a uniform powder feed during PTA, the powdered mixture was ground with water glass[20]. After this grinding, the mixture of B_4C, Fe-alloy and water glass was dried and crushed into powder[20]. This was an attempt to equalize the differences between the two materials[20].

2.2.5.6.2   Discussion.

It is important to be aware that the melting point temperatures for the Fe-alloy used in these tests and B_4C are different. Wang provides the melting temperature of the Fe-alloy as 1358K and the melting temperature of the B_4C as 2723K. Therefore, for the temperature range from 1358K up to approximately 2723K, a reaction between solid B_4C

61

and liquid Fe-alloy would occur. As the liquid Fe-alloy reacts with the B_4C particulates, a surface layer would be formed on the B_4C particles[20]. Once this layer has surrounded the B_4C particulate, the reaction process becomes slower, owing to the necessity of reactant diffusion through this layer[29]. In terms of reaction kinetics, this layer slows the progression of the reaction. In the tests done by Wang, the B_4C particulates did not reach a temperature, within the feed gas, that would cause them to melt; therefore, the B_4C particulates entered the weld pool as solids[20].

After the B_4C particulates enter the weld pool, the difference in the density of the Fe-alloy powder and the B_4C powder causes the B_4C particulates to float[20]. If the weld pool solidifies quickly, solid B_4C particulates will remain in the final MMC[20]. This was seen when the arc current was low and when the powder feed rate was increased[20]. If the solidification rate is not sufficiently fast, the B_4C particles will melt. In the case that the B_4C in the weld pool melts, the liquid B_4C remains separate from the liquid Fe-alloy[20]. That is, the liquid B_4C does not readily dissolve into the molten Fe-alloy.

Chemical reactions between the melted B_4C and the melted Fe-alloy can occur, producing Fe-borides[20]. An increased arc current encourages these reactions[20]. The larger the current, the faster the liquid B_4C disappears from the weld pool[20]. Wang found that most of the B_4C particulates are reacted with the liquid Fe-alloy during PTA when an arc current greater than 200A is used[20].

62

A micrograph of an experimental sample, after a PTA treatment at 100A arc current is

shown in Figure 2.30[20]. This sample was of 5wt% B_4C in the powder feed. In this

micrograph, there are B_4C particulates clearly identified embedded in the Fe-alloy

matrix[20]. XRD of a sample treated at 100A is shown in Figure 2.31. This diffraction

pattern identifies austenite (FCC (face centred cubic) iron) and solidified compounds,

such as Fe_2B and Fe_3C[20]. The XRD pattern also identified ferrite (BCC (body centred

cubic) iron) .The presence of martensite was suggested though Wang provided no

microstructural verification of this phase. The XRD pattern also contained several,

unidentified peaks, which were not addressed by Wang[20].
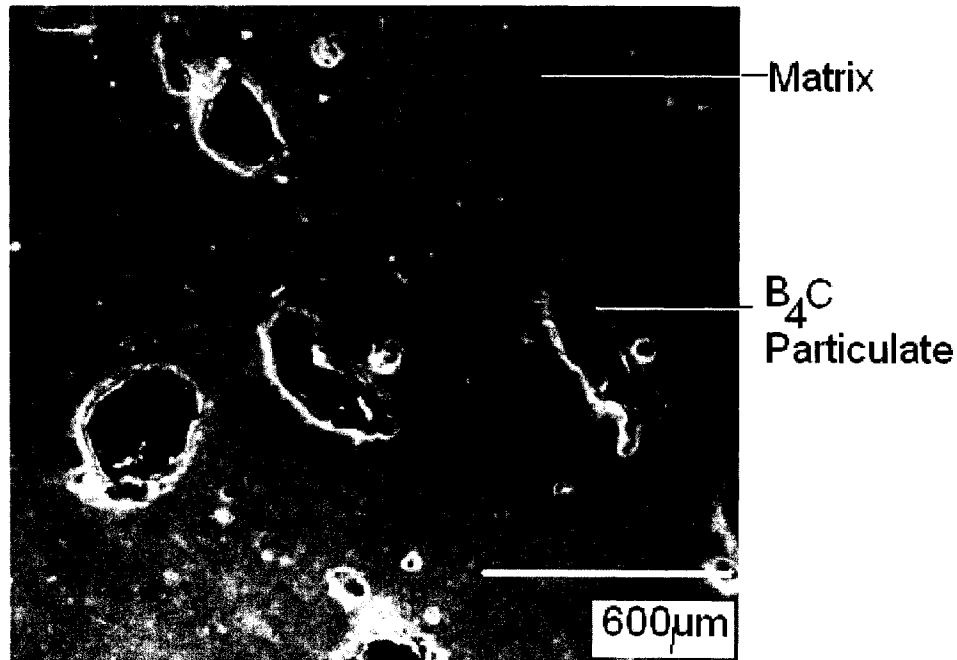
Figure 2.30: SEM micrograph of B_4C-Fe-alloy PTA coating[20].

63
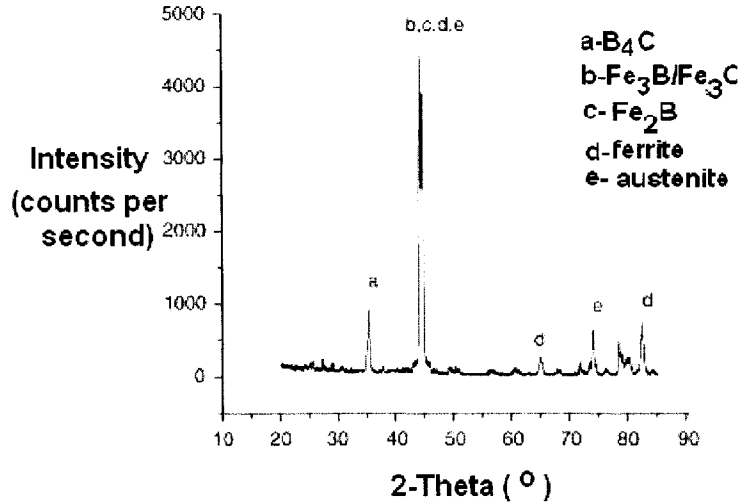
Figure 2.31: XRD of PTA Fe/B₄C, 100A arc current[20].

A micrograph of a 20wt% B₄C (powder feed) sample is shown in Figure 2.32[20]. This sample was subjected to an arc current of 240A[20]. In this micrograph, the interface between the substrate and the applied coating can be seen.
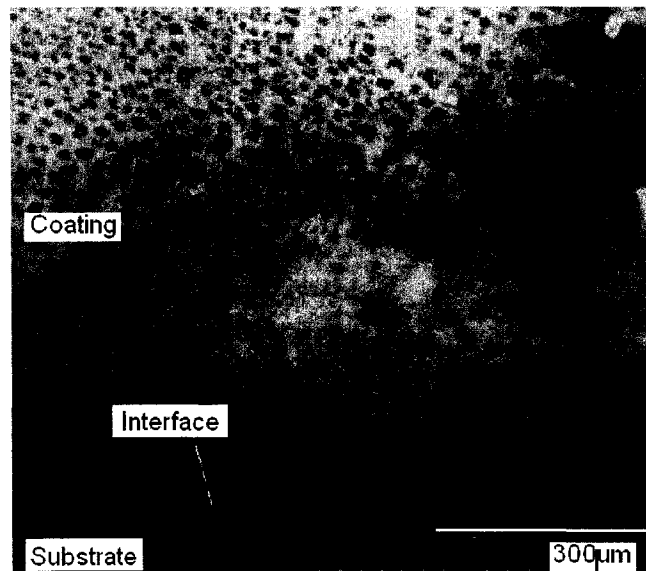
Figure 2.32: SEM micrograph of B₄C-Fe alloy showing interface[20].

64

XRD analysis of a sample fabricated at 240A, is shown in Figure 2.32. This analysis

identified FeB, Fe_2B, solidified eutectics containing cementite (Fe_3C) and Fe_3B as well as

martensite (no microstructural reference given) and austenite[20]. B_4C was not identified by

XRD in these samples[20]. B_4C not being identified indicates that there was a reaction

between the Fe and the B_4C, which consumed all or almost all of the B_4C.
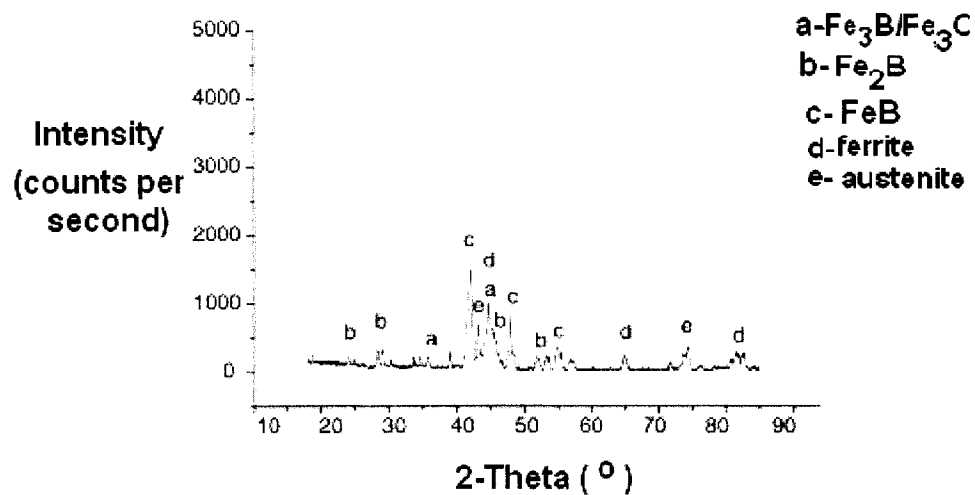
Figure 2.33: XRD pattern for Fe/B_4C, 240A[20].

2.2.6 Summary.

B_4C is a polar covalent carbide with an extremely high hardness[4, 9]. It is this high

hardness, which makes this material attractive in wear applications. However, oxidation

and instability at high temperature are concerns with this ceramic[15, 16]. There is clear

evidence of reactions between B_4C with matrix materials of Al[17], type 304 stainless

65

steel[18], Mg[19], NiCrBSi alloy[28] and Fe[20]. These studies involved elevated temperatures. In the Al experiments, stable aluminium borides were formed[17]. For the stainless steel, it was suggested that the boron carbide reacted with the alloying elements present, also to form stable metal borides[18]. For sintering with Mg, B_2O_3, magnesium borides and magnesium oxides formed[19]. Laser cladding of B_4C and a NiCrBSi alloy onto a Ti-alloy substrate resulted in the formation of titanium-borides, titanium carbides as well as chromium carbides[28]. PTA surfacing using a blend of Fe-alloy and B_4C powders was carried out[20]. These tests showed that Fe and B_4C form iron borides and iron carbides and that to maintain B_4C particulates during PTA, a low arc current (100A) was used[20].

The B_4C studies covered in the literature survey did not identify the fundamental reason for the failure of PTA Ni-B_4C MMC's. This work shall address the thermodynamic stability of B_4C in Ni and contrast it with the stability of WC in Ni at elevated temperature (T > 1773K). The next chapter, Chapter 3.0, the experiments designed for this work will be discussed.

66

3.0 Experimental Apparatus and Procedure.

3.1 Apparatus.

The behaviour of solid ceramic particulates of the ceramics, WC and B_4C, contacted by molten Ni was investigated in this work. The melting temperature of Ni is approximately $1730K$[9] while WC melts at $2800K$[15] and B_4C melts above $2700K$[15]. Therefore, the experimental design required the use of a furnace to reach and maintain a temperature above 1730K.

A 30kW induction furnace was employed in these tests. The coil was stripped down to the basic copper coil in order to tailor the system for the experiments in this work. Phenolic rods were then attached at three equidistant points on the coil to prevent the turns of the induction coil from contacting each other. The coil was then cemented with the refractory-grade ceramic, "Wet Super 3000 Mix 26 - Refractory Mortar" manufactured by "Vesuvius Canada Refractories Inc." To ensure that the coil cement was thoroughly dried, it was placed in an oven at approximately 398K overnight. Once the coil cement was dry, the housing unit for the coil was assembled. A pre-fabricated, high temperature, housing unit was purchased. This unit is made of "Indux® 98", a ramming material containing 98% MgO. The housing unit includes top and bottom plates and a cylinder to form the walls. The cemented induction coil was placed within this housing unit to form the entire melt unit (Figure 3.1).

67
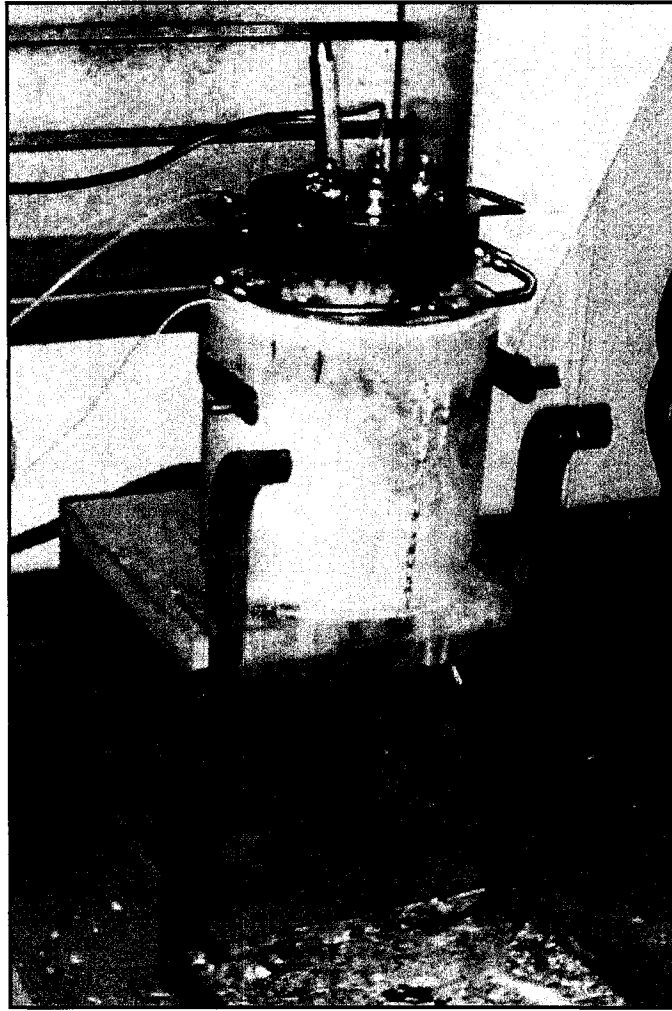
Figure 3.1: Completed furnace melt unit and cap.

Within the melt unit, a method to contain the mixture of molten Ni and ceramic was

needed. After trial and error, a crucible-within-a-crucible system was devised. This was

to ensure that, should the inner crucible crack during the experiments, the outer crucible

would contain the leaked material, allowing for the easy removal of both crucibles from

the melt unit. A large-diameter MgO crucible, with an inner diameter of approximately

20.3cm, was placed within the furnace coil and acted as the outer crucible. Refractory

68

tamping material, Inductogrog no. 150, was rammed into the space between this crucible and the coil. Then pelletised graphite was poured into the MgO crucible, under and around a smaller diameter alumina crucible, the inner crucible. This alumina crucible had an outer diameter of 8.9cm, which held the melt. This experimental set-up allowed the alumina crucible to be easily removed from the MgO crucible.

Since B_4C and Ni oxidize at high temperatures[15] an Ar atmosphere is necessary. To achieve this inert atmosphere over the Ni melts, a cap was designed and constructed (Figure 3.2). The cap was fabricated using mild carbon steel, which was lined with the refractory cement "Wet Super 3000 Mix 26 - Refractory Mortar". As an added precaution, a cooling coil, seen in both Figure 3.3a and Figure 3.3b was affixed to the cap to prevent overheating.

In the cap design, it was necessary to consider factors such as melt viewing, powder injection, melt sampling as well as gas injection. A large port was machined into the top of the cap to allow a port-plate (Figure 3.2), with ports for sampling and analysis machined into it. The port plate had five ports machined into it (Figure 3.2). The largest port was centred in this plate, and was used for melt viewing. The design of the viewing port is discussed in section 3.1.2.The remaining four ports were machined around the edges of the port plate. The first port was used for gas injection, which is discussed further in 3.1.1. The second port was used for powder injection, see section 3.1.3.

69

Another port was used for oxygen analysis, see section 3.1.4. The fifth port was used for

melt sampling, see section 3.1.5.
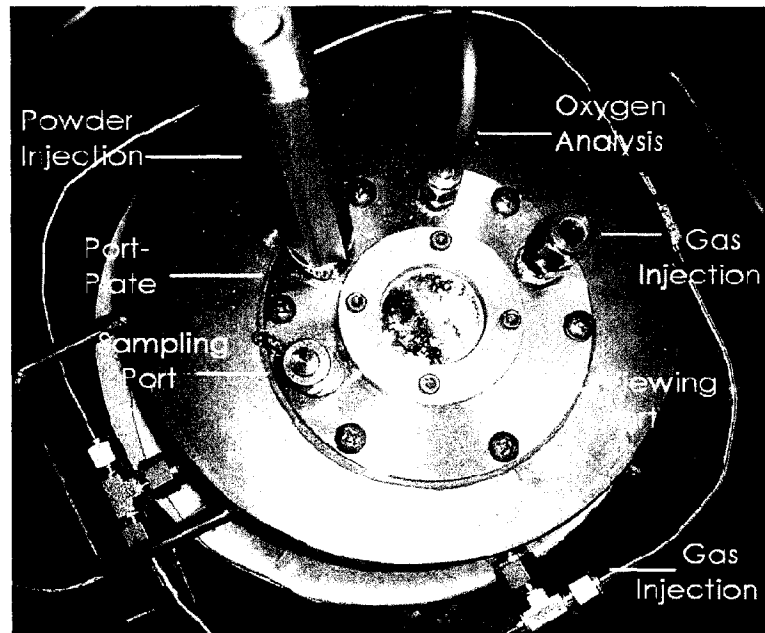
Figure 3.2: Melt unit cap.

3.1.1 Gas Injection.

There were two methods of gas injection employed in these experiments. The first

method utilized one of the ports that was machined into the port plate (Figure 3.2). An

alumina tube was fed through this port, placing the end above the surface of the melt.

It was decided that it would be beneficial to add more ports for gas injection to the melt

unit. This was accomplished by machining ports circumferentially around the cap. Four

70

gas injection ports were added in this manner, bringing the total number of gas injection ports to five (Figure 3.2). Figure 3.3 shows two schematic representations of the furnace cap, showing the circumferential gas injection line and ports. Figure 3.3a shows the exterior of the melt unit cap while Figure 3.3b shows the interior of the cap, identifying that the gas injection ports were machined through the refractory mortar to the interior of the cap.
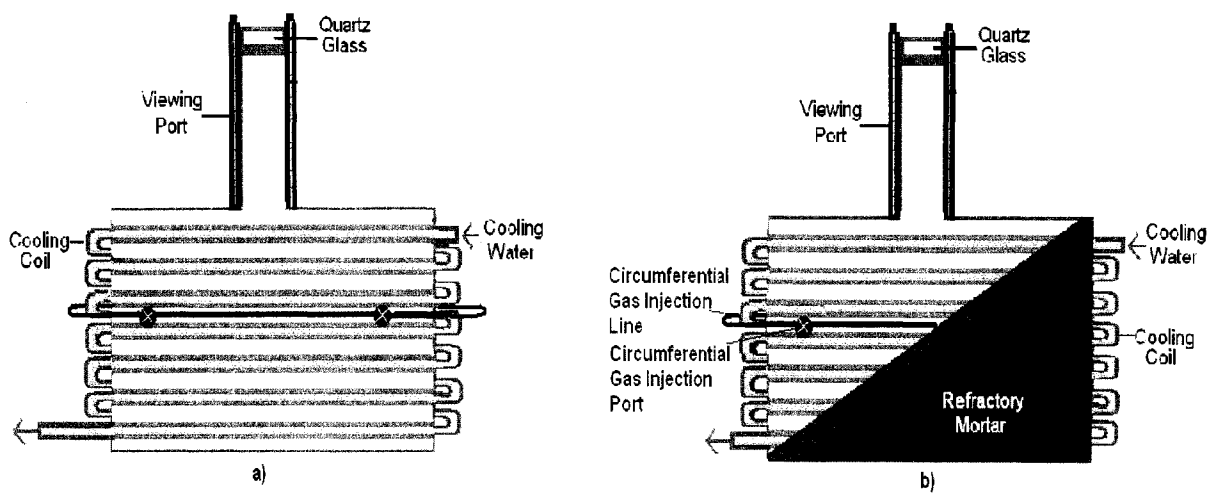
Figure 3.3: a) Side view of melt unit cap b) Side view of melt unit cap showing interior refractory mortar.

3.1.2 Melt Viewing.

A port was machined into the centre of the circular port plate for viewing the melt and for measuring the melt temperature. A circular piece of quartz glass was cut to fit this port. The function of this quartz window was to make temperature readings using an optical

71

pyrometer made by the Leeds & Northrup Company of Philadelphia. Two holding plates

were then machined to hold the glass in place (Figure 3.4).
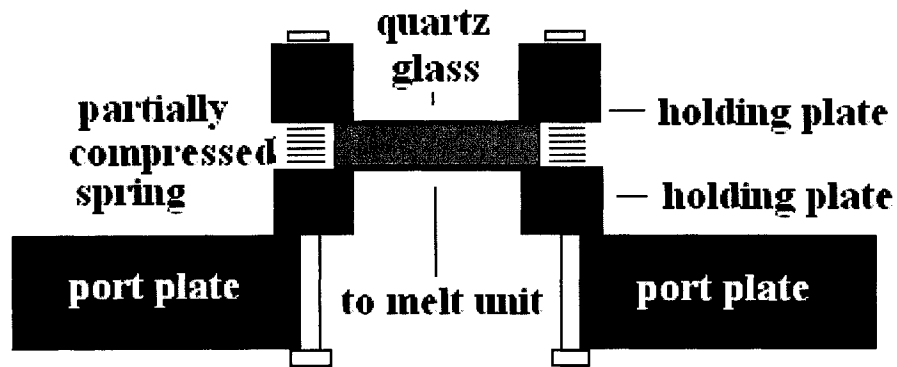
Figure 3.4: Viewing port.

Four screw holes were machined into each of the two plates. The screws used were

inserted into springs. The screws were then bolted to the top of the viewing port and to

the melt-facing side of the port-plate (Figure 3.4). These screws were not tightly bolted so

as to allow the springs to be partially compressed. This was to prevent exerting undue

pressure on the quartz glass, which could cause it to crack. This port-plate was then

bolted to the top of the furnace cap (Figure 3.2).

3.1.3 Powder Injection.

One of the ports seen in Figure 3.2 was utilised for powder injection. Figure 3.5 shows a

schematic of the powder injector. The pressurized powder injection unit was fabricated

72

from a stainless steel vessel. A gas inlet was machined into one end of the unit to permit pressurization. This pressurization was used to force the ceramic powder out of the powder injection unit. At the opposite end of the vessel, threads were included to allow the attachment of a ball valve through which powder flowed when opened.
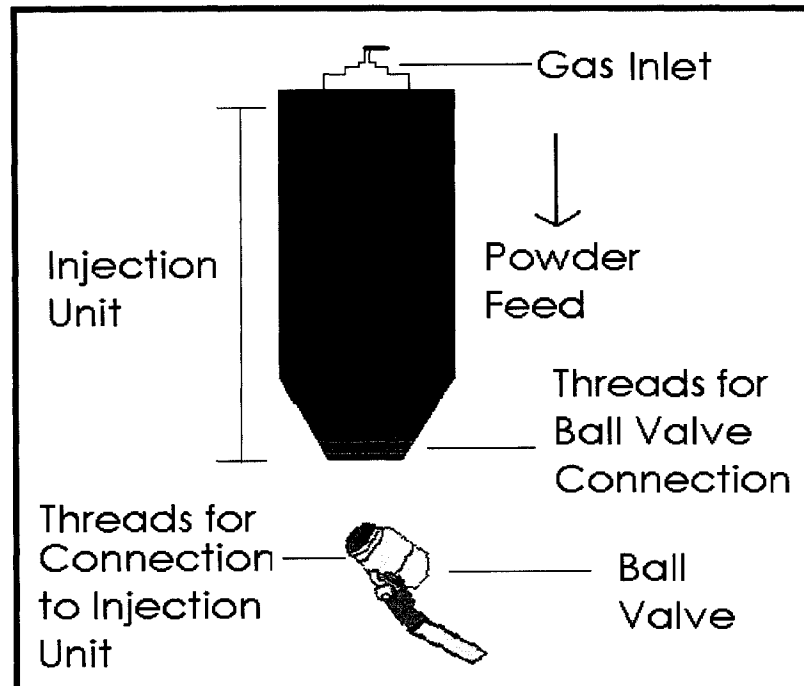
Figure 3.5: Pressurized powder injection unit.

3.1.4 Oxygen Analysis.

It was necessary to monitor the environment inside the melt unit to ensure that there were no major leaks in the system. An oxygen analyzer from Centorr Vacuum Industries[30] was employed for this purpose and showed O_2 levels at or below 300ppm (by volume) during

73

experiments. This analyzer uses a zirconia electrochemical cell, which measures the oxygen partial pressure[30]. The input gas to this type of cell must be cooled for accurate readings. Therefore, a method for cooling the gas prior to its entry to the analyzer was necessary. To accomplish this, a copper tube, run through cooling water, was used.

The 1.1cm diameter, copper tube was attached to one of the ports on the port-plate (Figure 3.2). A portion of this tube was then wound into a coil and run through a bucket of cooling water prior to reaching the oxygen analyser. Gas from on top of the melt ran through this copper tubing into the oxygen analyser.

3.1.5 Melt Sampling.

Sampling of the melt was carried out using 1.3cm diameter, Pyrex rods, approximately 70cm in length. An evacuated quartz tube was carefully attached onto the end of each rod, creating the joint seen in Figure 3.6. Quartz has a melting temperature of approximately 1980K. Contamination of the melt was not a significant concern through the melting of the quartz tubes, as this temperature was not reached during testing (section 3.3 further discusses the temperatures used). The end of these tubes that was not attached to the rod had small, thinned area at one end. To sample the melt, one end of the tube was plunged below the surface of the melt, the thermal shock this caused burst the thinned area of the tube. Since the tubes are evacuated a portion of the melt is drawn into

74

the tube (Figure 3.6). The Pyrex rod and ampule were then removed through one of the

ports in the furnace lid (Figure 3.2). Samples were then air-cooled.
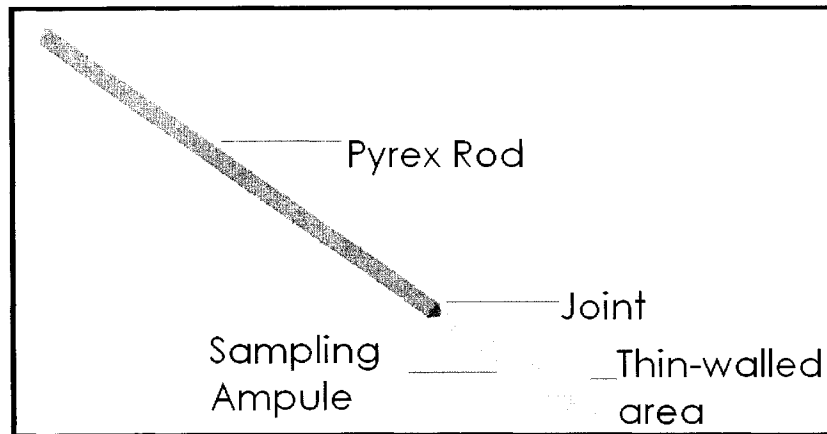
Figure 3.6: Sampling ampule and rod.

3.2 Materials and Procedure.

There were two materials that were required to perform these tests. These were the

ceramic powders and the nickel. The ceramic powders, WC and B_4C, were supplied by

Kennametal and Electro Abrasives respectively. The powders were determined to be

between the −70 mesh and +270 mesh sizes. This means that the particle diameters were

all between 210µm and 53µm.

The nickel used was supplied by INCO, at 99.7% purity. This nickel was used as the melt

material for these tests. These granules/ pellets ranged in diameter up to approximately

75

two centimetres. The nickel granules were poured into the alumina crucible prior to the

furnace cap (Figure 3.2) being placed over the furnace melt unit. The alumina tube for

gas injection was then placed in the nickel granules. The reason for this is that alumina is

prone to thermal shock. As the furnace heats, the alumina tube will slowly heat, avoiding

cracking from thermal shock. The melt unit, prior to the cap being placed over it, is

shown in Figure 3.7.
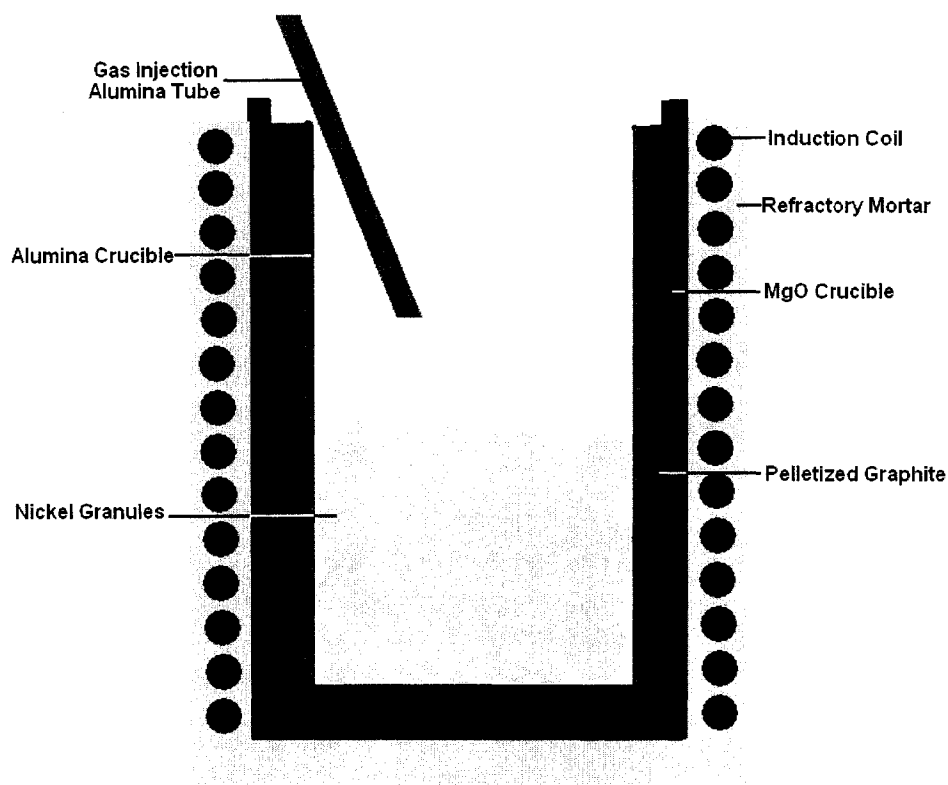
Figure 3.7: Schematic of the melt unit prior to heating.

After the nickel granules and the alumina tube were in place, the furnace cap was placed

onto the melt unit. A schematic of the experimental set-up is shown in Figure 3.8. All of

the ports and appendages are labelled on this schematic. It can be seen that the furnace

76

cap sat on the housing unit of the melt unit. That is, the diameter of the cap placed it outside the diameter of the MgO crucible.
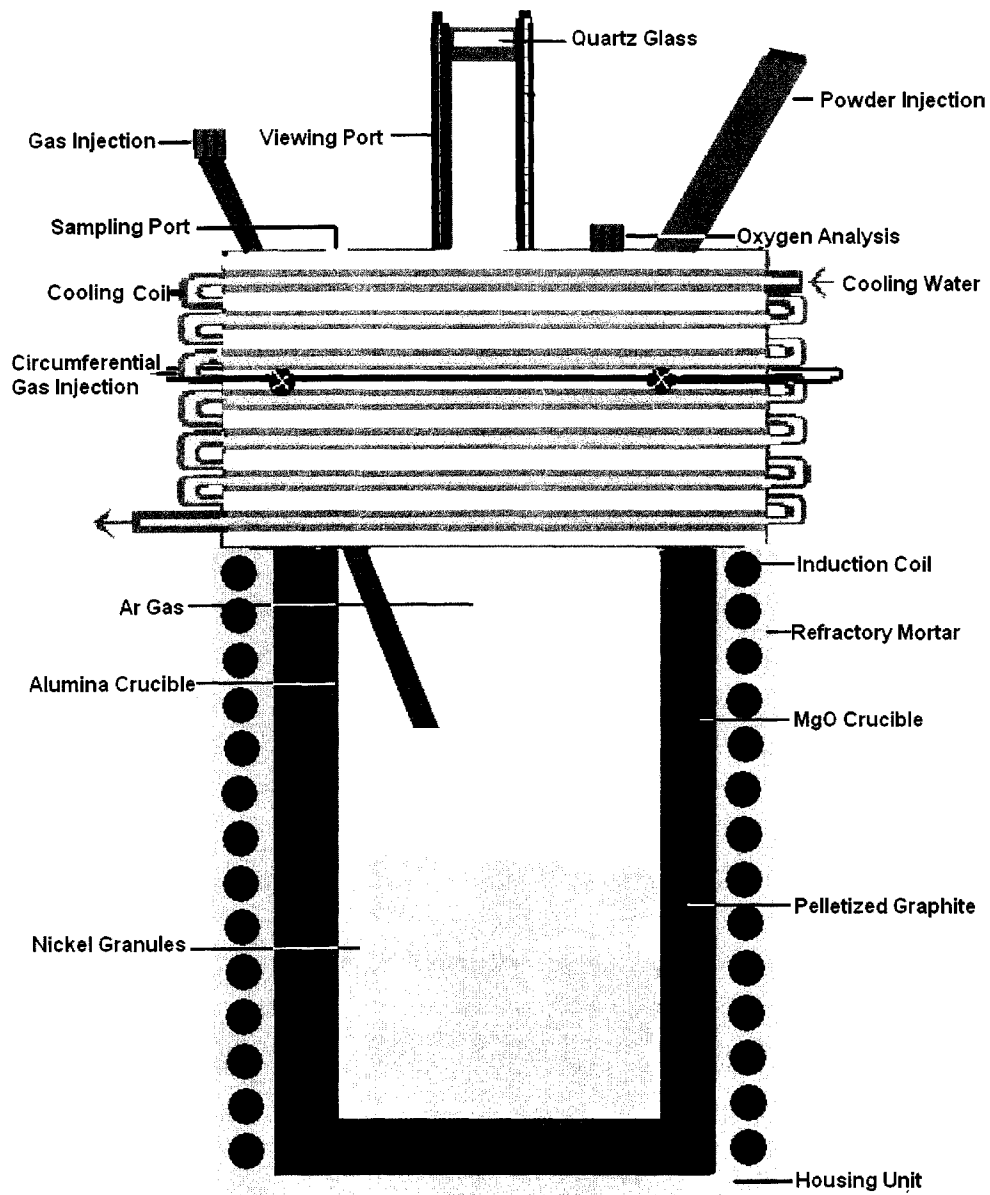
Figure 3.8: Schematic of the melt unit and furnace cap.

Once the nickel granules had melted, and the desired temperature had been reached, the

ceramic powder was added to the melt via the powder injection unit. The temperature within the unit was measured using the optical pyrometer previously mentioned.

A ball valve was used as the injection port for the ceramic powder (Figure 3.5). This valve was threaded on to the powder injection unit after a predetermined amount of ceramic powder was added (Figure 3.5). After the ball valve closed, argon gas was blown into the unit, pressurizing it. The unit was then tilted at an angle and opened, while the argon still flowed through the vessel. Tilting this unit during this process allowed gas to be blown from one end to the other without losing any ceramic powder. The valve was then closed and the pressurized powder injection unit attached to the furnace cap (Figure 3.9). The powder was added to the melt by opening the ball valve. This caused the ceramic powder to be blown onto the surface of the melt (Figure 3.9). The powder was then mixed into the nickel melt by the stirring action of the induction furnace. The ball valve and powder injection unit were then immediately removed from the furnace cap to avoid melting the seals in the ball valve. After removal, the short pipe used for powder injection was stuffed with insulation to avoid heat loss.

78
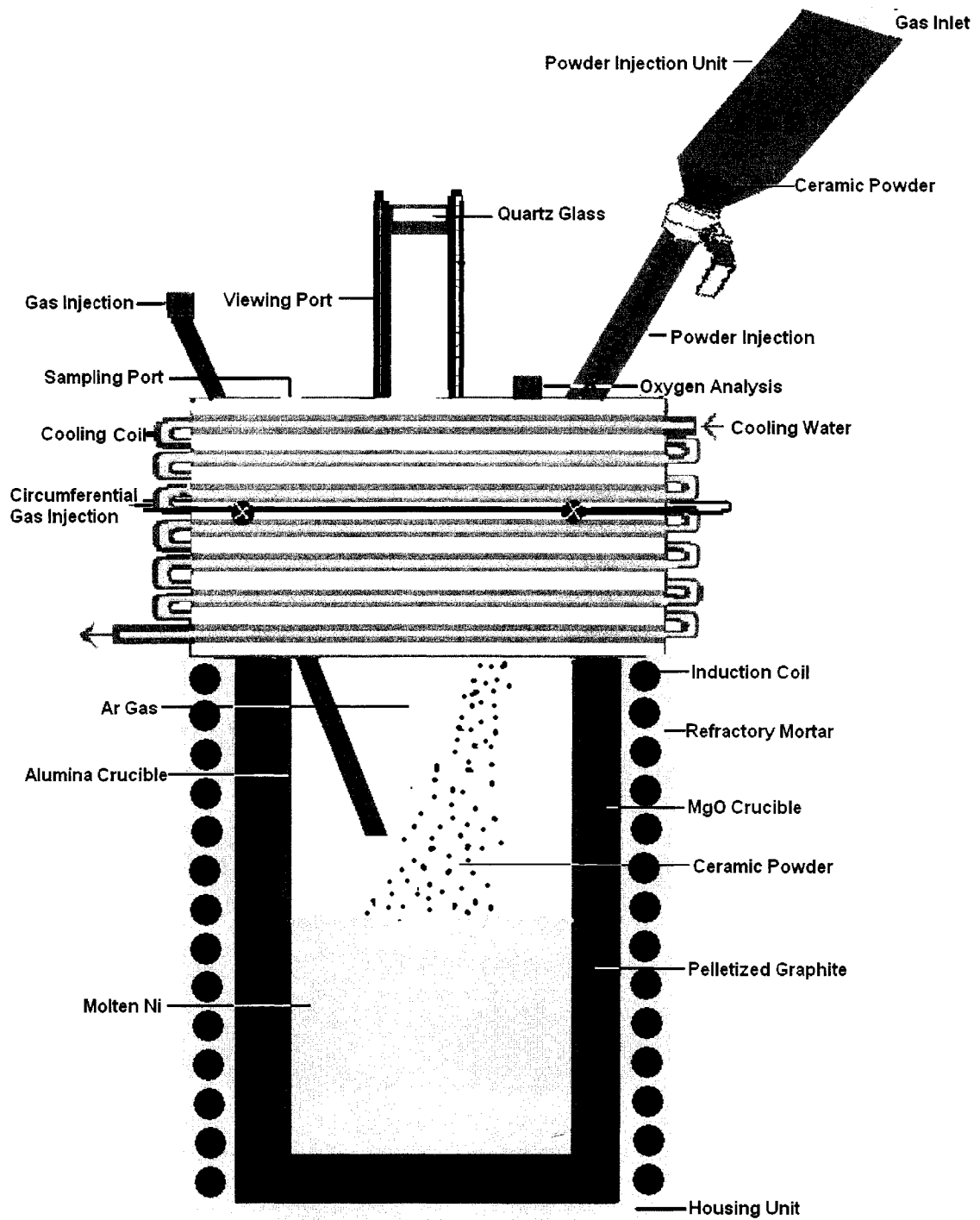
Figure 3.9: Schematic of the furnace including cap and powder injection unit.

79

The experiments carried out by Nagase et al. were used as an initial guide of sampling times for the Ni-B$_4$C system. Also, it was shown by Nagase et al., that the decomposition of boron carbide, at elevated temperature, could occur quickly, sampling of the melt in the Ni-B$_4$C system was scheduled to begin shortly after the addition of the ceramic powder to the molten melt. For consistency, the timing of the sampling in the WC-Ni system was similar.

3.3 Experimental Matrix.

The experiments involved the addition of ceramic powder to a molten nickel bath, creating an MMC. In both the WC and B$_4$C tests, experiments were carried out at temperatures from 1773K to 1973K. In several of the experiments, the ceramic powder was added to the molten bath more than once. The time of the first ceramic powder injection, addition #1, was considered to be time zero. As an example, in experiment B6, B$_4$C powder was added at time zero, at 7.1minutes and at 12.8minutes.

Table 3.1 and Table 3.2 show the experimental matrix that was used for the WC and B$_4$C experiments respectively. These tables give the test temperature, the addition number of the ceramic powder, the time of ceramic powder injection as well as the number of moles of Ni, WC or B$_4$C. Table 3.1 and Table 3.2 also include the molar ratios for the Ni-WC and the Ni-B$_4$C systems, $M^o_{(Ni/WC)}$, $M^o_{(Ni/B4C)}$. The molar ratio, in each system, is defined

80

as the number of moles of Ni to the number of moles of ceramic (WC or B_4C). In these tables, the calculated wt% Ni and wt% ceramic (WC or B_4C) values are included. As a results of the molten mixtures having ceramic powder added more than once, at varied times, the number of moles of Ni and ceramic (WC or B_4C) and the wt% values for Ni and ceramic (WC or B_4C) are cumulative.

In the Ni:WC experiments, $M^o_{(Ni/WC)}$ was varied from 3 to 250. In experiment W3, tungsten carbide powder was injected into the nickel melt only once. In experiments W5, W8, W10 and W12, tungsten carbide powder was injected at several times. Injecting the tungsten carbide several times changed the molar ratio of the system, as can be seen in Table 3.1.

In the Ni: B_4C tests $M^o_{(Ni/B4C)}$ ranged from 1 to 94 (Table 3.2). In experiments B1 and B2, boron carbide powder was injected only once, after the nickel was melted. In experiments B6, B7, B9 and B11, boron carbide was injected several times, thereby altering the molar ratio in the system, as can be seen in Table 3.2.

81

Table 3.1: Experimental schedule for Ni:WC experiments, showing nominal compositions.

Experiment #	T (K)	Addition #	Time of Addition (min)	Ni (mol)	WC (mol)	Nominal Molar Ratio $M^o_{(Ni/WC)}$	Wt% Ni	Wt% WC
W3	1773	1	0.00	17.0	0.1	167.0	98.0	2.0
W5	1773	1	0.00	12.8	1.0	12.5	79.0	21.1
W5	1773	2	21.4	12.8	2.0	6.3	65.2	34.8
W5	1773	3	32.6	12.8	3.1	4.2	55.6	44.4
W5	1773	4	42.5	12.8	4.1	3.1	48.4	51.6
W8	1873	1	0.0	12.8	0.1	250.5	98.7	1.3
W8	1873	2	3.0	12.8	0.1	125.2	97.4	2.6
W8	1873	3	4.7	12.8	0.2	83.5	96.2	3.9
W8	1873	4	6.1	12.8	0.2	62.6	95.0	5.1
W8	1873	5	7.5	12.8	0.3	50.1	93.8	6.3
W8	1873	6	9.9	12.8	0.3	41.7	92.6	7.4
W8	1873	7	10.5	12.8	0.4	35.8	91.5	8.5
W10	1973	1	0.0	12.8	0.1	250.5	98.7	1.3
W10	1973	2	2.3	12.8	0.1	125.2	97.4	2.6
W10	1973	3	3.8	12.8	0.2	83.5	96.2	3.9
W10	1973	4	5.2	12.8	0.2	62.6	95.0	5.1
W12	1873	1	0.0	8.5	0.1	83.5	96.2	3.9
W12	1873	2	3.2	8.5	0.2	41.7	92.6	7.4
W12	1873	3	6.0	8.5	0.3	27.8	89.3	10.7

82

Table 3.2: Experimental schedule for Ni:B₄C experiments,

showing nominal compositions.

Experiment #	T (K)	Addition #	Time of Addition (min)	Ni (mol)	B₄C (mol)	Nominal Molar Ratio M°(Ni/B4C)	Wt% Ni	Wt% B₄C
B1	1773	1	0.0	17.0	0.2	94.1	99.0	1
B2	1773	1	0.0	8.5	0.2	94.1	99.0	1
B6	1773	1	0.0	8.5	2.7	3.1	76.9	23.1
B6	1773	2	7.1	8.5	5.4	1.6	62.5	37.5
B6	1773	3	12.8	8.5	8.2	1.1	52.6	47.4
B7	1873	1	0.0	8.5	0.4	23.5	96.2	8.9
B7	1873	2	2.9	8.5	0.7	11.8	92.6	7.4
B7	1873	3	5.4	8.5	1.1	7.8	89.3	10.7
B7	1873	4	8.0	8.5	1.5	5.9	86.2	13.8
B9	1973	1	0.0	8.5	0.4	23.5	96.2	3.9
B9	1973	2	1.4	8.5	0.7	11.8	92.6	7.4
B9	1973	3	3.1	8.5	1.1	7.8	89.3	10.7
B11	1773	1	0.0	12.8	0.4	35.3	97.4	2.6
B11	1773	2	1.6	12.8	0.7	17.7	95.0	5.1
B11	1773	3	3.1	12.8	1.1	11.8	92.6	7.4

83

Sampling of the molten baths was done at various times. In the experiments that had

multiple additions of boron carbide or tungsten carbide added, samples were pulled at

various $M^o_{(Ni/WC)}$, $M^o_{(Ni/B4C)}$. For example, in experiment B6, samples were taken at

$M^o_{(Ni/B4C)}$ of 1.57 and 1.1. Sampling times are shown in Table 3.3 and Table 3.4 for the

Ni-WC and the Ni-B_4C experiments, respectively.

Table 3.3: Sampling schedule for Ni:WC experiments, $M^o_{(Ni/WC)}$.

Experiment #	Sampling Time (min)	Nominal Molar Ratio $M^o_{(Ni/WC)}$
W3	3.0	167.0
W3	9.5	167.0
W3	12.2	167.0
W5	10.2	12.5
W5	11.5	12.5
W5	37.0	4.2
W8	0.7	250.5
W8	3.2	125.0
W8	4.9	84.0
W8	10.7	36.0
W10	0.2	250.5
W10	2.9	125.0

84

Table 3.4: Sampling schedule for Ni:B$_4$C experiments, M^o$_{(Ni/B4C)}$.

Experiment #	Sampling Time (min)	Nominal Molar Ratio M^o$_{(Ni/B4C)}$
B1	8.5	94
B1	11.3	94
B2	11.8	94
B6	8.8	1.6
B6	13.5	1.1
B6	14.2	1.1
B7	0.9	23.5
B7	3.9	12
B7	6.5	7.8
B9	1.5	12
B9	3.3	7.8
B11	0.5	35
B11	2.5	18
B11	3.3	12

3.4 Analysis Techniques and Parameters.

The analysis of the experimental samples required a number of analytical techniques to

determine the exact nature of the reinforcement, WC or B$_4$C, in the Ni matrix and the

extent of any chemical reaction between reinforcement and matrix. To determine the

extent of mixing, chemical analysis of the MMC was carried out using Inductively

85

Coupled Plasma spectroscopy (ICP) and x-ray fluorescence (XRF). Optical microscopy was used to visualize the presence of the reinforcement in the Ni matrix. Subsequently, the samples were analysed using the electron microprobe with wavelength dispersive spectroscopy (WDS) to identify the location of the elements in the respective MMC with respect to the microstructure of the sample. Finally, x-ray diffraction, XRD, was used to identify species present in the respective MMC microstructure.

3.4.1 Yield of W and Yield of B.

Chemical analysis was used to determine the amount of W and the amount of B that entered the melt. There are several methods available to carry out chemical analysis[31]. One technique used is x-ray fluorescence. In this technique, a sample is dissolved and an x-ray beam impinged upon the sample, causing the sample to absorb energy[32]. This absorbed energy, if large enough, causes an inner-shell electron to be expunged from its orbit. An outer-shell electron then "falls-in" and replaces the inner-shell electron. When this happens, energy is released and the sample emits a characteristic x-ray[33]. These emitted characteristic x-rays are then detected and counted. By comparing these results against standards, quantitative chemical analysis is available. This technique is used for major element analysis, typically, 10-100ppm's of heavier elements[34], such as Ni, can be detected.

86

Inductively coupled plasma (ICP) is another chemical analysis technique. In this technique, the sample is dissolved and introduced into an Ar plasma stream as a mist[32]. This technique measures the spectrum of visible light emitted by the elements at the plasma's temperature[32]. A spectrometer is then used to measure the light that is emitted by the samples. The intensity of the light is measured by the spectrometer. An attached computer utilizes software to compare the intensity of the measured wavelengths to known standards, thereby identifying the concentrations of a wavelength of interest. This technique has the advantage of being able to analyse the lighter elements, such as boron, more effectively[32]. In fact, boron can be analysed down to a concentration of $5\mu g/l$[34].

3.4.2 Elemental Point Analysis.

The purpose of elemental point analysis is to determine if there are areas in a sample where the concentration of one or more elements is elevated with respect to other areas of the sample. Elemental point analysis can be done in both the energy dispersive spectroscopy equipped scanning electron microscope (EDS-equipped SEM) and the WDS-equipped electron microprobe.

In EDS and WDS, the electron beam is impinged upon the experimental sample inside a vacuum chamber[33]. When the electron beam strikes the sample, the beam and the atoms in the sample interact. This interaction occurs within the sample-beam interaction

87

volume, identified in Figure 3.10[33]. The two parameters, R_1 and S, which identify the

dimensions of the interaction volume, are described by Equation (3-1) and

Equation (3-2).

$$R_1 = \frac{0.1E_0^{1.5}}{\rho} \ (\mu m)$$

(3-1)

$$S = \frac{0.077E_0^{1.5}}{\rho} \ (\mu m)$$

(3-2)

In EDS, the characteristic x-rays emitted by the sample are collected using a

semiconductor detector. This detector causes the characteristic photon energy of the x-ray

to be converted to voltage, which is then measured. In WDS analysis, the characteristic

x-rays that are emitted from the sample strike a diffracting crystal, which diffracts the x-

rays. There are several diffracting crystals available. A layered dispersion element,

LDE2, crystal is used for B and C-detection[33]. For Ni, a lithium fluoride, LiFH, crystal is

used[32]. These diffracted x-rays then strike a detector, which measures them.

88
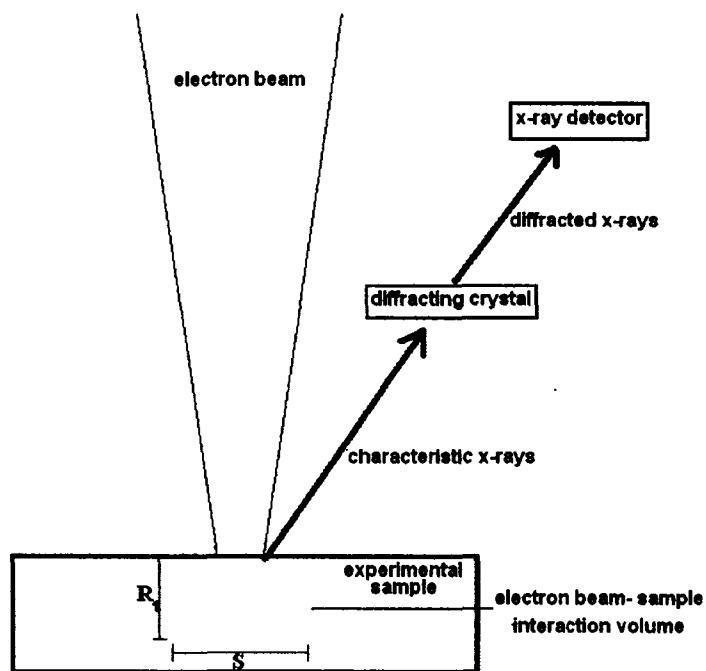
Figure 3.10: Experimental sample and electron beam interaction for WDS.

Analysis using WDS in the electron microprobe (EPMA) was chosen because the detection limits of WDS are superior when compared to EDS[33]. The EDS system can typically detect approximately 0.1wt% while the WDS system can detect down to 0.04wt%[33]. Therefore, an order of magnitude in resolution is gained by choosing the WDS system over the EDS system. In order to be consistent, it is necessary to evaluate many points within the microstructural feature of interest. For example, within one area of a sample, determining the wt% of each element, one could repeat the analysis 50-100times. This would allow the calculation of maximums, minimums, averages ($\bar{x}$) as well as standard deviations (σ). The manner in which the standard deviation is calculated is shown in Appendix A.

89

Table 3.5shows the parameters that were used for WDS analysis using the microprobe. These parameters include the spot size for the impinging beam. This number, 5μm, was during the imaging portion of analysis[33]. Imaging was used to identify features of interest for further analysis in the samples. These features of interest were then analysed using WDS.

Table 3.5: WDS/ Microprobe Parameters.

Beam Current (i_b)	Spot Size (imaging)		Accelerating Voltage (E_o)	Dwell Time
20.5nA	During imaging	During WDS	20kV	15ms
	10nm	5μm		

3.4.3 Compound Identification.

A commonly used technique, powder x-ray diffraction (XRD) was chosen for compound identification. In this technique, monochromatic x-rays, from a Co-tube source[35], are impinged on a powdered sample. Powder XRD was utilized for the experimental samples. All possible grain orientations of a sample are analyzed when the sample is in powder form. Therefore, the resulting spectrum is an average over all of the grain orientation of the powdered sample.

The lattice of atoms within the sample diffracts the impinging x-rays according to

90

Bragg's Law[36], seen in Equation (3-3).

$$n\lambda = 2d \sin\theta$$

(3-3)

Bragg's Law describes the relationship between the interplanar spacing in a molecule, the

wavelength of the impinging x-ray beam and the angle at which x-rays are diffracted[36]. A

schematic description of Bragg's Law is shown in Figure 3.11.
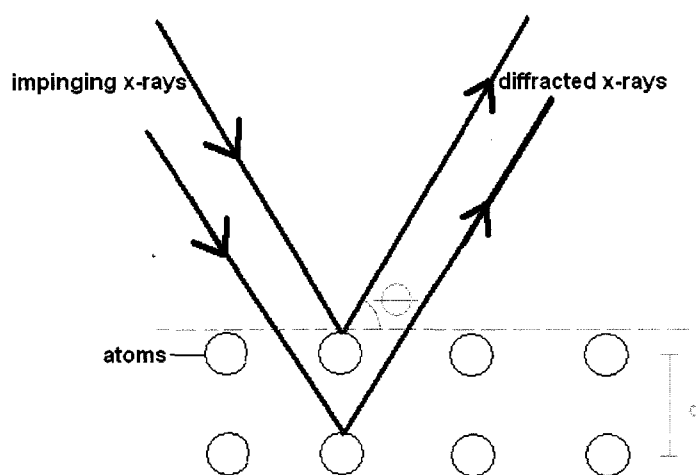
Figure 3.11: Schematic describing Bragg's Law[36].

A detector is used to measure the diffracted x-rays at different values of 2θ. These

measurements are used to generate a spectrum of the angles detected.

The XRD spectra produced reveals a significant amount of qualitative information. First,

the locations of the peaks along the ordinate axis are specific to an element or

compound[33, 37] thereby allowing the identification of a particular element or compound in

91

the sample being analysed. Second, the height of the diffraction peaks gives a qualitative measure of the proportions of elements/ compounds in the sample[35, 38]. The peak heights are plotted relative to the species with the maximum number of counts (number of times an angle is detected). Third, the width and location of the peaks for an experimental sample, in comparison to a diffraction pattern of a standard of the same composition, reveals information regarding the purity of the sample[35, 38]. For example, if a peak for Ni in an MMC is significantly wider than the standard peak for pure Ni, it suggests that there could be a solid solution or an alloy element in the Ni matrix. For example, if a Cu-Ni alloy is analysed using XRD, it will be found that the Ni peaks will be altered, when compared to standard Ni peaks because of Cu being dissolved into the Ni matrix[38].

The equipment used was a "Rigaku Geigerflex Powder Diffractometer with a Co tube and graphite monochromator"[35], run at 40kV and 30mA. On-line searching and matching of spectra relies on the JCPDS[37] database. This equipment uses a fixed, vertical goniometer system[35] with a moveable arm. This arm sweeps over the sample, which also moves. The relationship between the arm and the sample movement is 2 to 1. That is, for every 2° that this arm moves, the powdered sample moves 1 degree, meaning that at a 2-theta value of 90°, the samples is sitting at a 45° angle within the equipment. Samples were run from 2 to 90 ° at a rate of 2°/min. The abscissa on a diffraction plot measures the diffraction angle, 2θ. The ordinate axis of an XRD diffraction pattern shows the intensity, in counts, of the diffraction at a specific 2θ value.

92

XRD results show a spectrum of peaks that are unique to a compound. Though each spectrum is unique, peak overlapping in XRD can occur. By comparing spectra of different compounds, these overlaps can usually be resolved (Appendix B). The XRD equipment employs data processing techniques to aid in the identification of overlapped peaks[33]. To corroborate the observations found from the comparisons of the spectra, a phase diagram of the system, if available, can be used. At a given composition, a phase diagram can suggest which compounds should be present at room temperature. In conjunction with other methods, XRD can prove to be an extremely useful tool.

3.4.4 Sample Preparation.

3.4.4.1 Chemical Analysis.

It was necessary to dissolve the samples for chemical analysis by XRF and ICP. This dissolution was accomplished using a 50/50 mixture of hydrochloric acid (HCl) and nitric acid $(HNO_3)^{34}$.

3.4.4.2 Optical Microscopy and EPMA.

Sample preparation for optical microscopy and microprobe analysis was a multi-step procedure. The experimental samples were sectioned and mounted in a two-part epoxy resin called Epothin™, made by Buehler Inc. The samples were then ground for 1 minute

93

using 500grit SiC paper made by Struer. This was followed by 1minute of polishing

using first a Buehler Inc. 600grit diamond disc then 1minute of polishing using Struer

diamond paste on ET Enterprise Pellon paper. Further polishing was done for 5minutes

using Fisher Scientific 0.3µm Alumina Oxide powder on ET Enterprise Pellon paper. The

final polishing was done using 0.3µm Fisher Scientific Alumina Oxide powder on a

Buehler Inc microcloth, done for 1minute.

A strip of conductive Cu tape was used on the samples analysed by the microprobe to

prevent heating of the epoxy in which the experimental samples were encased[33].

3.4.4.3   XRD

There were two methods of preparation used for the samples that were analysed by XRD.

Some of the experimental samples were filed using a clean steel file. The samples were

placed in a vice grip with a portion left un-clamped. This un-clamped portion was then

filed, producing a powdered sample.

The rest of the XRD samples were reduced to powder using a pulverizer. The machine

you used is a "UA type disc pulversizer" manufactured by Braun Corporation. This

pulverizer has a motor rating of 3hp (horsepower).

94

4.0 Experimental Results.

4.1 Powder Addition to Melt.

It is important to discuss what was observed as the ceramic powders were added to the molten Ni. These observations aid the understanding of the yield of W and B from chemical analysis.

In the Ni-WC system, as the powder blew onto the surface of the melt, it appeared from visual observation of the melt through the viewing port that the powder was incorporated into the melt. The WC powder seemed to disappear very quickly from the melt surface. After the Ni-WC experiments were finished and cooled, the lid of the furnace was removed. A very small amount of WC was observed on the inside of the furnace cap. It was therefore concluded that almost all of the WC powder entered the melt.

The results with B_4C addition were different. After the experimental furnace was cooled to room temperature and the lid removed, there was a significant amount of B_4C powder on the inside of the lid, the sides of the furnace and above the melt surface. Since the B_4C particles are significantly lighter than the WC particles (both were of the same size, between $53\mu m$ and $210\mu m$) the probability that B_4C particles would be bounced off the melt surface or blown away from the melt by the circumferential gas injection is more

95

likely than for WC. Chiovelli, S.[4] also noted this bouncing of B_4C particles. As was

previously mentioned, Ar gas was being circumferentially blown into the furnace cap

during experimentation. The B_4C particles were likely light enough that this gas could

have blown some of them away from the melt surface towards the sides of the furnace

lid. Mixing of the addition of B_4C into the Ni melt appeared to be variable.

4.2 Chemical Analysis.

Chemical analysis of several samples was done in an attempt to determine how much of

the B_4C/ WC powder actually entered the molten nickel. The two methods of chemical

analysis that were used were ICP and XRF. A description of ICP and XRF is given in

section 3.4.1. ICP was used to analyse for boron content of the Ni-B_4C samples. XRF

was used to determine the wt%W in the Ni-WC samples. Only the wt% results for W,

from the WC-Ni and B, from the Ni-B_4C samples, are being presented. With respect to

carbon, it is assumed that the small flux of oxygen, due to leaks, during the experiments

would oxidize any free C present. Also, carbon present from other sources, such as the

carbon susseptor, would cause an erroneous C reading. For example, C dust could settle

within the melt unit after the graphite pellets were poured around the MgO crucible. It is

not feasible to eliminate this possible source of C; therefore, a C mass balance on the

sample was not pursued.

96

4.2.1 Chemical Analysis of the Ni-WC System.

There were five samples that were analysed using chemical analysis in this system. These samples were chosen to encompass a range of $M^o_{(Ni/WC)}$, temperatures (1773K to 1973K) and testing times (6.5min to 37min).

The results that were obtained from the chemical analysis for the Ni-WC system are shown in Table 4.1. This table shows the nominal amount of W added to the Ni melt as WC. Also shown is the wt% of W determined by XRF. The sum of the Ni melt and WC added are taken as the reference for these calculations. It can be seen from this table that the yield of W (given as the ratio of nominal W added to W analysed) varies from a high of 83% to a low of 24%. The low value of 24% is from the 37minute samples from experiment W5. In the chemical analysis, the HCl/HNO_3 acid mixture was unable to completely dissolve this sample. The reason for this is not known. It appears that this incomplete dissolution is related to the low yield of W in this sample.

97

Experimental Parameters				Nominal amount of W added as WC (wt%)	Chemical Analysis (wt%)	% Yield W
Exp #	T (K)	Sampling Time (min)	$M^{o}_{(Ni/WC)}$	W (nominal)	W (actual)	$\dfrac{W(actual)}{W(nominal)} x100$
W3	1773	9.5	167.0	2.0	0.8	43
W5*	1773	37	4.2	41.7	10.0	24
W5	1773	10	12.5	19.8	15.9	81
W8	1873	17	35.8	8.5	6.2	77
W10	1973	16	62.6	4.8	3.0	63
W12	1873	6.5	28	10.1	8.3	83

* Sample not fully dissolved.

The yield of tungsten will be used to discuss experimental results from this point forward. All of the reactant nickel is present in the melt. For example, for the 10minute sample from experiment W5, 81% of the W that entered the system in WC (200g), entered the molten bath. This means that, of the 187.7g of W (of 200g WC added), 152.07g of W actually entered the melt as WC.

98

4.2.2 Chemical Analysis of the Ni-B₄C System.

The chemical analysis of the Ni-B₄C system was carried out using ICP to determine the B content of the samples. There were twelve experimental samples that were chemically analysed in the Ni-B₄C system. These samples covered the range $M^{o}_{(Ni:B4C)}$ from 94 to 1.1. For these samples, it is expected that the yield of B₄C will be lower than the yield for the WC samples for reasons discussed in section 4.1. Table 4.2 shows the nominal wt% B added as B₄C, the wt% B, measured by ICP as well as the total yield of the boron. It can be seen that the maximum yield of boron was 44% and the minimum was 2%. These yield values will significantly affect the remainder of the analysis methods. Therefore, this yield of boron, calculated in the same manner as for the Ni-WC samples, will be used for discussion. In the cases where more than one sample was chemically analysed, an average yield value will be used for the discussion.

99

Table 4.2: Chemical analysis results, Ni-B$_4$C system, yield B.

Experimental Parameters				Nominal B added as B$_4$C (wt%)	Chemical Analysis (wt%)	% Yield B
Exp #	T (K)	Sampling Time (min)	$M^o_{(Ni:B4C)}$	B (nominal)	B (actual)	$\dfrac{B(actual)}{B(nominal)}x100$
B1	1773	8.5	94	0.8	0.3	44
B1	1773	11.3	94	0.8	0.2	23
B2	1773	11.7	94	0.8	0.1	13
B6	1773	1.0	3.1	18.1	0.4	2
B6	1773	14.2	1.1	37.1	0.6	2
B7	1873	3.8	12	5.8	0.9	15
B7	1873	8.5	5.9	10.8	1.2	11
B9	1973	1.5	12	5.8	1.7	30
B9	1973	4.2	7.8	8.4	1.1	13
B11	1773	0.5	35.3	2.0	0.6	29
B11	1773	2.5	17.7	3.9	0.9	23
B11	1773	3.2	12	5.8	0.2	4

The low yield of B in these experiments is likely due to a number of factors, which are quite complex. Some of these have been discussed in section 4.1 due to the physical addition of B$_4$C to the melt. Another reason for the loss of B in the system can be illustrated by analyzing the chemical analysis results from experiments B1 and B2. In these experiments, a single addition of B$_4$C was made at time 0s. Samples were removed from the melt at 8.5, 11.3 and 11.7 minutes after the B$_4$C addition to the melt. The %B

100

yield for these samples, shown in Table 4.2, decreases with increasing sampling time.

The loss of B from experiments B1 and B2 can be explained. The oxygen analysis exiting the furnace cap was measured to be approximately 300ppm's (section 3.1.4). The presence of O_2 over the melt could result in the formation of gaseous B_2O_3. At 1773K, the standard Gibbs free energy change, ΔG^o, for the formation of gaseous B_2O_3, is -767KJ/mol. This ΔG^o indicates that this process, to form $B_2O_3(g)$, would spontaneously occur. Since the gas phase above the melt was not analysed, the B within B_2O_3 was not detected.

4.3   Optical Microscopy (OM).

The experimental samples of Ni-WC and Ni-B_4C were examined first using optical microscopy to determine if there was any obvious evidence of reaction. The particle size of the ceramic powders, between 210μm and 53μm, would make it possible to view these particles at low magnification.

4.3.1   OM in the Ni-WC System.

Two experimental samples were chosen to represent the Ni-WC system for OM. When investigated using OM, the OM images of these samples were very clear. Other samples

101

investigated by OM were not as clear (though the features discussed for the two samples chosen were seen in the images not presented here). The micrographs shown in Figure 4.1, Figure 4.2 are from samples taken during experiment W5 and are representative of all samples viewed by OM. The yield of W in experiment W5 was 81%. In both Figure 4.1 and Figure 4.2 there are ceramic particles present. Figure 1.1 shows an image of a PTA treated Ni alloy –WC MMC[5]. The angular shape of the WC particles, identified by Neville et al., is typical of WC powders. This same appearance of the WC particles is evident in Figure 4.1 and Figure 4.2. Thus, a portion of the WC that was added to the system also entered the melt and remained. Also evident in Figure 4.1 and Figure 4.2 are porosity. The first type of porosity, type 1, appears to be the result of WC particles falling out of the Ni matrix. This conclusion is based on the shape of the porosity, which is angular and similar to the shape of WC powder. The second type of porosity, type 2, could be the result of dissolved gases, which precipitate out on solidification as spherical porosity[38, 39].

Though these micrographs show that there are ceramic particles embedded in the nickel matrix, this magnification does not allow the viewer to ascertain whether or not any reaction has occurred between the WC particles and the nickel matrix. Therefore, further analysis of these samples, using EPMA and XRD is warranted.

102

Figure 4.1: Micrograph of 11.5minute sample from experiment W2.

Figure 4.2: Micrograph of 37minute sample from experiment W2.

4.3.2 Optical Microscopy in the Ni-B₄C System.

In the Ni-B₄C system, several micrographs were taken at different magnifications. Two

images were chosen to represent the Ni-B4C system. These images were chosen because

of their clarity as well as their representative appearance. Representative micrographs,

103

from the 8.5minute sample from experiment B1, where the wt% B was determined to be 0.3wt% are shown in Figure 4.3, Figure 4.4.

Figure 4.3 shows a low magnification image of the 8.5minute sample from experiment B1. The solidification pattern of the samples is clearer by looking at a higher magnification micrograph (Figure 4.4). Two solidification steps can be identified on this micrograph. There are dendrite-like fingers present, surrounded by darker areas. From ICP analysis, the composition of the 8.5minute sample from experiment B1 was determined to be 0.4wt%. This analysis neglects the C concentration in the system (section 4.5.3.1). If a Ni-B alloy with a composition of 0.4wt%B is cooled from above 1730K, these two solidification steps can be described using the Ni-B phase diagram[21] (Figure 4.5). As the temperature drops below 1730K, a liquidus is crossed and solid Ni begins to form. Between 1730K, and approximately 1350K, a mixture of solid Ni and a liquid solution of Ni and B is present. In Figure 4.4, the areas labelled as dendrites are comprised of this solid Ni. When 1350K is reached, the remaining Ni and B will solidify together. This solidified Ni-B mixture is identified as the interdendritic regions in Figure 4.4. Further discussion of this solidification pattern can be found in the microprobe section of this work (Section 4.4).

104
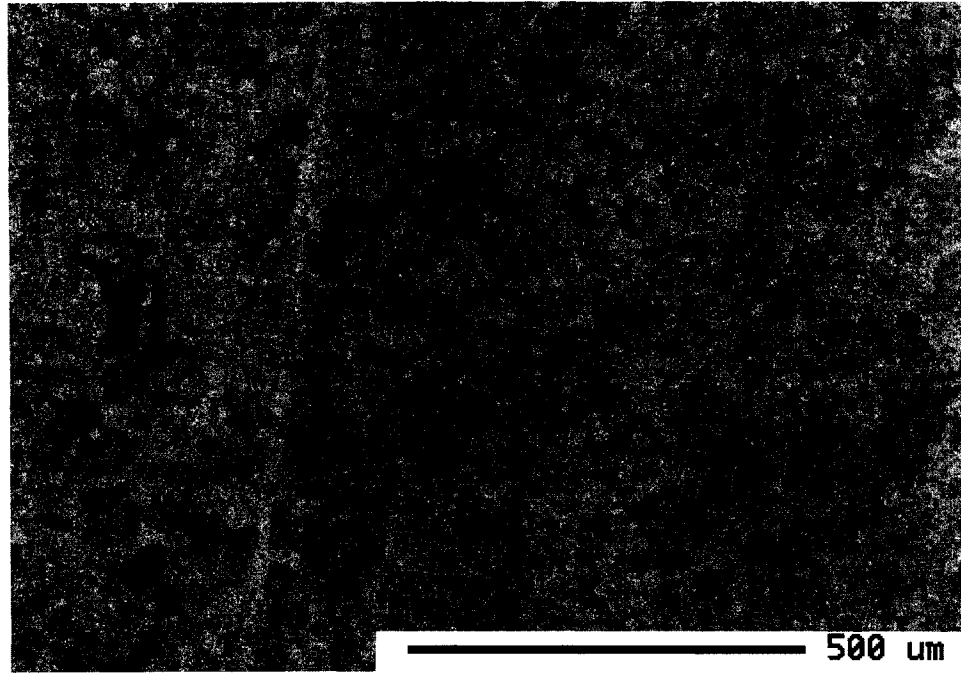
Figure 4.3: Optical micrograph of 8.5minute sample from experiment B1.

- dendritic region

- interdendritic region

50 um
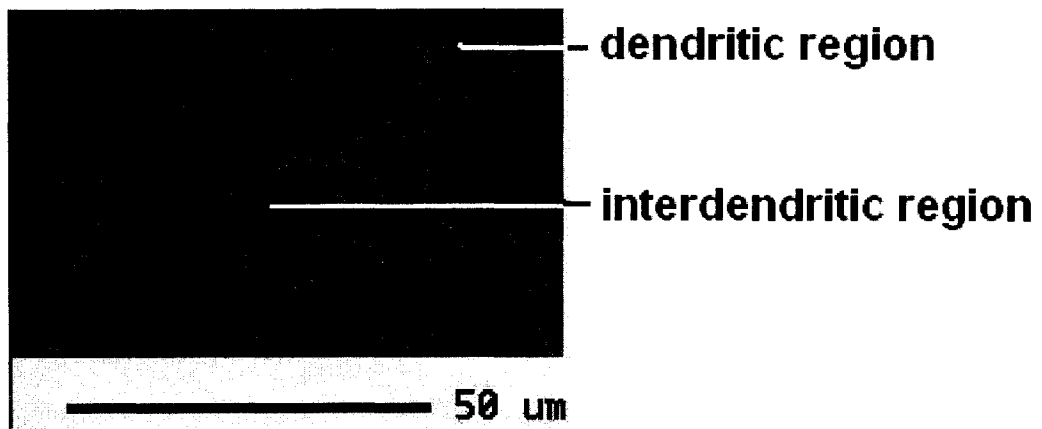
Figure 4.4: Optical micrograph of 8.5minute sample from experiment B1.

105
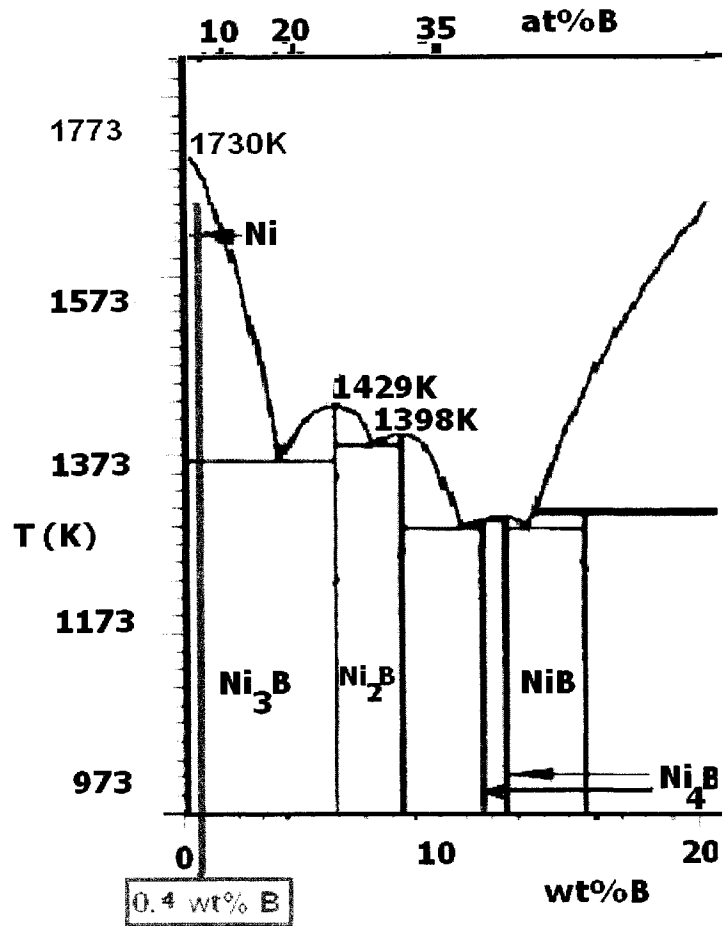
Figure 4.5: Ni-B phase diagram with 0.3wt%B identified.

The micrographs of the Ni-B$_4$C samples that were investigated by OM do not show any particles of boron carbide to be visible. However, it cannot be concluded that B$_4$C particles are not present in other areas of the sample not pictured. Therefore, Ni-B$_4$C samples will be further investigated using EPMA and XRD.

106

4.4 Microprobe (EPMA).

The presence of angular ceramic particles in the representative Ni-WC optical micrographs indicated that the WC particles did not decompose. However, if there is a reaction between Ni and a portion of the WC, optical microscopy will not provide a distribution of W throughout the Ni matrix. Elemental point analysis of a representative sample will determine the distribution of W in the sample.

In the representative Ni-B_4C optical micrographs, there were no B_4C particles identified. Elemental point analysis using the microprobe was used to further investigate a representative sample. If there was a reaction between the boron carbide particles and the nickel matrix, it is necessary to identify, for example, if the boron is located in a specific region of the samples.

Using a JEOL 8900 microprobe, several experimental samples were analysed. Elemental point analysis was combined with high magnification micrographs to determine if any species have segregated to grain boundaries or if an element is evenly distributed through the sample. This was accomplished by using WDS for the reasons outlined in section 3.4.2[33]. Three samples from two experiments, W3 and B1 were analysed. The analysed samples from these experiments are shown in Table 4.3.

107

Table 4.3: Samples analysed using WDS.

Experiment #	Sample Time (min)	% Yield	
		W	**B**
W3	9.5	43	-
W3	12.2	43	-
B1	8.5	-	44

4.4.1 EPMA in the Ni-WC System.

Two samples were chosen for elemental point analysis in the Ni-WC system. These samples were the 9.5minute and the 12.2minute sample from experiment W3. Both of the samples were from the experiment with the lowest yield of W, at 43%. As was previously discussed, in the Ni-WC system, the addition of WC to the molten melt was not difficult. A high yield of W implies a high yield of WC. If the yield of WC particulates was sufficiently high, the WC particulates would have impeded the investigation of the matrix material. Investigation of the matrix was necessary to determine if there was W present within the matrix itself. A micrograph of the 9.5minute sample from experiment W3 is shown in Figure 4.6. From this experimental sample, elemental point analysis was carried out at 95 discrete points. These points were chosen to represent areas of varying appearance throughout the microstructure. For example, some of the points were located within regions, which appeared darker in Figure 4.6 while others were chosen within

108

areas of lighter appearance.
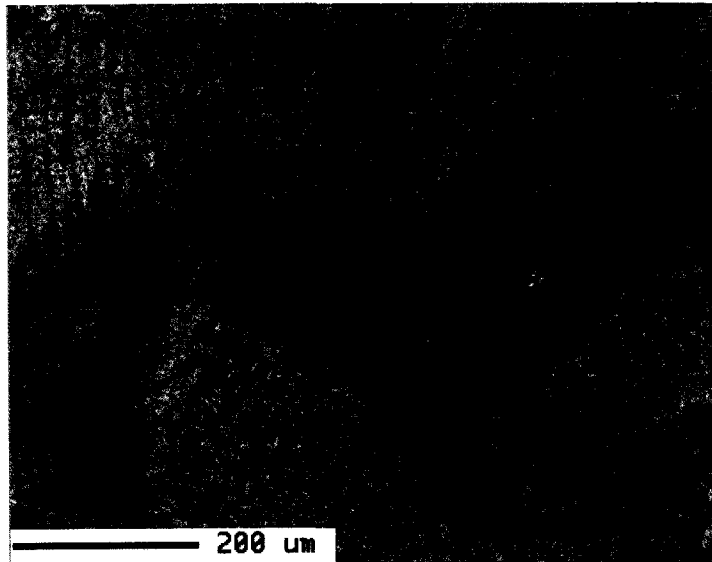
Figure 4.6: Image of the 9.5minute sample from experimentW3 (microprobe).

Table 4.4 gives a summary of the elemental point analysis results for the 9.5minute

sample from experiment W3. It can be seen that the maximum wt% W was 1.3 and the

minimum was 0.8wt%. The manner in which the standard deviation, σ, was calculated is

shown in Appendix A.

Table 4.4: Elemental point analysis results, 9.5minute sample, experiment W3.

Number of Data Points	Maximum wt% W (%)	Minimum wt% W (%)	Average wt% W (%)	Standard Deviation σ
95	1.3	0.8	1	0.2

109

The sample taken at 12.2minutes during experiment W3 was also analyzed using WDS. A microprobe image of this sample is shown in Figure 4.7. This image identifies two features of interest that were analysed using WDS. The features appear, in Figure 4.7, to be locations where angular, WC particles fell out of the matrix. Therefore, it is of interest to examine the area of the sample that would have been beneath the WC particles to determine if there is a W content different from the W content given for the 9.5minute sample (both are from experiment W3). Within these features, 1 and 2, there were 48 and 95 selected points to be analysed, respectively.
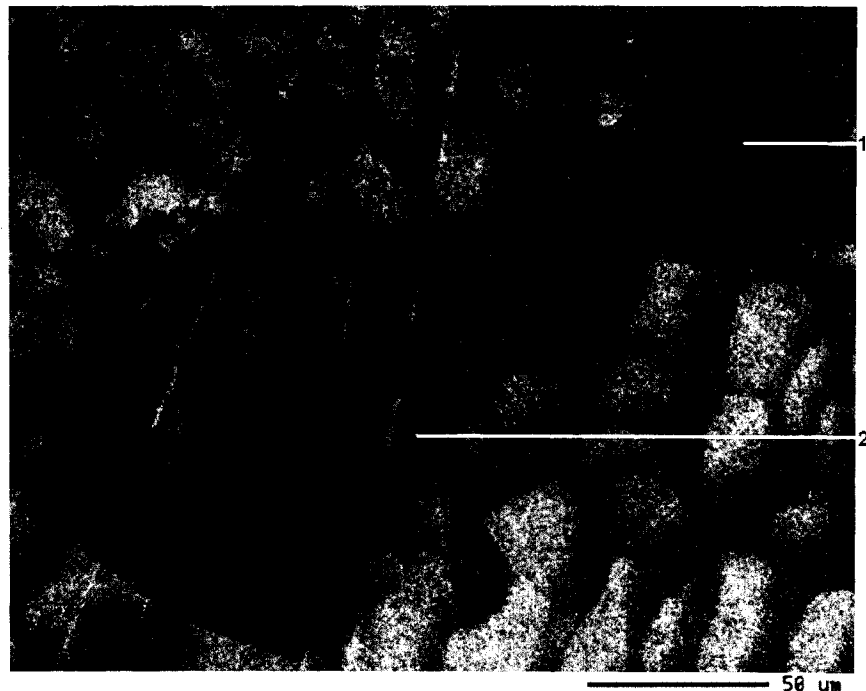
Figure 4.7: Image of the 12.2minute sample from experiment W3 (microprobe).

110

Table 4.5 gives a summary of the elemental point analysis results for the 12.2minute

sample from experiment W3. For the analysis of feature 1 in Figure 4.7, it can be seen

that the maximum wt%W is 1.3 while the minimum wt%W is 0.3. Using all 48 pieces of

data, the average W content was found to be 0.9wt%. This data had a calculated standard

deviation of 0.2 (see Appendix A). Feature 2 in Figure 4.7 contains a maximum wt%W

of 1.5 and a minimum wt%W of 0.1. Using all wt%W data from the 95 points evaluated,

the average W content was found to be 1wt% with a standard deviation of 0.3.

Table 4.5: Elemental point analysis results, 12.2minute sample, experiment W3

Feature Number (#)	Number of Data Points	Maximum wt% W (%)	Minimum wt% W (%)	Average wt% W (%)	Standard Deviation σ
1	48	1.3	0.3	0.9	0.2
2	95	1.5	0.1	1.0	0.3

The presence of W in the results from the 9.5minute sample and feature 1 and feature 2

from the 12.2minute sample suggests that a reaction occurred between the Ni matrix and

the WC particles. In both samples, this resulted in the distribution of W throughout the Ni

matrix.

111

4.4.2 EPMA in the Ni-B$_4$C System.

Investigating Ni-B$_4$C samples using OM did not show any visible B$_4$C particles in the

nickel matrix. WDS analysis was done for the 8.5minute sample from experiment B1.

This sample was chosen because it had the largest yield of B. As discussed in section 4.1,

there was difficulty getting the B$_4$C powder to enter the molten melt. The highest yield

sample was chosen to assure that a sufficient amount of B was present in the sample to

facilitate WDS analysis. The analysis of this sample provides further evidence of the

solidification pattern discussed in section 4.3.2.

A microprobe image of the 8.5minute sample from experiment B1 is shown in Figure 4.8.

This image shows dendritic and interdendritic regions. The dendritic regions are those,

which appear lighter in colour in Figure 4.8 while the interdendritic regions appear

almost black. The Ni-B phase diagram suggests that Ni dendrites will form upon cooling

between trace B and 4wt%B, which covers the range of wt%B values determined by ICP.

The Ni-B phase diagram also indicates that the interdendritic regions will contain a

mixture of both Ni and B.

Figure 4.8 shows an image of the 8.5minute sample from experiment B1 identifying the

regions that were analysed by WDS. There are nine features of interest identified. Within

these features four, elemental analyses were completed. Table 4.6 shows the WDS results

from the elemental analysis of these nine features. This table gives the maximum wt%B,

112

the minimum wt%B, the average wt%B as well as the calculated standard deviation in the

wt% data.

Figure 4.8: Image of the 8.5minute sample, experiment B1 (microprobe).

Table 4.6 indicates that the interdendritic regions of the sample have an elevated boron

content. The boron content of the interdendritic regions reaches a maximum of 12.6wt%.

However, in Table 4.6, the region identified as interdendritic, feature 9, does not appear

to contain B. A possible explanation for this is that the area analysed was not actually

interdendritic, but a small pore. Therefore, the WDS was analysing a dendrite.

113

Table 4.6: Elemental point analysis results, 8.5min sample, experiment B1, 4data points/ feature.

Feature Number (#)	Dendritic				Interdendritic			
	Maximum wt% B (%)	Minimum wt% B (%)	Average wt% B (%)	δ	Maximum wt% B (%)	Minimum wt% B (%)	Average wt% B (%)	δ
1					11.7	11.2	11.4	0.2
2	0.7	0	0.2	0.3				
3	0	0	0	0				
4					12.6	10.3	11.8	0.9
5	0	0	0	0				
6	0.2	0	0.1	0.1				
7	0.2	0	0.1	0.1				
8	0	0	0	0				
9					0	0	0	0

4.4.3 Summary of EPMA.

The WDS results, for representative samples and features, suggested several things. In the WC-Ni system, images of the two samples (Figure 4.6 and Figure 4.7) from experiment W3 show the formation of dendrites, which formed during the solidification

114

of the sample. The WDS analysis determined that there was W distributed through the matrix suggesting a reaction between WC and Ni occurred.

In the Ni-B_4C system, the dendritic solidification pattern seen in the micrograph of the 8.5minute sample from experiment B1, Figure 4.8, is in agreement with the solidification behaviour described on the Ni-B phase diagram (Figure 4.5). This sample, the 8.5minute sample was representative. The elemental point analysis done by WDS identified the areas within the samples where B was located, the interdendritic regions. WDS does not provide details as to the chemical nature of the B. In the future work section, section 6.2, the use of a field emission scanning electron microscope, an FESEM, to investigate the particle morphology will be discussed. Therefore, XRD will be used to identify the chemical nature of the B, specifically, if there are any B compounds forming and what these compounds are.

4.5 X-Ray Diffraction.

Optical microscopy was used to see if ceramic particles were visible at low magnification. For the Ni-WC system, WC particles were visible. In the Ni-B_4C system, there were no obvious ceramic particles present. To further investigate these results, the microprobe was used. At high magnification, investigation of the dendritic and inter-dendritic regions was completed, evaluating features of interest. For example, in the

115

8.5minute sample from experiment B1, it was noted that the interdendritic regions had a

significantly elevated level of boron. The XRD was used next to identify reaction

products that had formed. The standard XRD data for all species identified is shown in

Appendix C.

4.5.1   XRD of Raw Material.

The XRD spectrum for the as received WC powder is shown in Figure 4.9. There are two

high intensity peaks that are clearly shown at 2-theta values of approximately 41° and 57

°. Three, medium-intensity peaks are located at 37°, 76 ° and 87 °. One low-intensity peak

is found at a 2-theta value of 78 °. All of the peaks that are seen on this spectrum are

narrow in width. The peaks that are seen are in correspondence with the standard peaks

for WC[35].
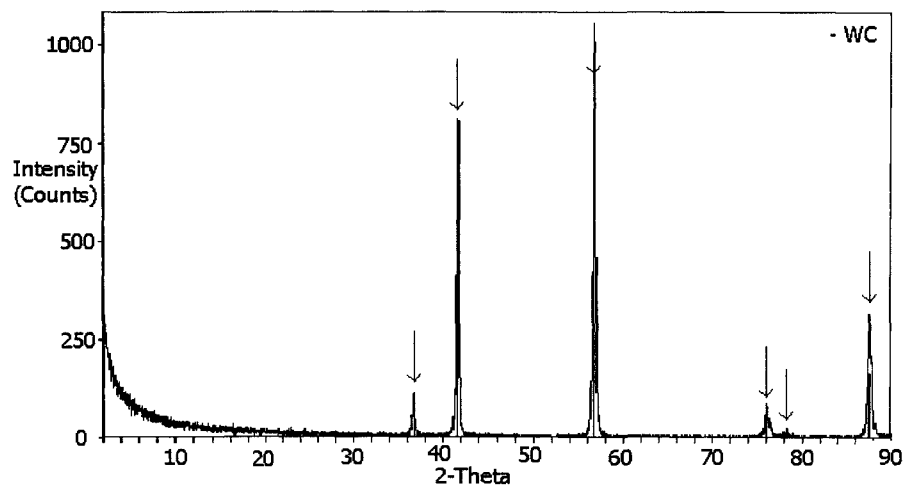
Figure 4.9: XRD of raw WC powder (Kennametal).

116

The XRD analysis of a sample of the boron carbide powder is shown in Figure 4.10. On this plot, there are 20 peaks that are identified. Table 4.7 gives a listing of the peaks that are associated with B_4C[35].

As previously discussed in section 2.2.1, the stoichiometry of B_4C is not always exact. That is, there are stoichiometries of boron carbide other than B_4C (section 3.4.3). There are five peaks, identified in Figure 4.10, that correspond to graphite[37].
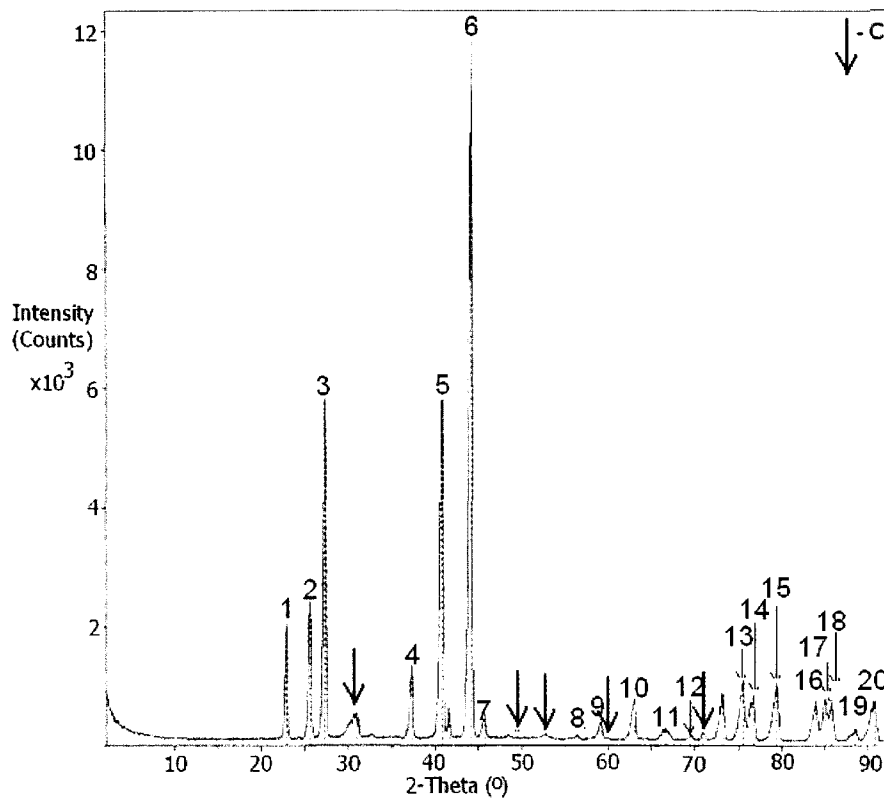
Figure 4.10: XRD of B_4C charge powder (Electro Abrasives).

117

Table 4.7: B$_4$C peak identification[35,37].

Peak #	2-Theta (°)	Peak #	2-Theta (°)
1	22.9	13	75.5
2	25.6	14	76.7
3	27.4	15	79.5
4	37.2	16	84.0
5	40.8	17	85.1
6	44.2	18	85.9
7	45.8	19	88.5
8	56.5	20	90.4
9	59.1		
10	63.0		
11	66.7		
12	69.6		

The third charge material, nickel, as supplied by INCO, was also analysed using XRD. The result of this analysis is shown in Figure 4.11. Figure 4.11 shows the presence of two peaks for nickel, located at 52° and 61°, as is expected[35]. There are some minor peaks in this pattern that can be attributed to nickel oxide, NiO. The standard free energy, $\Delta G°$ for

118

the formation of NiO from Ni and $O_2(g)$, at room temperature is $-212kJ/mol$. This means

that the formation of nickel oxide is spontaneous.
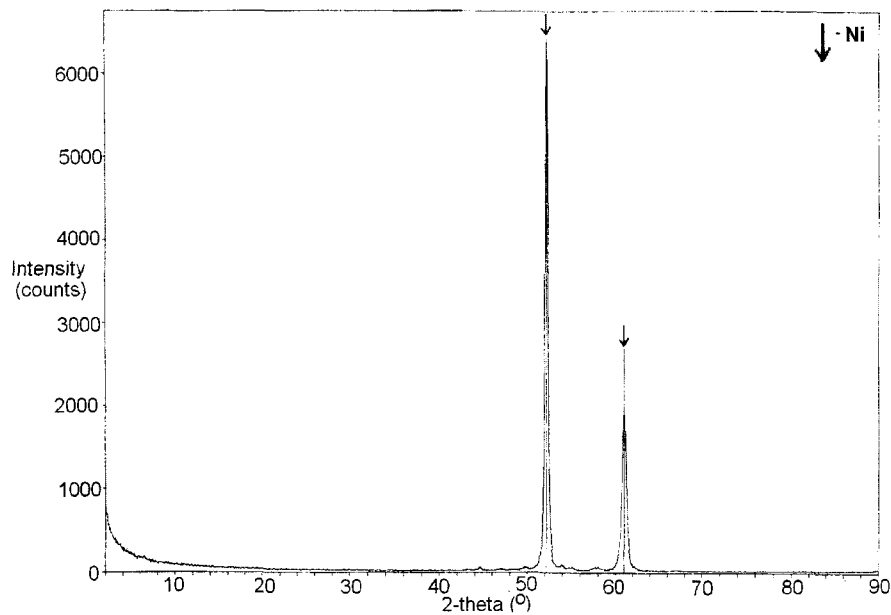
Figure 4.11: XRD of Ni charge material supplied by INCO.

4.5.2 XRD Results in the Ni-WC System.

There were two experimental samples chosen for XRD analysis in the Ni-WC system.

These samples were chosen from experiment W5, where the yield of W was found to be

81%. This yield would allow the identification of any reaction products above a

detectable level.

119

In the case of the Ni- WC system, OM and EPMA did not reveal the presence of reaction products. A more in-depth investigation, possibly using the FESEM would have allowed the identification of any reaction layer on the surface of the WC particulates. In a micrograph, taken on an optical microscope, of the 11.5minute sample from experiment W5 (Figure 4.1) it appears that the tungsten carbide particles, angular in shape, are present. WDS analysis using the microprobe determined that both the 9.5minute and 12.2minute sample from experiment W3 had a W level around 1wt% in both dendritic and interdendritic regions (section 4.4.1).

Figure 4.12 shows the XRD spectra for the 10.2minute sample from experiment W5. The WC peaks are clearly present, though in some cases, they are overlapped with other peaks. For example, there is an overlap of a WC peak and a C peak around 62°.

If the Ni peaks are inspected closely, it can be seen that the peaks have increased in breadth when compared to the nickel peaks of the charge Ni, shown in Figure 4.11. This broadening is attributed to the dissolution of tungsten in nickel[33]. Also identified in this diffraction pattern are the peaks for C (graphite) and Fe_3O_4. The presence of Fe_3O_4 is not unexpected as the samples were filed using steel files. During filing, a small amount of contamination may have occurred.

120
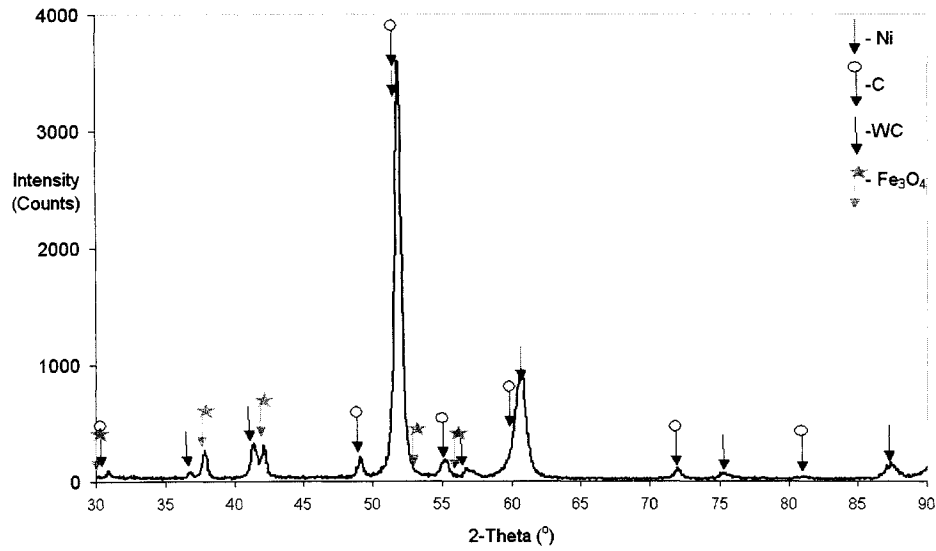
Figure 4.12: XRD of 10.2minute sample from experiment W5.

Figure 4.13 shows the diffraction pattern for the 11.5minute sample from experiment W5.

This diffraction is similar to the patterns shown in Figure 4.12 for the 10.2minute sample,

also from experiment W5. This sample also contains WC, Ni, C (graphite) and Fe_3O_4.
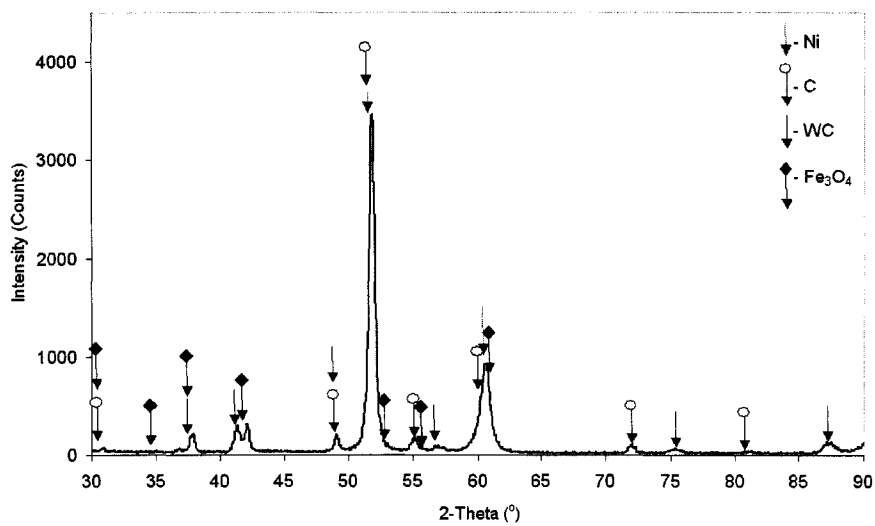
Figure 4.13: XRD of 11.5minute sample from experiment W5.

121

4.5.3 XRD Results in the Ni-B$_4$C System.

Several experimental samples were chosen for XRD analysis. The samples were chosen to represent the range of the boron yield values and the $M^o{}_{Ni:B4C}$ values. To accomplish this, there were 8 samples chosen for XRD analysis.

Table 4.8: Description of samples chosen for XRD.

Experiment	Sample Time (min)	$M^o{}_{Ni:B4C}$	B Yield (%)
B1	11.3	94	23
B7	0.9	24	13*
B7	3.8	12	13*
B9	1.5	12	30
B7	6.5	8	13*
B9	3.3	8	21
B6	8.8	1.6	2*
B6	13.5	1.1	2*

* Average for experiment.

Experimental samples from experiment B1 were found to contain less boron than was expected (revealed by chemical analysis). The yield of boron for the 11.3minute sample from experiment B1 was around 23%.Figure 4.14 shows the XRD spectrum of the 11.3minute sample. The nickel peak that is located at a 2-theta value of 52.2° appears to

122

be broader than the same nickel peak in Figure 4.11. This broadening could be attributed

to peak interference between the Ni and the Ni_3B peak or, it could signal the presence of

some dissolved B in the nickel, further evidence that there was a reaction between the Ni

and the B_4C particulates. No B_4C was identified in this sample, which could indicate that

all of the B_4C particulates reacted, an undesirable result for an MMC[3, 4].
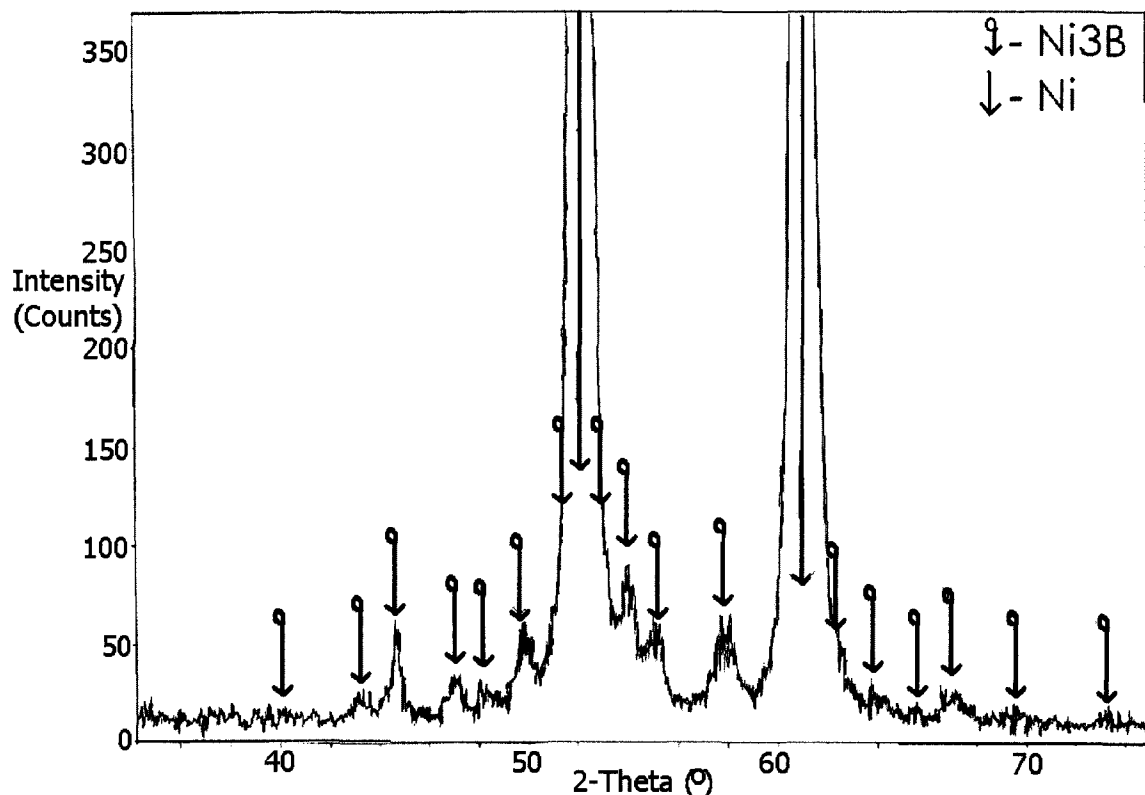
Figure 4.14: XRD of the 11.3minute sample from experiment B1.

Experiment B7 had several portions of B_4C added. The XRD spectrum of the sample

taken at 53seconds is shown in Figure 4.15. The average yield of B for experiment B7

was found to be around 13%. This means that only 2.05g of B out of the total 15.65g of B

123

added (as part of 20g of B_4C) actually entered the melt.

The XRD spectrum identified only Ni and Ni_3B. The higher intensity Ni_3B peaks located at 2-theta values of approximately 45°, 50°, 5 2° and 53° were easily identified. The two, nickel peaks at 52° and 61° were also clearly present. There were no peaks that could be attributed to B_4C in this spectrum.
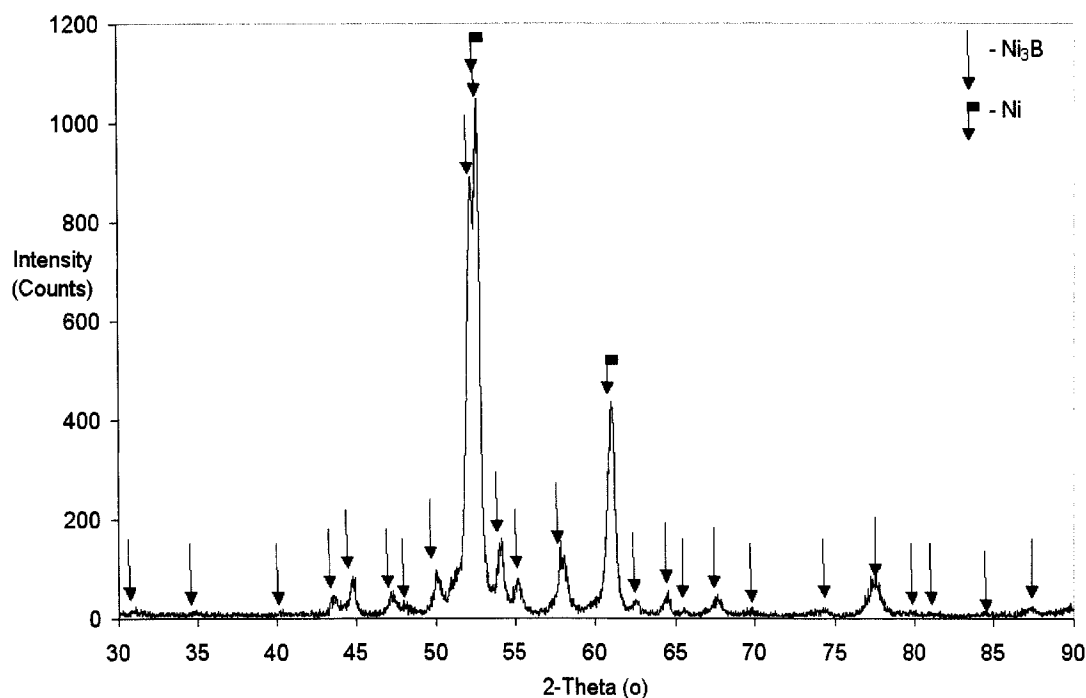
Figure 4.15: XRD of the 53second sample from experiment B7.

A second charge of B_4C was added during experiment B7 at 3minutes. The XRD spectrum for a sample taken at 3.8minutes is shown in Figure 4.16. Chemical analysis revealed that only around 13% of the B injected as B_4C entered the melt, significantly

124

affecting the Ni:B:C ratio in this sample (section 5.4 discusses the thermodynamic

implications of this). Again, there are no B₄C peaks identified in this diffraction pattern.
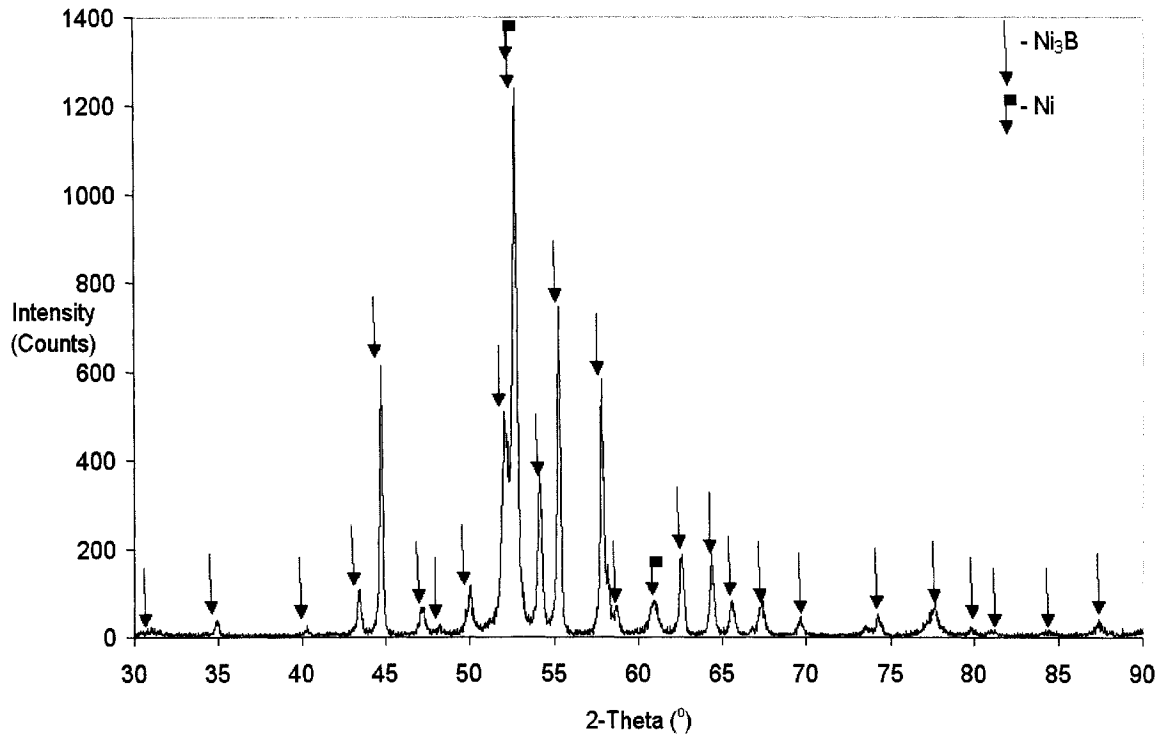
Figure 4.16: XRD of the 3.88minute sample from experiment B7.

During experiment B9, the sample taken at 1.5minutes was analysed by both chemical

analysis and XRD. Chemical analysis of this sample showed an approximate boron yield

of 30%. This means that, of the original 31.3g of B injected (in B_4C) only 9.3g of B

actually entered the melt. Again, this loss of B will significantly affect which Ni-B

compounds are formed in the system, as will be seen in the thermodynamics section of

this report. The XRD spectrum of this sample is shown in Figure 4.17. Ni_3B and Ni were

125

clearly identified. All of the peaks in Figure 4.17were attributed to Ni_3B and Ni.
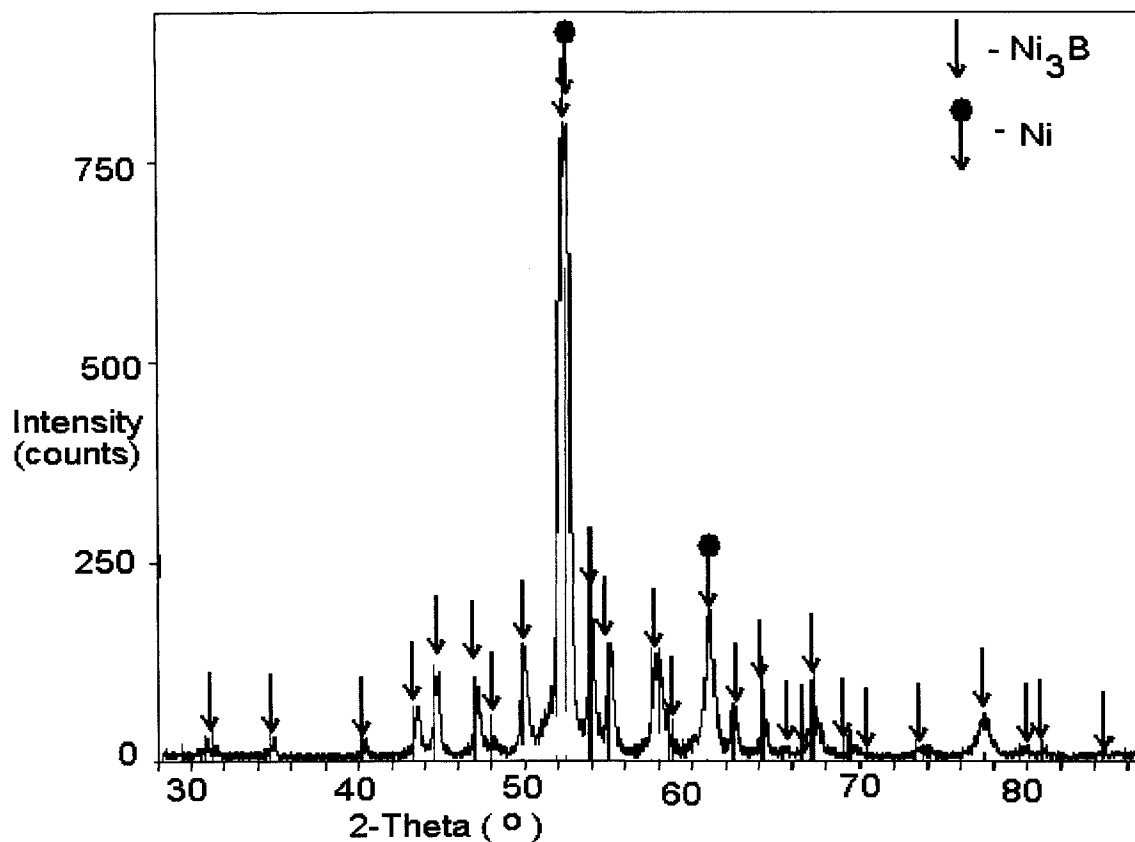
Figure 4.17: XRD of the 1.5minute sample from experiment B9.

In experiment B7, a third charge of B_4C was added at 5.5minutes. XRD of a sample

taken at 6.5minutes is shown in Figure 4.18. This spectrum revealed a mixture of Ni and

Ni_3B. The two, nickel peaks at 2-theta values of 52° and 61° were identified in this

spectrum. The remaining peaks in the spectrum were attributed to Fe_2O_3 and Fe_3O_4.

126
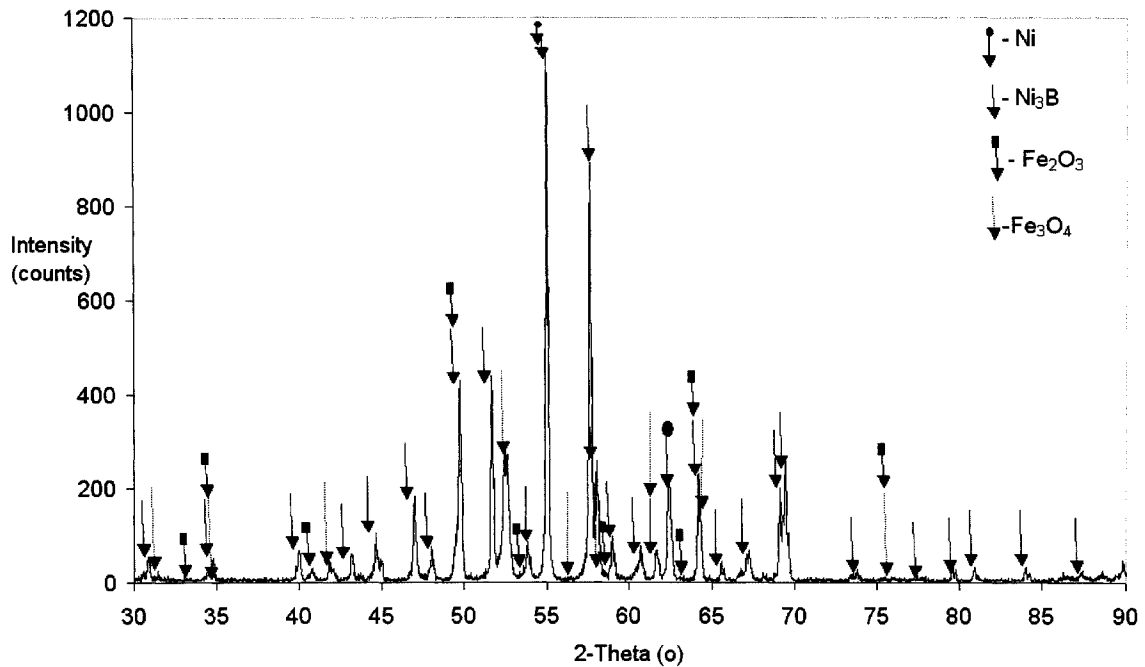
Figure 4.18: XRD of the 6.5minute sample from experiment B7.

Experiment B9 had a second infusion of B_4C added at 3 minutes. The average yield of boron in this experiment was given, by chemical analysis, to be around 21%. The melt was sampled at 3.3 minutes. XRD of this sample is shown in Figure 4.19. This scan showed the presence of Ni_3B and Ni. A comparison of Figure 4.18 and Figure 4.19 is made, it can be seen that the intensity of the Ni_3B peaks in Figure 4.19 is significantly lower than those seen in Figure 4.18. This indicates that there was a smaller amount of Ni_3B formed, at a molar ratio of 7.84, after 3.3minutes than there was after 6.5minutes. All of the peaks were attributed to Ni and Ni_3B in this diffraction pattern.

127
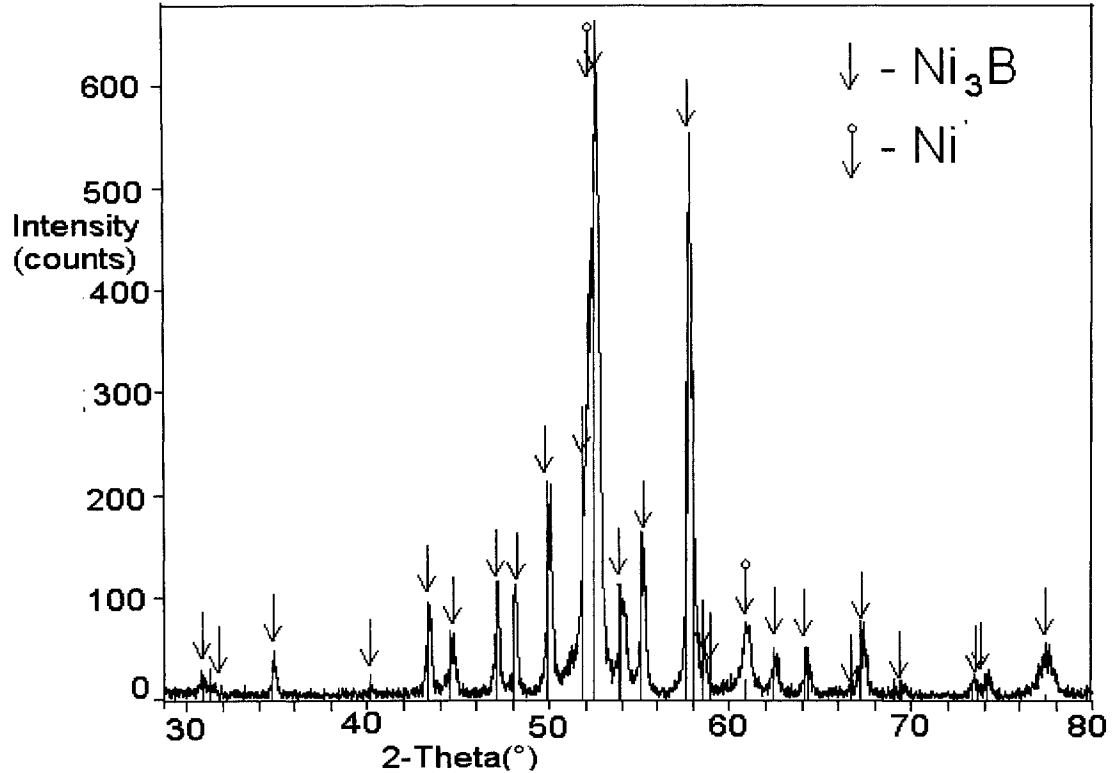
Figure 4.19: XRD of the 3.3minute sample from experiment B9.

Experiment B6 had several additions of B_4C added to the melt. Chemical analysis

revealed an average boron yield around 2%. XRD of a sample taken at 8.8minutes is

shown in Figure 4.20. Based on the high peak intensity Ni_3B was definitely present. The

XRD also suggests the presence of Ni_2B. The peak located at a 2-theta value of

approximately 29°, is not obscured by any Ni_3B peaks. This Ni_2B peak is of medium

intensity, while the adjacent Ni_3B peaks are of very low intensity. To form Ni_2B, the

yield of boron, in this case, had to be higher than the average yield of 2% given by the

128

chemical analysis. This result is anomalous based on the ICP result of 2%. This

diffraction pattern also included graphite peaks (C), peaks of Fe_2O_3 and the Ni peaks.
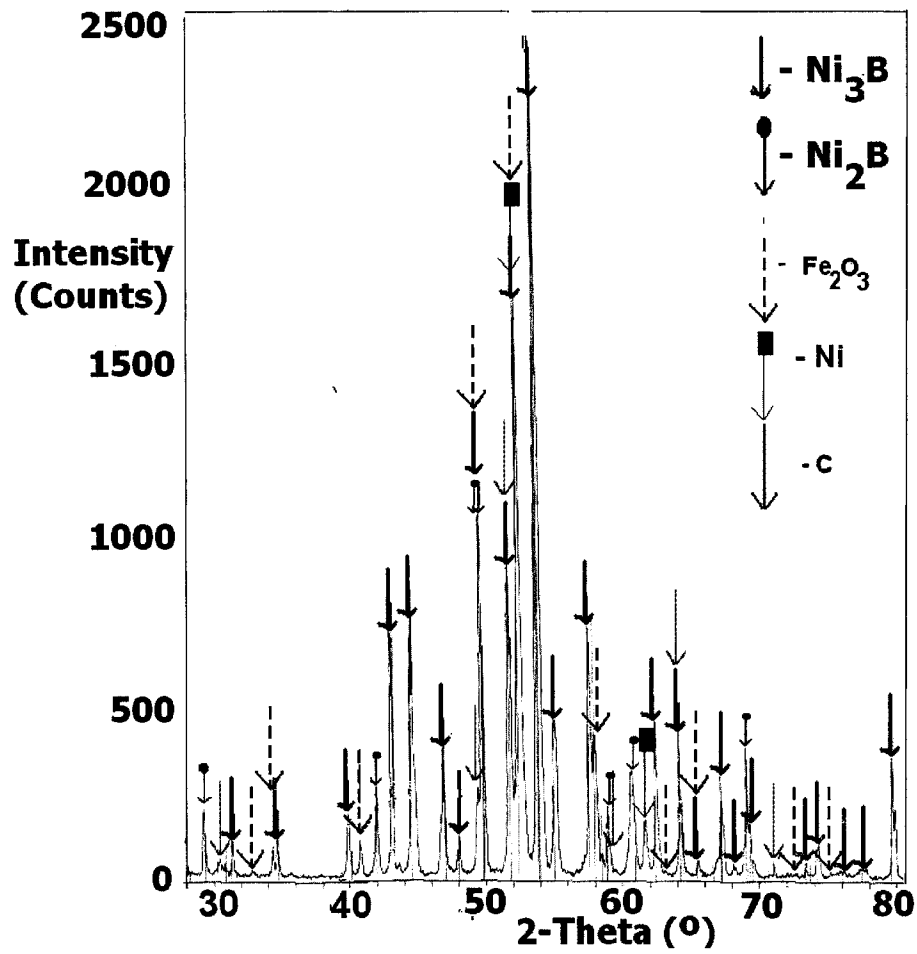
Figure 4.20: XRD of the 8.8minute sample from experiment B6.

Experiment B6, after an additional charge of B_4C had been added was sampled at

13.5minutes (from the time of the first B_4C charge). The XRD spectrum for the

129

13.5minute sample is shown in Figure 4.21. In this spectrum, the peaks for Ni_2B are

clearly present. The intensity of the Ni_2B peak (which has no overlap) located at a 2-theta

value of 29° is above 2000counts. A second, lower intensity Ni_2B peak is seen at an

approximate 2-theta value of 41°. The surrounding Ni_3B peaks, at approximately 39° and

43° do not obscure this Ni_2B peak. Again, based on the ICP results, Ni_2B should not

form. The peaks of Ni have been identified in Figure 4.21. Also, the diffraction peaks of

Fe_2O_3 and graphite (C) are identified.
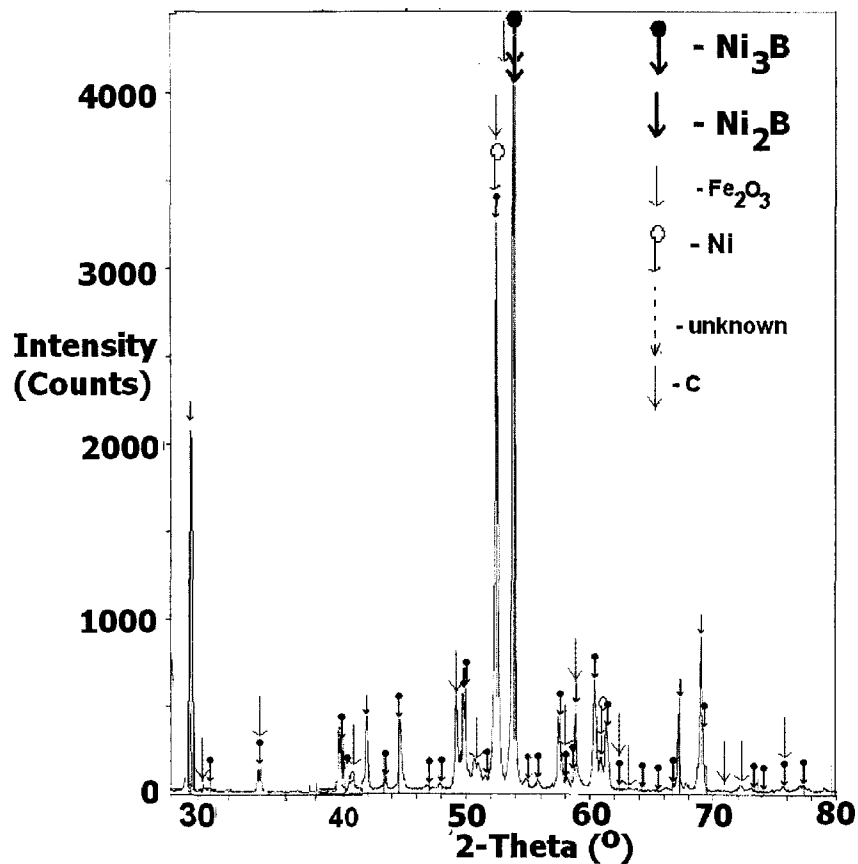
Figure 4.21: XRD of the 13.5minute sample from experiment B6.

130

There were several different phases that were identified using XRD. Table 4.9 shows the XRD products that were seen at what temperature and time.

Table 4.9: Reaction products as identified by XRD, Ni-B₄C system.

T (K)	Experiment #	Time (min)	Ni$_2$B	Ni$_3$B	Ni$_4$B$_3$	NiB
1773	B6	8.8	√	√	X	X
1773	B6	13.5	√	√	X	X
1873	B7	6.5	X	√	X	X
1973	B9	3.3	X	√	X	X
1873	B7	3.88	X	√	X	X
1973	B9	1.5	X	√	X	X
1873	B7	0.88	X	√	X	X
1773	B1	11.3	X	√	X	X

4.5.3.1 Phase Identification using the Ni-B Phase Diagram.

The Ni-B phase diagram, Figure 4.5 was used to verify the results given by XRD. C was not included in this analysis. The yield of boron was considered when identifying compounds on the Ni-B phase diagram. For example, the wt% of B in the 8.5minute sample from experiment B1 was determined by ICP to be 0.3wt%B. Neglecting the C

131

concentration, the Ni-B phase diagram identifies Ni$_3$B as the only reaction product at

0.3wt% B. Including C in this analysis would decrease the wt%B, which would still

result in Ni$_3$B being the only predicted reaction product. The 8.5minute sample from

experiment B1 represents the highest yield of B, at 44%. Therefore, the expected reaction

product for the remainder of the samples is expected to be Ni$_3$B. However, as was

previously discussed, the XRD diffraction patterns of samples from the (anomalous)

experiment B6 (Figure 4.20, Figure 4.21) show Ni$_2$B and Ni$_3$B as reaction products

(section 4.5.3). For this mixture of phases to occur, there would have to be a wt% B

between 6wt% and 8.4wt% (section 2.2.3). A ternary Ni-C-B phase diagram is developed

in the thermodynamics section (section 5.4) of this report.

Table 4.10: Compounds identified by the Ni-B phase diagram and XRD.

Experiment #	Sampling Time (min)	Yield B (%)	Phase Diagram (at wt% B from ICP)*	XRD (compounds)
B1	11.3	43.8	Ni$_3$B	Ni$_3$B
B6	8.8	2	Ni$_3$B	Ni$_2$B, Ni$_3$B
B6	13.5	2	Ni$_3$B	Ni$_2$B, Ni$_3$B
B7	0.88	13.1	Ni$_3$B	Ni$_3$B
B7	3.88	13.1	Ni$_3$B	Ni$_3$B
B7	6.5	13.1	Ni$_3$B	Ni$_3$B
B9	1.5	21.4	Ni$_3$B	Ni$_3$B
B9	3.3	21.4	Ni$_3$B	Ni$_3$B

* from chemical analysis.

132

4.5.4 Sources of Error in XRD.

XRD analysis can be an extremely useful tool in identifying compounds that could be present in a sample. The peaks that are shown in an XRD scan are characteristic of a material[32, 33, 37, 38]. However, there are complications that arise when using this method. The first problem with this method is that the characteristic peaks are not always located at exactly the reference 2-theta value[32, 33, 38]. Interaction between the peaks of two compounds can cause a shift in the location of the peaks, for example[33]. The second complication arises from the fact that the XRD equipment is only capable of identifying compounds, which are present in 3% or more[35].

While these complications seem to suggest that XRD is not a particularly useful tool in identification of compounds in a sample, this is not the case. In fact, XRD is widely accepted as one of the more useful tools in compound analysis due to its simplicity of use[32, 33, 38]. Also, this method, when used in conjunction with other methods, such as chemical analysis and phase diagram analysis is an indispensable tool in the identification of compounds present in samples of unknowns.

4.6 Experimental Summary.

The experimental work that was completed suggested that the Ni-WC system had a minor reaction occurring. The Ni-B$_4$C system had reactions occurring by way of the

133

decomposition of the B_4C particles. There were three analysis techniques used to draw these conclusions: optical microscopy, electron microprobe and XRD.

Chemical analysis, using XRF, determined that the yield of W was between 43% and 83% (section 4.2.1). OM of the Ni-WC samples revealed the presence of WC particulates, identified by their angular appearance, in the metal matrix at room temperature (section 4.3.1). This result only suggested that not all of the WC was reacted. WDS, using the electron microprobe, determined that there was a small amount of tungsten in both the dendritic and interdendritic region analysed (section 4.4.1). The presence of this W suggested that there was some breakdown/ reaction of the WC particles. XRD of the Ni-WC system determined that the samples analysed contained WC, C, Ni and iron oxide (section 4.5.2). Also, the increased breadth of the Ni peaks suggested the dissolution of another element, probably W (based on the WDS results), in the matrix. Together, these results suggest a reaction occurring between the nickel matrix and a portion of the WC particles, thus bonding the MMC.

Chemical analysis revealed that the amount of boron present in the experimental samples was significantly less than the amount of boron that was injected. The yield of B, determined by ICP, was between 2% and 44% (section 4.2.2). Optical microscopy revealed the absence of B_4C particles as well as the dendritic solidification pattern of the samples (section 0). Utilising the wt%B information from the ICP results, and the

134

information given by WDS, for the 8.5minute sample from experiment B1, it was determined that this sample should contain dendritic regions of Ni and interdendritic regions containing a solidified mixture of Ni and Ni_3B. This was determined using the Ni-B phase diagram (Figure 2.9).

The compounds that were formed in the $Ni-B_4C$ system were in agreement with what was expected, as revealed by the Ni-B phase diagram with the exception of experiment B6. The samples from experiment B6 clearly identified the presence of Ni_2B together with Ni_3B.

5.0 Thermodynamic Calculations.

The thermodynamic behaviour of the two systems investigated, Ni-WC and Ni-B$_4$C will be presented in this chapter. The purpose of this analysis is to theoretically verify the results that were seen experimentally. The thermochemical software, FACTSage[TM,40] was used to perform these calculations. Herein, FACTSage[TM,40] will be abbreviated as FACTSage[TM,40] (See Appendix D of this report for a description of how this software is utilized for this report).

In the previous chapter, experiments showed that a there is a reaction between Ni and WC, evidenced by the presence of dissolved W in the Ni matrix. This reaction does not go to completion as XRD results revealed the presence of WC in the samples. Therefore, thermodynamic calculations were carried out to verify this reaction. It was also shown that Ni readily reacts with B$_4$C. This reaction results in the formation of nickel borides, thereby causing the loss of the advantageous properties of boron carbide.

As a result of the loss of B$_4$C in reaction with Ni, thermodynamic calculations were done to search for an alternate matrix that will enable B$_4$C to remain chemically stable. If the B$_4$C remained stable, it would be possible to take advantage of the low density and high hardness of boron carbide for wear applications.

136

5.1 Thermodynamic Equations.

The reaction module of FACTSage[TM,40] was used to determine the thermodynamic properties of a balanced reaction. This module was used to determine the heat of reaction for the formation of binary compounds in the Ni-WC system and the Ni-B$_4$C system. The results of these calculations are seen in Appendix D of this report.

One of the most common parameters considered in metallurgical thermodynamics is the Gibb's free energy change, ΔG°. Equation (5-1) shows the way that ΔG° is calculated from the enthalpy (ΔH°) and entropy changes (ΔS°).

$$\Delta G^o = \Delta H^o - T\Delta S^o$$

(5-1)

Equation (5-1) can be expanded to include the standard enthalpy change, ΔH_f^o, the standard entropy change, ΔS_f^o and the heat capacity, ΔCp, as shown in Equation (5-2).

$$\Delta G^o = \Delta H_f^o + \int_{T_{ref}}^{T} \Delta Cp\, dT - T(\Delta S_f^o + \int_{T_{ref}}^{T} \frac{\Delta Cp}{T} dT)$$

(5-2)

The ΔH° of a reaction reveals whether or not the reaction is endothermic (positive) or exothermic (negative). The ΔS° indicates the degree of disorder of the system. A positive ΔS° indicates an increase in the disorder of the system. The ΔG° is known to indicate the

137

spontaneity of a system. A positive ΔG^{o} indicates that a process is not spontaneous and a negative ΔG^{o} is evidence that the process is spontaneous.

5.2 Thermodynamic Data.

The data that was used to complete these calculations is found in the SGTE Alloy Database from FACTSage[TM,40] version 5.4.1 and the FACTSage[TM,40] compound/solution database from FACTSage[TM,40] version 5.00. Appendix D of this report shows the $\Delta H^{o}_{f,298}$ and $\Delta S^{o}_{f,298}$ as well as the Cp's of the elemental and compound species in the two reaction systems: Ni-WC and Ni-B$_4$C. These three pieces of thermodynamic data are used in Equation (5-2) to calculate the Gibb's free energy change in the two reaction systems at any temperature of interest.

In the SGTE database, there are a limited number of ternary systems that have been analysed. Neither the Ni-W-C nor the Ni-B-C system has been included in the SGTE[40] (Scientific Group Thermodata Europe) alloy database. Assessment of these ternary systems is outside the scope of this work. However, FACTSage[TM,40] can analyse these systems based on a summation of the thermodynamic parameters from the assessed binary sub-systems Ni-W, Ni-C, Ni-B and Ni-C. Using the binary interaction parameters as a first approximation to the ternary system's thermodynamics will give insight into the behaviour of the system.

138

5.3 Ni-W-C System.

Figure 5.1 shows the ternary Ni-W-C phase diagram at 1773K. Each area of the phase diagram is clearly labelled. There are two points identified on this diagram, 23wt% WC[6] (*) and 65wt%WC[4] (**). Both of these values have been reported as successful proportions for Ni-WC MMC's.

At 23wt%WC, at 1773K, the system composition is in a two-phase region of the phase diagram. This region contains a mixture of $W_2C(s)$ and a liquid solution. As the proportion of WC is increased towards 65wt%, a phase boundary is crossed, entering a three-phase region. This region contains a mixture of $W_2C(s)$, C(s) and liquid solution. The liquid solution within this region is invariant, maintaining a composition of 10.41wt%C, 83.54wt%Ni and 6.05wt%W.

At 1773K, the reactants, Ni(l) and WC(s), were considered for values of the parameter n, seen in Equation (5-3).

$$nNi + WC$$

(5-3)

139
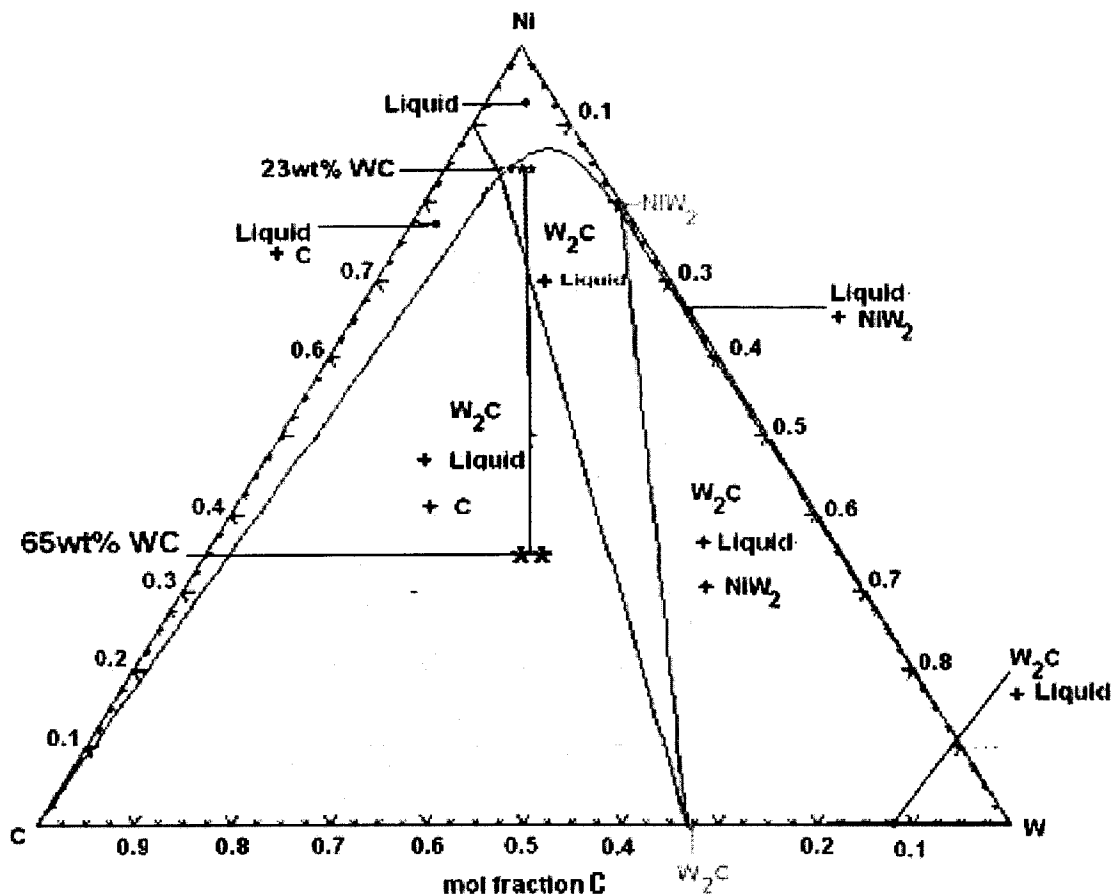
Figure 5.1: Ternary Ni-W-C System at 1773K.

Values of n ranged from 2moles (65wt%WC) to 11moles (23wt%WC). The wt% WC values are between the two wt%WC values deemed to produce successful MMC's[4, 5, 6]in the Ni-WC system (See Appendix E). For an n-value of 2, a mixture of an invariant, ternary solution, $W_2C(s)$ and $C(s)$ is predicted. As the n-value is increased (beyond 6) the system contains a mixture of a liquid, ternary solution and $W_2C(s)$.

The Ni-W-C system was also evaluated at 298K. In FACTSage[TM,40], there are some

140

issues with the choice of phases available for the Ni-W-C phase diagram at 298K. Nickel is FCC in structure at 298K while tungsten is BCC. In the phase diagram calculation module of FACTSage[TM,40], the choice of two solution phases, one FCC and one BCC is made. The reason for this is that, at elevated levels of nickel or tungsten, there will still be a trace amount of the other elements present. The selection of the FCC solution permits the W or C, not tied up in Ni-W compounds or present as free C, to exist in the solid solution (the same is true for the BCC solution with Ni and C, respectively).

There is a solution phase called the $M_6C(s)$ phase where the M represents a combination of Ni and W in this case. There has been discussion in literature of a ternary, Ni-W-C phase, $Ni_2W_4C(s)$[41]. However, there has been insufficient evidence that this phase will form; therefore, this solid phase was not included in the calculation of the ternary Ni-W-C phase diagram at 298K.

Figure 5.2 shows a ternary phase diagram for the Ni-W-C system at 298K. Any binary compounds formed in this system are identified along the binary axes. For example, on the Ni-W axis, $NiW_2(s)$ and $NiW(s)$ are observed.

As previously mentioned, the most effective Ni-WC MMC's have been identified as those containing 23wt% WC[6] and 65wt% WC[4]. For n-values between 2 (65wt% WC) and 12 (23wt% WC), it can be seen that the compositions are in a 3-phase region containing

141

an FCC, solid solution, C(s) and WC(s). The FCC solution in this case has a composition

which is fixed at 99% Ni (Balance, W, (trace C)). Again, because this region is a three-

phase region, the solid solution is invariant.
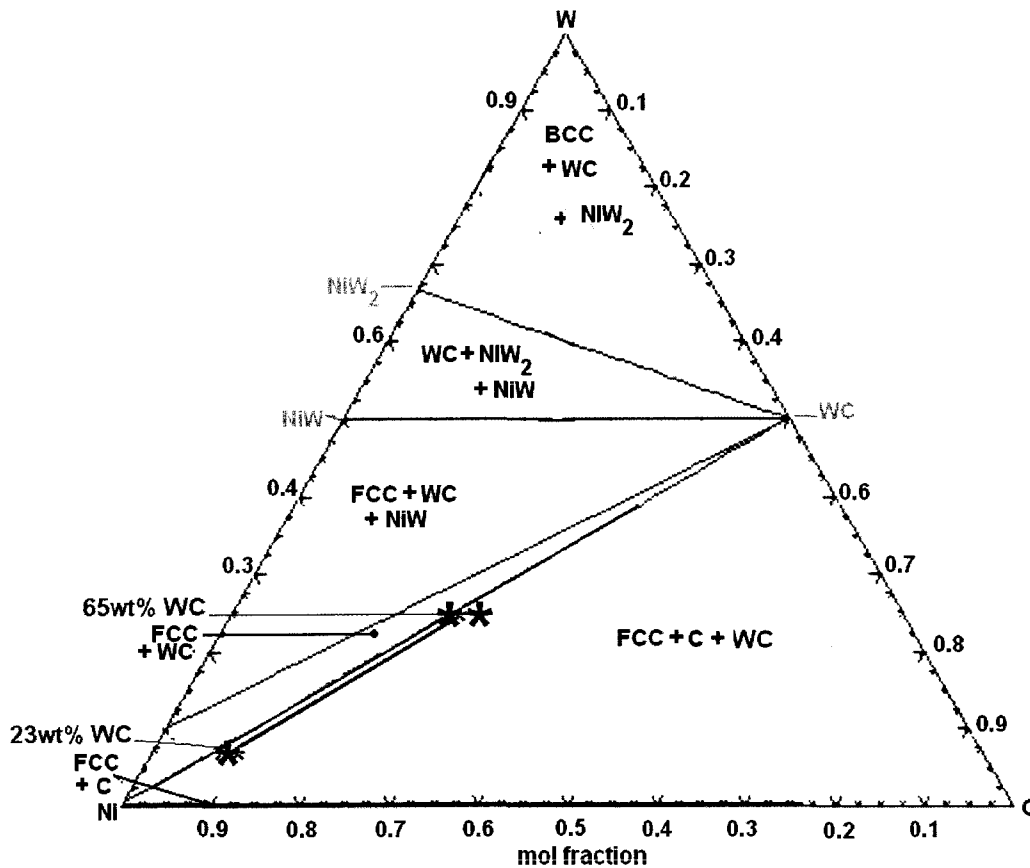
Figure 5.2: Ternary phase diagram for the Ni-W-C system at 298K.

The experimental results that were presented in Chapter 4.0 are in agreement with this

phase diagram. The elemental point analysis done on the microprobe showed that there

was a fairly even distribution of tungsten throughout the sample. This suggested that the

142

WC, at least partially, reacted with the Ni matrix. Finally, XRD showed the presence of Ni, WC and C. The ternary phase diagram, at 298K, showed that the WC samples between 23wt% WC and 65wt% WC should contain WC, C and a Ni-rich FCC solution.

Experimentally, it is extremely difficult to prevent the introduction of or the removal of oxygen from a reaction system. Usually, a few hundred ppm's of oxygen is expected. It is important to assess the effect oxygen can have on a system, as it can form gases, resulting in porosity in the final product.

Thermodynamic calculations at 298K were carried out for a small addition of O_2. The reason that this ternary diagram was not calculated at 1773K was that the effect of the presence of O_2 would be noted at 298K. In the optical micrographs of the experimental, Ni-WC samples (Figure 4.1 and Figure 4.2) porosity, type 2 was hypothesized to be the result of pore formation during solidification. Therefore, the ternary Ni-W-C diagram containing O_2 was calculated at 298K.

The amount of oxygen that is present in this system is described by Equation (5-4).

$$\frac{molO_2}{\sum(molNi, molW, molC)} = 0.001$$

(5-4)

143

This equation means that, over the ternary Ni-W-C phase diagram, there is a level of

oxygen equal to 0.001moles. The ternary phase diagram for the Ni-W-C system with the

addition of 0.001 moles of O_2 is seen in Figure 5.3. This phase diagram reveals the

presence of $WO_3(s)$. The W in this compound comes from the breakdown of some of the

WC(s) reactant.
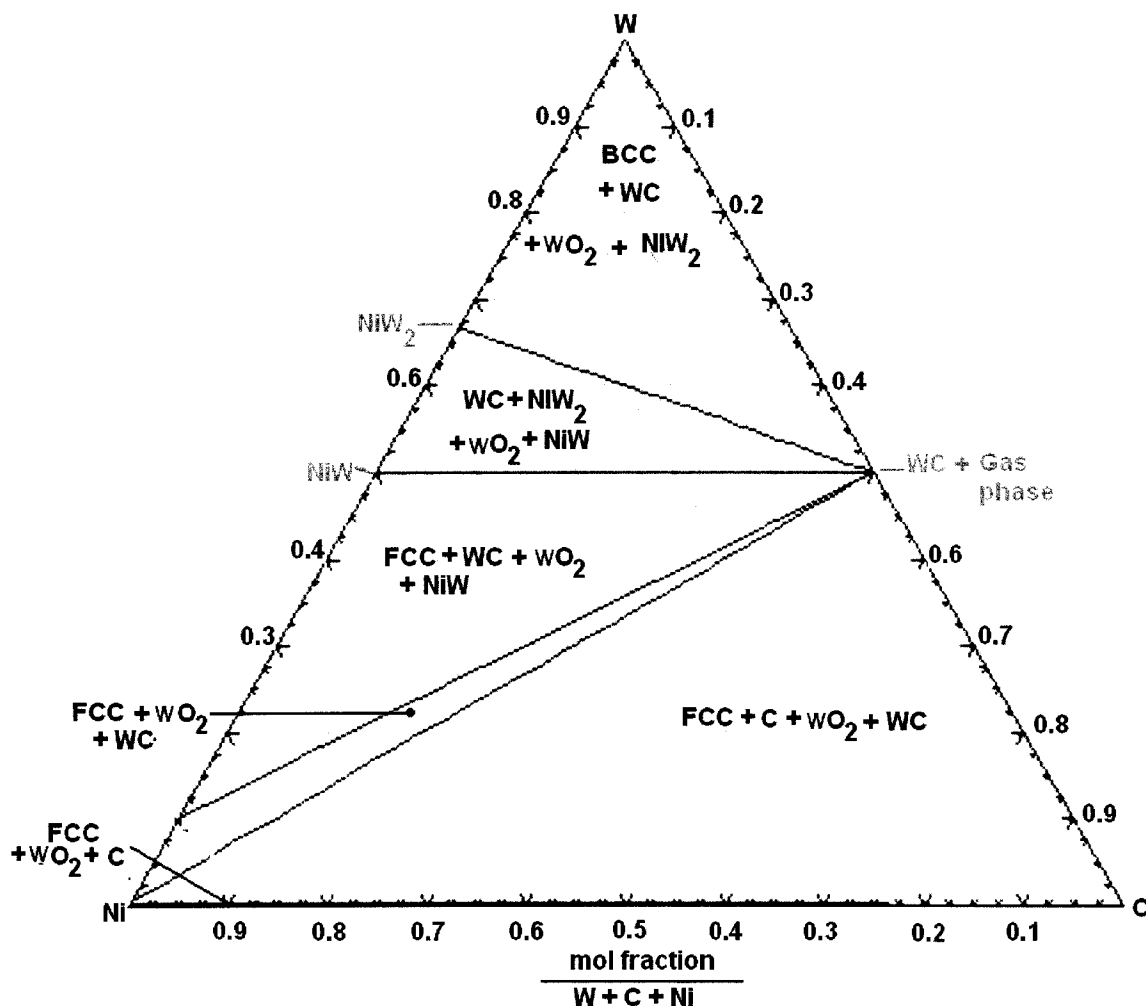
Figure 5.3: Ternary W-C-Ni phase diagram with addition of 0.001moles O_2, 298K.

5.3.1 Summary of Ni-W-C Thermodynamic Calculations.

The Ni-W-C system was assessed at 1773K and 298K using FACTSage[TM,40]. These temperatures reflect those used in the laboratory experiments of this research (section 3.3). Also, the n-values for inspection correspond to wt%WC values between 23wt%WC and 65wt%WC. These wt%WC values reflect those identified in the literature[4,6] as effective for the formation of Ni-WC MMC's.

The ternary Ni-W-C phase diagram at 1773K was presented. For a system with a composition corresponding to 23wt% WC (n-value of 12), a mixture of $W_2C(s)$ and a liquid solution is seen. As the wt%WC is increased, towards 65 (n-value of 1) a three-phase mixture of an invariant liquid solution, $W_2C(s)$ and C(s) is observed.

The ternary Ni-W-C phase diagram, at 298K, was also calculated using FACTSage[TM,40]. For a system composition equivalent to 23wt% WC (n-value of 12) up to a wt% WC of 65 (n-value of 1), a mixture of an invariant solid solution (Ni-rich), C(s) and WC(s) is seen. The experimental results in the Ni-WC system were considered together with this phase diagram. It was found that the results did, in fact, correspond to the phase diagram. The experimental samples contained W (dissolved in Ni), which corresponds to the Ni-rich, FCC solution and WC(s).

Experimentally, the equipment set-up in this research would allow a small amount of

145

oxygen to be present in the system. Therefore, the Ni-C-W system, at 298K, containing a small amount of oxygen, was evaluated. The presence of this small amount of oxygen did not discernibly alter any phase boundaries. It was found, however, that $WO_3(g)$ was formed for all of the compositions on the phase diagram.

5.4   Ni-B$_4$C System.

Figure 5.4 shows a ternary section of the Ni-B-C phase diagram at 1773K. There is an invariant point identified on the Ni-B-C phase diagram at 1773K. This point is where the liquid solution, C(s), B(s) and $B_4C(s)$ are in equilibrium.

Along the B-Ni axis, there are three areas distinct areas. Adjacent to the B-corner, there is a region where $B_4C(s)$ is in equilibrium with an invariant, liquid solution and B(s). As the amount of Ni is increased along this axis, the composition enters an area that contains a mixture of $B_4C(s)$ and liquid solution. Further increase of the nickel content pushes the composition into a region containing only a liquid, ternary solution.

On the Ni-C axis, there are two, phase compositional areas identified. At elevated levels of nickel, a ternary, liquid solution is seen. This is the same solution previously mentioned at elevated Ni levels. As the Ni content decreases along this axis, the composition enters a two-phase region made up of a ternary liquid solution and C(s). The

146

remaining area of the diagram is located along the B-C axis and has B$_4$C(s), an invariant, liquid solution and C(s).
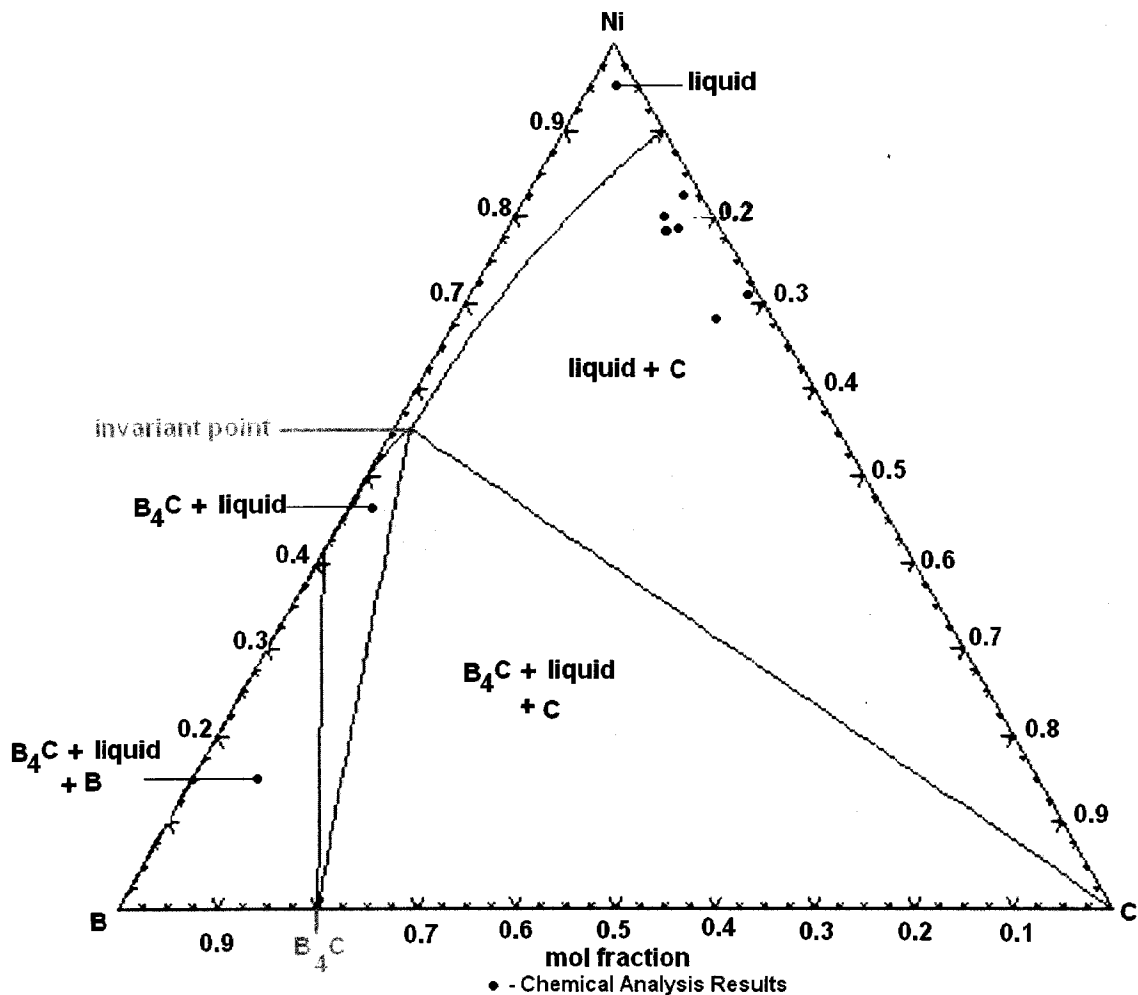
Figure 5.4: Ternary Ni-B-C phase diagram at 1773K.

The Ni-B-C system was also evaluated at 298K. At this temperature, it is expected that only solid phases will be seen. The chemical analysis results are shown on Figure 5.5. It can be seen that at the compositions given by chemical analysis, only Ni$_3$B(s), an FCC solution of almost pure Ni and C(s) will be seen. This result was the case in all but

147

experiment B6. Based on the XRD results, the experimental samples from B6 would be

located in the region of the diagram containing a mixture of C(s), $Ni_3B(s)$ and $Ni_2B(s)$.
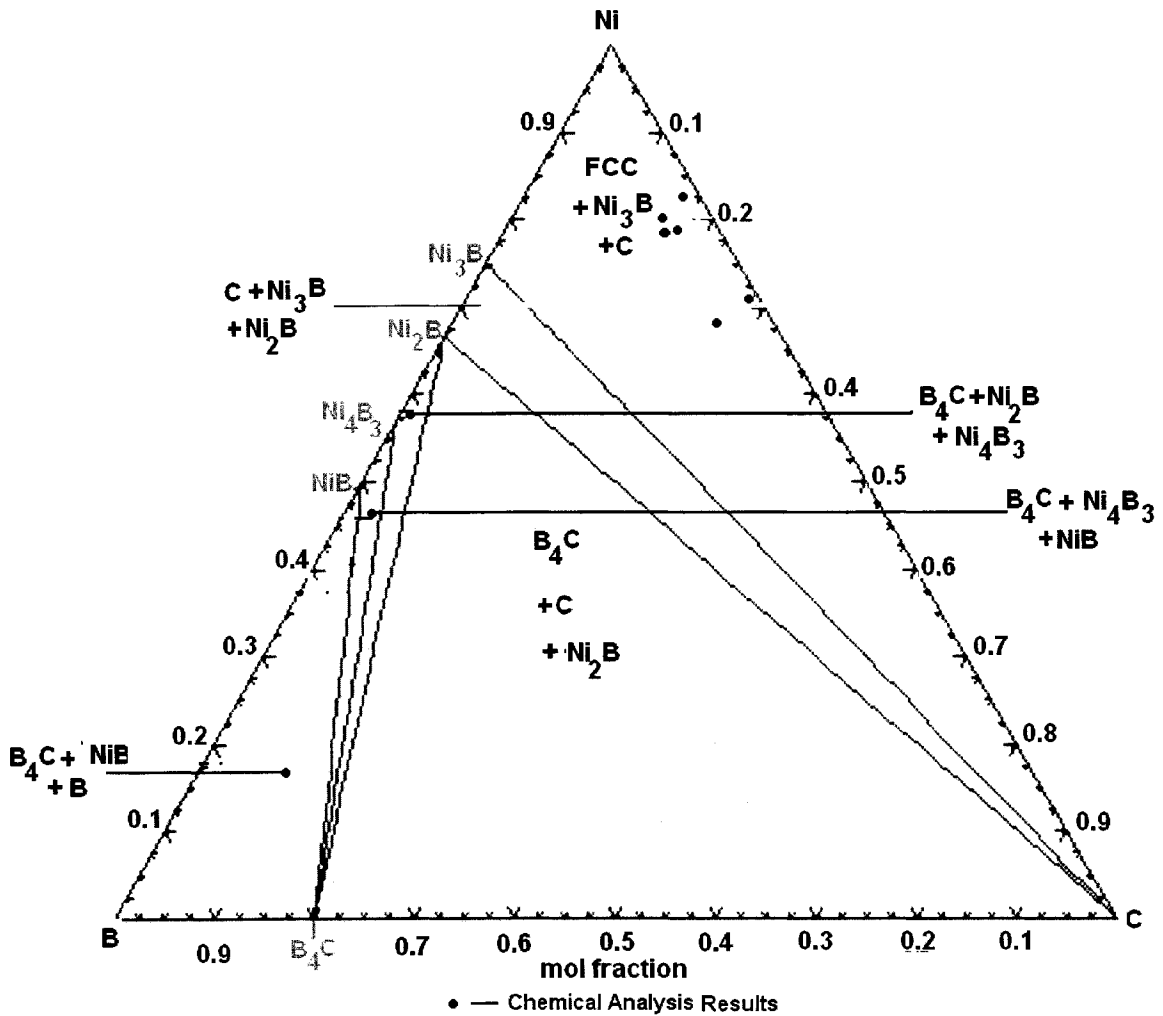
Figure 5.5: Ternary Ni-B-C phase diagram at 298K.

For the experimental apparatus used, section 3.0, it is extremely difficult to completely

remove oxygen from the system without the use of a vacuum pump. Therefore, the Ni-

B$_4$C-O$_2$ system was also evaluated at 298K. This temperature was chosen for the same

reasons as the Ni-WC samples. The micrographs of the Ni-B$_4$C experimental samples did

not show any obvious porosity. It is probable that in the Ni-B$_4$C melt, any gas bubbled to

the surface. The amount of oxygen that was introduced into this system is governed by

Equation (5-5).

$$\frac{molO_2}{\sum(molNi, molC, molB)} = 0.001$$

(5-5)

Equation (5-5) shows that there are 0.001moles of O$_2$ present. The ternary plot for the

Ni-B-C system at 298K with oxygen is seen in Figure 5.6. The ternary N-B-C system is

altered in the presence of oxygen. Along the Ni-C axis, there is a region present that

contains a mixture of a Ni-rich solid solution, B$_2$O$_3$(s), NiO(s) and C(s). This region is

not present on Figure 5.5. With respect to the rest of the phase diagram containing

oxygen, there are no discernible alterations to the phase boundaries. Also the remainder

of the phase diagram contains B$_2$O$_3$(s).
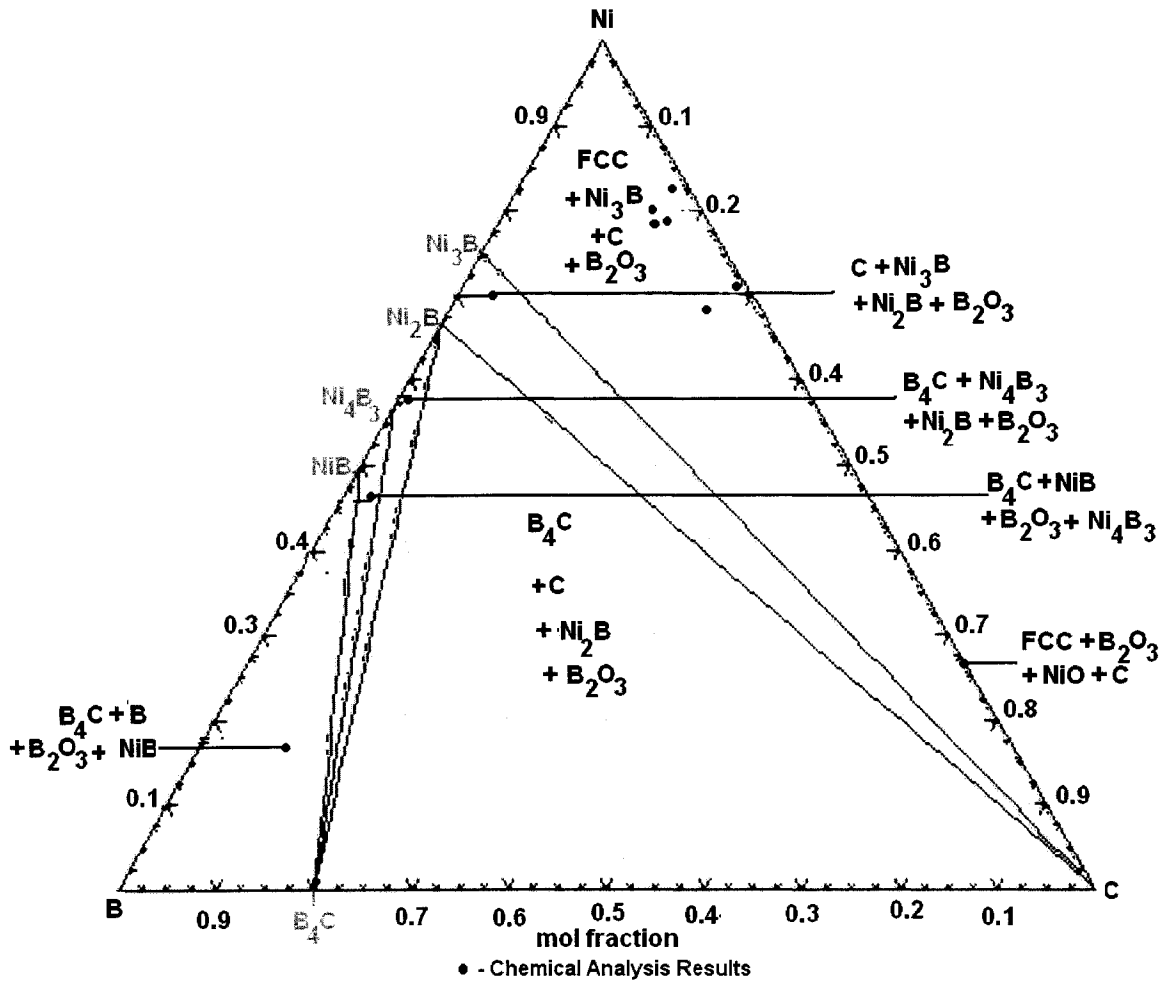
Figure 5.6: Ternary Ni-B-C phase diagram with 0.001moles O₂ (298K).

5.4.1 Summary of the Ni-B-C thermodynamics.

The Ni-B-C system was evaluated at 1773K and 298K using FACTSage[TM,40]. As was the case for the Ni-W-C thermodynamics, these temperatures were meant to reflect the reaction temperature for the experimental work performed for this research as well as to

150

reflect phases present at 298K, after sample cooling. The compositions that were considered in the Ni-B-C system were chosen to reflect the chemical analysis results.

On the ternary phase diagram at 1773K, the areas, which encompass the weight percent B values from the chemical analysis, are contained within an area containing a mixture of a ternary, liquid solution and C(s). At 298K, the ICP results are all located within the three-phase region containing C(s), $Ni_3B(s)$ and an invariant, FCC solid solution (99%Ni). The ICP results for experiment B6 put samples from this experiment in the region containing C(s), $Ni_3B(s)$ and an FCC solid solution. However, the XRD results showed the presence of Ni_3B and Ni_2B. These two results are in inconsistent.

An increase in the yield of B in the molten melt would aid in the maintenance of a portion of the $B_4C(s)$ that was added at 1773K. There are areas of the ternary, Ni-B-C phase diagram, at 298K, which contain $B_4C(s)$.

The Ni-B-C system was also evaluated for small amount of oxygen. Over all of the phase diagram (Figure 5.6), $B_2O_3(s)$ is observed. Along the Ni-C axis of this plot, there is a new region formed which contains FCC solution, $B_2O_3(s)$, NiO(s) and C(s). The phase boundaries on this diagram are not discernibly altered by the presence of a small amount of oxygen.

151

5.5 Other Options for Matrix Material.

The experimental and thermodynamic evaluation of the Ni-B$_4$C system revealed that nickel is not inert in the presence of boron carbide. At elevated temperature, the B$_4$C decomposes into boron and carbon. The boron dissolves in liquid nickel, consuming all B$_4$C in the system. Upon cooling, the boron forms nickel borides according to the molar ratio in the system.

It is therefore not feasible to take advantage of the wear resistance and light density of B$_4$C powder in a nickel matrix. Hence, other potential matrix materials are explored in place of nickel or in a solution with nickel to thermodynamically prevent the formation of nickel borides. Further, it was of interest to determine if the breakdown of B$_4$C could be prevented altogether. The metals explored were chromium, manganese and copper. These metals were chosen, as they are common, commodity metals[31]. Also, these three metals are frequently used as alloying additions in steels[1, 2, 3, 4, 5].

Each of these metals was considered in the ternary metal-boron-carbide system at 298K. The ternary phase diagrams presented were generated using FACTSage[TM,40]. This temperature was chosen to reflect the phases that would be formed upon cooling. The identification of a metal that does not form borides or carbides through the breakdown of B$_4$C(s) is ideal. When considering the ternary phase diagrams, if borides or carbides form, then the ΔG_f^o is likely high, and therefore, the boron carbide would probably

152

decompose.

5.5.1 Chromium

Figure 5.7 shows a ternary section of the Cr-B-C phase diagram at 298K. It can be seen

that there are several different sections on this phase diagram. The compound species that

form in this system are labeled along the binary axes. These compounds include, $B_4C(s)$,

$CrB(s)$ and $Cr_{23}C_6(s)$. At high levels of $Cr(s)$, the crystal structure of the solid solution

was assumed to be BCC like Cr. However, the binary Cr-B (Figure 5.8) and Cr-C (Figure

5.9) show almost no solid solubility at 298K. This means that this "solution" is very close

to pure $Cr(s)$.
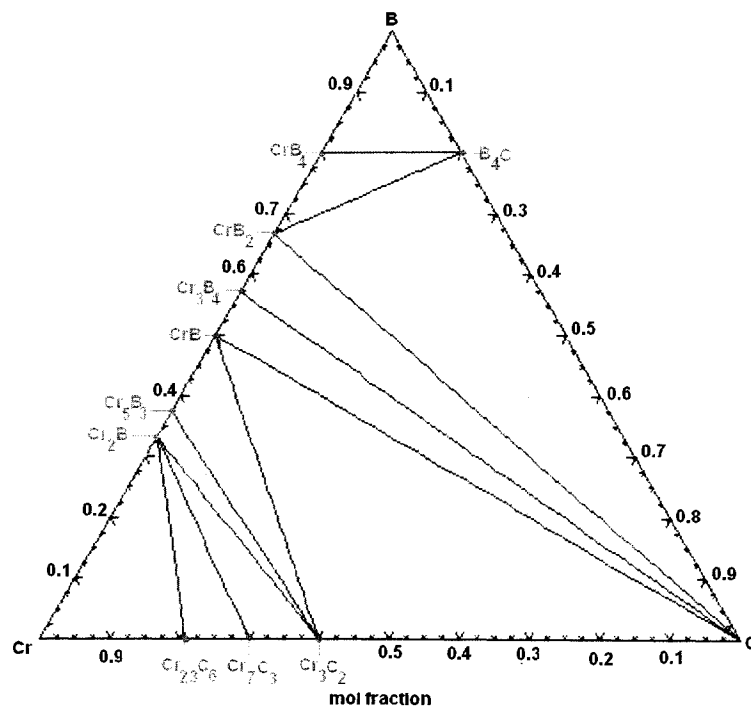
Figure 5.7: Cr-B-C phase diagram at 298K.

153
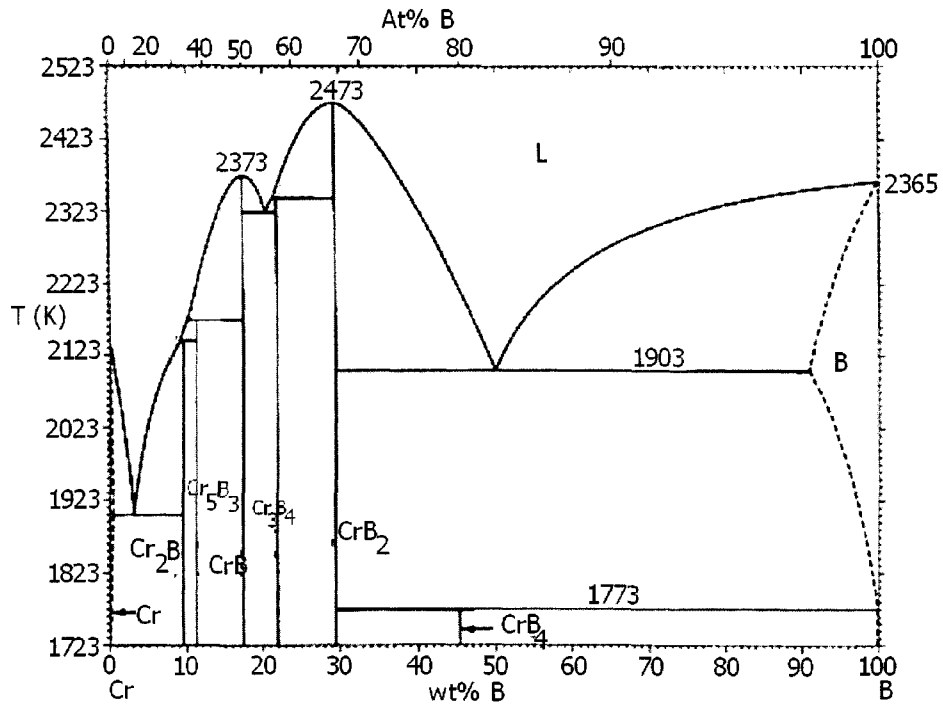
Figure 5.8: Binary Cr-B phase diagram[21].
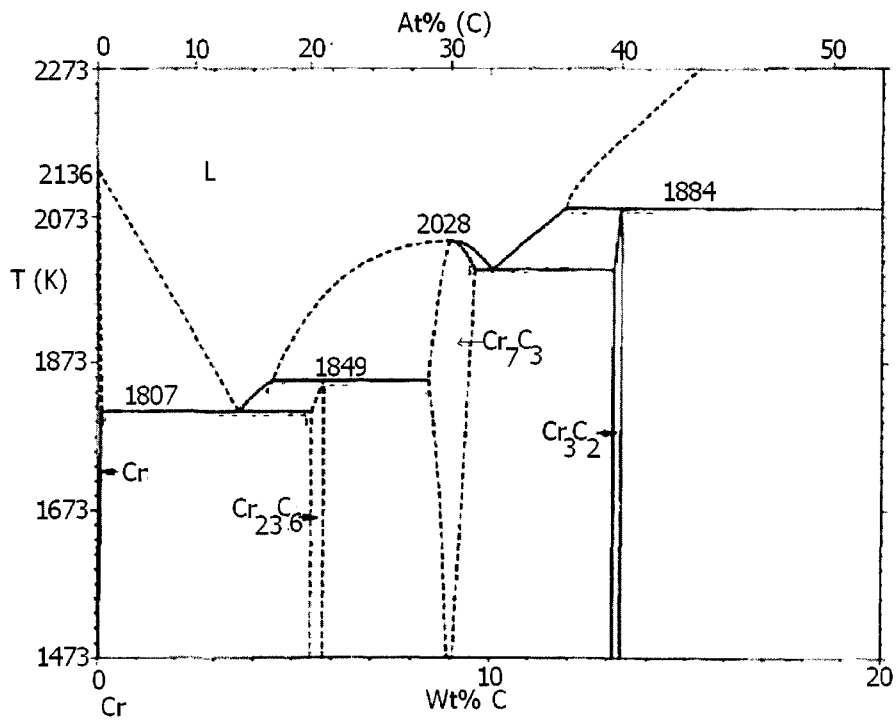
Figure 5.9: Binary Cr-C phase diagram[21].

154

As a result of the formation of chromium borides and chromium carbides, chromium is not a suitable candidate to replace nickel as a matrix for B_4C. Another disadvantage of using Cr is that it has a higher melting point than Ni, at 2148K. This means that to melt the Cr, would require a higher processing temperature than that for Ni.

It should also be noted that the nickel alloy that is commonly used for PTA usually contains some chromium. In a Ni matrix-WC MMC, this chromium is likely to act as a carbide-former that will tie any carbon freed from the WC that is dissolved in the melt. This would help to strengthen the bond between the Ni and WC.

In a Ni-B_4C MMC that contains Cr, the effect of Cr is not clear. At high levels of B, at 298K, the Cr-B-C phase diagram identifies the presence of $B_4C(s)$. However, there is excess boron in the system. In a system containing Ni(s) and Cr(s), this boron would form borides. It is possible that the borides may help to strengthen the bond between the $B_4C(s)$ and the metal similar to the way that Cr(s) acts in a Ni-WC MMC. However, laboratory experiments would be necessary to determine if this is the case.

5.5.2 Manganese

Manganese was considered as a matrix material to replace Ni in a system where B_4C is used as a ceramic additive. Manganese has a melting point of 1519K, which is below the

155

melting point of nickel, at 1728K. Using a metal with a lower melting point than nickel, would require less energy to melt the matrix material, which may result in cost savings.

The ternary Mn-B-C phase diagram is shown in Figure 5.10. This phase diagram has six distinct areas. The pure, compound phases of the system are labeled. There is one binary compound that is not included in FACTSage[TM,40], the $Mn_3B_4(s)$ phase. Based on the binary Mn-B diagram, shown in Figure 5.11, it is believed that this phase would be located between the MnB(s) and $MnB_2(s)$ phases on the Mn-B side of this diagram. At high concentrations of Mn(s), it was assumed that the structure of any solid solution would be cubic as the crystal structure of pure Mn(s) is cubic. It is also worth mentioning that, at high levels of Mn, B and C, solid solutions are not expected to form due to the low solid solubilities. This is hypothesized from the binary phase diagrams for the Mn-B (Figure 5.11), Mn-C (Figure 5.12) and B-C (Figure 2.8) systems.

156

Figure 5.10: Mn-B-C phase diagram at 298K.

Figure 5.11: Binary Mn-B phase diagram[21].

157
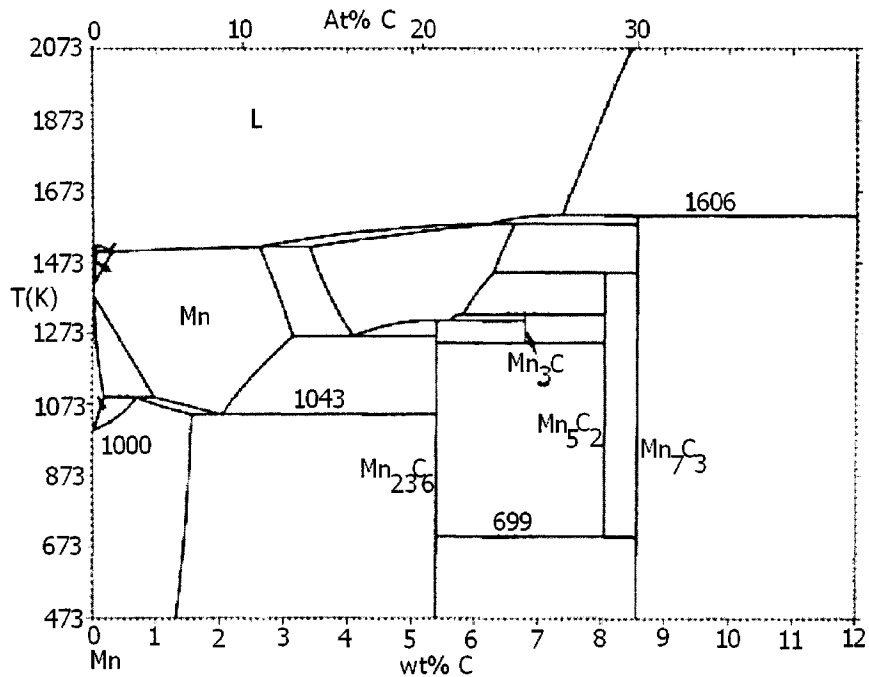
Figure 5.12: Binary Mn-C phase diagram[21].

Consideration of the ternary Mn-B-C phase diagram revealed that Mn is not a suitable

choice for a system with the ceramic B_4C. The reason for this is that, in this system, both

borides and carbides form.

5.5.3 Copper.

Copper was the third metal that was considered as a replacement or alloy for nickel for

the purpose of making an MMC with B_4C. The melting point of copper, 1357K, is

significantly lower than the melting point of nickel at 1728K. When a lower melting

point metal can be used, the energy required to form the B_4C-MMC could be reduced.

158

The SGTE database in FACTSage^{TM,40} was used to carry out these calculations. It is important to note that the Cu-B system is not assessed in this database. Therefore, a comparison between a FACTSage^{TM,40} -generated, Cu-B phase diagram and a Cu-B phase diagram presented by ASM[21] was made. This comparison is shown in Figure 5.13. It can be seen that Figure 5.13a) and Figure 5.13b) are very similar, except for a region on Figure 5.13b) that is located at 80wt%B and greater. Calculations for the purposes of this report will not be done at this elevated amount of boron; it is assumed that the FACTSage^{TM,40} phase diagram data for the Cu-B system is suitable for this report. Figure 5.14 shows the FACTSage^{TM,40} -generated, ternary Cu-B-C phase diagram at 298K. It is clear on this diagram that the only compound that forms in this system is $B_4C(s)$. The phase diagram in Figure 5.14 does not predict the formation of any copper-borides or copper-carbides at 298K.
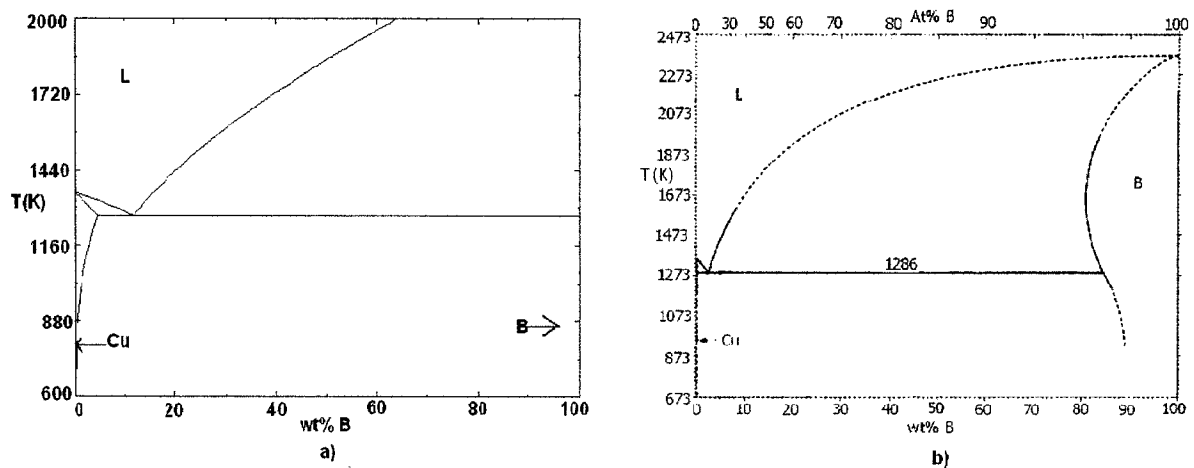
Figure 5.13: a) Cu-B phase diagram from FACTSage^{TM,40}.
b) Cu-B phase diagram from ASM[21].

159
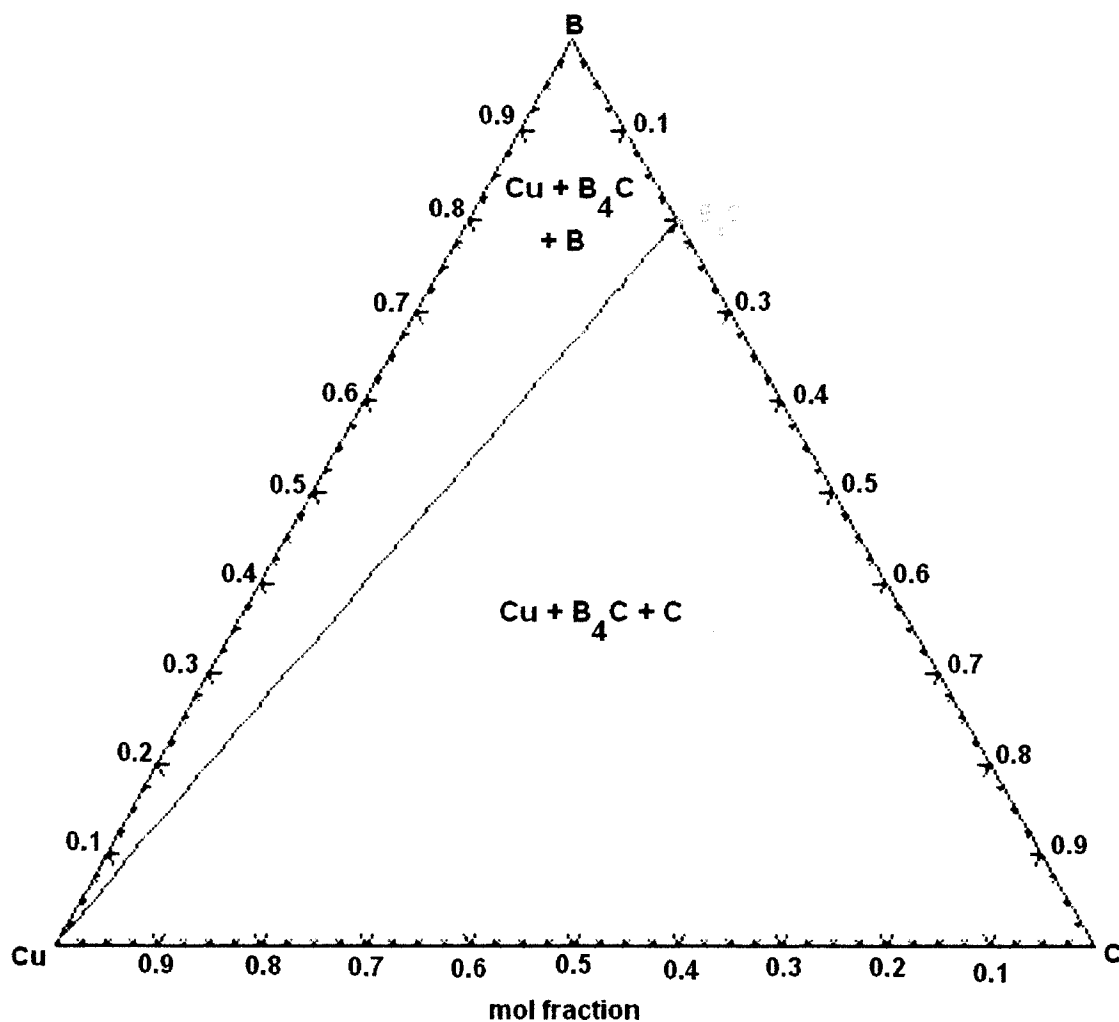
Figure 5.14: Cu-B-C phase diagram at 298K.

A thermodynamic analysis of the Cu-B-C system, at 1473K, has been found[42]. Froumin et al. completed a thermodynamic assessment of this system[42]. Figure 5.15 shows the ternary Cu-B-C phase diagram, in terms of mole fractions of the components, developed by Froumin et al.[42]. On this diagram, there are seven regions identified. The composition of these regions is in Table 5.1.

160

On Figure 5.15, there are two composition lines, labelled 1 and 2. Line 1 extends from pure B_4C (along the B-C axis) to an arbitrary point along the Cu-C axis (to be further discussed below). Line 2 extends from B_4C (along the B-C axis) to x_B^*. Compositions along line 2 represent a Cu-B solution in contact with B_4C. Lines 1 and 2 define two areas of composition, labelled G and H on Figure 5.15. Region G lies within IV while region H lies within II.

In section 1.0 and section 2.1.2, a typical composition of WC in a Ni-WC MMC was given as 65wt%. This corresponds to an MMC with a volume ratio of 50% (50vol% Ni, 50vol% WC). Applying the same volume ratio to a Cu-B_4C MMC would yield an MMC with 50vol% Cu and 50%vol% B_4C. This is equivalent to a mole fraction of 13%C, 50%B and 40%Cu. This composition is represented by the approximate area of interest labelled AI on Figure 5.15. Within AI, the compositions within region H are located adjacent to line 2 and therefore, it is assumed that most of the boron carbide within region H will be close to stoichiometric.

Figure 5.15 does not give a representation of what occurs in the ternary system upon cooling. For a sample with a composition the lies within region G, at 1473K, there will be graphite precipitate. Practically, this excess C can be removed with the addition of a carbide forming element, such as Cr. In the case where the composition lies within region H, at 1473K, a Cu-B solution is formed. The binary Cu-B phase diagram shows, that at a

161

B composition of x_B*, B will be precipitated upon cooling. The addition of a boride

forming element, such as Ni, will remove this excess B from the system. To further

illustrate, a discussion on the binary Cu-Ni system is followed by a discussion on the use

of a Cu-Ni alloy as the matrix material for a B_4C MMC. The same type of analysis could

be applied to other alloying elements such as Mn.
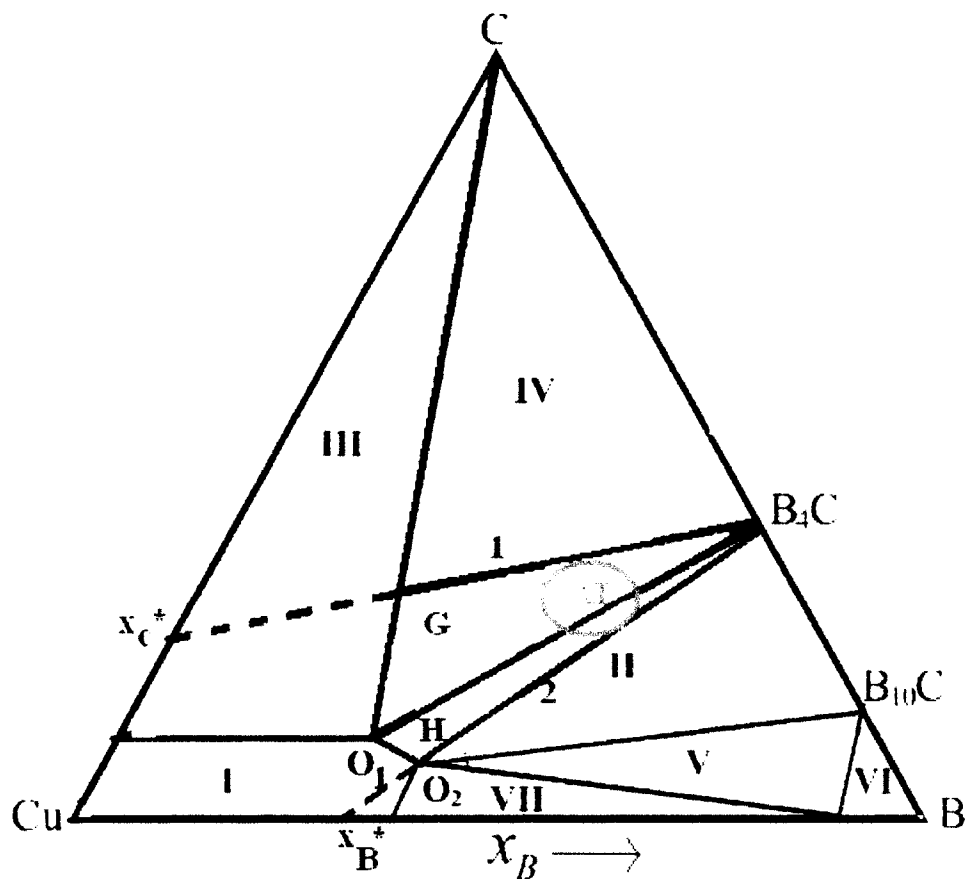
Figure 5.15: Ternary Cu-B-C phase diagram, 1473K. Cu corner not to scale[42].

162

Table 5.1: Compositions for the ternary Cu-B-C phase diagram[42].

Region on Phase Diagram	Composition
I	ternary liquid solution
II	ternary liquid solution + boron carbide
III	ternary liquid solution + graphite
IV	ternary liquid solution + graphite + B_4C
V	ternary liquid solution + $B_{10}C$ + B
V	B + Cu - B solution + $B_{10}C$
VII	ternary liquid solution + B saturated with Cu

5.5.3.1   Binary Cu- Ni System.

The binary phase diagram of the Ni-Cu system is shown in Figure 5.16. This diagram shows that nickel and copper are completely soluble in each other in the solid state over all phase compositions[21]. This solubility gives rise to a very homogenous structure in a binary Cu-Ni alloy.

There is a miscibility gap in the Cu-Ni system located between about 20wt% Ni and almost pure Ni. The α_1 and α_2 phases are comprised of a mix of Ni and Cu. The actual composition of these phases can be ascertained using a tie line within the miscibility

163

region[43].
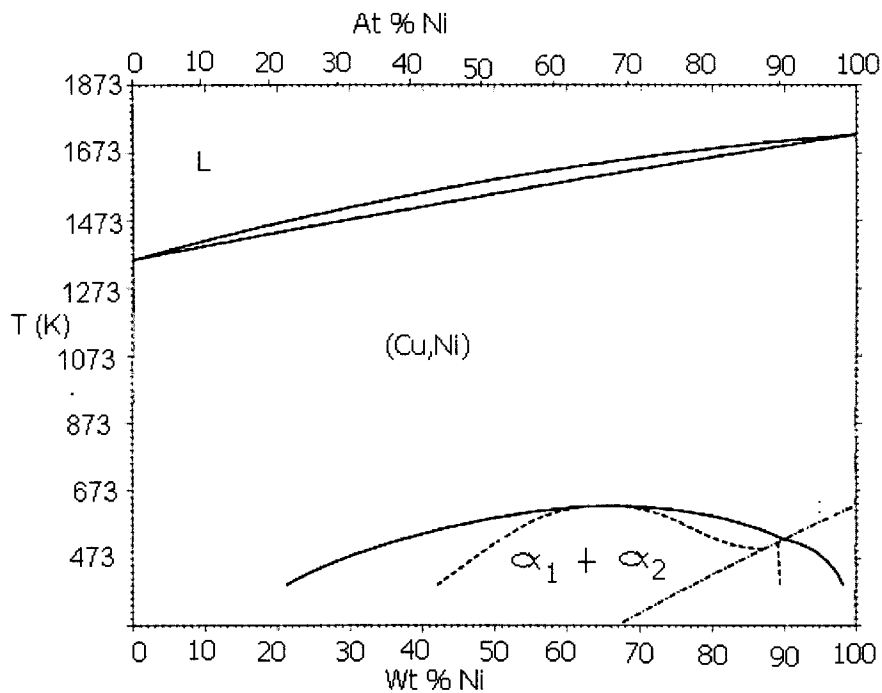
Figure 5.16: Binary phase diagram for the Cu-Ni system[21].

The SGTE database does not include analysis of the ternary Ni-Cu-B system.

FACTSage[TM,40] utilizes the calculated binary system data to approximate the ternary interaction parameters, thereby giving an impression of the ternary system.

5.5.3.2   Ternary Cu-B-Ni System.

A thermodynamic evaluation of the ternary Cu-B-Ni system was done to determine if a Cu-Ni alloy would thermodynamically form a suitable MMC. A thermodynamic analysis of the Ni-B-Cu system has not been located in the literature. In the SGTE database of

164

FACTSage[TM,40], two of the binary systems have been analysed: Ni-B, Ni-Cu[40](for Cu-B system, see above). As a first approximation for the ternary system, FACTSage[TM,40] uses a summation of the binary interaction parameters[40]. It is important to remember that because this system has not been experimentally analysed, only compositions close to pure Cu and pure Ni are considered reliable. Outside of this range the results may not be a trustworthy representation of what could occur[40].

The Cu-B-Ni system, at 298K is shown in Figure 5.17. The binary compounds associated with this ternary section are labelled along the appropriate binary sides. The effect of the Cu-Ni miscibility gap is also labelled. Above this labelled point, there are two, separate solid solutions. One of these solutions is high in Ni content and the other in Cu content. Additionally, it is clear on this ternary diagram, that FACTSage[TM,40] is overestimating the miscibility gap on the Cu corner. Established Cu-Ni phase diagrams[21] show that the miscibility gap extends to only approximately 80% Cu while FACTSage[TM,40] is showing the gap extending to approximately 87% Cu. This overestimation is the result of the summation of the binary interaction parameters to predict the unknown ternary system.

The two alloys that will be considered are the Ni-rich and Cu-rich alloys. Looking at alloys approaching pure nickel, say above a Ni mole fraction of 0.9, FACTSage[TM,40] predicts, in decreasing order, the formation of a Ni-rich solid solution (trace Cu), a Cu-rich solid solution (trace Ni) and a small amount of $Ni_3B(s)$. At high levels of Cu, above a

165

mole fraction of 0.9, Ni borides form, depending on the Ni and B compositions. At the highest nickel content, $Ni_3B(s)$ is formed. As the nickel content decreases, $Ni_2B(s)$, $Ni_4B_3(s)$ and $NiB(s)$ form.

On the ternary Ni-Cu-B phase diagram at 298K, the area closest to the B-corner of the diagram contains excess B. This area is highlighted. It is possible, that if carbon were added to this system, it would bond to this excess boron, forming $B_4C(s)$. Another option is the addition of a boride-forming metal such as chromium, Cr or manganese, Mn. The addition of one of these metals would form Cr-borides or manganese-borides, thereby eliminating the excess boron from the system.

166
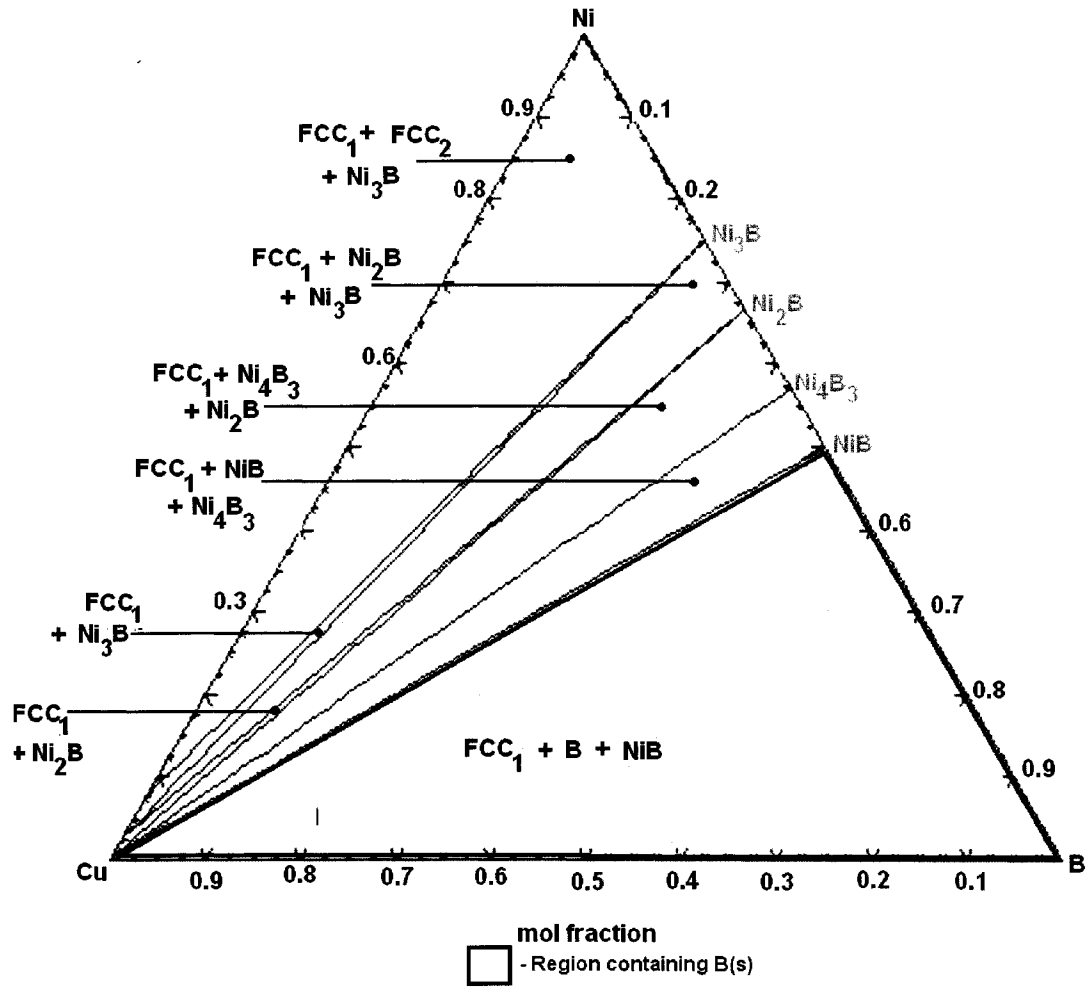
Figure 5.17: Cu-B-Ni phase diagram at 298K.

5.5.3.3   Ni-Cu-B system containing C.

At 298K, a ternary Cu-Ni-B phase diagram containing carbon was generated using

FACTSage[TM,40]. This diagram was generated to give a different perspective of the

quaternary Ni-B-Cu-C system. This phase diagram is seen in Figure 5.18. Along the Cu-

Ni axis of this diagram, the effect of the Cu-Ni miscibility gap is seen. The estimation

167

that FACTSage[TM,40] makes for this gap appears to be too close to pure Cu. As previously mentioned, this is an artefact of the way in which FACTSage[TM,40] calculates unknown ternary systems.

For the given phase diagram, the amount of boron present at any given composition is found according to Equation (5-6).

$$\frac{(molC)}{\sum(molCu, molNi, molB)} = 1$$

(5-6)

Phases appearing along the binary axes have been labelled. Along the binary Ni-B axis, there are labels identifying the compositions where the nickel-borides, $Ni_3B(s)$ and $Ni_2B(s)$ are in equilibrium with solid carbon. On the Cu-Ni axis, the effects of the Cu-Ni miscibility gap are identified.

It can be seen on Figure 5.18 that there are five distinct areas, containing different phase compositions. These areas have been labelled. There is a large region on this diagram which contains a mixture of an FCC, solid solution, $Ni_2B(s)$, $B_4C(s)$ and $C(s)$. The presence of $Ni_2B(s)$ and $B_4C(s)$ is encouraging as this indicates that, for a system with a composition within this area, a portion of experimental $B_4C(s)$ reacts, forming a bond, while a portion of the $B_4C(s)$ remains intact.

168
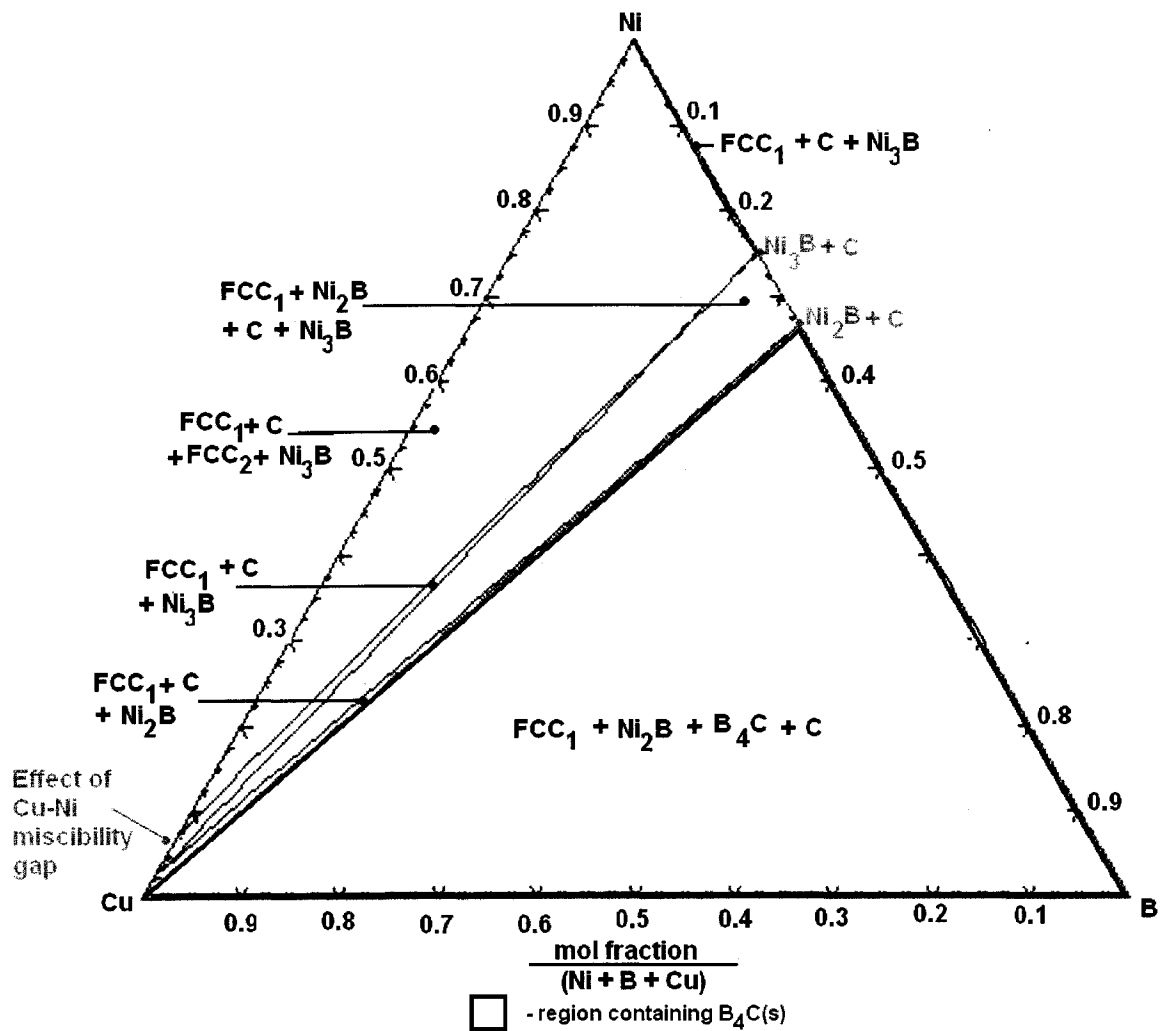
Figure 5.18: Ternary Cu-Ni-B phase diagram at 298K, containing C.

5.5.3.4   Ni-Cu-C system containing B.

A ternary section of the Cu-Ni-C phase diagram containing boron is shown in Figure 5.19. For the given phase diagram, the amount of boron present at any given composition is calculated using Equation (5-7).

169

$$\frac{(molB)}{\sum(molCu, molNi, molC)} = 1$$

It can be seen in this figure that there are four areas of differing phases. Each of these

areas is clearly labelled on the plot. Along the Cu-Ni axis, there is no evidence of the Cu-

Ni miscibility gap. This could be an artefact of the FACTSage[TM,40] calculation or

something that would be seen experimentally. Laboratory experiments would be required

to verify the presence/ absence of this gap.

This ternary plot is encouraging. The presence of free carbon in a large portion of this

phase diagram may prove to be troublesome. However, the addition of a carbide-former,

such as Cr, or Mn would remove this graphite. There is also a region, at elevated Cu

content, which contains excess boron. Again, the addition of a small amount of a boride-

forming substance, such as Cr or Mn, would take care of this. This phase diagram

illustrates, that by altering the compositions, thermodynamics predict that $B_4C(s)$ can be

maintained. The presence of nickel-borides together with $B_4C(s)$ is ideal. The nickel-

borides act as a joint between the matrix and the ceramic particles. Laboratory

experiments must be done to determine first, if experimental samples would truly contain

these phases and, second, what wt% B_4C, and what proportion of Cu:Ni would give the

best wear resistance.
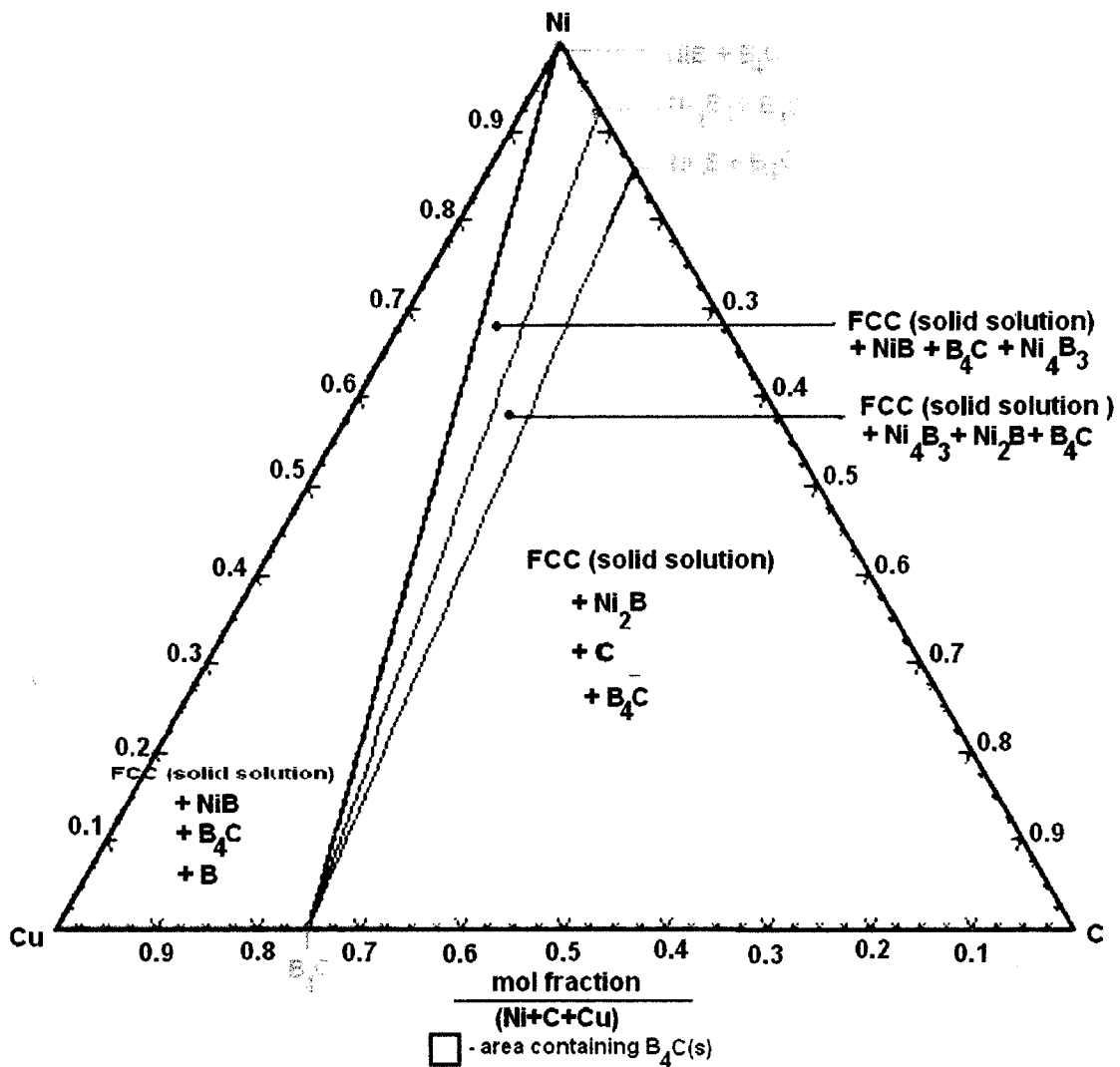
Figure 5.19: Cu-Ni-C ternary phase diagram at 298K containing B.

171

5.6 Summary of thermodynamics.

A thermodynamic analysis of the two reaction systems, Ni-WC and Ni-B$_4$C was carried out. In the Ni-WC system, the thermodynamic analysis supported the results that were seen experimentally (section 4.6). The Ni-B4C experimental results were consistent with the exception of the results seen from experiment B6 (section 4.6).

Ni was found to be an unsuitable matrix material for a B$_4$C MMC. As a result, thermodynamic calculations were done in order to determine if Cr, Mn or Cu could be used as a matrix material. It was found that Cr and Mn were not suitable because they, like Ni, react with B$_4$C. Thermodynamic calculations using Cu determined that Cu is inert in the presence of B$_4$C. Two, ternary phase diagrams, the Cu-Ni-B (with C addition) and the Cu-Ni-C (with B addition) were developed using FACTSage[TM,40]. There are regions on these phase diagrams, which contain B$_4$C (section 5.5.3.3 and section 5.5.3.4). The presence of B$_4$C on these phase diagrams suggests that a Cu-Ni alloy may be suitable for the matrix material in a B$_4$C MMC.

172

6.0 Summary/ Future Work.

In this chapter the experimental results and the thermodynamic analysis carried out in this work will be summarized. In addition, future work will be recommended. This will be to provide further confirmation of the reactions between WC and Ni and B_4C and Ni described in this thesis as well as recommendations to take advantage of the wear properties of B_4C in an MMC will be discussed.

6.1 Summary.

Industrially, wear becomes increasingly important over time. Cost-effective methods to minimize the effects of wear are more and more essential. A fairly recent development in this area has been the introduction of MMC's, which consist of a tough and ductile metal matrix containing ceramic particles dispersed throughout[9]. Frequently, these materials are used as coatings in situations where abrasive wear is present, such as in slurry pipelines in the oil industry.

There are several ultra-hard materials that are available in powdered form, including tungsten carbide and boron carbide. WC has proven to be an effective ceramic particle for use in MMC's. There are several processing routes, which result in a uniform

173

distribution of a WC-Ni MMC. Though not an exhaustive list, a few of these methods are PTA, liquid phase sintering as well as laser cladding. Each of these methods has been used in the successful production of a WC-Ni MMC.

Experimental work was done on the Ni-WC system at high temperature. Chemical analysis of experimental samples showed that the yield of W (from the WC reactant) ranged from 24% to 83%. Optical microscopy clearly showed the presence of WC particles within the Ni matrix at room temperature. EPMA analysis of Ni-WC samples revealed the presence of W dissolved within the nickel matrix as well, indicating that there was some decomposition/ reaction of the WC. XRD did not detect any Ni-W compounds formed but XRD did show Ni-peak broadening, suggesting that the W identified by WDS was dissolved in the nickel matrix. Therefore, the experimental samples contained nickel with dissolved W and WC(s) particulates.

The thermodynamic analysis of the Ni-WC system supported the experimental results seen in this work. The ternary Ni-W-C system, at 298K, for the compositions experimentally analysed in this work, predicts a solid solution, WC and, in cases of increased WC content, C(s). The presence of graphite (C(s)) would be considered detrimental to the performance of the MMC as this substance acts as a solid lubricant. Therefore, it would be advisable to use MMC's with compositions of WC that are low enough to prevent graphite formation or to add a carbide forming element, such as Cr.

174

PTA welding of a B$_4$C- Ni MMC has been attempted without success. The reason for this is that the boron carbide decomposed rapidly at high temperature (approaching 1800K in these tests). The B$_4$C was decomposed so quickly, in fact, that none of the experimental samples taken showed its presence at any time.

An evaluation of the experimental samples that were drawn was carried out in an attempt to determine what became of the boron and carbon from the B$_4$C. Chemical analysis of experimental samples revealed that yield of B (from B$_4$C) was very low, reaching a maximum of 44% for all the samples analysed. OM did not reveal any B$_4$C particulates in the Ni matrix. WDS showed that it was the interdendritic regions of the sample, which contained B. Subsequent XRD identified Ni$_3$B as the reaction product in all but one case. In experiment B6 the yield of B was low by ICP but XRD revealed the presence of Ni$_2$B(s) and Ni$_3$B(s). In experiment B6, it is clear that the injection of B$_4$C(s) powder was more successful than in other tests. The reason for this is unknown as the experimental set-up was unchanged. The formation of a mixture of Ni$_3$B(s) and Ni$_2$B(s) requires between 6wt%B and 8.4wt%B. At the boron yield values that were given by ICP, the ternary Ni-B-C phase diagram, developed in section 5.4, predicted the formation of Ni$_3$B(s) only.

The possibility of replacing Ni as the matrix material in the Ni-B$_4$C system was evaluated using FACTSage[TM,40]. These analyses revealed that both Cr and Mn are not suitable as

175

they readily form metal-borides and metal-carbides. Cu does not form borides or carbides so Cu was further investigated by FACTSage[TM,40]. The Cu-B-C, Cu-Ni-B and Cu-Ni-B-C systems were developed based on the established binary phase diagrams of these species.

On the Ni-B-Cu phase diagram, there is an area, which contains excess boron. This region is of interest, as this boron would likely be tied up as B_4C if C were added to this system. Or, the addition of a boride forming species would also tie up this excess B. To verify this, a Ni-Cu-B phase diagram, containing a small amount of carbon was also developed. On this diagram, there was one area, which contained $B_4C(s)$. This area also contained $Ni_2B(s)$, a solid solution (Ni, Cu, trace B, trace C) and C(s). The presence of $B_4C(s)$ is desired in an MMC for wear applications; however, the presence of graphite at some compositions may prevent the exploitation of the advantageous B_4C properties. The addition of a carbide-former, such as Cr, would take care of this graphite. At elevated Cu levels, there is free boron present. The addition of a boride-former, such as Mn, would tie up this boron as manganese borides. Experimental verification of these results would be helpful to determine if there are any kinetic barriers to the formation of the phases present on the ternary phase diagram.

176

6.2 Future Work.

6.2.1 High-Resolution Investigation of Microstructures.

High-resolution investigation of the interfacial region between the ceramic particulates and the Ni matrix was not carried out for this work. An FESEM provides superior spatial resolution (down to 1.5nm) when compared to the traditional SEM (around 10nm) and the electron microprobe[33], allowing high-resolution investigation of the interfacial microstructure(s). The FESEM also, typically uses a lower accelerating voltage than the SEM or the Microprobe, which causes less sample damage.

6.2.2 Wear Testing of Experimental Ingots.

The experiments carried out according to the procedure outlined in section 3.0 resulted in the formation of solidified ingots contained in the Alumina crucible. These ingots were removed from the Alumina crucibles upon cooling.

In the case of the Ni-WC system, the creation of a metallurgical bond between the WC particulates and the Ni matrix was confirmed by the analyses carried out in this work. Wear testing of the experimental ingots would provide insight into the interfacial bonding between the Ni matrix and the WC particulates. For the Ni-B_4C system, there was no experimental evidence that any of the injected B_4C particulates remained after processing was completed. The presence of nickel borides was confirmed by the analysis of

177

experimental samples. The wear behaviour of nickel borides has not been widely studied and, therefore, it would also be useful to carry out wear testing on the ingots from the Ni-B_4C tests.

6.2.3 Cu-Ni Alloy.

The evaluation of a Cu-Ni alloy as a potentially suitable matrix material for a B_4C MMC was done thermodynamically. To further verify the suitability of this alloy, experimental testing, with a similar set-up to the procedure outlined in section 3.0, with an improved method of ceramic powder injection needs to be done. Wear testing of the ingots produced from these experiments would also determine the optimal composition of the Ni-Cu alloy for wear resistance. Once the suitable composition has been determined, this Cu-Ni alloy should be tested using PTA.

178

References.

1 Llewellyn, Rees, "Materials for Controlling Wear in Surface Mining" CIM Bulletin

89(1002), 76-82, 1996.

2 Zhu, Hua, "Study on wear failures of mining machinery", *Meitan Xuebao/Journal of*

the China Coal Society **31**(3), 380-385, 2006.

3 Deuis, R.L., Yellup, J.M., Subramanian, C., "Metal-Matrix Composite Coatings by

PTA Surfacing", *Composites Science and Technology* **58**, 299-309, 1998.

4 Chiovelli, S., "Application of Boron Carbide as a Wear Resistant Overlay", Masters of

Engineering, University of Alberta, Edmonton, AB., Canada, 1999.

5 Neville, A., Reza, F., Chiovelli, S., Revega, T., "Erosion-Corrosion Behaviour of WC-

based MMC's in Liquid-Solid Slurries", *Wear* **259,** 181-195, 2005.

6 Grigorescu, I.C., Rauso, C. Dj., Drirs-Halouani, R., Lavelle, B., Giampaolo, R., Lira, J.,

"Phase Characterization in Ni Alloy-Hard Carbide Composites for Fused Coatings",

Surface and Coatings Technology, **76- 77,** 494-498, 1995.

7 Wu, P., Zhou, C.Z., Tang, X.N., "Microstructural Characterization and Wear Behaviour

of Laser Cladded Nickel-Based Tungsten Carbide Composite Coatings", *Surface and*

Coatings Technology, **166,** 84-88, 2003.

8 ASM Handbook.v7 Powder Metal Technologies and Applications: ASM Int.: Materials

Park, OH, 1998.

179

9 Callister, W. D., *Materials Science and Engineering*, 4th Ed, John Wiley and Sons: New York, 1997.

10 Kublii, V.Z., Velikanova, T.Ya., "Ordering in the Carbide W_2C and Phase Equilibria in the Tungsten-Carbon System in the Region of its Existence.", *Powder Metallurgy and Metal Ceramics*, **43**(11-12), 630-644, 2004.

11 Meng, Junhu, Lu, Jinjun, Wang, Jingbo, Yang, Shengrong, "Interfacial and Tribological Properties of Ni/Cr Alloy/Ceramic Tribo-Couples under Dry Sliding Contact", *Journal of the European Ceramic Society*, **26**, 2407-2412, 2006.

12 Li, Q., Lei, T.C., Chen, W.C., "Microstructural Characterization of WCp Reinforced Ni-Cr-B-Si-C Composite Coatings", *Surface and Coatings Technology* **114**, 285-291, 1999.

13 Thevenot, F., 'A Review on Boron Carbide', *Key Engineering Materials*, **56**, 59-88, 1991.

14 Rogl, Peter, *Phase Diagrams of Ternary Metal-Boron-Carbon Systems*, ASM International, Materials Park, OH, 1998.

15 Pierson & High O., *Handbook of Refractory Carbides and Nitrides: Properties, Characteristics, Processing and Applications*, Noyes Publications, New Jersey, 1996.

16 Jimenez, I., Sutherland, T., van Buuren, T., Carlisle, J.A., Terminello, L.J., "Photoemission and X-Ray Absorption Study of Boron Carbide and its Surface Thermal Stability", *Physical Review B*, **57**(20), 167-174, 1998.

17 Viala, J.C., Bouix, J., Gonzalez, G., Esnouf, C., "Chemical Reactivity of Alumnium with Boron Carbide", *Journal of Materials Science,* **32,** 4559-4573, 1997.

18 Nagase, F., Uetsuka, H., Otomo, T., "Chemical Interactions Between B_4C and Stainless Steel at High Temperatures", *Journal of Nuclear Materials,* **245,** 52-59, 1997

19 Jiang, Q.C., Wang, H.Y., Ma, B.X., Wang, Y., Zhao, F., "Fabrication of B_4C Particulate Reinforced Magnesium Matrix Composite by Powder Metallurgy", *Journal of Alloys and Compounds* **386,** 177-181, 2005.

20 Wang, Xibao, "The Metallurgical Behaviour of B_4C in the Iron-Based Surfacing Alloy During PTA powder Surfacing", *Applied Surface Science* **252,** 2021-2028, 2005.

21 ASM Handbook, v3 Phase Diagrams. ASM Int.: Materials Park, OH, 1993.

22 Turkdogan, E.T., Hancock, R.A.; Herlitz, S.I.," The Solubility of Graphite in Manganese, Cobalt and Nickel", *Journal of the Iron and Steel Institute,***182,** 274-277, 1956.

23 E.K. Storms, E.G. Sklarz, "Vaporization Thermodynamics of Ni-B (Liquid) and Ni-B-C (Liquid)", *Journal of Less Common Metals,* **135,** 229-237, 1987.

24 Copland, Evan H., Jacobson, Nathan S., "Thermodynamic Activity Measurements with Knudsen Cell Mass Spectrometry", *Interface* **10(2),** 28-31, 2001.

25 Lim, C.Y.H., Leo, D.K., Ang, J.J.S., Gupta, M., "Wear of Magnesium Composites Reinforced with Nano-Sized Alumina Particles", *Wear* **259,** 620-625, 2005.

26 Lee, Won-Bae, Lee, Chang-Young, Kim, Myoung-Kyun, Yoon, Jung-Il, Kim, Young-Jig, Yoen, Yun-Mo, Jung, Seoung-Boo, "Microstructures and Wear Property of Friction

181

Stir Welded AZ91 Mg/SiC Particle Reinforced Composite", *Composites Science and Technology* **66,** 1513-1520, 2006.

27 Shackelford, James, Alexander, William, *CRC Materials Science and Engineering Handbook*, 3rd Ed, CRC Press, USA, 2001.

28 Meng, Q.W., Geng, L., Zhang, B.Y., "Laser Cladding of Ni-Base Composite Coatings onto Ti-6Al-4V Substrates with Pre-Placed B_4C+NiCrBSi Powders" *Surface and Coatings Technology* **200,** 4923-4928, 2006.

29 Levenspiel, Octave, *Chemical Reaction Engineering*, 2nd Ed, John Wiley and Sons, New York, USA, 1962.

30 Centorr Vacuum Industries, 2005, Available at http://centorr.com.

31 Gauthier, Michelle, M., *Engineered Materials Handbook Desk Edition*, ASM Int.: Materials Park, OH, 1995.

32 ASM Handbook V10, Materials Characterization, ASM Int.: Materials Park, Ohio, 1992.

33 Goldstein, J., *Scanning Electron Microscopy and X-Ray Microanalysis*, Springer Science and Business Media Inc., New York, USA, 2003.

34 Rip, Wilhemenia (Syncrude Research Centre), Private Communication, 2005.

35 X-Ray Diffraction Laboratory, University of Alberta, [Online Document], Available at http://easweb.eas.ualberta.ca/facilities/xraydiffraction.cfm, 2006.

36 Reed-Hill, Robert E., Abbaschian, Reza, Physical Metallurgy Principles, 3rd Ed, PWS-Kent Pub., Boston, USA, 1992.

182

37 International Centre for Diffraction Data, JCPDS Database, 2006,

Available at www.icdd.com

38 ASM Handbook V11, Failure Analysis and Prevention, ASM Int.: Materials Park,

Ohio, 2002.

39 ASM Handbook V9, Metallography and Microstructures, ASM Int.: Materials Park,

Ohio, 2004.

40 Bale, C.W., Chartrand, P., et al., FactSage Software and Databases, 2001,

Available At http://www.factsage.com, 2001.

41 Mirchandani, Prakash, Kastura, Laslob, Friederichs, John, "Nonmagnetic Nickel

Tungsten Cemented Carbide Compositions and Articles made from the Same", U.S.

Patent 5273571, Dec.28, 1993.

42 Froumin, N., Frage, N., Aizenshtein, M., Dariel, M.P., "Ceramic-Metal Interaction

and Wetting Phenomena in the B_4C/Cu System.", *Journal of the European Ceramic

Society* **23**, 2821-2828, 2003.

43 Porter,D.A., Easterling, K.E., *Phase Transformations in Metals and Alloys*, 2nd Ed,

Chapman and Hall, London, U.K., 1992.

A.0 Standard Deviation Sample Calculations.

The standard deviation for the elemental mapping result was calculated using Equation (
A-1.

$$\sigma = \sqrt{\frac{1}{N} * \sum_{i=1}^{N} (x_i - \bar{x})^2}$$

(A-1)

where σ = standard deviation
N = number of data points
x_i = discrete data point, i
$\bar{x}$ = average of discrete data points

Table A.1 gives the 95 pieces of data that was used to calculate the maximum wt%W

(1.3wt%), minimum wt%W (0.8wt%), average wt%W ($\bar{x}$, 1) and the standard deviation

(σ, 0.2) for the 9.5minute sample from experiment W3.

184

Table A.1: wt%W data (95discrete data points, 9.5minute sample, experiment W3).

Point (#)	W (wt%)	Point (#)	W (wt%)	Point (#)	W (wt%)	Point (#)	W (wt%)
1	1.1	31	0.9	61	0.9	91	1.2
2	1.1	32	1.0	62	0.9	92	1.1
3	1.0	33	0.7	63	1.1	93	1.1
4	1.1	34	0.5	64	1.2	94	1.1
5	1.1	35	1.2	65	0.9	95	1.0
6	1.0	36	1.2	66	0.5		
7	1.1	37	1.2	67	0.7		
8	1.1	38	1.2	68	1.1		
9	0.4	39	0.9	69	1.1		
10	0.6	40	0.6	70	1.1		
11	1.1	41	0.7	71	1.2		
12	1.1	42	1.3	72	1.2		
13	1.2	43	1.1	73	1.1		
14	1.1	44	1.2	74	1.2		
15	1.2	45	1.1	75	1.0		
16	1.2	46	1.1	76	1.2		
17	0.7	47	1.1	77	0.8		
18	1.1	48	1.1	78	0.6		
19	1.0	49	1.2	79	0.8		
20	0.9	50	0.3	80	0.8		
21	0.6	51	0.7	81	0.9		
22	0.6	52	0.8	82	0.9		
23	0.9	53	0.8	83	0.7		
24	0.9	54	0.7	84	0.8		
25	1.1	55	0.8	85	0.6		
26	1.1	56	1.1	86	1.0		
27	1.0	57	0.7	87	1.2		
28	1.2	58	0.8	88	1.0		
29	0.6	59	1.1	89	1.1		
30	1.1	60	1.1	90	1.0		

185

B.0 Resolving Peak Overlap in XRD.

For the Ni-B$_4$C system, there are a number of binary nickel borides that can form. In Figure B.1, the 2-Theta values corresponding to the peaks of Ni$_2$B and Ni$_3$B are plotted as a function of their intensity. There are several peaks that are very close to overlapping. The peaks around a 2-theta value of 54° are close to overlap (Figure B.1). However, it is easy to clarify which substance is present by looking to other peaks. For example, three medium-intensity peaks for Ni$_3$B are located at 2-theta values between 55.4° and 48°. This region does not have any Ni2B peaks. A second area to help separate Ni$_3$B and Ni$_2$B is found between 2-theta values of 55° and 58°. In this region, there are a few medium-intensity peaks of Ni$_3$B and no Ni$_2$B peaks.
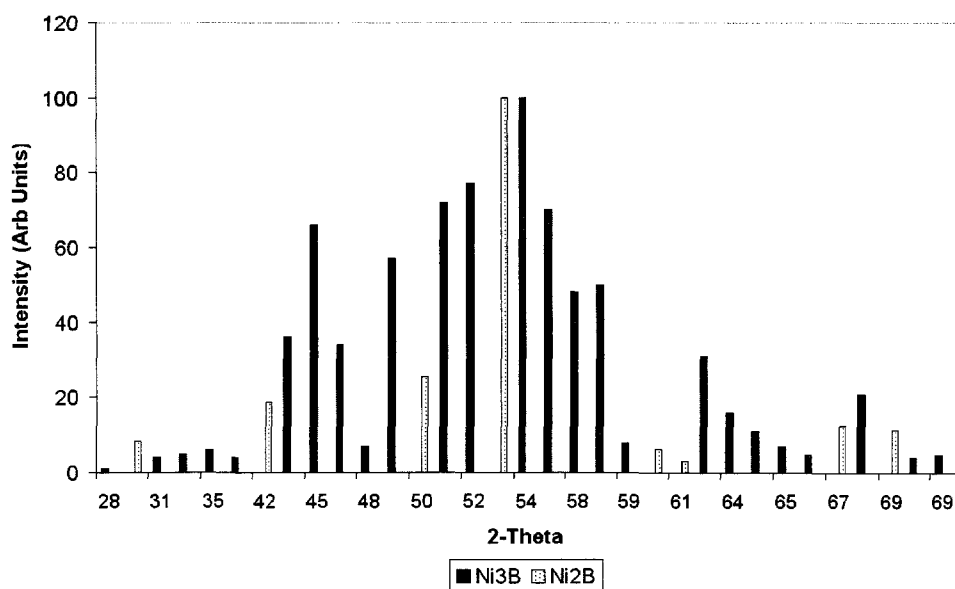
Figure B.1: Comparison of XRD patterns of Ni$_3$B and Ni$_2$B.

186

A plot of the Ni versus Ni_3B peaks is shown in Figure B.2. The two, nickel peaks that are

identified are located at 2-theta values of 52.2° and 61° respectively. The Ni peak at

52.2° is very close to a major peak for Ni_3B, at 52.4°, making peak interference likely.

Therefore, the nickel peak located at 61° is used to determine if Ni is present in a sample

with Ni_3B. If this peak is distinguishable, the presence of Ni is assumed. The large

number of Ni_3B peaks makes it easy to determine the presence of Ni_3B.
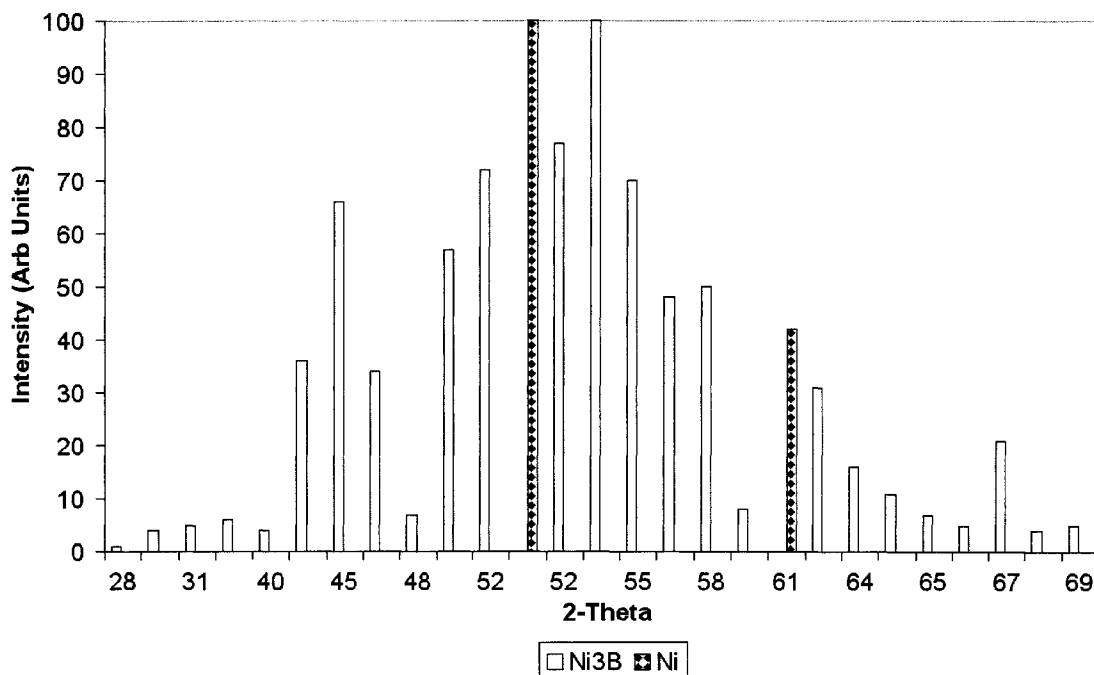
Figure B.2: Comparison of XRD patterns of Ni_3B and Ni.

Figure B.3 shows a plot of the peaks for Ni and Ni_2B. The high-intensity Ni peak at 52.2°

could obscure the Ni_2B peak located at 53.9°. The medium-intensity Ni peak, located at

61°, is free from overlap with any Ni_2B peaks, allowing the identification of Ni

separately from Ni_2B.

187
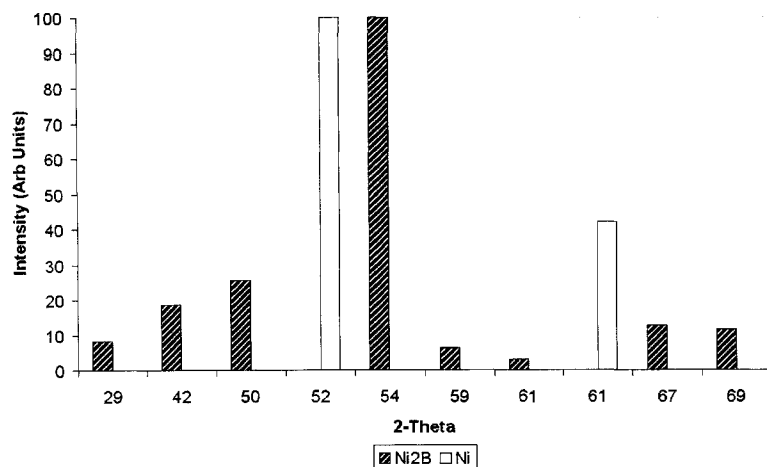
Figure B.3: Comparison of XRD patterns of Ni₂B and Ni.

When the XRD peaks for Ni_4B_3 and Ni are compared, it can be seen that there is a near

overlap of the medium-intensity, Ni peak at a 2-theta value of 61 °. The lesser peak for

Ni, at 52.2 °, can be resolved from the surrounding Ni_4B_3 peaks at 51.6 ° and 54.3 °.
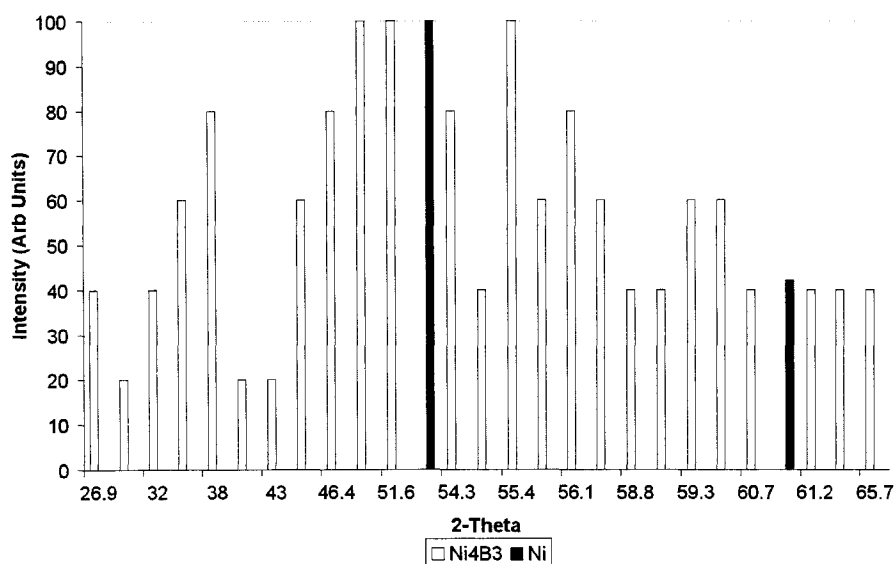
Figure B.4: Comparison of XRD patterns of Ni₄B₃ and Ni.

188

When comparing the XRD patterns for Ni_2B and Ni_4B_3, it can be seen that there are enough peaks that are separated to facilitate the judgement of either substance being present. For example, there is an area of Ni_4B_3 peaks, which extends from a 2-theta value of 55° to 58.8°. This region does not contain any Ni_2B peaks. If a sample does not contain Ni_4B_3, the presence of Ni_2B will be simple to ascertain. If a sample contains both Ni_4B_3 and Ni_2B, it is almost impossible to determine if Ni_2B is present. The reason for this is that the Ni_4B_3 peaks obscure the Ni_2B peaks. It may be possible to distinguish between the high-intensity, Ni_2B peak at 53.8° and the medium-intensity, Ni_4B_3 peak at 54.3°.
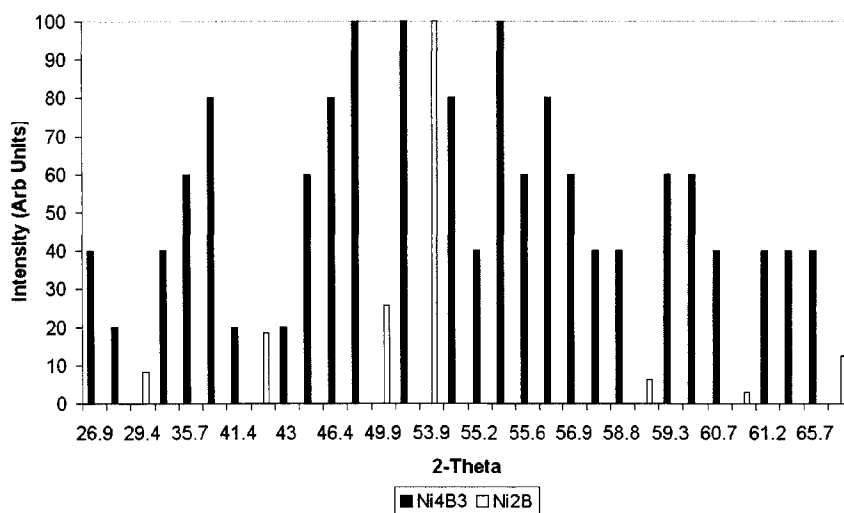
Figure B.5: Comparison of XRD patterns of Ni_4B_3 and Ni_2B.

When comparing the 2-theta values for Ni_4B_3 and Ni_3B, there are several areas, which allow the separation of these two compounds. There are three, medium-intensity Ni_4B_3 peaks located between 55.2° and 56.1° that are not obscured by any Ni_3B peaks.

189

For Ni3B, there is a peak located at a 2-theta value of 52.4°, which has other Ni3B peaks

adjacent to it. The surrounding Ni4B3 peaks at 51.6° and 54.3° peaks do not obscure this

peak.
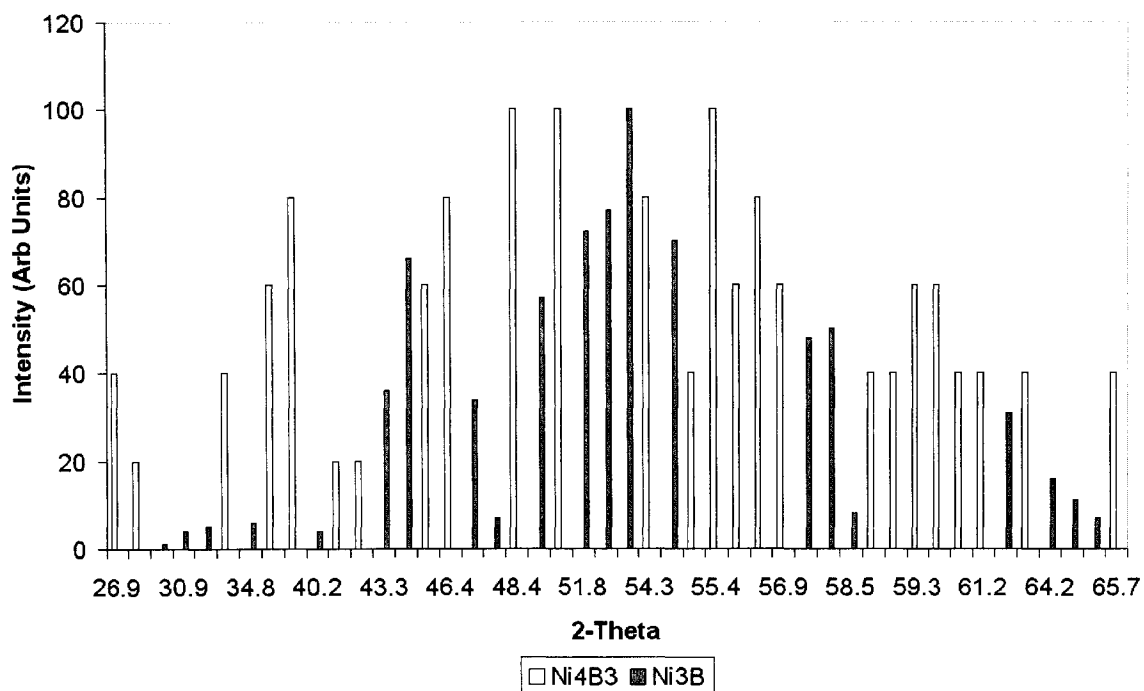
Figure B.6: Comparison of XRD patterns of Ni4B3 and Ni3B.

The most significant issue with XRD is that it can be extremely difficult to resolve the

peaks of different substances, which are located at similar 2-theta values. Therefore,

XRD is not a method that can definitively determine if a compound is present in a sample

where a compound's peaks are significantly overlapped or obscured by the peaks of

another compound.

190

C.0 XRD Cards.

191

PDF#00-006-0567(RDB): QM=Indexed(I); d=(Unknown); I=Diffractometer	PDF Card

Boron Nickel

NiB

Radiation=CuKα	Lambda=1.5418	Filter=Ni
Calibration=	2T=28.136-75.082	I/Ic(RIR)=I
Ref: American Electro Metal Company, Yonkers, New York, USA.		
Private Communication		

Orthorhombic - Powder Diffraction, Cmcm (63)	Z=4	mp=
CELL: 2.936 x 7.38 x 2.968 <90.0 x 90.0 x 90.0>	P.S=oC8.00	
Density(c)=7.179 Density(m)= Mwt=69.51 Vol=64.31	F(10)=27.2(0.037,10/0)	
Ref: Ibid.		

Unit Cell: Space group from Blum, J. Phys. Rad., 13 431 (1952), who also reports: a=2.925, b=7.396, c=2.966. Unit Cell Data Source: Powder Diffraction.

Strong Lines: 2.31/X 2.72/8 1.88/7 2.01/4 1.85/4 1.59/2 1.48/2 3.68/2

10 Lines, Wavelength to Compute Theta = 1.78899Å(Co), I%-Type = (Unknown)

#	d(Å)	I(f)	h	k	l	2-Theta	Theta	1/(2d)	#	d(Å)	I(f)	h	k	l	2-Theta	Theta	1/(2d)
1	3.6800	16.0	0	2	0	28.136	14.068	0.1359	6	1.8450	35.0	0	4	0	58.002	29.001	0.2710
2	2.7200	75.0	1	1	0	38.399	19.200	0.1838	7	1.5930	20.0	1	3	1	68.321	34.161	0.3139
3	2.3100	100.0	0	2	1	45.564	22.782	0.2165	8	1.5680	10.0	0	4	1	69.566	34.783	0.3189
4	2.0100	40.0	1	1	1	52.850	26.425	0.2488	9	1.4840	18.0	0	0	2	74.136	37.068	0.3369
5	1.8850	70.0	1	3	0	56.658	28.329	0.2653	10	1.4680	12.0	2	0	0	75.082	37.541	0.3406

192

PDF#03-065-2409(RDB){Deleted}: QM=Indexed(I); d=Calculated; I=Calculated	PDF Card

Boron Nickel

BNi₃

Radiation=CuKα1	Lambda=1.5405999	Filter=
Calibration=	2T=28.309-180.000	I/Ic(RIR)=1.54
Ref: S.Rundqvist		
Acta Chem. Scand., v12 p658 (1958)		

Orthorhombic - (Unknown), Pbnm (62)		Z=4	mp=
CELL: 4.389 x 5.211 x 6.619 <90.0 x 90.0 x 90.0>		P.S=oP16.00	
Density(c)=8.201 Density(m)=	Mwt=186.91 Vol=151.38	F(30)=999.9(0.000,30/0)	
Ref: Ibid.			

Deleted Or Rejected By: Delete: same as 01-089-3822. Temperature Factor: IB=Ni,B. Minor Warning: No e.s.d reported/abstracted on the cell dimension. No Rfactor reported/abstracted. NIST Collection Code: N AL0691.

Strong Lines: 1.97/X 2.05/8 2.02/7 1.93/7 2.36/7 2.12/6 1.86/5 1.84/4

148 Lines, Wavelength to Compute Theta = 1.78899Å(Co), I%-Type = Peak Height

#	d(Å)	I(f)	h	k	l	2-Theta	#	d(Å)	I(f)	h	k	l	2-Theta	#	d(Å)	I(f)	h	k	l	2-Theta
1	3.6579	0.6	1	0	1	28.309	37	1.3032	0.5	1	3	3	86.686	73	1.0394	1.0	2	2	5	118.762
2	3.3569	0.3	1	1	0	30.908	38	1.2960	14.0	3	1	2	87.288	74	1.0238	1.4	1	3	5	121.775
3	3.3095	4.7	0	0	2	31.362	39	1.2807	0.2	2	1	4	88.603	75	1.0238	1.4	0	4	4	121.775
4	2.9939	5.6	1	1	1	34.768	40	1.2782	0.2	0	4	1	88.821	76	1.0213	1.8	4	1	2	122.289
5	2.6055	2.0	0	2	0	40.157	41	1.2757	0.1	3	2	0	89.047	77	1.0159	0.1	0	2	6	123.413
6	2.4244	27.9	0	2	1	43.302	42	1.2674	2.3	1	0	5	89.784	78	1.0140	0.1	1	5	0	123.804
7	2.3568	67.2	1	1	2	44.611	43	1.2595	3.0	2	3	2	90.502	79	1.0112	0.1	4	2	0	124.393
8	2.2405	32.0	1	2	0	47.062	44	1.2526	2.7	3	2	1	91.140	80	1.0103	0.3	3	2	4	124.596
9	2.1945	8.1	2	0	0	48.109	45	1.2489	13.2	1	4	0	91.488	81	1.0023	1.2	1	5	1	126.361
10	2.1222	63.0	1	2	1	49.858	46	1.2315	3.3	1	1	5	93.162	82	0.9996	1.9	4	2	1	126.970
11	2.0472	83.3	0	2	2	51.817	47	1.2272	3.4	1	4	1	93.583	83	0.9989	1.4	2	4	3	127.151
12	2.0225	74.9	2	1	0	52.499	48	1.2193	2.2	3	0	3	94.380	84	0.9968	1.3	1	4	4	127.617
13	1.9713	100.0	1	0	3	53.971	49	1.2122	2.4	0	4	2	95.106	85	0.9897	0.6	1	2	6	129.326
14	1.9342	72.8	2	1	1	55.092	50	1.1903	2.2	3	2	2	97.440	86	0.9856	0.2	2	0	6	130.332
15	1.8553	51.6	1	2	2	57.649	51	1.1872	14.0	3	1	3	97.777	87	0.9729	0.9	3	4	0	133.673
16	1.8438	42.8	1	1	3	58.044	52	1.1802	6.4	0	2	5	98.562	88	0.9695	3.1	1	5	2	134.624
17	1.8290	4.1	2	0	2	58.560	53	1.1784	3.3	2	2	4	98.768	89	0.9685	3.4	2	1	6	134.923
18	1.7257	30.3	2	1	2	62.440	54	1.1685	1.8	1	4	2	99.908	90	0.9671	6.3	4	2	2	135.315
19	1.6838	16.6	0	2	3	64.180	55	1.1589	24.7	2	3	3	101.034	91	0.9646	6.7	3	1	5	136.032
20	1.6785	9.7	2	2	0	64.406	56	1.1558	14.4	1	3	4	101.412	92	0.9626	2.7	3	4	1	136.641
21	1.6547	7.5	0	0	4	65.444	57	1.1397	10.0	1	2	5	103.411	93	0.9493	1.5	2	3	5	140.879
22	1.6270	2.2	2	2	1	66.705	58	1.1218	9.9	0	4	3	105.762	94	0.9414	0.1	2	5	0	143.665
23	1.6151	28.8	1	3	0	67.260	59	1.1190	16.2	3	3	0	106.143	95	0.9320	1.8	2	5	1	147.361
24	1.5720	1.4	1	2	3	69.361	60	1.1076	11.0	2	1	5	107.719	96	0.9285	1.3	0	4	5	148.875
25	1.5691	4.9	1	3	1	69.511	61	1.1043	6.2	3	2	3	108.187	97	0.9269	1.1	3	3	4	149.592
26	1.4970	2.2	2	2	2	73.389	62	1.1043	6.2	2	4	1	108.187	98	0.9244	1.9	1	0	7	150.790
27	1.4909	1.4	2	1	3	73.737	63	1.1032	6.2	3	3	1	108.356	99	0.9214	0.9	2	2	6	152.261
28	1.4842	3.9	1	1	4	74.123	64	1.1032	6.2	0	0	6	108.356	100	0.9214	0.9	1	5	3	152.261
29	1.4515	0.4	1	3	2	76.087	65	1.0972	5.1	4	0	0	109.217	101	0.9193	1.2	4	2	3	153.330
30	1.4285	0.4	3	0	1	77.536	66	1.0869	0.3	1	4	3	110.776	102	0.9186	1.3	4	3	1	153.704
31	1.3968	4.1	0	2	4	79.638	67	1.0737	2.6	4	1	0	112.835	103	0.9186	1.3	3	2	5	153.704
32	1.3777	2.5	3	1	1	80.973	68	1.0726	2.1	3	1	4	113.017	104	0.9145	0.9	4	0	4	156.003
33	1.3359	1.1	2	2	3	84.074	69	1.0600	1.5	4	1	1	115.096	105	0.9110	3.1	1	3	6	158.185
34	1.3311	0.7	1	2	4	84.446	70	1.0600	1.5	3	3	2	115.096	106	0.9084	2.8	1	4	5	159.904
35	1.3212	0.1	2	0	4	85.222	71	1.0516	0.4	2	3	4	116.557	107	0.9055	4.3	2	5	2	162.113
36	1.3032	0.5	0	4	0	86.686	72	1.0480	0.2	1	1	6	117.189	108	0.9007	0.1	4	1	4	166.532

193

Boron Nickel

BNi3

#	d(Å)	I(f)	h	k	l	2-Theta	#	d(Å)	I(f)	h	k	l	2-Theta	#	d(Å)	I(f)	h	k	l	2-Theta
109	0.8932	0.3	4	3	2	—	123	0.8552	3.2	4	3	3	—	137	0.8222	3.0	3	5	2	—
110	0.8902	0.4	3	4	3	—	124	0.8488	0.7	3	5	0	—	138	0.8183	0.8	2	5	4	—
111	0.8888	0.2	0	2	7	—	125	0.8450	0.1	1	6	1	—	139	0.8156	4.8	1	3	7	—
112	0.8712	0.1	1	2	7	—	126	0.8419	1.6	3	5	1	—	140	0.8156	4.8	5	0	3	—
113	0.8702	0.1	5	0	1	—	127	0.8419	1.6	0	4	6	—	141	0.8135	3.4	4	4	2	—
114	0.8685	1.8	0	6	0	—	128	0.8401	1.2	0	6	2	—	142	0.8092	0.1	4	3	4	—
115	0.8685	1.8	3	1	6	—	129	0.8387	0.4	3	4	4	—	143	0.8076	0.5	2	6	0	—
116	0.8659	1.3	5	1	0	—	130	0.8374	0.2	5	1	2	—	144	0.8068	2.0	5	2	2	—
117	0.8659	1.3	2	5	3	—	131	0.8339	0.5	4	1	6	—	145	0.8050	2.2	1	5	5	—
118	0.8646	0.5	1	5	4	—	132	0.8339	0.5	3	2	6	—	146	0.8036	3.1	4	2	5	—
119	0.8629	1.2	4	2	4	—	133	0.8319	1.4	5	2	0	—	147	0.8036	3.1	1	1	8	—
120	0.8611	1.4	0	6	1	—	134	0.8268	3.1	1	4	6	—	148	0.8016	1.5	2	6	1	—
121	0.8566	0.8	2	1	7	—	135	0.8254	3.2	5	2	1	—							
122	0.8552	3.2	3	3	5	—	136	0.8254	3.2	1	6	2	—							

194

PDF#00-048-1223(RDB): QM=Star(S); d=Diffractometer; I=Diffractometer	PDF Card

Boron Nickel
BNi₃

Radiation=CuKα1	Lambda=1.54056	Filter=Graph
Calibration=Internal(SI)	2T=28.277-108.975	I/Ic(RIR)=S
Ref: Grier, D., McCarthy, G., North Dakota State Univ., Fargo, ND, USA. ICDD Grant-In-Aid (1993)		

Orthorhombic - Powder Diffraction, Pnma (62)		Z=4	mp=
CELL: 5.2112 x 6.62 x 4.3955 <90.0 x 90.0 x 90.0>		P.S=oP16.00	
Density(c)=8.187 Density(m)= Mwt=186.91	Vol=151.64	F(30)=119(0.008,30/0)	
Ref: Ibid.			

General Comments: Average relative standard deviation in Intensity of the 10 strongest reflections for 3 specimen mounts = 11.1%. Subject to preferred orientation. Validated with a calculated pattern. Major nickel impurity present. Additional Patterns: To replace 00-019-0834. Color: Silvery gray metallic. Sample Source or Locality: Sample purchased from Cerac, Inc., Milwaukee, Wisconsin, USA, 99%. Unit Cell Data Source: Powder Diffraction.

Color: Silvery gray metallic

Strong Lines: 1.97/X 2.03/8 2.05/7 1.94/7 2.36/7 2.12/6 1.84/5 1.86/5

61 Lines, Wavelength to Compute Theta = 1.78899Å(Co), I%-Type = (Unknown)

#	d(A)	I(f)	h	k	l	2-Theta	Theta	1/(2d)	#	d(A)	I(f)	h	k	l	2-Theta	Theta	1/(2d)
1	3.6620	1.0	0	1	1	28.277	14.138	0.1365	32	1.3791	3.0	1	1	3	80.873	40.437	0.3626
2	3.3580	4.0	1	0	1	30.898	15.449	0.1489	33	1.3366	1.0	2	3	2	84.016	42.008	0.3741
3	3.3140	5.0	0	2	0	31.318	15.659	0.1509	34	1.3348	1.0	3	1	2	84.155	42.077	0.3746
4	2.9940	6.0	1	1	1	34.767	17.383	0.1670	35	1.3314	1.0	2	4	1	84.419	42.210	0.3755
5	2.6050	4.0	2	0	0	40.165	20.083	0.1919	36	1.3031	2.0	4	0	0	86.697	43.349	0.3837
6	2.4230	36.0	2	1	0	43.329	21.664	0.2064	37	1.3031	2.0	3	3	1	86.697	43.349	0.3837
7	2.3580	66.0	1	2	1	44.586	22.293	0.2120	38	1.2975	13.0	1	2	3	87.165	43.583	0.3854
8	2.2410	34.0	2	0	1	47.050	23.525	0.2231	39	1.2678	4.0	0	5	1	89.748	44.874	0.3944
9	2.1970	7.0	0	0	2	48.051	24.026	0.2276	40	1.2601	5.0	3	2	2	90.447	45.224	0.3968
10	2.1230	57.0	2	1	1	49.838	24.919	0.2355	41	1.2538	5.0	2	1	3	91.029	45.514	0.3988
11	2.0480	72.0	2	2	0	51.795	25.898	0.2441	42	1.2490	10.0	4	0	1	91.478	45.739	0.4003
12	2.0250	77.0	1	0	2	52.428	26.214	0.2469	43	1.2318	4.0	1	5	1	93.132	46.566	0.4059
13	1.9719	100.0	0	3	1	53.952	26.976	0.2536	44	1.2274	4.0	4	1	1	93.567	46.784	0.4074
14	1.9366	70.0	1	1	2	55.018	27.509	0.2582	45	1.2205	3.0	0	3	3	94.259	47.129	0.4097
15	1.8559	48.0	2	2	1	57.629	28.814	0.2694	46	1.2119	3.0	4	2	0	95.138	47.569	0.4126
16	1.8447	50.0	1	3	1	58.012	29.006	0.2710	47	1.1914	4.0	2	2	3	97.318	48.659	0.4197
17	1.8304	8.0	0	2	2	58.509	29.254	0.2732	48	1.1885	14.0	1	3	3	97.637	48.818	0.4207
18	1.7273	31.0	1	2	2	62.377	31.189	0.2895	49	1.1806	6.0	2	5	0	98.517	49.258	0.4235
19	1.6838	16.0	2	3	0	64.178	32.089	0.2969	50	1.1686	3.0	4	2	1	99.893	49.946	0.4279
20	1.6795	11.0	2	0	2	64.362	32.181	0.2977	51	1.1595	20.0	3	3	2	100.968	50.484	0.4312
21	1.6550	7.0	0	4	0	65.433	32.716	0.3021	52	1.1562	14.0	3	4	1	101.366	50.683	0.4325
22	1.6283	5.0	2	1	2	66.644	33.322	0.3071	53	1.1400	9.0	2	5	1	103.376	51.688	0.4386
23	1.6155	21.0	3	0	1	67.242	33.621	0.3095	54	1.1218	13.0	4	3	0	105.760	52.880	0.4457
24	1.5723	4.0	2	3	1	69.348	34.674	0.3180	55	1.1200	14.0	3	0	3	106.004	53.002	0.4464
25	1.5698	5.0	3	1	1	69.475	34.737	0.3185	56	1.1082	9.0	1	5	2	107.639	53.819	0.4512
26	1.4980	3.0	2	2	2	73.329	36.664	0.3338	57	1.1051	7.0	2	3	3	108.079	54.040	0.4524
27	1.4920	2.0	1	3	2	73.672	36.836	0.3351	58	1.1051	7.0	4	1	2	108.079	54.040	0.4524
28	1.4846	4.0	1	4	1	74.101	37.050	0.3368	59	1.1041	6.0	3	1	3	108.223	54.111	0.4529
29	1.4518	0.0	3	2	1	76.068	38.034	0.3444	60	1.1034	6.0	0	6	0	108.323	54.162	0.4531
30	1.4301	1.0	0	1	3	77.434	38.717	0.3496	61	1.0989	5.0	0	0	4	108.975	54.488	0.4550
31	1.3970	5.0	2	4	0	79.628	39.814	0.3579									

195

PDF#00-048-1222(RDB): QM=Star(S); d=Diffractometer; I=Diffractometer		PDF Card

Boron Nickel

BNi$_2$

Radiation=CuKα1	Lambda=1.54056	Filter=Graph
Calibration=Internal(SI)	2T=29.366-162.116	I/Ic(RIR)=S

Ref: Parks, J., McCarthy, G., North Dakota State Univ., Fargo, ND, USA.
    ICDD Grant-In-Aid (1993)

Tetragonal - Powder Diffraction, I4/mcm (140)			Z=4	mp=
CELL: 4.9905 x 4.9905 x 4.2474 <90.0 x 90.0 x 90.0>			P.S=tI12.00	
Density(c)=8.05	Density(m)=	Mwt=128.21	Vol=105.78	F(25)=118.7(0.007,28/0)

Ref: Ibid.

General Comments: Average relative standard deviation in intensity of the 10 strongest reflections for 3 specimen mounts = 30.9%. Subject to preferred orientation. Several unknown trace impurity reflections present in sample. Validated by a calculated pattern. Additional Patterns: To replace 00-025-0576. Sample Source or Locality: Sample obtained from Cerac, Inc., Milwaukee, Wisconsin, USA. Unit Cell Data Source: Powder Diffraction.

Strong Lines: 1.98/X 2.49/3 2.12/2 1.62/1 1.82/1 1.20/1 3.53/1 1.58/1

25 Lines, Wavelength to Compute Theta = 1.78899Å(Co), I%-Type = Peak Height

#	d(Å)	I(f)	h	k	l	2-Theta	Theta	1/(2d)	#	d(Å)	I(f)	h	k	l	2-Theta	Theta	1/(2d)
1	3.5290	11.0	1	1	0	29.366	14.683	0.1417	14	1.1640	10.0	4	1	1	100.433	50.216	0.4296
2	2.4950	31.0	2	0	0	42.018	21.009	0.2004	15	1.1159	1.0	4	2	0	106.565	53.282	0.4481
3	2.1240	22.0	0	0	2	49.813	24.906	0.2354	16	1.0756	1.0	4	0	2	112.532	56.266	0.4649
4	1.9757	100.0	2	1	1	53.840	26.920	0.2531	17	1.0618	2.0	0	0	4	114.796	57.398	0.4709
5	1.8196	12.0	1	1	2	58.890	29.445	0.2748	18	1.0290	6.0	3	3	2	120.751	60.376	0.4859
6	1.7644	5.0	2	2	0	60.924	30.462	0.2834	19	1.0169	0.0	1	1	4	123.195	61.598	0.4917
7	1.6170	13.0	2	0	2	67.171	33.586	0.3092	20	0.9878	0.0	4	2	2	129.783	64.892	0.5062
8	1.5784	11.0	3	1	0	69.042	34.521	0.3168	21	0.9787	1.0	5	1	0	132.112	66.056	0.5109
9	1.3572	1.0	2	2	2	82.459	41.229	0.3684	22	0.9771	1.0	2	0	4	132.553	66.276	0.5117
10	1.2666	4.0	3	1	2	89.856	44.928	0.3948	23	0.9202	6.0	4	1	3	152.851	76.426	0.5434
11	1.2475	2.0	4	0	0	91.620	45.810	0.4008	24	0.9096	1.0	2	2	4	159.087	79.544	0.5497
12	1.1955	11.0	2	1	3	96.873	48.436	0.4182	25	0.9055	4.0	5	2	1	162.116	81.058	0.5522
13	1.1763	4.0	3	3	0	99.004	49.502	0.4251									

196

PDF#03-065-2691(RDB): QM=Indexed(I); d=Calculated; I=Calculated		PDF Card

Boron Nickel

BNI₂

Radiation=CuKα1	Lambda=1.5405999	Filter=
Calibration=	2T=29.370-180.000	I/Ic(RIR)=6.05
Ref: T.Bjurstrom		
Ark. Kemi, Mineral. Geol., v11A p5 (1933)		

Tetragonal - (Unknown), I4/mcm (140)		Z=4	mp=
CELL: 4.99 x 4.99 x 4.245 <90.0 x 90.0 x 90.0>		P.S=tI12.00	
Density(c)=8.057 Density(m)= Mwt=128.21 Vol=105.70		F(30)=999.9(0.000,32/0)	
Ref: Ibid.			

Additional Patterns: See PDF 01-082-1697. Temperature Factor: IB=Ni,B. Minor Warning: No e.s.d reported/abstracted on the cell dimension. No Rfactor reported/abstracted. NIST Collection Code: N AL2236.

Strong Lines: 1.98/X 2.12/3 2.49/2 1.62/1 1.58/1 1.20/1 1.16/1 3.53/1

33 Lines, Wavelength to Compute Theta = 1.78899Å(Co), I%-Type = Peak Height

#	d(Å)	I(f)	h	k	l	2-Theta	Theta	1/(2d)	#	d(Å)	I(f)	h	k	l	2-Theta	Theta	1/(2d)
1	3.5285	8.4	1	1	0	29.370	14.685	0.1417	18	1.0612	1.6	0	0	4	114.889	57.444	0.4711
2	2.4950	19.1	2	0	0	42.018	21.009	0.2004	19	1.0288	5.7	3	3	2	120.799	60.399	0.4860
3	2.1225	25.6	0	0	2	49.850	24.925	0.2356	20	1.0163	0.1	1	1	4	123.325	61.662	0.4920
4	1.9753	100.0	2	1	1	53.853	26.926	0.2531	21	0.9876	0.2	4	2	2	129.833	64.916	0.5063
5	1.8188	6.3	1	1	2	58.919	29.459	0.2749	22	0.9786	0.1	5	1	0	132.139	66.069	0.5109
6	1.7642	2.9	2	2	0	60.931	30.465	0.2834	23	0.9766	0.8	2	0	4	132.682	66.341	0.5120
7	1.6167	12.9	2	0	2	67.187	33.594	0.3093	24	0.9197	3.7	4	1	3	153.096	76.548	0.5436
8	1.5780	11.4	3	1	0	69.063	34.532	0.3169	25	0.9094	0.4	2	2	4	159.227	79.613	0.5498
9	1.3567	0.6	2	2	2	82.493	41.246	0.3685	26	0.9053	3.5	5	2	1	162.275	81.138	0.5523
10	1.3158	0.1	3	2	1	85.657	42.828	0.3800	27	0.8887	0.7	5	1	2	—		
11	1.2664	4.8	3	1	2	89.879	44.939	0.3948	28	0.8821	0.2	4	4	0	—		
12	1.2475	1.1	4	0	0	91.620	45.810	0.4008	29	0.8806	2.0	3	1	4	—		
13	1.1950	11.1	2	1	3	96.924	48.462	0.4184	30	0.8558	1.0	5	3	0	—		
14	1.1761	4.0	3	3	0	99.022	49.511	0.4251	31	0.8317	1.5	6	0	0	—		
15	1.1639	9.9	4	1	1	100.447	50.223	0.4296	32	0.8146	0.1	4	4	2	—		
16	1.1158	0.7	4	2	0	106.578	53.289	0.4481	33	0.8083	0.4	4	0	4	—		
17	1.0755	1.9	4	0	2	112.549	56.275	0.4649									

197

PDF#00-012-0416(RDB): QM=Indexed(I); d=Guinier; I=Film/Visual

Boron Nickel

Ni₄B₃

Radiation=CrKα	Lambda=2.2909	Filter=
Calibration=	2T=26.869-65.701	I/Ic(RIR)=I
Ref: Rundqvist.		
Acta Chem. Scand., v13 p1193 (1959)		

Monoclinic - Powder Diffraction, C2/c (15)	Z=4	mp=
CELL: 6.43 x 4.882 x 7.818 <90.0 x 103.3 x 90.0>	P.S=mC28.00	
Density(c)=7.432 Density(m)= Mwt=267.23 Vol=238.83	F(25)=18.6(0.048,28/0)	
Ref: Ibid.		

General Comments: Exists also in an orthorhombic modification. Unit Cell Data Source: Powder Diffraction.

Strong Lines: 2.05/X 2.18/X 1.92/X 2.27/8 2.74/8 1.90/8 1.96/8 2.92/6

25 Lines, Wavelength to Compute Theta = 1.78899Å(Co), I%-Type = (Unknown)

#	d(Å)	I(f)	h	k	l	2-Theta	Theta	1/(2d)	#	d(Å)	I(f)	h	k	l	2-Theta	Theta	1/(2d)
1	3.8500	40.0	1	1	0	26.869	13.435	0.1299	14	1.9230	100.0	2	2	0	55.441	27.720	0.2600
2	3.8000	20.0	0	0	2	27.230	13.615	0.1316	15	1.9170	60.0	3	1	0	55.629	27.815	0.2608
3	3.2500	40.0	1	1	1	31.951	15.976	0.1538	16	1.9010	80.0	0	0	4	56.139	28.069	0.2630
4	2.9180	60.0	-1	1	2	35.702	17.851	0.1714	17	1.8790	60.0	-3	1	2	56.855	28.428	0.2661
5	2.7450	80.0	-2	0	2	38.036	19.018	0.1821	18	1.8230	40.0	-2	2	2	58.770	29.385	0.2743
6	2.5300	20.0	1	1	2	41.410	20.705	0.1976	19	1.8210	40.0	-2	0	4	58.840	29.420	0.2746
7	2.4400	20.0	0	2	0	43.012	21.506	0.2049	20	1.8090	60.0	-1	1	4	59.270	29.635	0.2764
8	2.3220	60.0	0	2	1	45.316	22.658	0.2153	21	1.8050	60.0	2	2	1	59.414	29.707	0.2770
9	2.2700	80.0	-1	1	3	46.414	23.207	0.2203	22	1.7710	40.0	3	1	1	60.673	30.337	0.2823
10	2.1820	100.0	2	0	2	48.402	24.201	0.2291	23	1.7570	40.0	0	2	3	61.208	30.604	0.2846
11	2.0540	100.0	0	2	2	51.633	25.816	0.2434	24	1.7130	40.0	-3	1	3	62.957	31.479	0.2919
12	1.9600	80.0	-3	1	1	54.307	27.153	0.2551	25	1.6490	40.0	-2	2	3	65.701	32.850	0.3032
13	1.9310	40.0	-2	2	1	55.191	27.596	0.2589									

198

Boron Nickel

Ni_4B_3

Radiation=CrKα	Lambda=2.2909	Filter=
Calibration=	2T=17.234-65.566	I/Ic(RIR)=I
Ref: Rundqvist.		
Acta Chem. Scand., v13 p1193 (1959)		

Orthorhombic - Powder Diffraction, Pnma (62)	Z=4	mp=
CELL: 11.948 x 2.9791 x 6.5637 <90.0 x 90.0 x 90.0>	P.S=oP28.00	
Density(c)=7.597 Density(m)= Mwt=267.23 Vol=233.63	F(30)=33.9(0.024,37/0)	
Ref: Ibid.		

General Comments: Exists also in a monoclinic modification. Unit Cell Data Source: Powder Diffraction.

Strong Lines: 2.07/X 1.93/8 2.25/8 1.76/8 2.47/8 1.92/8 1.79/8 1.91/8

30 Lines, Wavelength to Compute Theta = 1.78899Å(Co), I%-Type = (Unknown)

#	d(Å)	I(f)	h	k	l	2-Theta	Theta	1/(2d)	#	d(Å)	I(f)	h	k	l	2-Theta	Theta	1/(2d)
1	5.9700	20.0	2	0	0	17.234	8.617	0.0838	16	2.1100	80.0	4	1	0	50.166	25.083	0.2370
2	4.4200	20.0	2	0	1	23.352	11.676	0.1131	17	2.0700	100.0	2	1	2	51.205	25.602	0.2415
3	3.2800	20.0	0	0	2	31.651	15.826	0.1524	18	2.0550	20.0	2	0	3	51.606	25.803	0.2433
4	3.1700	40.0	1	0	2	32.780	16.390	0.1577	19	2.0080	60.0	4	1	1	52.906	26.453	0.2490
5	2.9900	60.0	4	0	0	34.815	17.407	0.1672	20	1.9910	40.0	6	0	0	53.394	26.697	0.2511
6	2.8760	60.0	2	0	2	36.241	18.121	0.1739	21	1.9310	80.0	5	0	2	55.191	27.596	0.2589
7	2.7180	20.0	4	0	1	38.428	19.214	0.1840	22	1.9180	80.0	3	0	3	55.598	27.799	0.2607
8	2.7130	40.0	0	1	1	38.502	19.251	0.1843	23	1.9060	80.0	6	0	1	55.978	27.989	0.2623
9	2.6450	40.0	1	1	1	39.532	19.766	0.1890	24	1.7930	80.0	5	1	1	59.852	29.926	0.2789
10	2.5340	60.0	3	0	2	41.341	20.671	0.1973	25	1.7740	40.0	4	1	2	60.560	30.280	0.2818
11	2.4710	80.0	2	1	1	42.446	21.223	0.2023	26	1.7640	80.0	0	1	3	60.939	30.470	0.2834
12	2.2490	80.0	5	0	1	46.873	23.436	0.2223	27	1.7440	60.0	1	1	3	61.714	30.857	0.2867
13	2.2100	40.0	4	0	2	47.751	23.875	0.2262	28	1.7020	60.0	6	0	2	63.411	31.706	0.2938
14	2.1690	60.0	1	1	2	48.711	24.356	0.2305	29	1.6910	40.0	2	1	3	63.872	31.936	0.2957
15	2.1520	60.0	1	0	3	49.121	24.561	0.2323	30	1.6520	60.0	7	0	1	65.566	32.783	0.3027

199

PDF#00-004-0850(RDB): QM=Star(S); d=(Unknown); I=Diffractometer	PDF Card

Nickel, syn

NI

Radiation=CuKα1	Lambda=1.5405	Filter=NI
Calibration=	2T=52.179-180.000	I/Ic(RIR)=S
Ref: Swanson, Tatge.		
Natl. Bur. Stand. (U.S.), Circ. 539, vl p13 (1953)		CAS#7440-02-0

Cubic - Powder Diffraction, Fm3̄m (225)   Z=4   mp=

CELL: 3.5238 x 3.5238 x 3.5238 <90.0 x 90.0 x 90.0>   P.S=cF4.00

Density(c)=8.911   Density(m)=   Mwt=58.7   Vol=43.76   F(8)=87.9(0.011,8/0)

Ref: Ibid.

Additional Patterns: See PDF 01-087-0712. Analysis: Spectrographic analysis show <0.01% each of Mg, Si and Ca. Color: White. Sample Source or Locality: Sample obtained from Johnson Matthey Company, Ltd. Temperature of Data Collection: Pattern taken at 26 C. Unit Cell Data Source: Powder Diffraction.

Color: White

Strong Lines: 2.03/X 1.76/4 1.25/2 1.06/2 0.79/2 0.81/1 1.02/1

8 Lines, Wavelength to Compute Theta = 1.78899Å(Co), I%-Type = (Unknown)

#	d(Å)	I(f)	h	k	l	2-Theta	Theta	1/(2d)	#	d(Å)	I(f)	h	k	l	2-Theta	Theta	1/(2d)
1	2.0340	100.0	1	1	1	52.179	26.089	0.2458	5	1.0172	7.0	2	2	2	123.133	61.566	0.4915
2	1.7620	42.0	2	0	0	61.016	30.508	0.2838	6	0.8810	4.0	4	0	0	—		
3	1.2460	21.0	2	2	0	91.762	45.881	0.4013	7	0.8084	14.0	3	3	1	—		
4	1.0624	20.0	3	1	1	114.695	57.347	0.4706	8	0.7880	15.0	4	2	0	—		

200

PDF#01-071-4918(RDB): QM=Indexed(I); d=Calculated; I=Calculated	PDF Card

Magnetite

Fe₃O₄

Radiation=CuKα1	Lambda=1.5405999	Filter=
Calibration=	2T=21.257-180.000	I/Ic(RIR)=4.92

Ref: Holgersson, S.
   Lunds Univ. Arsskr., Avd. 2, v23 p1 (1927)

Cubic - (Unknown), Fd3̄m (227)   Z=8   mp=

CELL: 8.4 x 8.4 x 8.4 <90.0 x 90.0 x 90.0>   P.S=cF56.00

Density(c)=5.189   Density(m)=   Mwt=231.54   Vol=592.70   F(30)=999.9(0,30/0)

Ref: Ibid.

Calculated Pattern Original Remarks: MDF 19-629. Cell of sample from Nordmarken, Vermland, Sweden: 8.412. Cell synthetic Fe2 Fe O4: 8.417. ICSD Collection Code: 56120. Sample Source or Locality: Specimen from Dalarna, Sweden. ANX: AB2X4. Wyckoff Sequence: e d a (FD3-MS). Minor Warning: No R value given in the paper.

Strong Lines: 2.53/X 1.48/3 2.97/3 1.62/3 2.10/2 4.85/1 1.09/1 1.71/1

34 Lines, Wavelength to Compute Theta = 1.78899Å(Co), I%-Type = Peak Height

#	d(Å)	I(f)	h	k	l	2-Theta	Theta	1/(2d)	#	d(Å)	I(f)	h	k	l	2-Theta	Theta	1/(2d)
1	4.8497	10.2	1	1	1	21.257	10.629	0.1031	18	1.0936	8.3	7	3	1	109.759	54.879	0.4572
2	2.9699	29.7	2	2	0	35.058	17.529	0.1684	19	1.0500	3.1	8	0	0	116.838	58.419	0.4762
3	2.5327	100.0	3	1	1	41.364	20.682	0.1974	20	1.0262	0.1	7	3	3	121.300	60.650	0.4872
4	2.4249	7.7	2	2	2	43.294	21.647	0.2062	21	1.0187	0.1	6	4	4	122.832	61.416	0.4908
5	2.1000	20.4	4	0	0	50.422	25.211	0.2381	22	0.9899	1.0	8	2	2	129.265	64.632	0.5051
6	1.9271	0.6	3	3	1	55.313	27.656	0.2595	23	0.9699	4.2	7	5	1	134.502	67.251	0.5155
7	1.7146	8.1	4	2	2	62.890	31.445	0.2916	24	0.9635	0.9	6	6	2	136.354	68.177	0.5189
8	1.6166	26.1	5	1	1	67.191	33.595	0.3093	25	0.9391	1.8	8	4	0	144.521	72.261	0.5324
9	1.4849	34.0	4	4	0	74.082	37.041	0.3367	26	0.9220	0.2	9	1	1	151.930	75.965	0.5423
10	1.4199	0.8	5	3	1	78.098	39.049	0.3521	27	0.9165	0.1	8	4	2	154.830	77.415	0.5455
11	1.4000	0.1	4	4	2	79.423	39.712	0.3571	28	0.8954	0.5	6	6	4	174.727	87.363	0.5584
12	1.3282	2.5	6	2	0	84.673	42.337	0.3765	29	0.8806	3.0	9	3	1	—		
13	1.2810	6.2	5	3	3	88.579	44.289	0.3903	30	0.8573	6.2	8	4	4	—		
14	1.2664	2.6	6	2	2	89.879	44.939	0.3948	31	0.8442	0.1	9	3	3	—		
15	1.2124	2.0	4	4	4	95.083	47.541	0.4124	32	0.8237	1.2	8	6	2	—		
16	1.1762	0.4	5	5	1	99.011	49.506	0.4251	33	0.8121	3.7	9	5	1	—		
17	1.1225	2.3	6	4	2	105.666	52.833	0.4454	34	0.8083	0.9	10	2	2	—		

201

PDF#00-039-1346(RDB): QM=Star(S); d=Diffractometer; I=Diffractometer	PDF Card

Maghemite-C, syn

Fe$_2$O$_3$

Radiation=CuKα	Lambda=1.54178	Filter=Graph
Calibration=Internal(Si)	2T=17.387-117.936	I/Ic(RIR)=1.4

Ref: Schulz, D., McCarthy, G., North Dakota State University, Fargo, North Dakota, USA.
   ICDD Grant-in-Aid (1987)

Cubic - Single Crystal, P4₁32 (213)   Z=10.67   mp=
CELL: 8.3515 x 8.3515 x 8.3515 <90.0 x 90.0 x 90.0>   P.S=cP53.33
Density(c)=4.856   Density(m)=4.9   Mwt=159.69   Vol=582.50   F(30)=94.9(0.009,35/0)
Ref: Lindsley, D.

General Comments: Pattern reviewed by Syvinski, W., McCarthy, G., North Dakota State University, Fargo, North Dakota, USA, ICDD Grant-in-Aid (1990). Agrees well with experimental pattern. Additional weak reflections (indicated by brackets) were observed. Additional Patterns: To replace 00-004-0755 and 00-024-0081. Color: Light brown. Sample Source or Locality: Sample from Control Data as used in hard disks. Sample Preparation: Space group dependent upon preparation (Bernal et al.). Unit Cell Data Source: Single Crystal.

Color: Light brown

Strong Lines: 2.52/X 2.95/4 1.48/3 1.61/2 2.09/2 1.70/1 1.09/1 1.27/1

41 Lines, Wavelength to Compute Theta = 1.78899Å(Co), I%-Type = Peak Height

#	d(Å)	I(f)	h	k	l	2-Theta	Theta	1/(2d)	#	d(Å)	I(f)	h	k	l	2-Theta	Theta	1/(2d)
1	5.9180	5.0	1	1	0	17.387	8.693	0.0845	22	1.4758	34.0	4	4	0	74.617	37.309	0.3388
2	4.8220	4.0	1	1	1	21.381	10.690	0.1037	23	1.4537	1.0	4	4	1	75.951	37.975	0.3439
3	3.7400	5.0	2	1	0	27.675	13.838	0.1337	24	1.4322	1.0	5	3	0	77.300	38.650	0.3491
4	3.4110	5.0	2	1	1	30.406	15.203	0.1466	25	1.3919	0.0	4	4	2	79.978	39.989	0.3592
5	2.9530	35.0	2	2	0	35.265	17.633	0.1693	26	1.3730	1.0	6	1	0	81.308	40.654	0.3642
6	2.7840	2.0	2	2	1	37.483	18.741	0.1796	27	1.3547	1.0	6	1	1	82.644	41.322	0.3691
7	2.6435	2.0	3	1	0	39.556	19.778	0.1891	28	1.3204	3.0	6	2	0	85.288	42.644	0.3787
8	2.5177	100.0	3	1	1	41.622	20.811	0.1986	29	1.3042	1.0	5	4	0	86.606	43.303	0.3834
9	2.4119	3.0	2	2	2	43.538	21.769	0.2073	30	1.2730	5.0	5	3	3	89.283	44.641	0.3928
10	2.3163	1.0	3	2	0	45.433	22.717	0.2159	31	1.2590	2.0	6	2	2	90.548	45.274	0.3971
11	2.2320	1.0	3	2	1	47.251	23.626	0.2240	32	1.2450	0.0	6	3	0	91.857	45.928	0.4016
12	2.0886	16.0	4	0	0	50.716	25.358	0.2394	33	1.2314	0.0	6	3	1	93.172	46.586	0.4060
13	2.0255	1.0	4	1	0	52.414	26.207	0.2469	34	1.2053	1.0	4	4	4	95.827	47.914	0.4148
14	1.9685	0.0	3	3	0	54.053	27.027	0.2540	35	1.1931	0.0	6	3	2	97.133	48.566	0.4191
15	1.8224	2.0	4	2	1	58.791	29.395	0.2744	36	1.1810	1.0	7	1	0	98.472	49.236	0.4234
16	1.7045	10.0	4	2	2	63.307	31.654	0.2933	37	1.1365	0.0	7	2	1	103.823	51.912	0.4399
17	1.6703	1.0	4	3	0	64.760	32.380	0.2993	38	1.1159	2.0	6	4	2	106.565	53.282	0.4481
18	1.6379	1.0	5	1	0	66.203	33.101	0.3053	39	1.0966	0.0	7	3	0	109.313	54.656	0.4560
19	1.6073	24.0	5	1	1	67.631	33.815	0.3111	40	1.0872	7.0	7	3	1	110.722	55.361	0.4599
20	1.5507	1.0	5	2	0	70.456	35.228	0.3224	41	1.0439	3.0	8	0	0	117.936	58.968	0.4790
21	1.5248	2.0	5	2	1	71.837	35.918	0.3279									

PDF#01-071-5088(RDB): QM=Star(S); d=Calculated; I=Calculated		PDF Card

Hematite

Fe$_2$O$_3$

Radiation=CuKα1	Lambda=1.5405999	Filter=
Calibration=	2T=28.110-160.000	I/Ic(RIR)=3.23
Ref: Wolska, E., Schwertmann, U.		
Z. Kristallogr., v189 p223 (1989)		

Rhombohedral - (Unknown), R3̄c (167)		Z=6	mp=
CELL: 5.0385 x 5.0385 x 13.74 <90.0 x 90.0 x 120.0>		P.S=hR10.00 (å)	
Density(c)=5.267 Density(m)= Mwt=159.69	Vol=302.08	F(30)=999.9(0,32/0)	
Ref: Ibid.			

Calculated Pattern Original Remarks: From heated goethite. Transformation from goethite to hematite at 453 K. Sample1 heated to 1073 K, completely dehydrated. Atomic coordinates as in 56372. ICSD Collection Code: 56372. ANX: A2X3. Wyckoff Sequence: e c (R3-CH).

Strong Lines: 2.70/X 2.52/7 1.69/4 1.84/3 3.68/3 1.49/3 1.45/3 2.21/2

62 Lines, Wavelength to Compute Theta = 1.78899Å(Co), I%-Type = Peak Height

#	d(Å)	I(f)	h	k	l	2-Theta	Theta	1/(2d)	#	d(Å)	I(f)	h	k	l	2-Theta	Theta	1/(2d)
1	3.6833	32.6	0	1	2	28.110	14.055	0.1357	32	1.0302	0.1	1	3	7	120.527	60.263	0.4854
2	2.6990	100.0	1	0	4	38.709	19.355	0.1853	33	0.9984	0.1	3	2	1	127.255	63.628	0.5008
3	2.5192	72.9	1	1	0	41.595	20.797	0.1985	34	0.9957	0.1	1	2	11	127.878	63.939	0.5021
4	2.2900	2.0	0	0	6	45.985	22.992	0.2183	35	0.9893	2.2	3	1	8	129.427	64.714	0.5054
5	2.2074	19.6	1	1	3	47.811	23.906	0.2265	36	0.9716	0.4	2	2	9	134.039	67.020	0.5146
6	2.0794	1.9	2	0	2	50.957	25.478	0.2405	37	0.9611	5.1	3	2	4	137.098	68.549	0.5203
7	1.8417	34.7	0	2	4	58.117	29.058	0.2715	38	0.9575	2.6	0	1	14	138.196	69.098	0.5222
8	1.6945	42.1	1	1	6	63.723	31.862	0.2951	39	0.9522	4.1	4	1	0	139.906	69.953	0.5251
9	1.6375	0.5	2	1	1	66.222	33.111	0.3053	40	0.9406	0.1	2	3	5	143.979	71.990	0.5316
10	1.6037	2.4	1	2	2	67.805	33.902	0.3118	41	0.9323	0.5	1	4	3	147.275	73.637	0.5363
11	1.5982	7.7	0	1	8	68.071	34.035	0.3129	42	0.9208	1.1	0	4	8	152.529	76.264	0.5430
12	1.4868	26.6	2	1	4	73.976	36.988	0.3363	43	0.9082	5.0	1	3	10	160.094	80.047	0.5506
13	1.4545	26.1	3	0	0	75.902	37.951	0.3438	44	0.8997	0.3	3	0	12	167.695	83.847	0.5558
14	1.4141	0.2	1	2	5	78.477	39.238	0.3536	45	0.8950	2.5	2	0	14	176.001	88.001	0.5586
15	1.3495	2.4	2	0	8	83.031	41.516	0.3705	46	0.8899	0.1	2	1	13	—		
16	1.3106	9.0	1	0	10	86.083	43.042	0.3815	47	0.8792	5.8	1	4	6	—		
17	1.3056	2.3	1	1	9	86.487	43.244	0.3830	48	0.8692	0.1	3	1	11	—		
18	1.2596	5.6	2	2	0	90.491	45.246	0.3969	49	0.8649	0.9	2	3	8	—		
19	1.2278	2.0	3	0	6	93.530	46.765	0.4072	50	0.8609	0.3	1	1	15	—		
20	1.2145	0.9	2	2	3	94.867	47.434	0.4117	51	0.8543	2.5	4	0	10	—		
21	1.2055	0.1	1	3	1	95.802	47.901	0.4148	52	0.8473	0.3	2	2	12	—		
22	1.1919	1.5	3	1	2	97.268	48.634	0.4195	53	0.8458	2.1	0	5	4	—		
23	1.1896	3.5	1	2	8	97.517	48.758	0.4203	54	0.8434	4.7	1	2	14	—		
24	1.1626	4.4	0	2	10	100.593	50.296	0.4301	55	0.8397	3.3	3	3	0	—		
25	1.1450	0.3	0	0	12	102.745	51.372	0.4367	56	0.8260	0.1	3	3	3	—		
26	1.1414	6.5	1	3	4	103.193	51.596	0.4380	57	0.8231	0.1	2	4	1	—		
27	1.1037	6.1	2	2	6	108.283	54.141	0.4530	58	0.8187	0.2	4	2	2	—		
28	1.0774	0.6	0	4	2	112.250	56.125	0.4641	59	0.8091	3.1	3	2	10	—		
29	1.0556	6.3	2	1	10	115.847	57.924	0.4736	60	0.8079	0.6	1	4	9	—		
30	1.0424	0.4	1	1	12	118.212	59.106	0.4797	61	0.8018	3.2	2	4	4	—		
31	1.0397	2.1	4	0	4	118.709	59.355	0.4809	62	0.7991	0.6	0	2	16	—		

PDF#00-041-1487(RDB): QM=Indexed(I); d=Diffractometer; I=Diffractometer		PDF Card

Graphite-2H

C

Radiation=CuKα1		Filter=Ni
Calibration=External(Si)	2T=30.732-115.662	I/Ic(RIR)=7.78
Ref: Sanc, I., Polytechna, Foreign Trade Corporation, Panska, Czechoslovakia.		
ICDD Grant-in-Aid (1990)		CAS#7782-42-5

Hexagonal - Powder Diffraction, P6₃/mmc (194)	Z=4	mp=

CELL: 2.4704 x 2.4704 x 6.7244 <90.0 x 90.0 x 120.0>   P.S=hP4.00

Density(c)=2.245   Density(m)=2.16   Mwt=12.01   Vol=35.54   F(10)=18.5(0.042,13/0)

Ref: Ibid.

Aust. J. Chem., v42 p479 (1989)

Additional Patterns: To replace 00-001-0640, 00-001-0646, 00-002-0456, 00-003-0401, 00-023-0064, 00-025-0284 and 00-034-0567 and validated by calculated pattern 00-025-0284. Color: Black. Sample Source or Locality: Specimen from Netolice, Czechoslovakia. Temperature of Data Collection: Pattern taken at 25(1) C. Unit Cell Data Source: Powder Diffraction.

Color: Black

Strong Lines: 3.38/X 2.04/1

10 Lines, Wavelength to Compute Theta = 1.78899Å(Co), I%-Type = (Unknown)

#	d(Å)	I(f)	h	k	l	2-Theta	Theta	1/(2d)	#	d(Å)	I(f)	h	k	l	2-Theta	Theta	1/(2d)
1	3.3756	100.0	0	0	2	30.732	15.366	0.1481	6	1.5478	1.0	1	0	3	70.609	35.305	0.3230
2	2.1386	2.0	1	0	0	49.449	24.724	0.2338	7	1.2341	3.0	1	1	0	92.909	46.454	0.4052
3	2.0390	6.0	1	0	1	52.041	26.020	0.2452	8	1.1604	3.0	1	1	2	100.863	50.432	0.4309
4	1.8074	0.0	1	0	2	59.328	29.664	0.2766	9	1.1208	0.0	0	0	6	105.890	52.945	0.4461
5	1.6811	4.0	0	0	4	64.293	32.147	0.2974	10	1.0567	0.0	2	0	1	115.662	57.831	0.4732

204

PDF#00-050-1083(RDB): QM=Calculated(C); d=Calculated; I=Calculated														PDF Card

Carbon

C

Radiation=CuKα1		Lambda=1.5405999	Filter=
Calibration=		2T=49.148-127.140	I/Ic(RIR)=C

Ref: Ownby, P., Yang, X., Liu, J.
J. Am. Ceram. Soc., v75 p1876 (1992)   CAS#7440-44-0

Hexagonal - (Unknown), P6₃/mmc (194)   Z=12   mp=
CELL: 2.5221 x 2.5221 x 12.3557 <90.0 x 90.0 x 120.0>   P.S=hP12.00
Density(c)=3.516   Density(m)=   Mwt=12.01   Vol=68.06   F(11)=250(0.002,22/0)
Ref: Ibid.

Additional Patterns: To replace 00-026-1082. See PDF 01-079-1470.

Strong Lines: 2.06/X 2.06/X 2.15/4 1.26/4 1.26/4 1.93/2 1.08/2 1.08/2

15 Lines, Wavelength to Compute Theta = 1.78899Å(Co), I%-Type = (Unknown)

#	d(Å)	I(f)	h	k	l	2-Theta	Theta	1/(2d)	#	d(Å)	I(f)	h	k	l	2-Theta	Theta	1/(2d)
1	2.1509	41.0	0	1	1	49.148	24.574	0.2325	9	1.1623	10.0	0	1	9	100.634	50.317	0.4302
2	2.0593	100.0	0	1	2	51.490	25.745	0.2428	10	1.0879	2.0	0	2	1	110.616	55.308	0.4596
3	2.0593	100.0	0	0	6	51.490	25.745	0.2428	11	1.0754	16.0	0	2	2	112.564	56.282	0.4649
4	1.9296	17.0	0	1	3	55.235	27.617	0.2591	12	1.0754	16.0	1	1	6	112.564	56.282	0.4649
5	1.6366	2.0	0	1	5	66.262	33.131	0.3055	13	1.0556	1.0	0	2	3	115.856	57.928	0.4737
6	1.3729	5.0	0	1	7	81.315	40.658	0.3642	14	0.9989	0.0	0	1	11	127.140	63.570	0.5006
7	1.2610	36.0	0	1	8	90.365	45.182	0.3965	15	0.9989	0.0	0	2	5	127.140	63.570	0.5006
8	1.2610	36.0	1	1	0	90.365	45.182	0.3965									

PDF#00-035-0798(RDB): QM=Star(S); d=Diffractometer; I=Diffractometer	PDF Card

Boron Carbide

B₄C

Radiation=CuKα1	Lambda=1.5405982	Filter=Graph
Calibration=Internal(SI)	2T=22.934-97.611	I/Ic(RIR)=S
Ref:		
Natl. Bur. Stand. (U.S.) Monogr. 25, v21 p43 (1985)		CAS#12069-32-8

Rhombohedral - Powder Diffraction, R3̄m (166)		Z=9	mp=
CELL: 5.6003 x 5.6003 x 12.086 <90.0 x 90.0 x 120.0>		P.S=hR15.00	
Density(c)=2.515 Density(m)=	Mwt=55.25	Vol=328.27	F(25)=58(0.012,34/0)
Ref:			

Additional Patterns: To replace 00-006-0555. Color: Greenish black. Sample Source or Locality: The compound was obtained from the Aesar Division of Johnson Matthey, Inc., Seabrook, New Hampshire, USA. Temperature of Data Collection: The mean temperature of data collection was 23.5 C. Unit Cell: Rhombohedral cell: a=5.166, α=65.65. Unit Cell Data Source: Powder Diffraction.

Color: Greenish black

Strong Lines: 2.38/X 2.56/6 3.78/5 4.03/2 4.50/1 1.46/1 1.40/1 1.71/1

25 Lines, Wavelength to Compute Theta = 1.78899Å(Co), I%-Type = Peak Height

#	d(Å)	I(f)	h	k	l	2-Theta	Theta	1/(2d)	#	d(Å)	I(f)	h	k	l	2-Theta	Theta	1/(2d)
1	4.4995	14.0	1	0	1	22.934	11.467	0.1111	14	1.4605	13.0	1	2	5	75.535	37.767	0.3423
2	4.0330	21.0	0	0	3	25.629	12.814	0.1240	15	1.4423	10.0	0	1	8	76.660	38.330	0.3467
3	3.7828	49.0	0	1	2	27.356	13.678	0.1322	16	1.3995	12.0	2	2	0	79.457	39.728	0.3573
4	2.8031	11.0	1	1	0	37.218	18.609	0.1784	17	1.3369	8.0	1	3	1	83.990	41.995	0.3740
5	2.5647	64.0	1	0	4	40.825	20.412	0.1950	18	1.3228	7.0	2	2	3	85.100	42.550	0.3780
6	2.3769	100.0	0	2	1	44.212	22.106	0.2104	19	1.3128	8.0	3	1	2	85.900	42.950	0.3809
7	2.3001	4.0	1	1	3	45.772	22.886	0.2174	20	1.2820	2.0	2	0	8	86.492	44.246	0.3900
8	1.8906	0.0	0	2	4	56.474	28.237	0.2645	21	1.2605	3.0	3	0	6	90.410	45.205	0.3967
9	1.8127	4.0	2	1	1	59.135	29.567	0.2758	22	1.2571	6.0	2	1	7	90.722	45.361	0.3977
10	1.7120	11.0	2	0	5	62.999	31.499	0.2921	23	1.2112	0.0	1	1	9	95.213	47.606	0.4128
11	1.6261	2.0	1	0	7	66.746	33.373	0.3075	24	1.2065	1.0	4	0	1	95.697	47.848	0.4144
12	1.5674	0.0	2	1	4	69.596	34.798	0.3190	25	1.1887	4.0	0	4	2	97.611	48.806	0.4206
13	1.5004	9.0	3	0	3	73.194	36.597	0.3333									

206

PDF#99-000-3892: QM=Uncommon(?); d=Other/Unknown; I=(Unknown)		PDF Card

Unnamed 0290
WC

Radiation=CuKa1	Lambda=1.5406	Filter=
Calibration=	2T=36.717-165.208	I/Ic(RIR)=
Ref: JADE's Userfile		

Hexagonal, P6̄m2 (187)			Z=1	mp=
CELL: 2.903 x 2.903 x 2.835 <90.0 x 90.0 x 120.0>			P.S=	
Density(c)=14.3	Density(m)=	Mwt=	Vol=20.7	
Ref: Ibid.				

NOTE: Hardness is greater than 8. Locality: Mengyin, Shandong prov., China. Black, steel-grey. Min-Group: Tungsten Carbide. Ref: American Mineralogist 74 (1989), 948. Ref: American Mineralogist 84 (1999), 1468. Ref: Transactions (Doklady) of the USSR Academy of Sciences, Earth Science Sections 352 (1997), 81. Ref: Powder Diffraction File (International Center for Diffraction Data) 25-1047.

Strong Lines: 2.52/X 1.88/X 2.84/4 1.24/3 1.29/2 1.15/2 0.90/2 1.45/2

8 Lines, Wavelength to Compute Theta = 1.78899Å(Co), I%-Type = (Unknown)

#	d(Å)	I(f)	h	k	l	2-Theta	Theta	1/(2d)	#	d(Å)	I(f)	h	k	l	2-Theta	Theta	1/(2d)
1	2.8400	40.0				36.717	18.359	0.1761	5	1.2930	20.0				87.545	43.773	0.3867
2	2.5180	100.0				41.616	20.808	0.1986	6	1.2360	30.0				92.722	46.361	0.4045
3	1.8840	100.0				56.691	28.345	0.2654	7	1.1500	20.0				102.123	51.062	0.4348
4	1.4540	20.0				75.932	37.966	0.3439	8	0.9020	20.0				165.208	82.604	0.5543

207

PDF#99-000-3816: QM=Uncommon(?); d=Other/Unknown; I=(Unknown)	PDF Card

Tungsten
W

Radiation=CuKa1	Lambda=1.5406	Filter=
Calibration=	2T=47.386-126.887	I/Ic(RIR)=
Ref: JADE's Userfile		

Cubic, Im3m (229)		Z=2	mp=
CELL: 3.157 x 3.157 x 3.157 <90.0 x 90.0 x 90.0>		P.S=	
Density(c)=19.26 Density(m)= Mwt=	Vol=31.5		
Ref: Ibid.			

NOTE: Not approved by CNMMN. Locality: Bolshaya Polya River, Urals (sub-polar), Russia, (FSU). Min-Group: Chromium. Ref: Doklady Akademlla Nauk (in Russian) 340 (1995), 681. Ref: American Mineralogist 81 (1996), 1284. Ref: Doklady Akademlla Nauk (in Russian) 373 (2000), 523. Ref: American Mineralogist 86 (2001), 942. Ref: Transactions (Doklady) of the USSR Academy of Sciences, Earth Science Sections 385A (2002), 714.

Strong Lines: 1.00/X 1.29/X 2.23/X 1.58/7 1.12/6

5 Lines, Wavelength to Compute Theta = 1.78899Å(Co), I%-Type = (Unknown)

#	d(Å)	I(f)	h	k	l	2-Theta	Theta	1/(2d)	#	d(Å)	I(f)	h	k	l	2-Theta	Theta	1/(2d)
1	2.2260	100.0				47.386	23.693	0.2246	4	1.1190	60.0				106.140	53.070	0.4468
2	1.5770	70.0				69.112	34.556	0.3171	5	1.0000	100.0				126.887	63.444	0.5000
3	1.2920	100.0				87.630	43.815	0.3870									

208

PDF#01-071-3817(RDB): QM=Blank(B); d=Calculated; I=Calculated	PDF Card

Tungsten

W

Radiation=CuKα1	Lambda=1.5405999	Filter=
Calibration=	2T=29.014-180.000	I/Ic(RIR)=15.5

Ref: Hartmann, H., Ebert, F., Brettschneider, O.
  Z. Anorg. Allg. Chem., v198 p116 (1931)

Cubic - (Unknown), Pm3n (223)   Z=8   mp=
CELL: 5.05 x 5.05 x 5.05 <90.0 x 90.0 x 90.0>   P.S=cP8.00 (Å)
Density(c)=18.964   Density(m)=   Mwt=183.85   ·Vol=128.79   F(25)=999.9(0,27/0)
Ref: Ibid.

Calculated Pattern Original Remarks: The structure is probably W3 O with O in 2a, cp. too low Dm, cp. Cr3 O = 15904. ICSD Collection Code: 52344. ANX: N. Wyckoff Sequence: c a (PM3-N). Minor Warning: No R value given in the paper. No e.s.d. reported/abstracted on the cell dimension. Significant Warning: ICSD Warning: The coordinates are those given in the paper but the atomic distances do not agree with those calculated during testing. The coordinates are probably correct.

Strong Lines: 2.26/X 2.06/7 2.53/4 1.35/3 1.40/2 1.10/1 1.26/1 0.94/1

25 Lines, Wavelength to Compute Theta = 1.78899Å(Co), I%-Type = Peak Height

#	d(Å)	I(f)	h	k	l	2-Theta	Theta	1/(2d)	#	d(Å)	I(f)	h	k	l	2-Theta	Theta	1/(2d)
1	3.5709	0.1	1	1	0	29.014	14.507	0.1400	14	1.1020	11.5	4	2	1	108.525	54.263	0.4537
2	2.5250	35.7	2	0	0	41.496	20.748	0.1980	15	1.0767	5.3	3	3	2	112.363	56.182	0.4644
3	2.2584	100.0	2	1	0	46.665	23.333	0.2214	16	1.0308	0.1	4	2	2	120.395	60.197	0.4850
4	2.0617	73.9	2	1	1	51.427	25.714	0.2425	17	0.9904	0.1	5	1	0	129.158	64.579	0.5049
5	1.7854	0.1	2	2	0	60.132	30.066	0.2800	18	0.9378	9.8	5	2	0	145.055	72.528	0.5332
6	1.5970	0.1	3	1	0	68.129	34.065	0.3131	19	0.9220	6.3	5	2	1	151.940	75.970	0.5423
7	1.4578	6.4	2	2	2	75.699	37.849	0.3430	20	0.8927	5.9	4	4	0	—		
8	1.4006	16.3	3	2	0	79.381	39.691	0.3570	21	0.8661	0.1	4	3	3	—		
9	1.3497	27.7	3	2	1	83.020	41.510	0.3705	22	0.8417	3.3	6	0	0	—		
10	1.2625	10.4	4	0	0	90.228	45.114	0.3960	23	0.8302	2.6	6	1	0	—		
11	1.2248	0.1	4	1	0	93.826	46.913	0.4082	24	0.8192	7.6	5	3	2	—		
12	1.1903	0.1	4	1	1	97.439	48.719	0.4201	25	0.7985	0.1	6	2	0	—		
13	1.1292	6.4	4	2	0	104.772	52.386	0.4428									

PDF#01-071-6719(RDB): QM=Blank(B); d=Calculated; I=Calculated															PDF Card

Nickel Oxide

NiO

Radiation=CuKα1	Lambda=1.5405999	Filter=
Calibration=	2T=43.583-180.000	I/Ic(RIR)=4.73

Ref: Rodic, D., Spasojevic, V., Kusigerski, V., Tellgren, R., Rundlof, H.
      Phys. Status Solidi B, v218 p527 (2000)

Rhombohedral - Profile Analysis, R3̄m (166)	Z=3	mp=
CELL: 2.9517 x 2.9517 x 7.217 <90.0 x 90.0 x 120.0>	P.S=hR2.00	
Density(c)=6.834 Density(m)= Mwt=74.7 Vol=54.45	F(17)=50.1(0.016,21/0)	

Ref: Ibid.

Calculated Pattern Original Remarks: ICSD   entry Z92127   is filename FIZZ92127. ICSD Collection Code: 92127. Temperature of Data Collection: 10 K. ANX: AX. Wyckoff Sequence: b a (R3-MH). Significant Warning: Reported temperature factors were outside the range 0.001<U<0.1. U=0.012 was used in the calculation. Unit Cell Data Source: Rietveld or profile fit analysis.

Strong Lines: 2.09/X 2.41/6 2.41/4 1.47/3 1.48/3 1.26/1 1.26/1 1.20/1

20 Lines, Wavelength to Compute Theta = 1.78899Å(Co), I%-Type = Peak Height

#	d(Å)	I(f)	h	k	l	2-Theta	Theta	1/(2d)	#	d(Å)	I(f)	h	k	l	2-Theta	Theta	1/(2d)
1	2.4096	56.4	1	0	1	43.583	21.791	0.2075	11	0.9576	2.1	2	1	1	138.158	69.079	0.5221
2	2.4057	43.7	0	0	3	43.657	21.828	0.2078	12	0.9569	1.5	2	0	5	138.389	69.195	0.5225
3	2.0859	100.0	0	1	2	50.787	25.393	0.2397	13	0.9562	1.3	1	0	7	138.621	69.310	0.5229
4	1.4758	26.0	1	1	0	74.614	37.307	0.3388	14	0.9333	5.2	1	2	2	146.841	73.421	0.5357
5	1.4741	27.1	1	0	4	74.720	37.360	0.3392	15	0.9324	5.3	1	1	6	147.218	73.609	0.5363
6	1.2580	10.3	1	1	3	90.642	45.321	0.3975	16	0.8517	4.4	3	0	0	—		
7	1.2580	10.3	0	1	5	90.642	45.321	0.3975	17	0.8517	4.4	2	1	4	—		
8	1.2046	8.0	2	0	2	95.882	47.941	0.4150	18	0.8507	2.2	0	1	8	—		
9	1.2028	4.0	0	0	6	98.088	48.044	0.4157	19	0.8029	1.7	1	2	5	—		
10	1.0430	3.7	0	2	4	118.109	59.055	0.4794	20	0.8029	1.7	0	3	3	—		

210

PDF#99-000-0501: QM=Uncommon(?); d=Other/Unknown; I=(Unknown)		PDF Card

Bunsenite
NiO

Radiation=CuKa1	Lambda=1.5406	Filter=
Calibration=	2T=43.574-180.000	I/Ic(RIR)=
Ref: JADE's Userfile		

Cubic, Fm3̄m (225)   Z=4   mp=
CELL: 4.179 x 4.179 x 4.179 <90.0 x 90.0 x 90.0>   P.S=
Density(c)=6.9   Density(m)=   Mwt=   Vol=73.0
Ref: Ibid.

NOTE: Locality: Johanngeorgenstadt, Sachsen (Saxony), Germany. Vitreous/adamantine dark pistachio green. Min-Group: Periclase. PDF: 04-0835; 47-1049. Ref: Handbook of Mineralogy (Anthony et al.), 3 (1997), 65. Ref: USA National Bureau of Standards Circular 539, 1 (1953), 47. Ref: Quantitative Data File for Ore Minerals, 3rd edition, (1993) 66. Ref: Proceedings of the Japan Academy 55 (1979), 43.

Strong Lines: 2.09/X 2.41/9 1.48/6 0.85/2 0.93/2 1.26/2 1.04/1 1.21/1

8 Lines, Wavelength to Compute Theta = 1.78899Å(Co), I%-Type = (Unknown)

#	d(Å)	I(f)	h	k	l	2-Theta	Theta	1/(2d)	#	d(Å)	I(f)	h	k	l	2-Theta	Theta	1/(2d)
1	2.4100	90.0				43.574	21.787	0.2075	5	1.2060	10.0				95.754	47.877	0.4146
2	2.0880	100.0				50.732	25.366	0.2395	6	1.0440	10.0				117.917	58.959	0.4789
3	1.4760	60.0				74.605	37.303	0.3388	7	0.9340	20.0				146.553	73.276	0.5353
4	1.2590	20.0				90.548	45.274	0.3971	8	0.8530	20.0				—		

211

D.0 Thermodynamics.

Equation D-1 shows the equation, which minimizes the total Gibbs energy of the system

at T, n_i, x_i and P_i.

$$G = \sum_{ideal \atop gas} n_i(g_i^o + RT\ln P_i) + \sum_{Pure \atop Condensed \atop Phases} n_i g_i + \sum_{Solution} n_i(g_i^o + RT\ln x_i + RT\ln \gamma_i) + \sum_{Solution} \ldots$$

Equation D-1

When a given system is at equilibrium, the Gibbs energy is minimized. Most systems do

not behave in the ideal manner that is described in Equation D-1. There are several

models to describe the behaviour of non-ideal systems. In FACTSage[TM,40], the Redlich-

Kister-Muggianu polynomial formulation is utilized to define an excess Gibb's free

energy term Equation D-2 shows this polynomial expression, which describes the liquid

solutions.

$$G_{ex} = x_m x_n \sum_{j=0}^{j} L (x_n - x_m)^j$$

Equation D-2

The solid solutions that are calculated use sublattice models, which consider the

behaviour of interstitials and vacancies.

212

D.1 FACTSage[TM,40].

D.1.1 Reaction Module of FACTSage[TM,40].

The reaction module of FACTSage[TM,40] was used to determine the heats of reaction for the formation of one mole of each of the binary compounds in the Ni-WC and Ni-B4C systems. The formation of WC from W and C reactants will be discussed as an example. Figure D.1 shows the screen where the reactants are entered. It can be seen that the reaction requires 1mol of W and 1 mol of C to form 1mol of WC. The temperature is left as T for this screen.
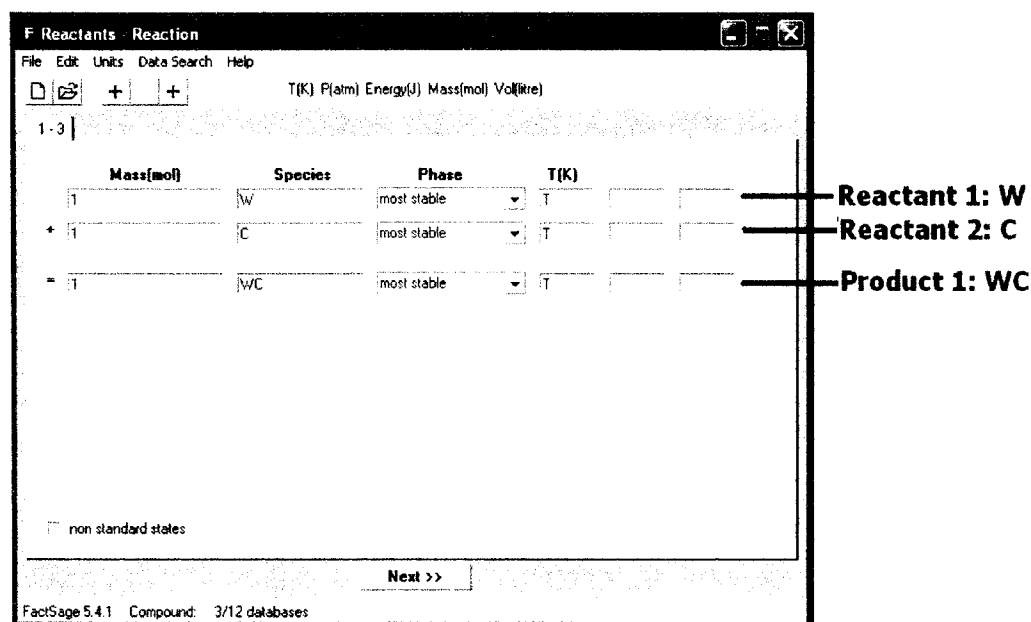
Figure D.1: Reactant input for reaction module of FACTSage[TM,40].

213

The next screen of the reaction module is seen in Figure D.2. The input reaction

temperature, in Kelvin, is entered at the bottom left of the screen. After a temperature is

entered, the calculate button is clicked, giving the results of the reaction at the chosen

temperature. The user may then enter another temperature to obtain the results of the

calculation at that temperature and so on. It should also be noted that the results that are

shown include the enthalpy change, the Gibb's free energy change, the volume change,

the entropy change as well as the heat capacity change for the system at the chosen

temperature. Also included is the equilibrium constant, K_{eq} for the calculated reaction.
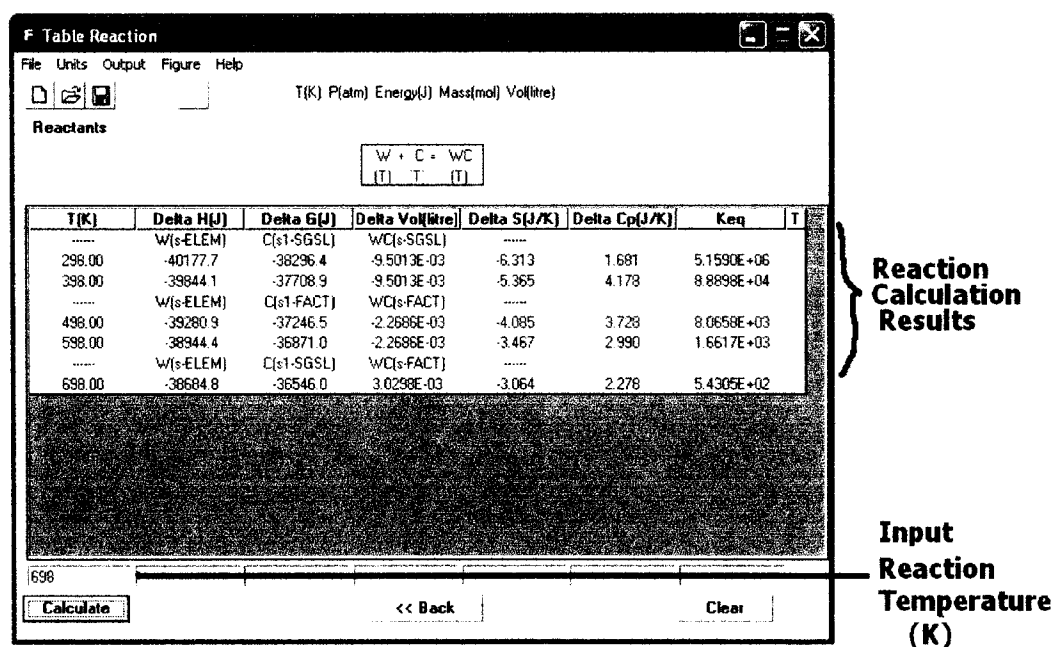
Figure D.2: Reaction calculation results.

214

D.1.2 Equilibrium module of FACTSage[TM,40].

In the equilibrium module is where most of the thermodynamic calculations for this report were carried out. Following is a description of how data is entered into this module. Figure D.3 shows an example of the input screen in the equilibrium module of FACTSage[TM,40].

Figure D.3: Reaction Table for equilibrium module of FACTSage[TM,40].

After the reactant information has been added into the program, the next step is to add the reaction information. This is done on the second page of the equilibrium module (Figure D.4). Included in this information is the type of products that are desired, gaseous, liquid, solution and solid (Figure D.4).

215
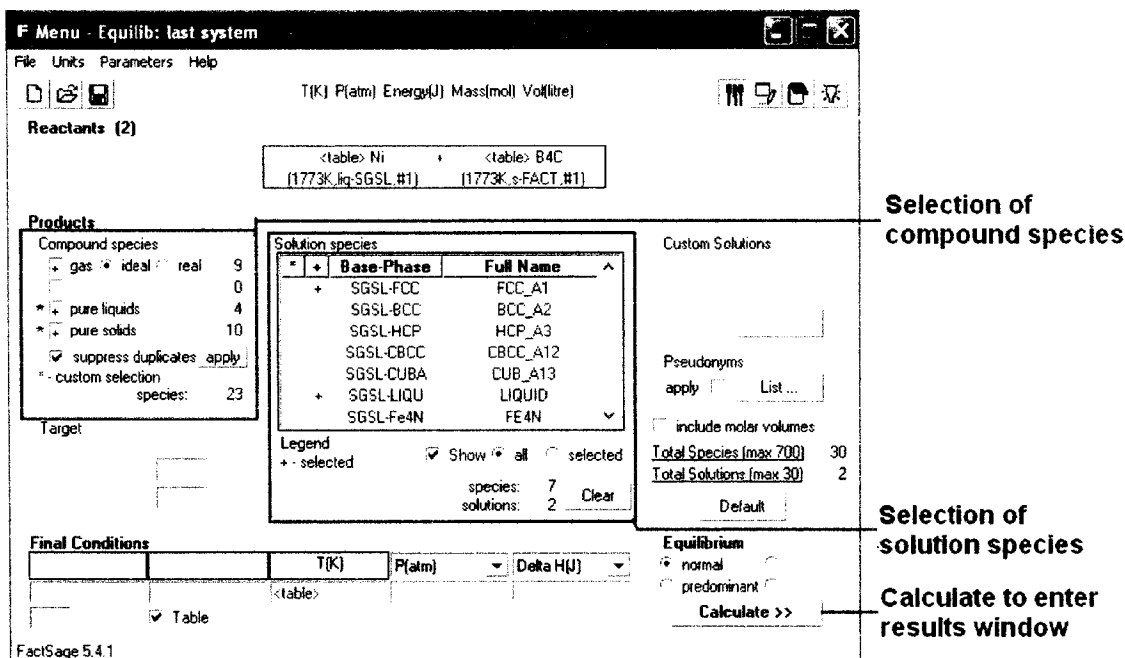
Figure D.4: Second Page of FACTSage^{TM,40} Equilibrium Module.

The next step is to click on calculate to see the results of the thermodynamic calculations.

The results screen will then be opened. On this screen, there is shown the reactant moles,

the product moles, the product activities/ fugacities (Figure D.5).

Output   Edit   Show Pages

☐ 🗁 🔍   T(K) P(atm) Energy(J) Mass(mol) Vol(litre)

-1- | -2- | -3- | -4- | -5- | -6- | -7- | -8- | -9- |

```
T = 1773.00 K
P = 1.00000E+00 atm
V = 0.00000E+00 dm3


STREAM CONSTITUENTS      AMOUNT/mol    TEMPERATURE/K    PRESSURE/atm
Ni(liq)_SGSL             1.7000E+01    1773.00          1.0000E+00
B4C(s)_FACT              1.8000E-01    1773.00          1.0000E+00


                         EQUIL AMOUNT  MOLE FRACTION    FUGACITY
PHASE: gas_ideal         mol                            atm
Ni_FACT                  0.0000E+00    1.0000E+00       8.3186E-06
B_FACT                   0.0000E+00    6.8435E-07       5.6928E-12
C_FACT                   0.0000E+00    1.0789E-09       8.9747E-15
C3_FACT                  0.0000E+00    4.3659E-12       3.6318E-17
C2_FACT                  0.0000E+00    1.7317E-12       1.4405E-17
BC_FACT                  0.0000E+00    1.5052E-13       1.2521E-18
B2_FACT                  0.0000E+00    2.9185E-15       2.4278E-20
C4_FACT                  0.0000E+00    5.7840E-18       4.8115E-23
C5_FACT                  0.0000E+00    7.1815E-19       5.9739E-24
TOTAL:                   0.0000E+00    1.0000E+00       8.3186E-06
PHASE: FCC_A1            mol           MOLE FRACTION    ACTIVITY
B1C1                     0.0000E+00    5.2479E-06       9.6961E-07
B1Va1                    0.0000E+00    1.7251E-03       5.2270E-04
Ni1C1                    0.0000E+00    3.0276E-03       2.5051E-03
Ni1Va1                   0.0000E+00    9.9524E-01       9.1502E-01
TOTAL:                   0.0000E+00    1.0000E+00       9.1941E-01
PHASE: LIQUID           mol           MOLE FRACTION    ACTIVITY
B                        7.2000E-01    4.0223E-02       1.3626E-03
C                        1.8000E-01    1.0056E-02       4.9629E-04
Ni                       1.7000E+01    9.4972E-01       9.4369E-01
TOTAL:                   1.7900E+01    1.0000E+00       1.0000E+00
                         mol                            ACTIVITY
Ni(liq)_SGSL             0.0000E+00                     9.4370E-01
Ni_fcc_al(s)_SGSL        0.0000E+00                     9.1502E-01
C_graphite(s)_SGSL       0.0000E+00                     7.3615E-02
Ni3C_cementite(s)_SGSL   0.0000E+00                     5.9363E-02
Ni3B_ni3b(s)_SGSL        0.0000E+00                     5.5775E-02
C_diamond_a4(s2)_SGSL    0.0000E+00                     3.8368E-02
'Ni2B'_m2b_tet(s)_SGSL   0.0000E+00                     2.9083E-02
NiB_nib(s)_SGSL          0.0000E+00                     9.5318E-03
B_beta_rhombo_(s)_SGSL   0.0000E+00                     3.1168E-03
B(liq)_SGSL              0.0000E+00                     1.3626E-03
C(liq)_SGSL              0.0000E+00                     4.9629E-04
'Ni4B3'_ni4b3(s)_SGSL    0.0000E+00                     2.2469E-06
B4C(s)_FACT              0.0000E+00                     3.0487E-10
B4C(liq)_FACT            0.0000E+00                     2.0703E-11
*****************************************************************
  DELTA_Cp      DELTA_H       DELTA_S       DELTA_G       DELTA_V
   J.K-1         J            J.K-1          J            dm3
*****************************************************************
 2.01843E+00  -3.30193E+04   2.23599E+01  -7.26634E+04  0.00000E+00
```

Gaseous product species

Solid solution product

Compound product species

Figure D.5: Results Screen from FACTSage[TM,40]

217

D.2   Thermodynamic Data.

D.2.1   Heat Capacities.

D.2.1.1   Cp of Elements.
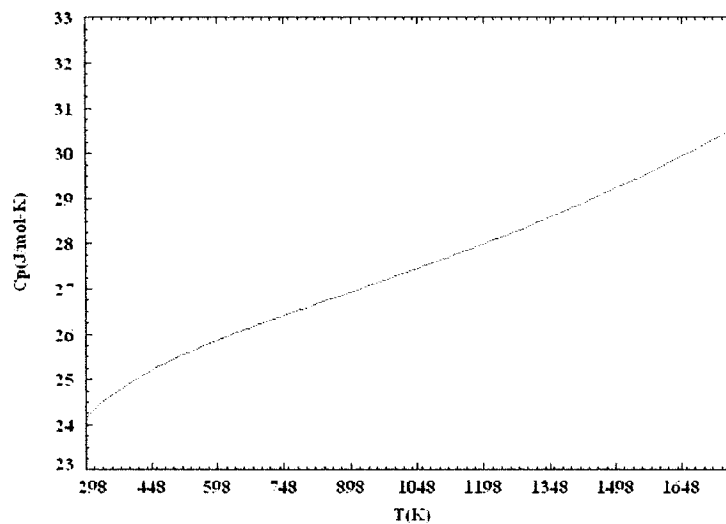
Figure D.6: Cp for solid W from 298K to 1773K.
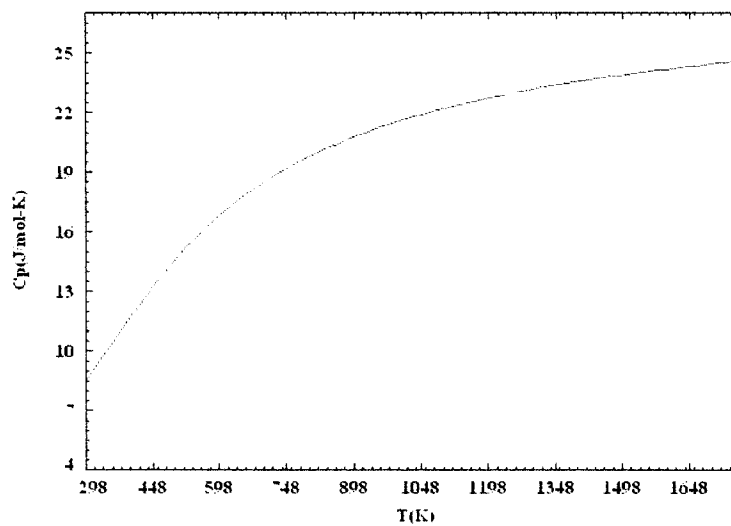
Figure D.7: Cp for solid C from 298K to 1773K.

218
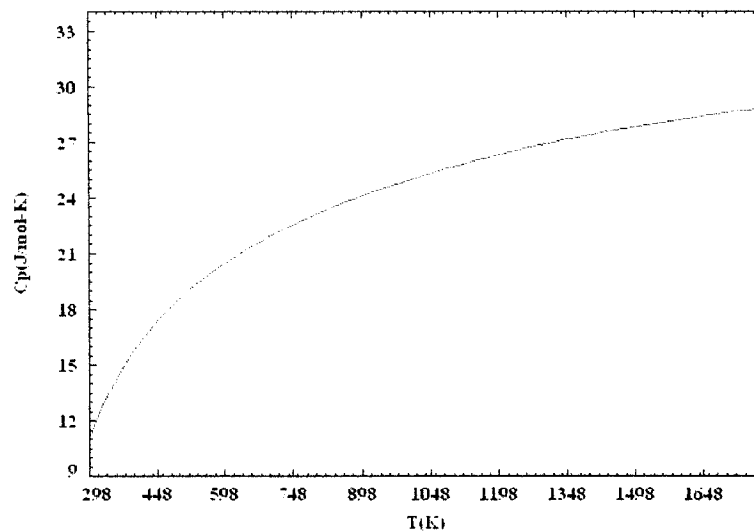
Figure D.8: Cp for B from 298K to 1773K.

The heat capacity of solid nickel, below the melting point, 1728K, is shown in Figure

D.9.
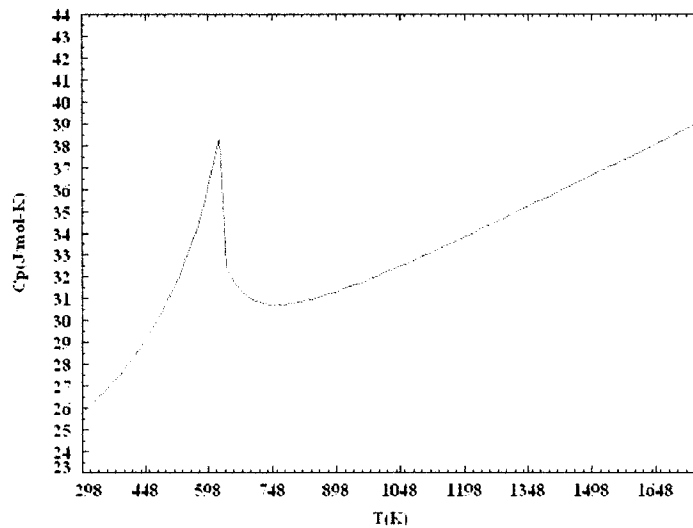
Figure D.9: Cp of solid Ni below 1728K.

219

The heat capacity of liquid nickel is shown in Figure D.10 above 1728K.
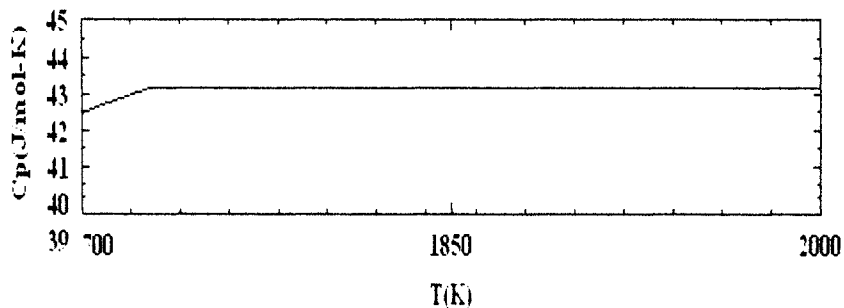
Figure D.10: Cp of liquid Ni above 1728K.

D.2.2 Cp of Compounds.

D.2.2.1   Ni-WC System.

There are several compounds that may be present in the Ni-WC system. The compound

WC is one of the reactant species in this system and was seen in the experimental results.

The enthalpy and entropy of formation for this compound is shown in Table D.1. Also

shown in this table is the thermodynamic data for the formation of the Ni-W compounds

Ni_4W, NiW and NiW_2. These are the compounds that may form in the Ni-WC reaction

system. As previously discussed, there are no stable Ni-C compounds formed.

220

Table D.1: Thermodynamic data for compounds in the Ni-WC system.

Compound	$\Delta H^o_{f,298}(J\,/\,mol)$	$\Delta S^o_{f,298}(J\,/\,mol \cdot K)$
WC	-40178	-6.31
Ni_4W	-31379	-1.22
NiW	-7047	0.185
NiW_2	-7050	0.143

The other thermodynamic parameter that is important is the heat capacity, Cp, of the compounds. The Cp values are used to calculate the Gibb's free energy change at a specified temperature.

Figure D.11, Figure D.12, Figure D.13 and Figure D.14 show the Cp values for WC, Ni_4W, NiW and NiW_2.

221
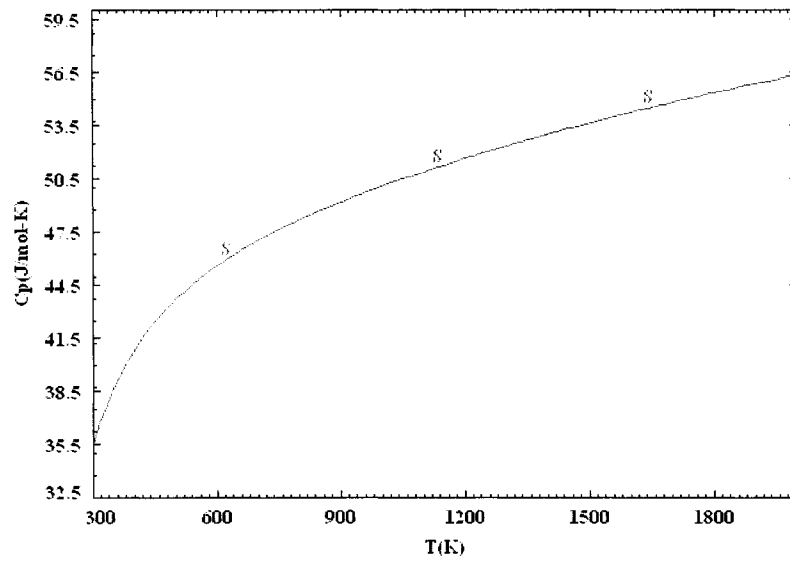
Figure D.11: Cp vs. T for WC.
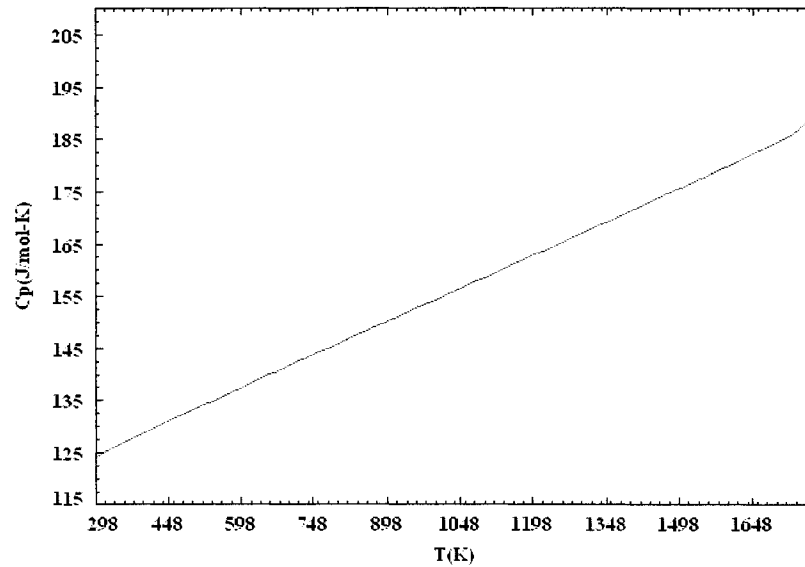
Figure D.12: Cp vs. T for Ni₄W.

222
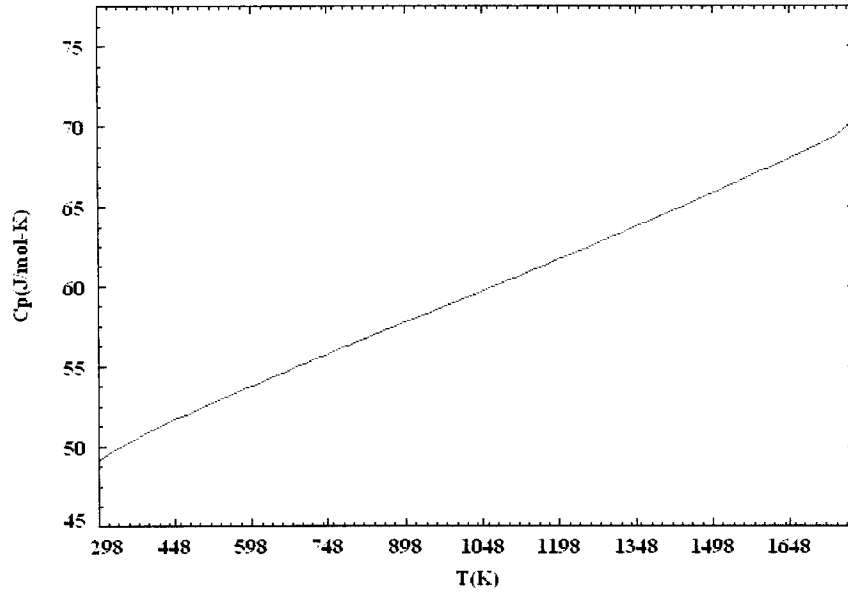
Figure D.13: Cp vs. T for NiW.
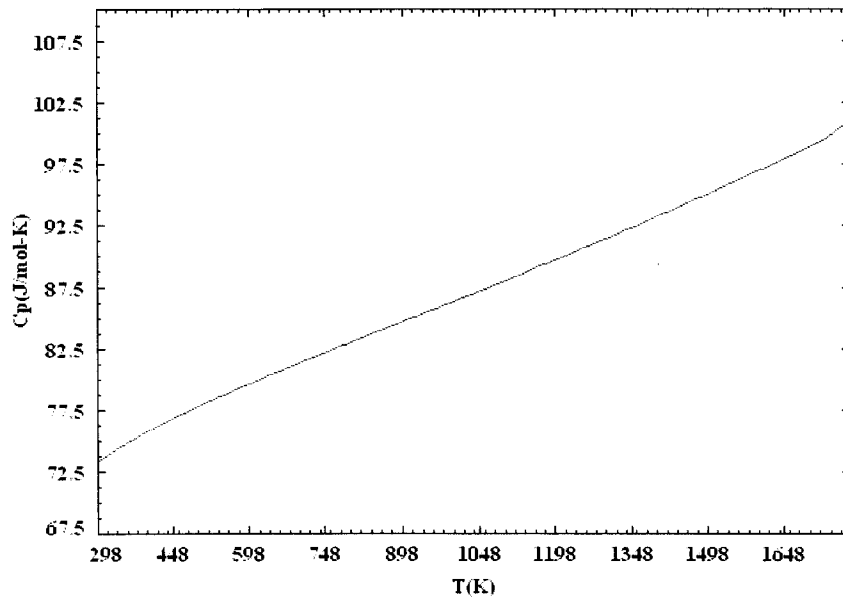
Figure D.14: Cp vs. T for NiW$_2$.

223

D.2.3 Ni-B₄C System.

There are several compounds that may be present in the $Ni-B_4C$ system. The standard

enthalpy of formation and the standard entropy of formation for the nickel borides Ni_2B,

Ni_3B, Ni_4B_3 and NiB are shown in Table D.2.

Table D.2: Thermodynamic data for the compounds in the Ni-B₄C system.

Compound	$\Delta H^o_{f,298}$	$\Delta S^o_{f,298}$
B_4C	-62676	-2.17
Ni_2B	-64119	-11.76
Ni_3B	-64482	-3.60
Ni_4B_3	-311706	-22.24
NiB	-100415	-5.57
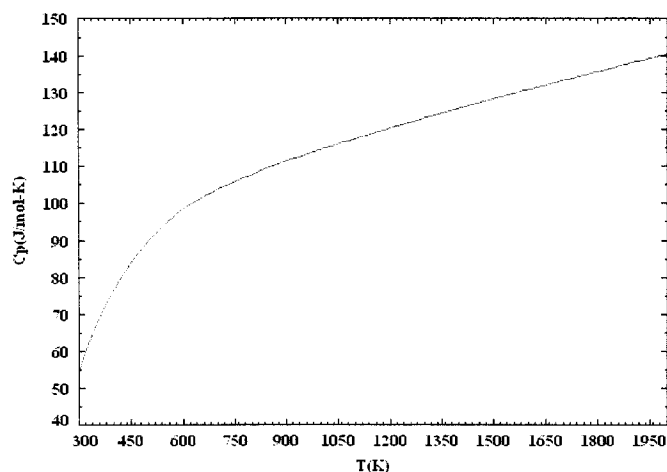
Figure D.15: Cp vs. T for B₄C.

224
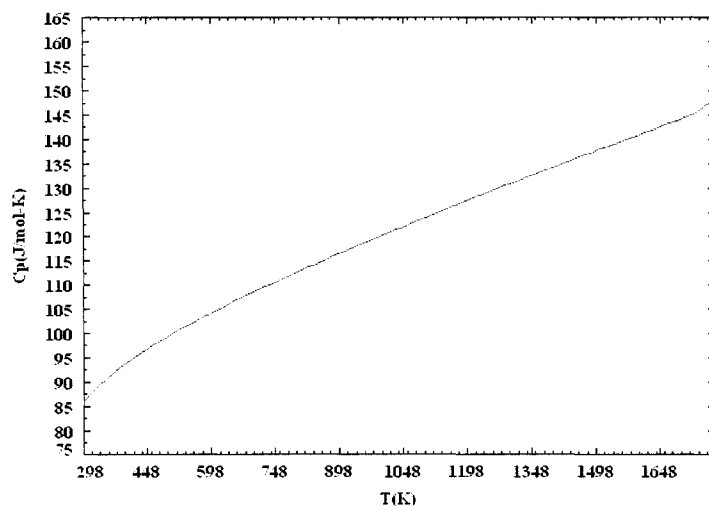
Figure D.16: Cp vs. T for Ni₂B.
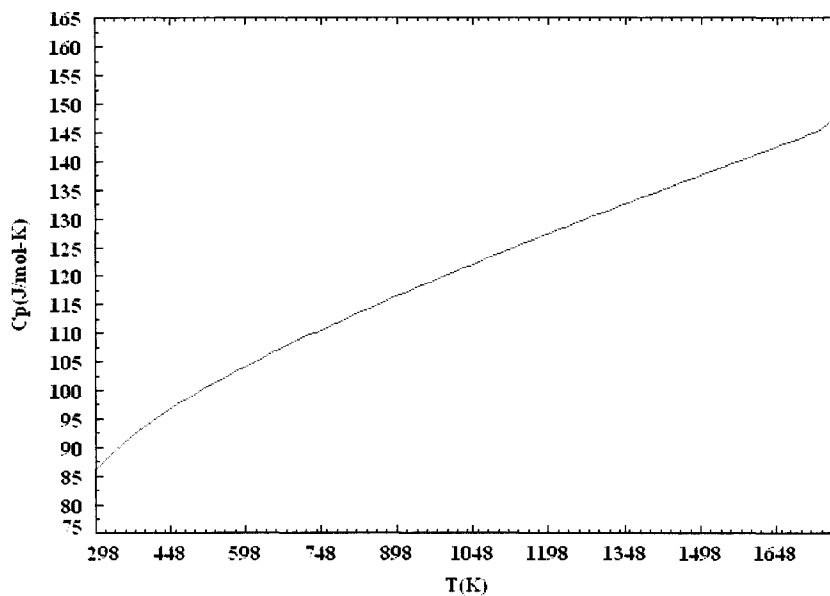
Figure D.17: Cp vs. T for Ni₃B.

225
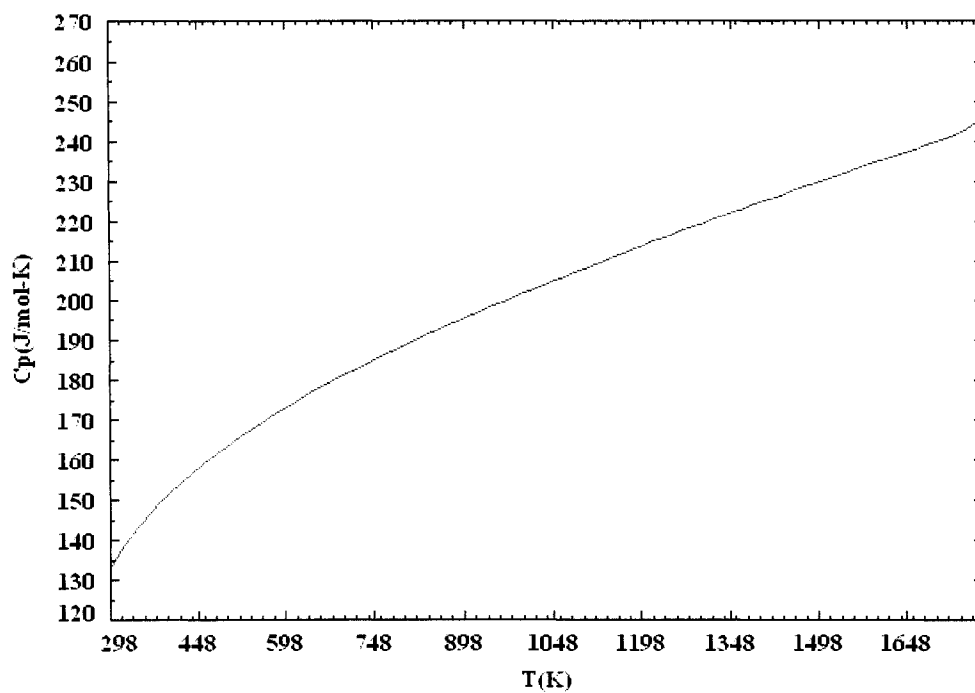
Figure D.18: Cp vs. T for Ni₄B₃.

226

E.0 Thermodynamic Tables/ Sample Calculations.

E.1 Ni-WC System.

Table E.1: Comparison of parameter n to wt% WC reactant.

Parameter n	
Ni (mol)	**wt%WC**
5	40.02
5.5	37.75
6	35.73
6.5	33.92
7	32.28
7.5	30.79
8	29.43
8.5	28.18
9	27.04

```
0.001 Ni + WC
 (1773,1,liq-SGSL,#1)  (1773,1,s-FACT,#1)

    0.11970E-02 mol   ( 0.10413        C                          SGSL
                      + 0.83541        Ni                         SGSL
                      + 0.60461E-01    W                          SGSL)
                        (1773.00 K, 1 atm, LIQUID)

                      + 0.49996    mol  W2C                       FACT
                        (1773.00 K, 1 atm, S1, a= 1.0000)

                      + 0.49991    mol  C_graphite                SGSL
                        (1773.00 K, 1 atm, S1, a= 1.0000)

                      + 0.00000    mol  Ni                        SGSL
                        (1773.00 K, 1 atm, L1, a=0.79130)

                      + 0.00000    mol  Ni_fcc_al                 SGSL
                        (1773.00 K, 1 atm, S1, a=0.76726)

                      + 0.00000    mol  WC_mc_shp                 SGSL
                        (1773.00 K, 1 atm, S1, a=0.63349)
****************************************************************************
   DELTA H      DELTA G      DELTA V      DELTA S    Cp_SUM_PHASES   PROD V
    (J)          (J)          (1)         (J/K)        (J/K)          (1)
****************************************************************************
 4.15733E+04 -6.48508E+03  0.00000E+00  2.71057E+01  1.14107E+01  0.00000E+00
```

Figure E.1: Sample calculation, Ni-WC system at 1773K.

227

```
0.001 Ni + WC + 0.000001 O2
(1773,1,liq-SGSL,#1) (1773,1,s-FACT,#1) (1773,1,g-FACT,#1)

   0.19998E-05 mol   (  0.99990          CO                      FACT
                     +  0.90770E-04      CO2                     FACT
                     +  0.69752E-05      Ni                      FACT
                     +  0.11312E-09      C3O2                    FACT
                     +  0.11250E-09      C2O                     FACT
                     +  0.15782E-11      NiO                     FACT
                     +  0.12799E-11      O                       FACT
                     +  0.12191E-12      C                       FACT
                     +  0.91039E-13      C3                      FACT
                     +  0.26582E-14      C2                      FACT
                     +  0.21595E-15      Ni(CO)4                 FACT
                     +  0.18828E-15      O2                      FACT
                     +  0.81620E-16      WO                      FACT
                     +  0.93092E-17      WO2                     FACT
                     +  0.27633E-17      C5                      FACT
                     +  0.16384E-17      C4                      FACT
                     +  0.13599E-18      W                       FACT
                     +  0.89659E-19      WO3                     FACT
                     +  0.10810E-27      (WO3)2                  FACT
                     +  0.43609E-31      O3                      FACT
                     +  0.15217E-36      W3O8                    FACT
                     +  0.10826E-39      (WO3)3                  FACT
                     +  0.52518E-53      (WO3)4                  FACT)
                        (1773.00 K, 1 atm, gas_ideal)

+  0.11970E-02 mol   (  0.10413          C                       SGSL
                     +  0.83541          Ni                      SGSL
                     +  0.19540E-09      O                       SGSL
                     +  0.60461E-01      W                       SGSL)
                        (1773.00 K, 1 atm, LIQUID)

                     +  0.49996      mol  W2C                     FACT
                        (1773.00 K, 1 atm, S1, a= 1.0000)

                     +  0.49991      mol  C_graphite             SGSL
                        (1773.00 K, 1 atm, S1, a= 1.0000)

**************************************************************************
   DELTA H       DELTA G       DELTA V       DELTA S     Cp_SUM_PHASES   PROD V
    (J)           (J)           (l)           (J/K)         (J/K)         (l)
**************************************************************************
 4.15731E+04  -6.48562E+03  1.45464E-04  2.71059E+01  1.14107E+01  2.90953E-04
```

Figure E.2: Sample calculation, Ni-WC-O$_2$ system at 298K.

228

E.2 Ni-B₄C System.

Table E.2: Comparison of parameter m to wt%Ni reactant.

Parameter m	
B₄C (mol)	wt%B₄C
0.01	0.99
0.04	3.82
0.08	7.36
0.13	10.74
0.17	13.80
0.19	15.25
0.32	23.09
0.64	37.48
0.96	47.36

```
T = 1773.00 K
P = 1.00000E+00 atm
V = 0.00000E+00 dm3

STREAM CONSTITUENTS        AMOUNT/mol    TEMPERATURE/K   PRESSURE/atm
Ni(liq)_SGSL               1.0000E-03       1773.00      1.0000E+00
B4C(s)_FACT                1.0000E+00       1773.00      1.0000E+00

                           EQUIL AMOUNT  MOLE FRACTION     ACTIVITY
PHASE: LIQUID                 mol
B                          7.7234E-04    4.2847E-01      1.6985E-01
C                          3.0222E-05    1.6766E-02      6.7417E-03
Ni                         1.0000E-03    5.5477E-01      2.2713E-01
TOTAL:                     1.8026E-03    1.0000E+00      1.0000E+00
                              mol                         ACTIVITY
B4C(s)_FACT                9.9981E-01                    1.0000E+00
C_graphite(s)_SGSL         1.6286E-04                    1.0000E+00
C_diamond_a4(s2)_SGSL      0.0000E+00                    5.2120E-01
B_beta_rhombo_(s)_SGSL     0.0000E+00                    3.8853E-01
NiB_nib(s)_SGSL            0.0000E+00                    2.8598E-01
Ni(liq)_SGSL               0.0000E+00                    2.2713E-01
Ni_fcc_a1(s)_SGSL          0.0000E+00                    2.2023E-01
'Ni2B'_m2b_tet(s)_SGSL     0.0000E+00                    2.0870E-01
B(liq)_SGSL                0.0000E+00                    1.6985E-01
Ni3B_ni3b(s)_SGSL          0.0000E+00                    9.6937E-02
B4C(liq)_FACT              0.0000E+00                    6.7908E-02
'Ni4B3'_ni4b3(s)_SGSL      0.0000E+00                    1.4882E-02
Ni3C_cementite(s)_SGSL     0.0000E+00                    1.1243E-02
C(liq)_SGSL                0.0000E+00                    6.7417E-03
***********************************************************************
  DELTA_Cp      DELTA_H      DELTA_S       DELTA_G       DELTA_V
   J.K-1          J          J.K-1           J            dm3
***********************************************************************
 2.16511E-03  1.14563E+00  1.29701E-02  -2.18504E+01  0.00000E+00
```

Figure E.3: Sample Calculation, Ni-B₄C system at 1773K.

229